Study of different SOA structures impact on the transmission of IMDD OOFDM signals

Mohamad Hamze

THÈSE / UNIVERSITÉ DE BRETAGNE OCCIDENTALE
sous le sceau de l'Université européenne de Bretagne

pour obtenir le titre de
DOCTEUR DE L'UNIVERSITÉ DE BRETAGNE OCCIDENTALE
Mention : Optoélectronique - Hyperfréquences
École Doctorale SICMA 0373

Présentée par
Hamze Mohamad
Préparée au Laboratoire Lab-STICC UMR CNRS 6285
École Nationale d'Ingénieurs de Brest (ENIB)
et Arts Sciences and Technology University in Lebanon (AUL)

Study of different SOA structures impact on the transmission of IMDD OOFDM signals

Soutenue le 09/06/2015, devant le jury composé de :

Christelle AUPETIT-BERTHELEMOT
Professeur des Universités, XLIM, Université de Limoges / Présidente
Izzat DARWAZEH,
Professor, University College of London / Rapporteur
Christophe PEUCHERET
Professeur des Universités, Foton, ENSSAT / Rapporteur
Chao LU
Professor, Hong Kong Polytechnic University / Examinateur
Ammar SHARAIHA
Professeur des Universités, Lab-STICC, ENIB / Directeur de thèse
Mikael GUEGAN
Maître de Conférences, Lab-STICC, ENIB / Co-Encadrant
Ali Hamié
Professor, lab CRITC, AUL - Liban / Co-Encadrant
Pascal MOREL
Maître de Conférences, Lab-STICC, ENIB / Co-Encadrant
Adnan HAMZE
Professor, président de AUL - Liban / Invité

Acknowledgements

I would like to express my sincere gratitude to my thesis director Prof. Ammar Sharaiha from ENIB and my thesis co-director Prof. Ali Hamie form AUL for their guidance, support, patience, and time spent with me on producing this work. The ideas and experience they have given me where invaluable for the work done. Without their support, it would have been extremely difficult to complete the thesis.

I would like also to express my sincere gratitude to my co-supervisors Dr. Mikael Guegan and Dr. Pascal Morel from ENIB for their support, help, and guidance throughout the work, and for the time spent in helping me in simulations, experimental work, and writing of the thesis, it has been a pleasure working with them.

I thank Prof. Izzat Darwazeh from University College London, and Prof. Christophe Peucheret from ENSSAT for accepting to be my thesis reviewers, I also thank Prof. Christelle Aupetit-Berthelemot and Prof. Chao Lu for accepting to be my thesis examiners.

I thank a lot Prof. Adnan Hamze President of AUL University for the moral and financial support during my thesis.

I would like to thank all the people at both ENIB and AUL who have helped me during my thesis, for their freindship, and for the enjoyable environment.

Finally, I can never thank enough my parents for their support in all aspects, I will be always grateful to them.

Table of contents

RÉSUMÉ

Ce travail de thèse est une étude sur l'impact de différentes structures de SOA sur les performances de transmission de signaux optiques OFDM lorsque le SOA est utilisé comme modulateur d'intensité et lorsque les signaux optiques OFDM transmis sont détectés en détection directe (IMDD-OOFDM). Cette étude s'effectue dans le cadre des réseaux d'accès de nouvelle génération.

CHAPITRE 1 : GÉNÉRALITÉS SUR LES SYSTÈMES DE TRANSMISSION IMDD-OOFDM

Évolution des réseaux optiques

Suite à la demande toujours accrue des consommateurs, les réseaux de communication ont beaucoup évolué ces dernières années : le câble coaxial a été remplacé dès 1950 par le câble de cuivre puis par la fibre optique à partir des années 80, pour les réseaux à longue et moyenne portées. En effet, le produit débit- distance (BL, où B est le débit binaire (bit/s) et L l'espacement entre les répéteurs (km)), utilisé comme un facteur de mérite, est limité dans les câbles coaxiaux et cuivre, en raison des pertes qui augmentent fortement avec la fréquence du signal transporté (Fig. R-1). Ainsi, trouver un nouveau support de transmission offrant des valeurs de BL plus élevées est devenu nécessaire et l'avènement de la fibre optique s'est très rapidement avéré depuis les années 80 comme la meilleure solution en raison de sa faible atténuation et de sa grande bande passante.

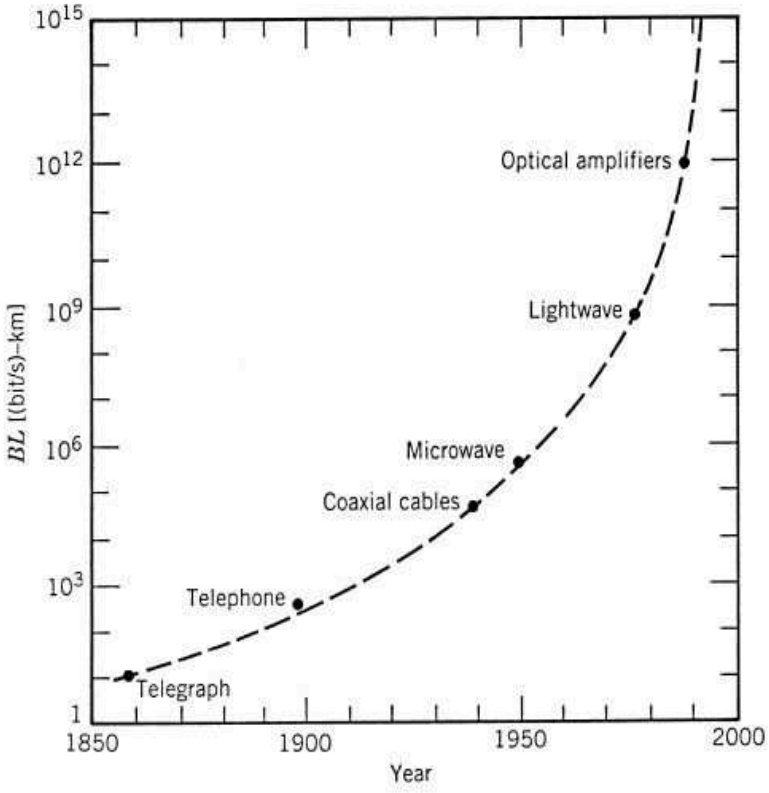

Figure R- 1: Augmentation du produit BL au cours de la période 1850-2000. [1].

Aujourd'hui, la fibre peut transmettre la lumière dans le moyen infrarouge (autour de 1,5µm) avec des pertes de l'ordre de 0,2 dB/km sur une bande spectrale de près de 200nm (soit environ 25THz) [1]. Dans un premier temps, pour allonger la distance de transmission des communications optiques longues distances, des répéteurs optoélectroniques ont été utilisés. Puis, progressivement dès les années 90, l'avènement de l'amplification tout-optique (amplificateurs à fibre dopé EDFA) a permis de remplacer ces répéteurs pour développer des réseaux optiques transparents (au format de modulation), surmonter le goulot d'étranglement électronique et permettre l'amplification de signaux optiques multiplexés en longueur d'onde (amplification multicanaux WDM), gage d'une montée significative certaine du débit.

D'un point de vue topologique, l'infrastructure du réseau optique peut être découpée/organisée en zones géographiques comme le montre la figure R-2. Les trois échelles couramment utilisées sont : le réseau d'accès (Access network), le réseau métropolitain (Edge network) et le réseau cœur (Core network).

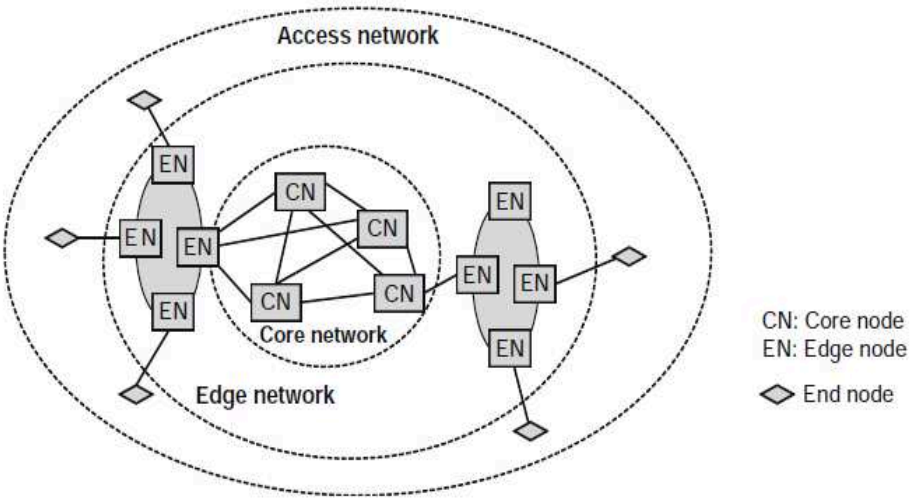

Figure R- 2 : Exemple d'une architecture type de réseau optique.

La Figure R- 3 indique l'évolution récente (40 dernières années) du débit binaire sur les réseaux cœur et accès. Ce débit a été multiplié par 100 sur la dernière dernière décennie pour les réseaux d'accès afin de répondre à l'énorme demande en capacité de trafic liée aux nouveaux services comme majoritairement la télévision HD et les jeux vidéos en réseau. Cette augmentation spectaculaire du débit a été rendue possible grâce à plusieurs techniques : le multiplexage temporel (TDM : Time Division Multiplexing), le multiplexage spectral (WDM : Wavelength Division Multiplexing), les formats de modulation avancés, la transmission cohérente et les techniques de traitement du signal.

Dans le cadre des réseaux optiques passifs (PON), parmi plusieurs techniques, l'emploi de l'OOFDM-PON (OOFDM-PON : Optical Orthogonal Frequency Division Multiplexing-Passive Optical Networks) et la modulation

OOFDM adaptative (AMOOFDM) [2, 3] sont considérés comme des formats prometteurs pour la mise en œuvre pratique des prochaines générations de réseaux d'accès large bande. Ces formats disposent d'un grand nombre d'avantages inhérents comme par exemple, leur haute efficacité spectrale, leur excellente adaptabilité aux performances composant/système/réseau en raison des imperfections des capacités de bits adaptative et la puissance de chargement (PL : Power Loading), le potentiel des solutions techniques rentables, en raison de la pleine utilisation des progrès rapides dans le traitement de signal numérique (DSP). En plus de tous ces avantages, l'OOFDM peut aussi améliorer considérablement la reconfiguration dynamique et la flexibilité du système émetteur-récepteur pour réaliser des PON élastiques et maintenir leur compatibilité avec TDM PON existants [4].

Il est important de préciser que pour les réseaux d'accès optiques, les systèmes à modulation d'intensité et détection directe (IMDD : Intensity Modulation and Direct Detection) sont préférés en raison de leur simplicité de mise en œuvre et de leur faible coût comparativement à la détection cohérente.

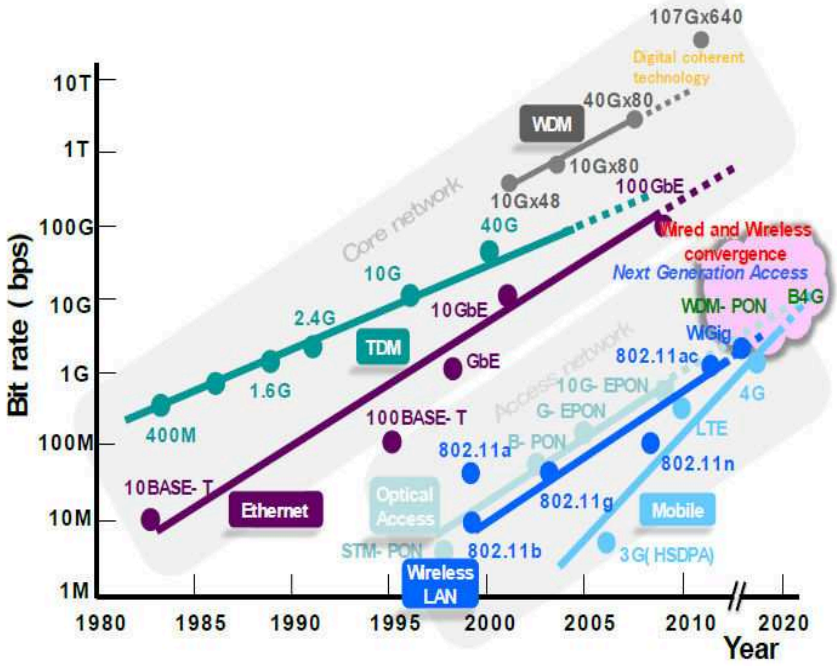

Figure R- 3 : Evolution du débit binaire dans les réseaux optiques cœur et d'accès.

Pour ces systèmes IMDD, l'emploi d'amplificateurs optiques à semi-conducteurs (SOA) et d'amplificateurs optiques à semi-conducteurs réflectifs (RSOA) en tant que modulateurs d'intensité est envisagé en particulier en raison de leur grand intérêt pour des applications large bande (colorless) de type WDM-PON. Dans ce contexte, le travail de thèse a porté sur l'étude de l'impact de différentes structures SOA sur la transmission de signaux OOFDM pour les systèmes IMDD OOFDM. Il a été effectué dans le cadre d'une collaboration entre l'ENIB en France, l'Université AUL au Liban, et l'Université de Bangor au Royaume-Uni. L'étude expérimentale et théorique concernant l'amplificateur

optique à semi-conducteur réflectif a été menée en France au Lab-STICC, UMR CNRS (6285) à l'ENIB, tandis que l'étude théorique et numérique sur les systèmes AMOOFDM utilisant différentes structures de SOA a été effectuée à l'Université AUL au Liban.

Chapitre 2 : Modélisation d'un RSOA et validation expérimentale

Nous avons utilisé un modèle large bande de SOA qui a été réalisé durant le travail de thèse de P. Morel [5, 6]. Ce modèle est un modèle large bande implémenté dans le domaine temporel et permettant de simuler la plupart des effets non-linéaires du SOA. La modélisation repose sur des équations d'évolution des porteurs écrites dans chacune des M sections de calcul et en considérant la densité de porteurs constante au sein de chaque section (Fig. R-4).

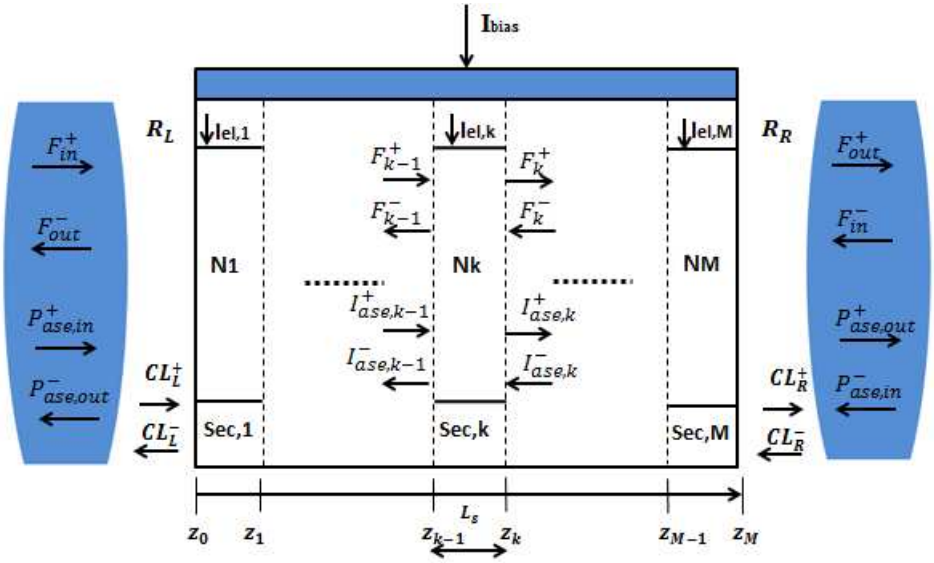

Figure R- 4 : Principe de modélisation de la cavité du SOA découpée en M sections.

Afin de résoudre les M équations différentielles liées aux sections de calcul, nous avons utilisé le simulateur de circuits électroniques ADS d'Agilent Technologies [6]. Ce dernier a l'avantage de permettre la réalisation de plusieurs types de simulations telles que la simulation DC (courant continu), AC (courant alternatif), temporelle (transitoire) et HB (équilibre harmonique). Le modèle utilisé a été validé pour un RSOA disponible au laboratoire (CIP SOA-RL-OEC 1550) dont les caractéristiques sont données dans l'annexe de cette thèse.

Les paramètres du modèle ont été obtenus par optimisation. Les mesures ont été effectuées sur une large plage de puissance optique incidente, de la longueur d'onde et de courant de polarisation. Nous avons obtenu une bonne concordance entre les résultats de simulation et les mesures en termes de gain, de facteur de bruit, et de puissance de saturation (Fig. R-5). Nous avons également validés le modèle d'un point de vue dynamique en obtenant des résultats conformes aux mesures en termes de bande passante électrique, de produits de

distorsion d'intermodulation et de facteur de couplage phase amplitude α_H (Fig ; R-6).

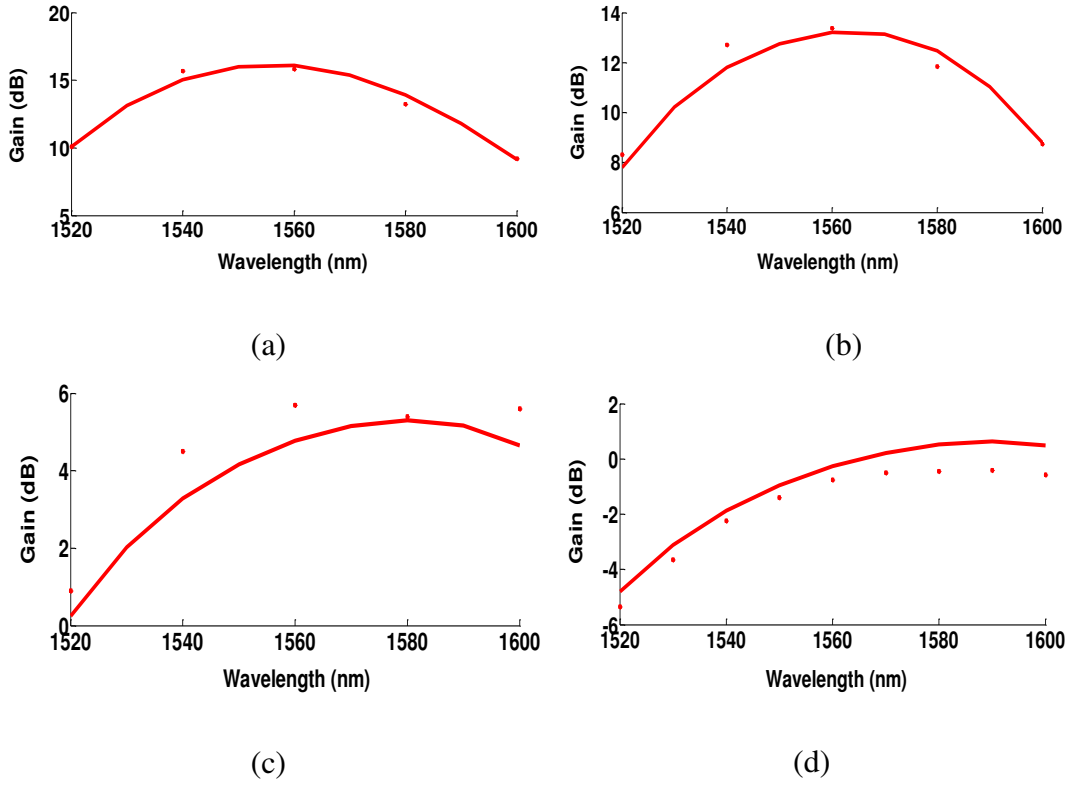

Figure R- 5 : Résultats de mesure (pointillés) et de simulation (ligne pleine) pour le gain du RSOA en fonction de la longueur d'onde avec un courant de polarisation de 70 mA et une puissance d'entrée de (a) -20 dBm (b) -10 dBm (c) de 0 dBm et (d) 4 dBm.

La Figure R- 5 montre le gain optique simulé et mesuré en fonction de la longueur d'onde, pour un courant de polarisation de 70 mA et pour quatre puissances optiques d'entrée différentes. La Figure R- 6 montre les résultats des mesures et des simulations du facteur α_H dans la bande passante du gain optique du RSOA. Un bon accord est obtenu entre les deux résultats pour une bande passante optique de 60 nm.

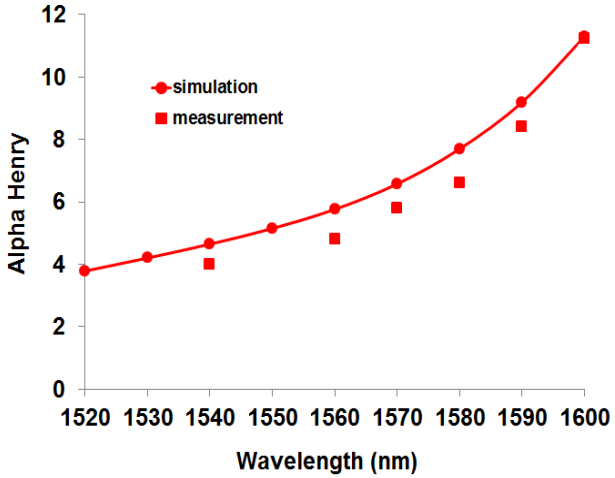

Figure R- 6 : Résultats de mesure et de simulation du facteur de couplage phase amplitude α_H en fonction de la longueur d'onde avec un courant de polarisation de 80 mA et une puissance optique d'entrée de -7 dBm, le signal de pompe a une longueur d'onde de 1550 nm.

Chapitre 3 : Analyse expérimentale et numérique des SOA en tant que modulateurs d'intensité et convertisseurs de longueur d'onde pour les systèmes de transmission IMDD-OOFDM

Dans cette partie, nous présentons d'abord la chaîne de co-simulation développée, et le dispositif expérimental mis en place, puis nous analysons ensuite les résultats expérimentaux et numériques concernant les performances du RSOA en tant qu'émetteur IMDD-OOFDM et en tant que convertisseur de longueur d'onde. Cette étude est effectuée en fonction de la puissance optique d'entrée, la longueur d'onde et le courant de polarisation.

Plateforme de co-simulation pour la simulation IMDD-OOFDM

La Figure R- 7 présente la plateforme de co-simulation IMDD-OOFDM que nous avons développée. L'émetteur et le récepteur sont mis en œuvre dans MATLAB, le modèle de RSOA est implémenté dans ADS. Le modèle de la fibre SMF est simulé par le logiciel VPI.

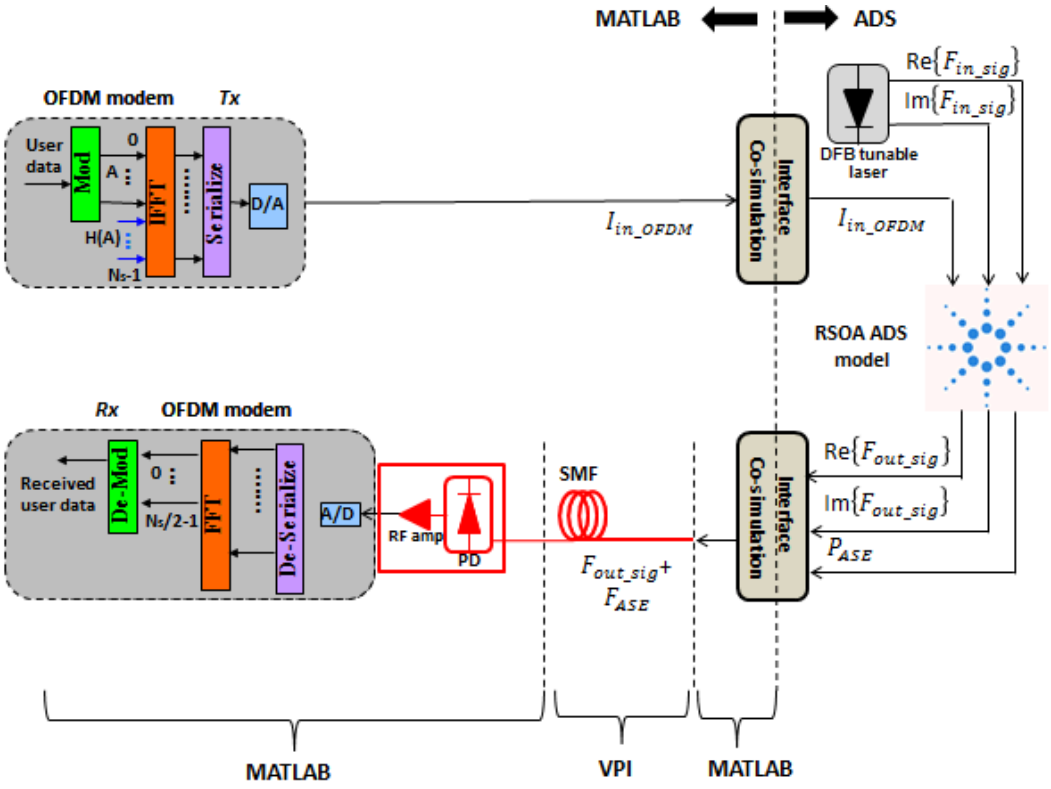

Figure R- 7 : Plateforme de co-simulation IMDD-OFDM pour un RSOA.

Dispositif expérimental IMDD-OOFDM

La Figure R- 8 montre le montage expérimental mis en place pour l'IMDD-OOFDM au Lab- STICC, UMR CNRS 6285.

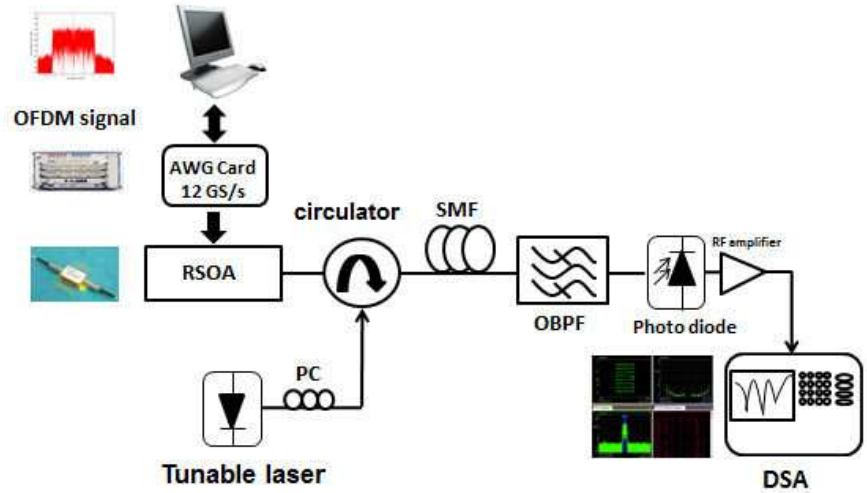

Figure R- 8 : Schéma du dispositif expérimental utilisé.

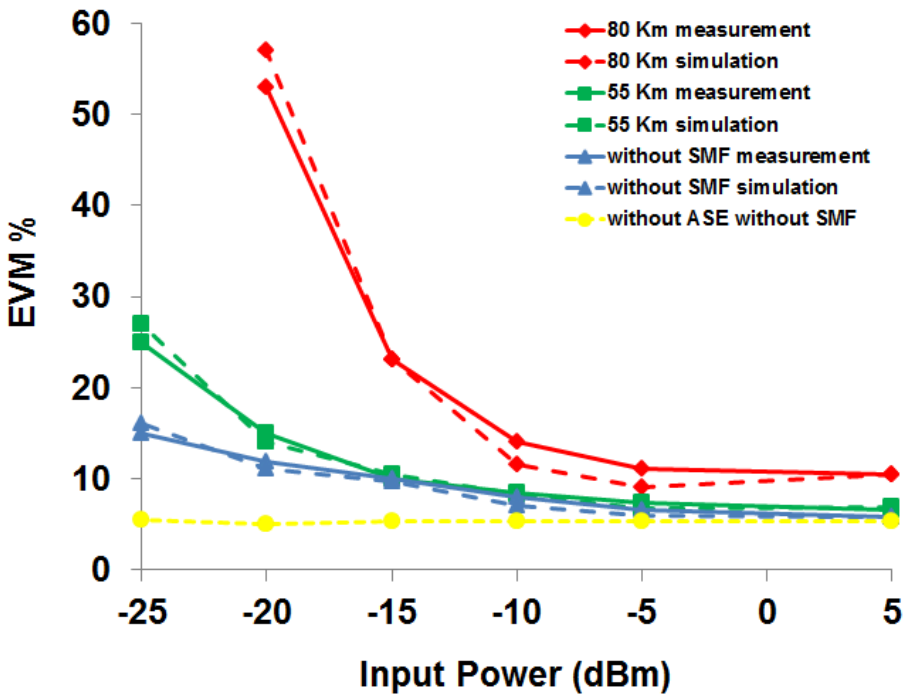

Figure R- 9 : EVM en fonction de la puissance d'entrée pour le signal 16 QAM - OOFDM pour différentes longueurs de fibre SMF. La largeur de la bande passante de signal est de 500 MHz, le RSOA est polarisé à 65 mA, le signal OOFDM est à 1570 nm, et le courant OFDM est de 7 mA.

Tout en utilisant le dispositif expérimental développé, nous avons validé la plateforme de co-simulation dans diverses configurations. La Figure R- 9 montre que la plateforme de simulation est validée en comparant l'EVM (Error Vector Magnitude) obtenue en simulation et en mesure, pour différentes longueurs de la fibre SMF et en fonction de la puissance optique incidente. Après cette validation de la plate-forme de co-simulation, nous avons continué l'analyse des performances de transmission du RSOA toujours en fonction de la puissance optique incidente et de la longueur de fibre mais également en fonction de l'ASE, de la bande passante électrique et des non-linéarités du RSOA. Nous avons ainsi montré théoriquement qu'une capacité minimale de transmission de 8,9 Gb/s sur 100 km pouvait être atteinte sur une plage spectrale de 100 nm à l'aide d'une modulation adaptative AMOOFDM (Figures R- 10 et R- 11).

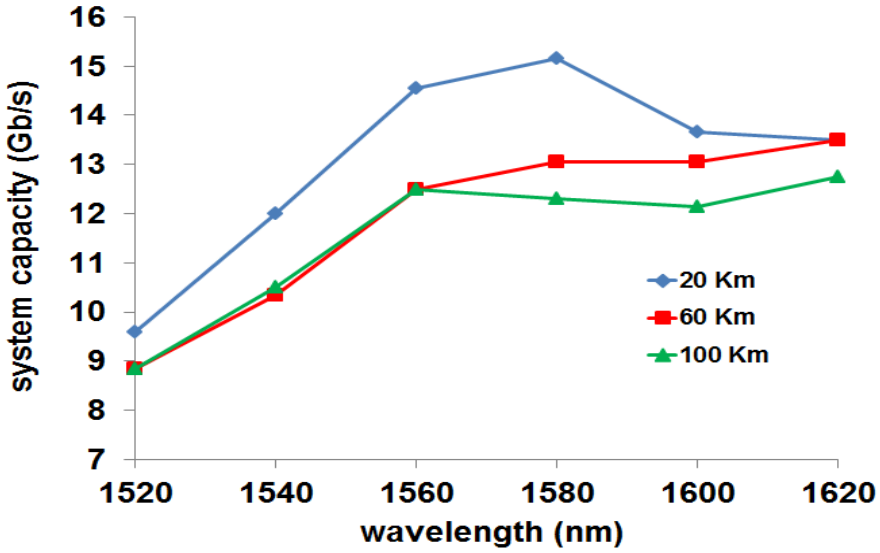

Figure R- 10 : Capacité de transmission en fonction de la longueur d'onde pour un signal de type AMOOFDM et pour différentes distances de transmission.

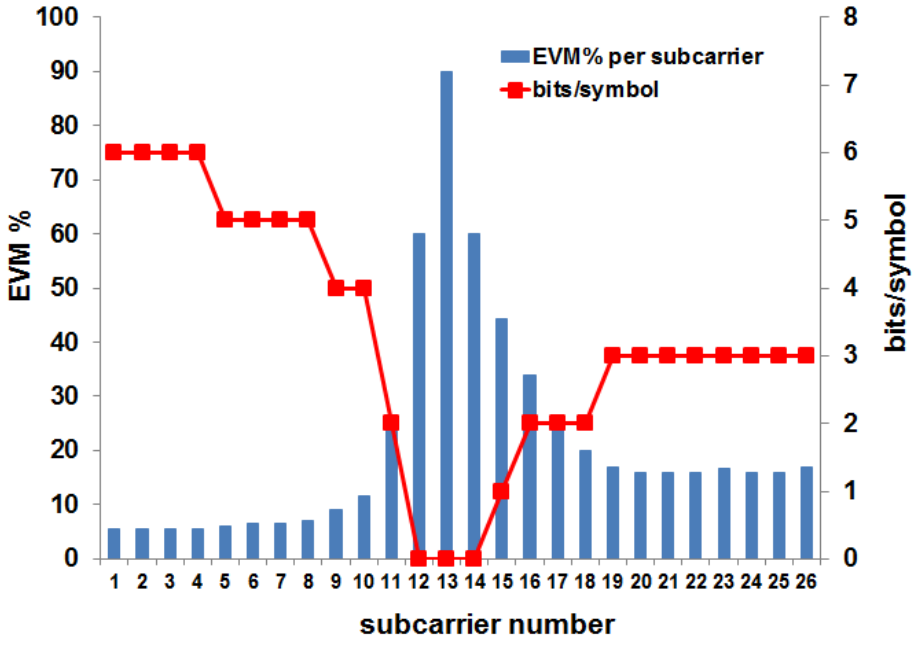

Figure R- 11 : Exemple de l'utilisation de la modulation adaptative d'un signal transmis OOFDM 6 GHz sur 100 km SMF.

Nous avons également démontré expérimentalement, pour la première fois à notre connaissance, la conversion de longueur d'onde de signaux optiques OOFDM-16QAM sur une large plage spectrale de 70 nm en utilisant l'effet de modulation croisée du gain (XGM) dans le RSOA.

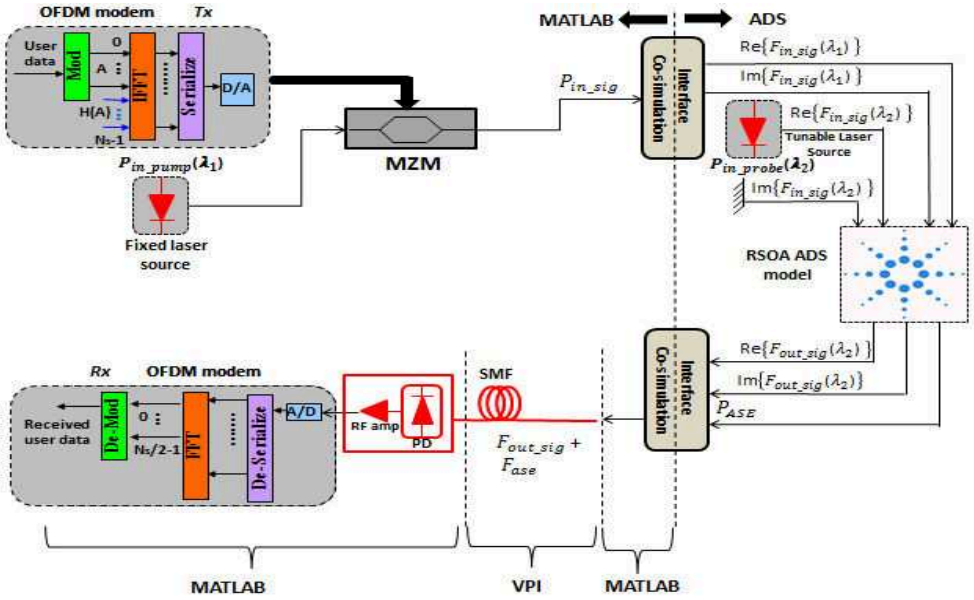

Figure R- 12 : Plate-forme de co-simulation implémentée pour la conversion de longueur d'onde de signaux OOFDM utilisant le RSOA.

La Figure R- 12 montre la plate-forme de co-simulation implémentée pour la conversion de longueur d'onde de signaux OOFDM, en utilisant la modulation croisée du gain (XGM) du RSOA. Bien que le RSOA utilisé ne soit pas optimisé pour des applications de conversion de longueur d'onde, nous avons montré qu'à l'aide de l'AMOOFDM-IMDD, une capacité de transmission d'au moins 11 Gb/s pouvait être atteinte sur une large bande passante optique de 90 nm ; ceci dans le cas d'une distance de 60 km de fibre SMF (Figure R- 13).

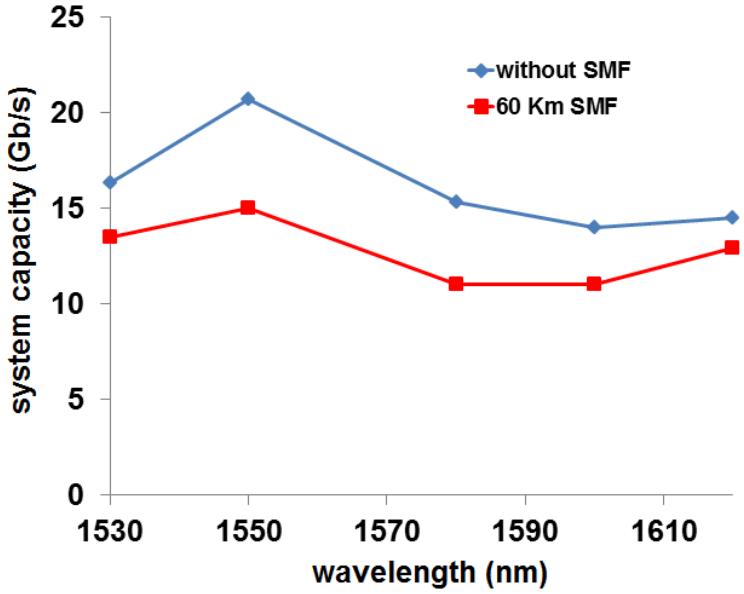

Figure R- 13 : Capacité de transmission en fonction de la longueur d'onde pour un signal converti AMOOFDM

Chapitre 4 : Étude théorique et numérique d'un système de transmission IMDD à base d'AMOOFDM en utilisant différentes structures de SOA

Dans ce chapitre, nous présentons l'emploi de la modulation d'intensité AMOOFDM dans un système de transmission IMDD et en utilisant différentes structures de SOA. Le système est conçu de manière à effectuer une étude théorique et numérique concernant le potentiel de l'utilisation de l'OOFDM pour les futurs réseaux d'accès optiques qui fonctionnent à capacité de transmission élevée et pour des distances allant jusqu'à 100 km. La Figure R- 7 montre la structure générale du système de transmission utilisé. Nous expliquons d'abord le système en détail, puis nous présentons les résultats de travaux antérieurs réalisés sur l'utilisation de ce système avec des lasers DFB, une architecture SOA et un RSOA en tant que modulateurs d'intensité. Nous détaillons ensuite notre nouveau travail sur l'utilisation de SOA à îlots quantiques (QD-SOA), deux SOA à deux électrodes (2ESOA), deux SOA en cascade dans une configuration de contrapropagative (TC-SOA-CC), tous utilisés en tant que modulateurs d'intensité dans le système IMDD-AMOOFDM développé. Dans ce travail, nous avons développé un modèle pour chaque type de SOA étudié. Les résultats obtenus démontrent le potentiel de l'utilisation de ces trois structures SOA pour les futurs systèmes IMDD incorporant l'AMOOFDM.

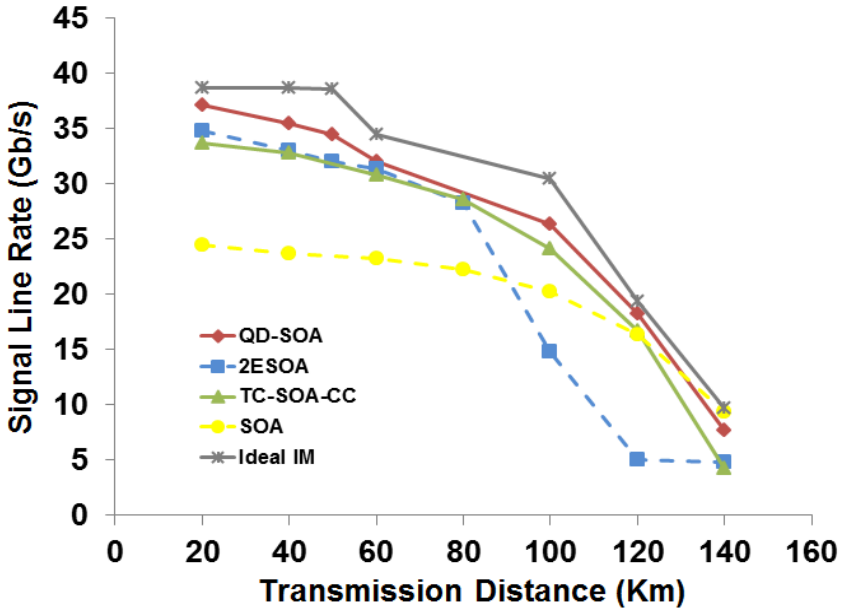

Figure R- 14 : Capacité de transmission en fonction de la distance parcourue pour les structures SOA étudiées.

Nous avons montré que les trois configurations peuvent fournir une capacité de transmission de 30 Gb/s sur des distances de transmission jusqu'à 60 km. Nous avons montré également que le QD-SOA présente les meilleures performances en termes de capacité de transmission pour des distances allant jusqu'à 140 km en comparaison avec les deux autres configurations SOA. La

Figure R- 14 présente une comparaison entre 5 structures de SOA différentes et utilisées comme modulateurs d'intensité avec une puissance d'entrée de 10 dBm. Ces résultats prouvent que la meilleure performance en termes de capacité est bien celle du QD-SOA, et que ce dernier atteint la même capacité qu'un modulateur d'intensité idéal pour une distance de transmission de 20 km d'une part et comprise entre 120 et 140 km d'autre part. La structure 2ESOA présente la même capacité que le TC SOA -CC jusqu'à 80 km. Après, nous voyons une très forte dégradation en raison du faible taux d'extinction offert par le 2ESOA, qui implique une dégradation des performances pour des distances de transmission au-delà de 100 km. La performance du SOA est beaucoup moins élevée que les autres configurations. Mais elle reste cependant nettement meilleure que celle du 2ESOA pour des distances supérieures à 90 km et que celle du TC SOA -CC pour des distances supérieures à 120 km.

Conclusion

Ce travail de thèse est divisé en deux grandes parties. La première porte sur le développement d'une plateforme de co-simulation IMDD-OFDM pour un RSOA utilisé comme modulateur d'intensité et aussi en tant que convertisseur de longueur d'onde. Les résultats obtenus par simulation sont validés expérimentalement sur une large gamme de puissance optique incidente, de longueur d'onde, de bande passante et de courant de polarisation. La plateforme validée, des simulations numériques sont effectuées afin d'étudier l'effet de plusieurs paramètres sur la qualité de transmission comme le bruit de l'ASE, la bande passante électrique du signal, la préamplification, la longueur de la fibre monomode, la dispersion chromatique, la distorsion d'intermodulation, la modulation multi-porteuse, le format de modulation. Cette étude a permis également d'exploiter la modulation croisée du gain (XGM) du RSOA pour la réalisation d'une conversion de longueur d'onde sur une large bande de 100 nm.

La deuxième partie est une étude théorique et numérique d'un système de transmission de type AMOOFDM qui utilise trois structures de SOA différentes. Ces trois structures (QD-SOA, TC-SOA-CC et 2ESOA) sont comparées en termes de capacité de transmission, de distance de transmission, de consommation d'énergie et de flexibilité en termes de conditions d'exploitation. Le QD-SOA et le TC-SOA-CC sont également étudiés en termes de compensation de dispersion chromatique. Ce travail a permis de montrer les principaux paramètres limitant la capacité du système de transmission tels que la bande passante du signal, l'écrêtage du signal, le taux d'extinction et l'impact des effets non linéaires du SOA a été étudié.

INTRODUCTION

There has been a huge increase in the demand for high speed communication in the past decade due to the need of high speed applications such as the internet, video on demand, high definition TV, and other application oriented communications. These high speed needs make it impossible to avoid the use of the optical fiber as a means of communication even for the access network stage. In order to increase more the transmission capacity of optical networks, a variety of spectrally efficient advanced modulation formats are used as in wireless communication systems. For optical access networks, intensity modulation and direct detection (IMDD) is preferred due to its simplicity, low complexity, and low cost as compared to the coherent optical and all optical options. Passive optical networks (PONs) are being widely adopted and practically implemented as a promising "future-proof" high-speed strategy for broadband access due to their low cost, high reliability, and easy maintenance. A PON with longer reach can further enhance cost efficiency for the broadband optical access network. Long-reach PON (LR-PON) extends the coverage span of PONs from the traditional 20 km range to 100 km and beyond by exploiting optical amplifiers in the middle of the transmission fiber spans. LR-PON combines optical access and metro into an integrated system. The merging of the two types of networks simplifies the hierarchical architecture of the telecommunications network with the long-reach access linked directly to the backbone network, which reduces the number of equipment interfaces, network elements, and even nodes, resulting in energy savings and green communications [7]. Another technique which is also required and currently inevitable for increasing the optical access network capacity is wavelength division multiplexed-PON (WDM-PON). WDM systems will require optical components that have a wide optical bandwidth. Semiconductor Optical Amplifiers (SOAs) and reflective SOAs (RSOAs) are very good candidates for these systems as transmitters in particular for IMDD optical orthogonal frequency division multiplexing (IMDD-OOFDM) signals [8].

In this context, the thesis work deals with study of different SOA structures impact on the transmission of IMDD OOFDM which has been done in the framework of a collaboration between AUL University in Lebanon, Bangor University in UK, and ENIB in France. The experimental and theoretical study concerning a reflective semiconductor optical amplifier has been done in France in Lab-STICC, UMR CNRS (6285) whereas the theoretical and numerical study about AMOOFDM using different SOA structures was conducted at AUL University in Lebanon. The used OFDM transceiver had been previously developed at Bangor University in the UK in the School of Electronic Engineering

This manuscript is divided into four chapters in addition to the introduction and the conclusion. Chapter one consists of an overview on IMDD-OFDM transmission systems. Chapter 2 and chapter 3 are grouped in one part which represents the work conducted mainly at Lab-STICC at ENIB. We present in chapter 2 a comprehensive SOA/RSOA model used in a co-simulation platform dedicated to IMDD-OOFDM transmission systems. This model was fitted on a commercially available RSOA device by performing parameter extraction, and validated experimentally in static and dynamic regimes over a large number of operating conditions (optical bandwidth, input power, bias current, ext.…). Chapter 3 is devoted to the presentation of the developed co-simulation platform for IMDD-OOFDM and OOFDM wavelength conversion transmission systems. We also present the measurement setup using the RSOA as intensity modulator and wavelength converter. We perform a numerical and experimental study in which we analyze the transmission performance in terms of optical input power, fiber length, amplified spontaneous emission (ASE) noise, electrical bandwidth, number of subcarriers, and single carrier or multicarrier transmission.

Chapter 4 is in the second part, conducted mainly at AUL, where we present a theoretical and numerical study of an adaptively modulated OOFDM (AMOOFDM) transmission system using three different SOA configurations (a quantum dot SOA (QD-SOA), a two electrode SOA (2ESOA) and two cascaded SOAs in a counter-propagating configuration (TC-SOA-CC)) as intensity modulators in the developed AMOOFDM IMDD system. We have developed a model for each SOA type, verified the models in static regime, and performed a study of the transmission system in terms of system capacity vs reach performance, optimum operating conditions, signal clipping effect, and fiber chromatic dispersion effects.

1 OVERVIEW ON IMDD-OOFDM TRANSMISSION SYSTEMS

1.1 Evolution of optical transmission systems

There has been an evolution in communication networks due to the increased consumer demand; The bit rate-distance product (BL) is used as a figure of merit for communication systems, where B is the bit rate (bit/sec) and L is the repeater spacing (km).

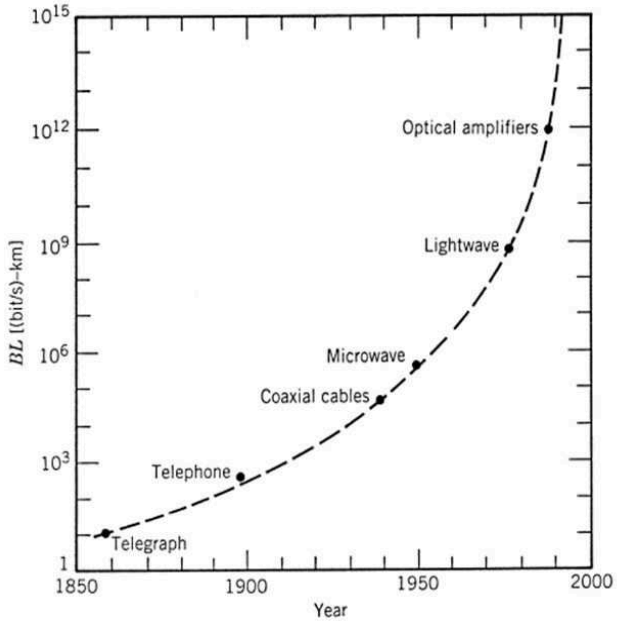

Figure 1- 1 : Increase in bit rate distance product BL during the period 1850-2000. The emergence of a new technology is marked by a solid circle [1].

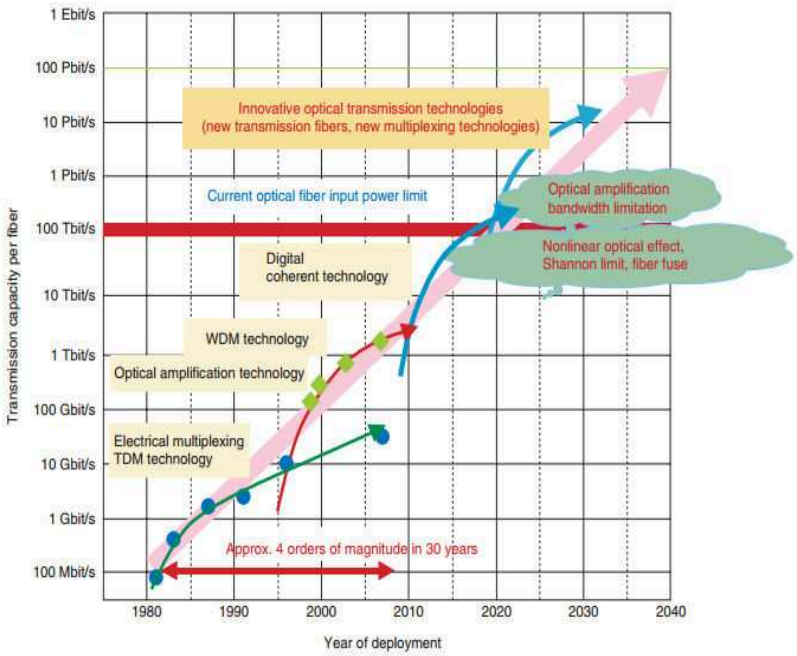

Figure 1- 2 : Evolution in optical transmission technology [9].

In coaxial cables, the bandwidth of communication systems was limited due to the frequency dependent cable losses and the microwave communication

systems that where available around 1970 had a BL product of 100 (Mbit/sec)-km. A new medium of transmission at higher BL values was needed and optical fiber was selected as the best option due to their ability to guide laser light since the 1960's. The main problem was that optical fibers in the 1960s had a high loss of around 1000 dB/km. The fiber optic revolution started in the 1970 (corning) when a fiber with 17 dB/km was available, and in 1978 (NTT) with a loss of only 0.2 dB/km at 1550 nm [1]. In optical telecommunication bands, semiconductor lasers operating continuously at room temperature were demonstrated [1]. The availability of both compact optical sources and low loss optical fibers has led to a worldwide effort for developing fiber optic communication systems. In order to reach long distances for optical fiber communication systems, optoelectronic repeaters were used at the beginning [1]. The problem was solved with the 4th generation of optical systems with the advent of optical fiber amplification. Optical amplifiers allowed the development of optical transparent networks and allowed overcoming the electronic bottleneck. The bit rate was also increased by the use of wavelength division multiplexing (WDM) [1]. WDM is used in the Atlantic and Pacific fiber optic cables and many other places. While WDM techniques were mostly used in long-haul systems employing EDFA for online amplification. Access networks were requiring more bandwidth [1]. Figure 1- 2 shows three main technological innovations that have helped in the development of optical transmission technologies, time division multiplexing (TDM) technology based on electrical multiplexing, optical amplification technology combined with wavelength division multiplexing (WDM) technology, and digital coherent technology, which is currently undergoing research and development [9].

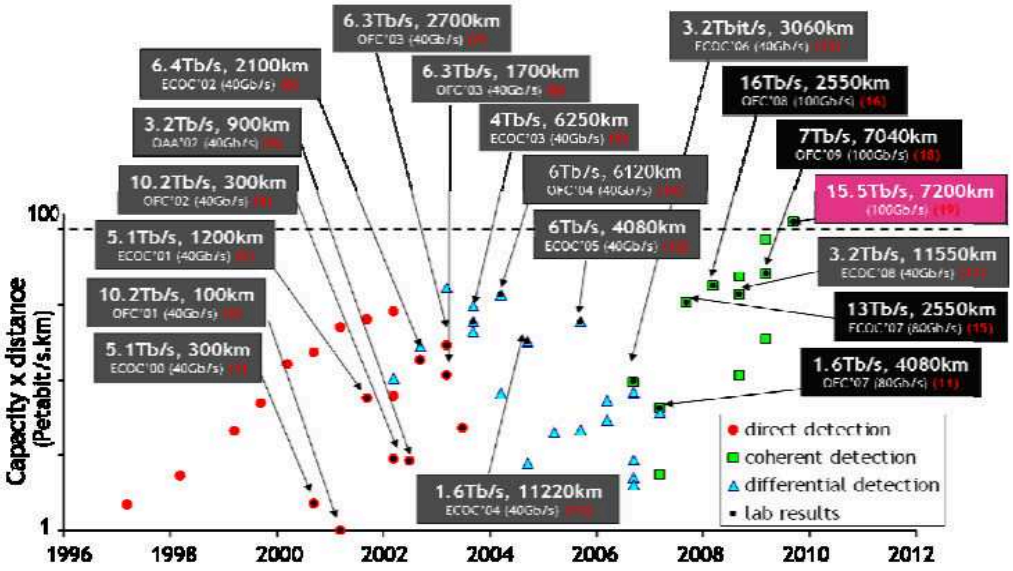

Figure 1- 3 : Capacity × distance product over the last 16 years [from Alcatel-Lucent Bell Labs].

Figure 1- 3 shows the product 'capacity x distance' of many published research works of the last 16 years. Many system manufacturers are present on

this graph and there are details concerning the work done by Alcatel-Lucent. The important point to notice is the saturation concerning the improvement of the 'capacity x distance' product in the recent years for the direct detection case. New technologies are required to continue to increase the 'capacity x distance' product. The use of a wide optical bandwidth amplifier is seen as a key approach.

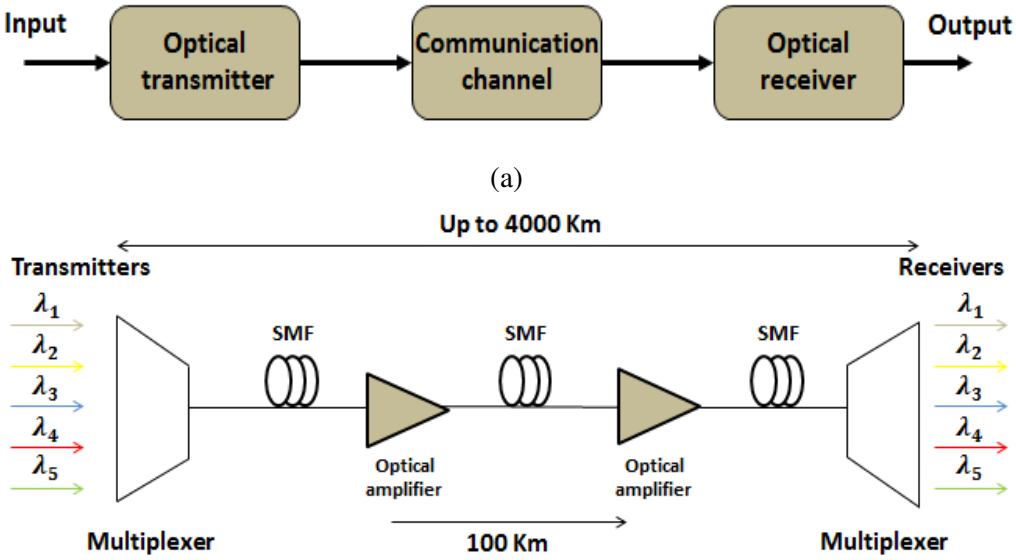

Figure 1- 4 : Schematic diagram (a) a system of optical fiber communication and (b) WDM systems.

Figure 1- 4(a) shows the diagram of an optical fiber communication system. It consists of a transmitter, a communication channel, and a receiver. Optical fiber communication systems are classified into two categories: long haul and short haul, depending if the optical signal is transmitted over long or short distances. Telecommunication systems require long haul high capacity trunk lines. Many transoceanic optical systems have been installed to create an international network of optical fibers. Transmission distances of several thousand kilometers can be achieved by using optical amplifiers to compensate the attenuation of the fiber. Moreover, the technology of WDM increases the capacity of a fiber optic network by optimizing the use of the optical bandwidth of the channel. The diagram of a WDM system is shown in Figure 1- 4(b). The different wavelengths of the modulated data from multiple users are combined by a multiplexer and are transmitted over an optical fiber. The signal is typically amplified every 60-80 km (depending on the reach and total OSNR degradation) over a distance of several thousand kilometers. Upon reception, the wavelengths are separated by a demultiplexer. In order to increase more the transmission capacity of optical networks, advanced modulation formats are used. These modulation formats allow sending a higher rate of bits so that we can increase the system capacity; Unless electrical and optical components with much higher bandwidth become commercially available, the use of advanced modulation formats seems unavoidable. There have been a number of demonstrations of various modulation

formats, for example, 50 Gb/s per polarization using 4-level pulse amplitude modulation (PAM-4) over 100m SMF [10], 50 Gb/s carrierless amplitude and phase (CAP) modulation over 5 km SMF link [11], 103 Gb/s duobinary transmission over 1 km SMF [12], 400 Gb/s (100 Gb/s per lane) multiband carrierless amplitude/phase (CAP) signal transmission over 20 km (or 40 km optically amplified) SMF [13], 112 Gb/s quadrature amplitude modulation-16 (QAM-16) over 4 km SMF link [14], and 448 Gb/s (112 Gb/s per wavelength) optical OFDM over 10 km SMF [15], and 1-Tb/s dual-carrier 80-GBaud PDM-16QAM WDM transmission at 5.2 b/s/Hz over 3200 km [16]. Additionally, there has been some work on enhancing the bandwidth efficiency of the transmission system, optical-spectrally efficient frequency division multiplexing (O-SEFDM) was used in order to enhance the OOFDM bandwidth efficiency by 25% [17].

The optical network infrastructure can be expressed according to a classification by the geographical area as shown in Figure 1- 5. The three scales commonly used are: access networks (LAN: local area network), metropolitan area networks (MAN: metropolitan area network) or edge network, and core networks (WAN: wide area network). LAN is limited to a small area of a few km's, for example a building geographical area, the MAN network is spread over tens of kilometers and the WAN is national or international coverage.

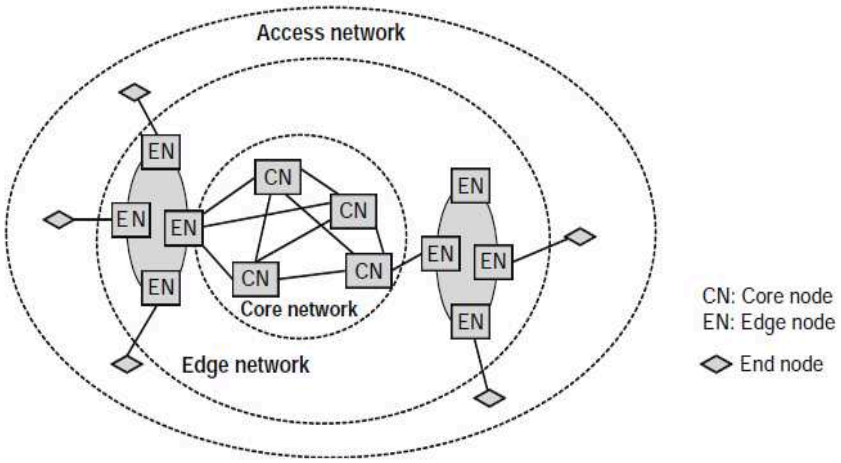

Figure 1- 5 : A typical optical networking architecture [18].

In order to reduce the cost and complexity in the access network, passive optical networks (PONs) are used. In PON architecture, a single fibre originates from a central location, typically an optical line terminal (OLT) in a local exchange as shown in Figure 1- 6. At a point close to the customers, a passive optical splitter on the street divides the fibre between a number of optical network units (ONUs), where there is usually one ONU per customer premises. The cost reduction offered by a PON might not be enough for the future telecommunications network. A PON with longer reach can further enhance cost efficiency for the broadband optical access network. Long-reach PONs (LR-PONs)

extend the coverage span of PONs from the traditional 20 km range to 100 km and beyond by exploiting optical amplifiers in the middle of the transmission fiber spans [19]. LR-PONs combines optical access and metro into an integrated system. The merging of the two types of networks simplifies the hierarchical architecture of the telecommunications network with the long-reach access linked directly to the backbone network, which reduces the number of equipment interfaces, network elements, and even nodes, resulting in energy savings and green communications [7].

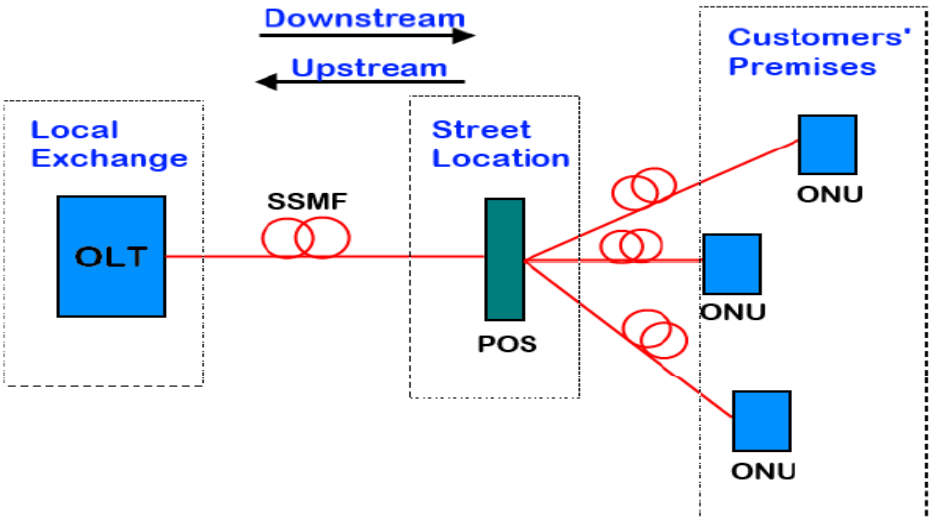

Figure 1- 6 : PON architecture. OLT: Optical line terminal. SSMF: Standard single-mode fibre. POS: Passive optical splitter. ONU: Optical network unit [20].

Figure 1- 7 shows the evolution of transmission capacity of core and access networks over time. The transmission speed of optical access networks has increased by around 100 times in the last decade. In future access networks many technologies are being investigated, these include: time division multiplexed passive optical network (TDM-PON), wavelength division multiplexed passive optical networks (WDM-PON), time and wavelength division multiplexed passive optical networks (TWDM-PON), and optical orthogonal frequency division multiplexed passive optical networks (OOFDM-PON) [21]. The application of OFDM to optical communications has relatively occured recently (starting in 2005) [22], but there are an increasing number of papers on the theoretical and practical performance of OFDM in many optical systems including optical wireless, single mode optical fiber, multimode optical fiber, and plastic optical fiber [22].

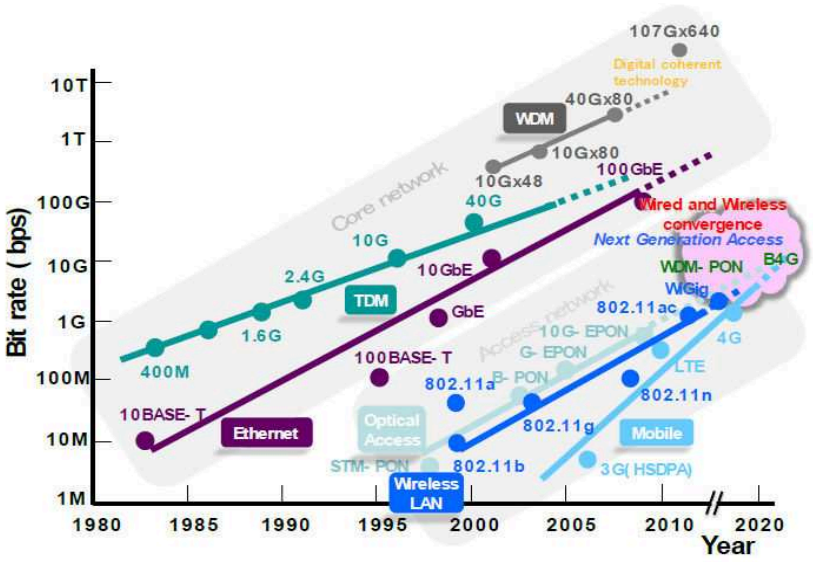

Figure 1- 7 : Evolution of bit rate in the optical access network [23]

OOFDM and adaptively modulated OOFDM (AMOOFDM) [2, 3] are regarded as a promising candidate technology for practical implementation in next-generation, high-speed passive optical networks (PONs) beyond time and wavelength division multiplexed (TWDM) PONs (NG- PON2) since OOFDM has a large number of inherent and unique advantages including, for example, high spectral efficiency, excellent performance adaptability to component/system/ network imperfections owing to its capabilities of adaptive bit and power loading, potential for providing cost-effective technical solutions due to the full utilization of rapid advances in modern digital signal processing (DSP) technology, and rich DSP-enabled transceiver performance self-awareness and networking functionalities [4]. In addition to all the aforementioned salient advantages, OOFDM can also considerably enhance the dynamic transceiver flexibility and reconfigurability for realizing elastic PONs, and maintain their compatibility with existing TDM PONs, as well as offer hybrid dynamic bandwidth allocation (DBA) in both the frequency and time domains [4]. For optical access networks, intensity modulation and direct detection (IMDD) is preferred, up today, due to its simplicity, low complexity, and low cost as compared to the coherent optical and all optical options. Few examples of pervious work on OFDM IMDD systems are: 25 Gbit/s was achieved by directly modulated, directly detected OFDM using channel flattening [24]. A real time IM-OFDM transmission system with 11.25-Gb/s transmission capacity over 25 km SMF was demonstrated [25]. The employment of SOAs and RSOAs as intensity modulators has also attracted special research interest for cost-sensitive application scenarios such as WDM passive optical networks (WDM-PONs). In reality, the use of RSOA is a promising solution to the implementation of colorless optical network units (ONU) for WDM architectures. They can be remotely seeded and guarantee adequate amplification over the whole C-band. Few examples of this work are: A bidirectional hybrid OFDM-WDM-PON system for 40-Gb/s downlink and 10-Gb/s uplink transmission using RSOA remodulation was done in [26]. A

numerical study of more than 30 Gb/s over 60 km SMF was demonstrated using semiconductor optical amplifier (SOA) and reflective semiconductor optical amplifier (RSOA) with OFDM IMDD system [27, 28].

1.2 Orthogonal frequency-division multiplexing (OFDM)

Orthogonal frequency-division multiplexing (OFDM) is a method of encoding digital data on multiple carrier frequencies. OFDM has developed into a popular scheme for wideband digital communication whether wireless or over copper wires, used in applications such as digital television and audio broadcasting, DSL Internet access, wireless networks, power line networks, and 4G mobile communications.

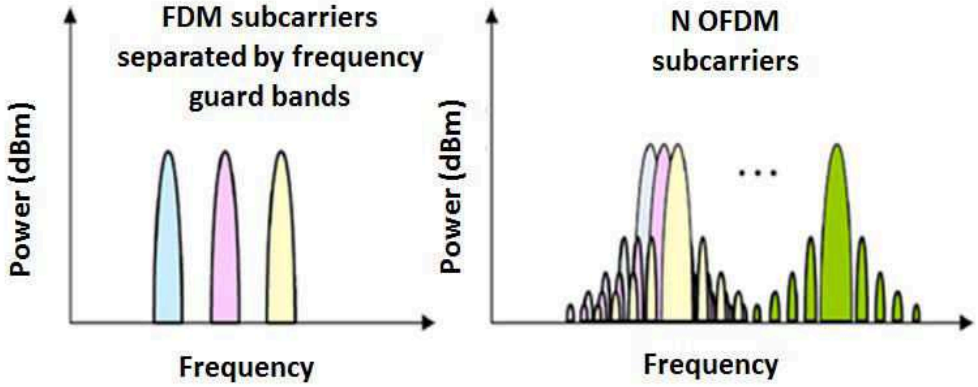

Figure 1- 8 : Spectra for FDM and OFDM.

Figure 1- 8 shows spectra for FDM and OFDM. In frequency division multiplexing (FDM) there are frequency guard bands between the subcarriers. In OFDM the spectra of individual subcarriers overlap. The subcarrier frequencies are chosen so that the signals are mathematically orthogonal over one OFDM symbol period. Because of the orthogonality property, as long as the channel is linear, the subcarriers can be demodulated without interference and without the need for analog filtering to separate the received subcarriers. Both modulation and multiplexing are achieved digitally using an inverse Fast Fourier transform (IFFT) and as a result, the required orthogonal signals can be generated precisely and in a very computationally efficient way [22]. Demodulation and demultiplexing is performed by a fast Fourier transform (FFT). Each sub-carrier is modulated with a conventional modulation scheme (such as quadrature amplitude modulation or phase-shift keying). As the OFDM signal is a sum of N sinusoidal signals, we will have high peaks due to constructive interference. We use a common criterion, the PAPR (peak-to-average power ratio), to describe the concept of peak power as follows:

$$PAPR = \frac{max\{|e_t(t)|^2\}}{\langle |e_t(t)|^2 \rangle} \tag{1.1}$$

Where $\langle |e_t(t)|^2 \rangle$ is the average signal power of the time domain OFDM signal. High PAPR is one of the most important drawbacks of the OFDM modulation format. The major problem lies in the fact that components of optical transmission links such as optical fiber and optical amplifiers become nonlinear for a high power signal [29]. In addition, in the presence of a high PAPR, the low levels of the OFDM signal may be masked by the peak values according to the number of bits of the DAC of the arbitrary waveform generator (AWG). Methods are used to reduce the high PAPR in OFDM as clipping (Figure 1- 9) and coding the original OFDM signal before transmitting into the communication link [30, 31]. The clipping by digital signal processing can be expressed as follows [18]:

$$x'[n] = \begin{cases} -k.\sigma & x[n] \leq -k.\sigma \\ x[n] & -k.\sigma \leq x[n] \leq k.\sigma \\ k.\sigma & x[n] \geq k.\sigma \end{cases} \quad (1.2)$$

Where x[n] and x '[n] are respectively the non- truncated and truncated signal. σ is the standard deviation of x[n], and k is the clipping ratio. The factor k can be found by setting a threshold of maximum acceptable penalty associated with clipping.

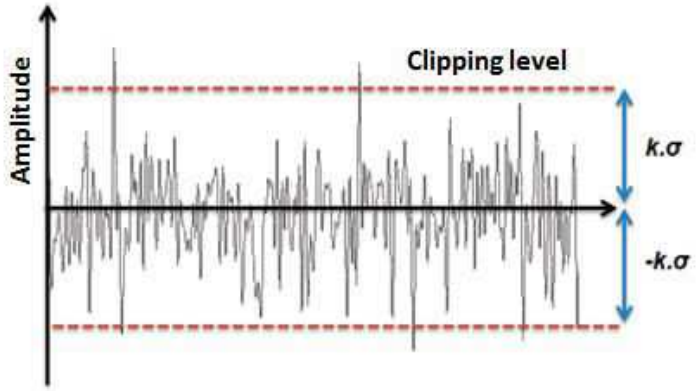

Figure 1- 9 : Arbitrary OFDM signal truncated between two clipping thresholds -k and k [18].

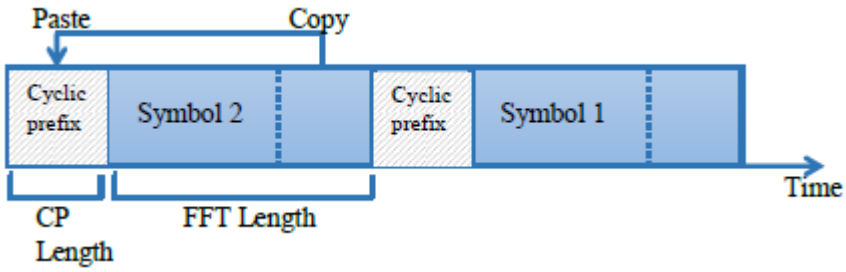

Figure 1- 10 : Adding cyclic prefix to the OFDM signal

In most OFDM systems, a cyclic prefix (CP) is added to the start of each time domain OFDM symbol before transmission. In other words a number of samples from the end of the symbol are appended to the start of the symbol

(Figure 1- 10). Although the CP introduces some redundancy, and reduces the overall data rate, the use of the CP eliminates both intersymbol interference (ISI) and intercarrier interference (ICI) from the received signal and is the key to simple equalization in OFDM [22].

1.2.1 *Evaluation criteria for optical OFDM signals*

The quality of optical signals is a very important parameter in optical communications. Several metrics are in common use, like optical signal-to-noise power ratio (OSNR), Q-factor, error vector magnitude (EVM) and bit error rate (BER). In this work we have used two metrics in order to evaluate the signal quality, bit error rate (BER), and error vector magnitude (EVM).

1.2.1.1 Error vector magnitude (EVM)

Measuring the EVM provides important information on the performance of transmitters and receivers in digital communications. The EVM can determine the type of damage present in a signal and helps to identify their source. EVM is the accumulation of a given vector differences between the ideal reference signal and the measured time signal. It is set to N symbols mean squared error $\vec{V}_{ERR}$ and normalized to unity by $|\vec{V}_{REF}|$ where $|\vec{V}_{REF}|$ is the magnitude of the vector reference signal (Figure 1- 11) and is usually expressed in % rms (root mean square):

$$EVM = \frac{\langle|\vec{V}_{ERR}|\rangle}{|\vec{V}_{REF}|} \tag{1.3}$$

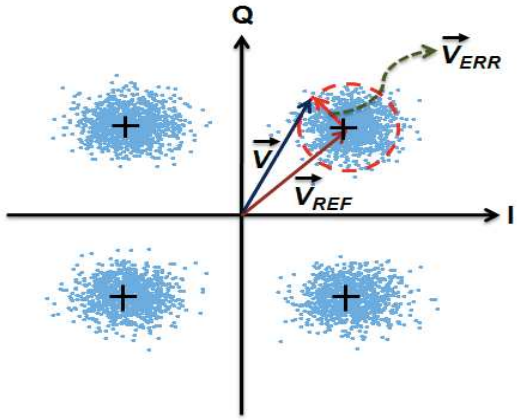

Figure 1- 11: Error vector magnitude (EVM). $\vec{V}_{ERR}$: Error vector; $\vec{V}_{REF}$: reference vector [29].

1.2.1.2 Bit error rate (BER)

In digital transmission, the number of bit errors is the number of received bits of a datastream over a communication channel that have been altered

due to noise, interference, distortion or bit synchronization errors. The bit error rate (BER) is the number of bit errors divided by the total number of transferred bits. The relationship between BER, EVM and M-QAM modulation format for AWGN channel is given by [32].

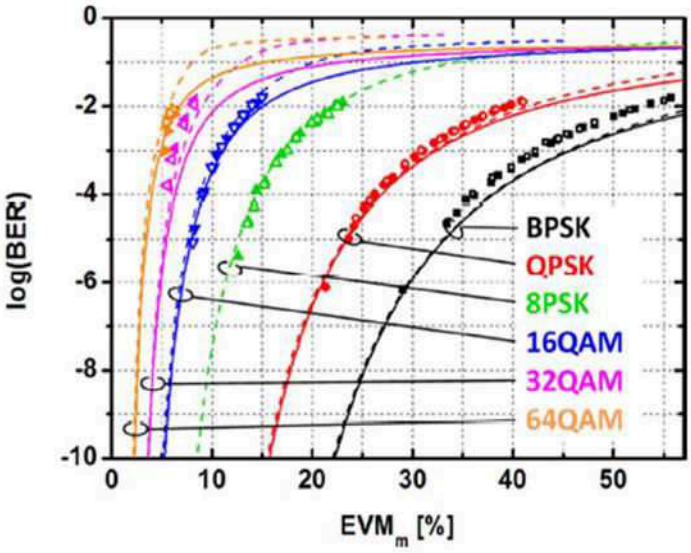

Figure 1- 12 : EVM versus BER [32].

In our work we consider our results valid if we have BER $= 2 \times 10^{-3}$ which can be corrected by forward error correction (FEC) techniques. This BER value corresponds to the EVM values seen in Table 1 according to Figure 1- 12.

Table 1 : Corresponding EVM for each modulation format for an expected BER equal to $2*10^{-3}$.

Modulation format	**EVM %**
BPSK	45 %
QPSK	32 %
8 QAM	17.5 %
16 QAM	12.5 %
32 QAM	7.5 %
64 QAM	5 %

1.2.2 *Calculation of BER for an OFDM signal*

The total channel bit error rate (BER_T), is defined as [27]:

$$BER_T = \frac{\sum_{k=1}^{M_s} En_k}{\sum_{k=1}^{M_s} Bit_k} \tag{1.4}$$

M_s is the total number of data carrying subcarriers. En_k is the total number of detected errors and Bit_k is the total number of transmitted binary bits. Both En_k

and Bit_k are for the k-th subcarrier, whose sub-channel BER, BER_k is given by $BER_k = En_k/Bit_k$.

1.3 Optical OFDM IMDD transmission system

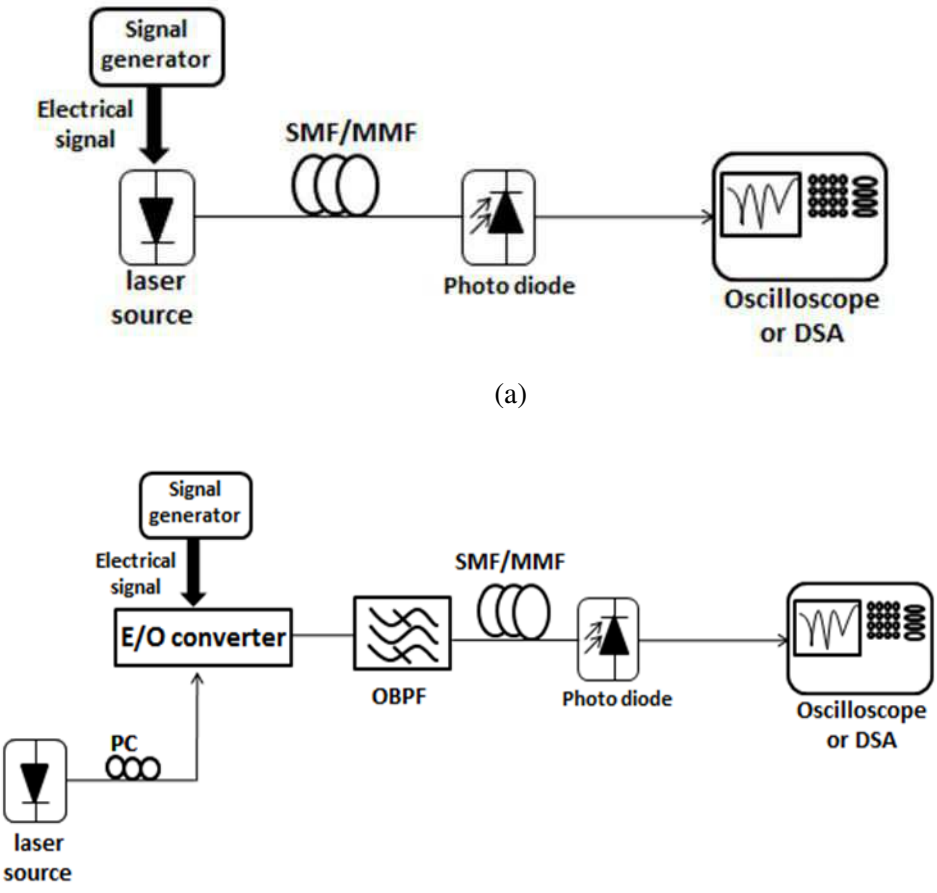

Figure 1- 13: IMDD setup, (a) direct modulation (b) external modulation, OBPF: optical band pass filter, DSA: digital signal analyzer, E/O: electrical to optical converter, PC: polarization controller.

Most existing optical networks are based on the intensity modulation and direct detection (IMDD) concept. The simplicity, low cost, and low complexity of IMDD systems render it advantageous for optical access networks since coherent optical systems are more expensive and more complex in design. The system setup can be seen in Figure 1- 13. An electrical signal modulates the optical signal by using an optical transmitter. The role of an optical transmitter is to convert a signal from the electrical domain to the optical domain. There are two distinct methods for modulating optical waves: direct laser modulation and external modulation. In Figure 1- 13(a), the laser source is directly modulated. Direct modulation of a laser source is achieved by modulating the electric current applied to the device directly. This provides a simple and efficient data transfer in

the optical domain. For the transmission of radio frequency (RF) signals by optical means, this technique is most often used to perform amplitude modulation. A disadvantage of this type of modulation is the fact that the amplitude modulation of the electrical current is accompanied by a frequency modulation due to chirp. The chirp broadens the spectrum of the optical signal, which increases the effect of chromatic dispersion in the optical fiber. In Figure 1- 13(b), the intensity of the continuous wave (CW) laser is modulated in this case by an external modulator device. The advantage of using an external modulator is to increase the maximum link distance because the effect of laser chirp can be reduced. External modulators that are mainly used are Mach-Zehnder modulator (MZM) and electro-absorption modulator (EAM). The obtained optical signal is transmitted into an optical filter that is tuned to the desired wavelength. After the optical filter, the optical signal is transmitted through a fiber and at the end of the line transmission, the optical signal is photodetected by a PIN photodiode or an avalanche photodiode (APD). Afterwards, the photodetected signal is demodulated and analyzed by using an oscilloscope or a digital signal analyzer.

For the OFDM transmitter (Figure 1- 14), we first use a serial to parallel converter that receives the M serial bits to be transmitted, and those bits are divided into P subblocks of m_n bits for each subblock. Those P subblocks will be mapped by the constellation modulator.

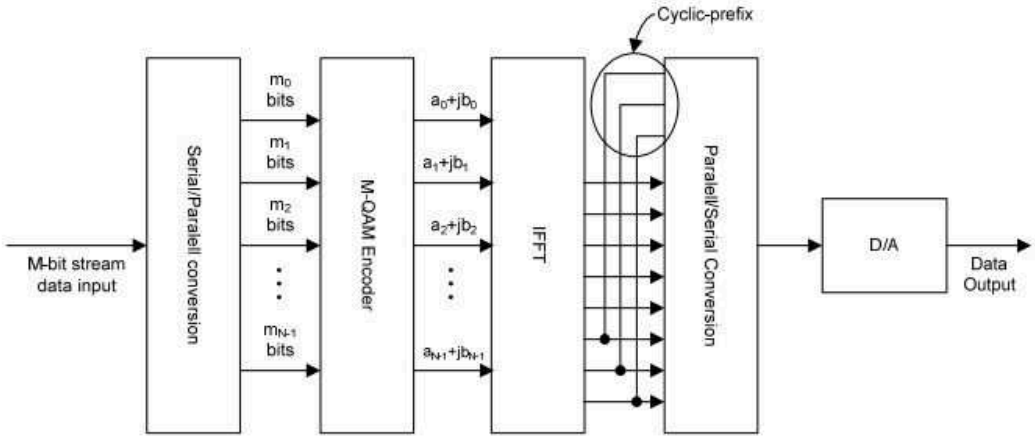

Figure 1- 14 : OFDM transmitter.

The M-QAM encoder converts input data into complex valued constellation points, according to a given constellation, 4QAM, 16-QAM, 32-QAM and so on. The Inverse Fast Fourier Transform (IFFT) is used to perform multiplexing on the complex data, The cyclic prefix (CP) is a copy of the last N samples from the IFFT, which are placed at the beginning of the OFDM frame. After the CP the signal is serialized and converted to the analog domain.

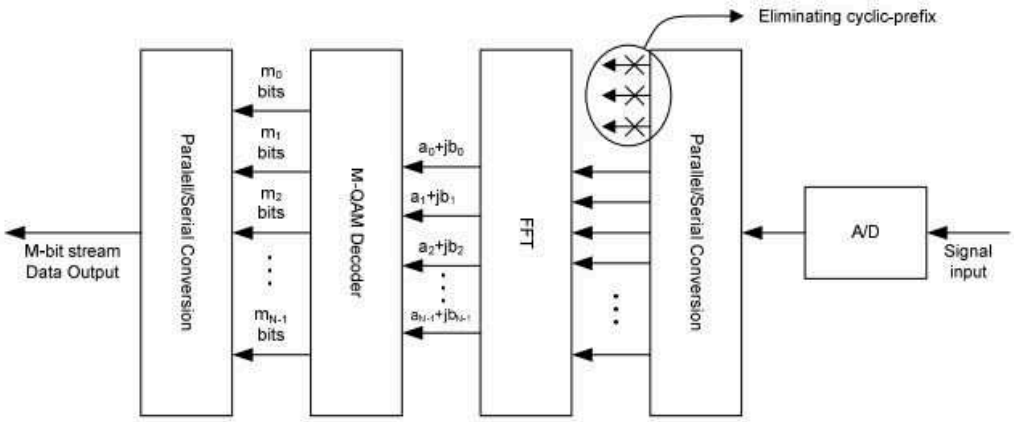

Figure 1- 15 : OFDM receiver.

For the OFDM receiver (Figure 1- 15), the received signal is in the time domain, it goes through a serial to parallel converter and cyclic prefix removal. The signal is then passed through an N-point fast Fourier transform to be converted to frequency domain. At the decoder, we define a threshold to facilitate the decision making in the receiver constellation. Appendix C gives a mathematical description of how to model this transmission system.

1.3.1 *Optical transmitter devices*

The role of the optical transmitter is to convert an electrical input signal into the corresponding optical signal and then launch it into the optical fiber serving as a communication channel. The major component of an optical transmitter is an optical source. Fiber optic communication systems employ semiconductor optical sources such as semiconductor lasers [1]. Semiconductor lasers are of different types (Fabry Perot (FP) lasers, distributed feedback (DFB) lasers, vertical cavity surface emitting lasers, etc…).

1.3.1.1 DFB lasers

Distributed feedback (DFB) semiconductor lasers were developed during the 1980's and are used routinely for WDM lightwave systems. Despite the technological complexities, DFB lasers are routinely produced commercially, they are nearly used in all 1.55 μm systems operating at bit rates of 2.5 Gb/s or more. DFB lasers are reliable enough that they have been used since 1992 in all transoceanic lightwave systems [1]. The optical signal output from a semiconductor laser in continuous wave (CW) mode shows fluctuations in intensity, phase, and frequency. The intensity fluctuation results in a limited signal to noise ratio (SNR), while the phase fluctuation leads to a nonzero spectral linewidth $\Delta\nu$. The relative intensity noise (RIN) often expressed in dB/Hz is

defined as the ratio between the average of the density of the spectrum of optical intensity fluctuations and the square of the instantaneous optical intensity

$$RIN = 10\log\left(\frac{\langle \Delta I^2 \rangle}{I^2}\right) \tag{1.5}$$

Figure 1- 16 shows the RIN for a DFB laser and a FP laser.

The spectral linewidth Δυ can be given by [18]:

$$\Delta v = \frac{R_{sp}}{4\pi \bar{P}}(1 + \alpha_H^2) \tag{1.6}$$

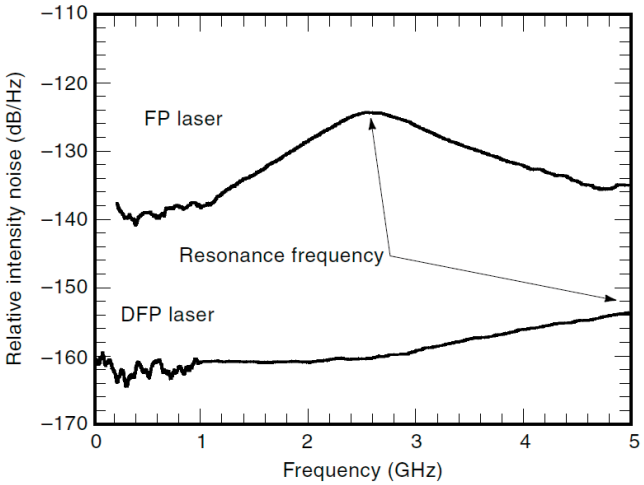

Figure 1- 16 : Spectra of relative intensity noise of a DFB and a FP laser [33].

Where R_{sp} is the recombination rate due to spontaneous emission and α_H is the phase amplitude coupling factor or Henry factor (linewidth enhacement factor). $\bar{P}$ is the average power of the optical signal at the laser output.

1.3.1.2 External modulation

At bit rates of 5 Gb/s or higher, the frequency chirp imposed by direct modulation becomes large enough that direct modulation of semiconductor lasers is rarely used. For such high speed transmitters, external modulation is used. Two commonly used external modulators are Mach-Zehnder modulator (MZM) and electro-absorption modulator (EAM). We will present MZM modulator only.

I. Mach-Zehnder modulator (MZM)

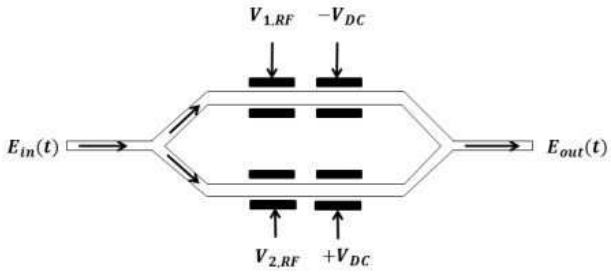

Figure 1- 17 : Mach-Zehnder modulator principle.

The MZM is based on the electrooptical effect [29]. The refractive index n of the material used, for example, $LiNbO_3$, changes according to the bias voltage V applied to its electrodes. Changing Δn index leads to optical phase change $\Delta\varphi$:

$$\Delta\varphi = \frac{2\pi}{\lambda}\Delta nL = \pi\frac{V}{V_\pi} \tag{1.7}$$

Where λ is the wavelength of light, L is the length of the electrode and V_π represents the bias voltage that causes a phase shift of π rad. If we apply two bias voltages V_{DC} and two RF voltages $V_{RF,1}$ and $V_{RF,2}$ on the two electrodes of the modulator according to Figure 1- 17, the output optical field $E_{out}(t)$ is related to the optical input field $E_{in}(t)$ as following:

$$\begin{aligned} E_{out}(t) &= \frac{1}{2}[e^{i\Delta\varphi_1} + e^{i\Delta\varphi_2}]E_{in}(t) \\ &= \frac{1}{2}\left[e^{i\left(\frac{\pi V_{1,RF}-V_{DC}}{2\ V_\pi}\right)} + e^{i\left(\frac{\pi V_{2,RF}+V_{DC}}{2\ V_\pi}\right)}\right]E_{in}(t) \end{aligned} \tag{1.8}$$

Where V_π is the differential voltage to which a phase shift of π rad is obtained between the two waveguides. If $V_{2,RF} = -V_{1,RF} = V_{RF}$ equation (1.8) becomes:

$$E_{out}(t) = \cos\left(\frac{\pi}{2}\frac{V_{RF}+V_{DC}}{V_\pi}\right)E_{in}(t) \tag{1.9}$$

The MZM can be used for intensity and phase modulation formats such as on-off keying (OOK), binary-phase shift keying (BPSK), quadrature phase shift keying (QPSK), ext.. MZM modulators are suitable for use in metro, long-haul (LH) and ultra long-haul (ULH) networks. The $LiNbO_3$ fabricated MZM modulators can operate satisfactorily over a range of wavelengths from 1300 nm to 1550 nm. They are widely used in today's digital optical broadband communications. However, it has some disadvantages such as high optical loss, high energy consumption and difficulty of integration with a laser.

1.3.2 *Optical fiber channel*

At the heart of the optical communication systems, optical fibers are used as the transmission channel. An optical fiber consists of a cylindrical central core of silica surrounded by a cladding having a refractive index n_g slightly lower than that of the core material. The light is confined in the core by the phenomenon of total reflection. There are two main types of optical fibers used in communication systems: multimode fibers (MMFs) and single mode fibers (SMFs). Multimode fibers are still used for local area networks (short distances) and single mode fibers (SMFs) for access/metropolitan/core network applications. The main benefits of fibers are their large transmission capacity, low weight, very low attenuation and immunity to electromagnetic interference. Despite its advantages, there remain constraints that impose a compromise between speed and distance such as losses in the line (link power budget), the chromatic dispersion, polarization mode dispersion and fiber nonlinear effects. We briefly explain each of these phenomenas.

1.3.2.1 Fiber losses

The optical signal that is propagating through an optical fiber suffers from attenuation. The optical signal attenuation is a very important factor since a minimum optical signal level must be present at the receiver so as to be properly detected. The attenuation of an optical signal is generally expressed in dB/km using the following relationship:

$$\alpha(dB/km) = -\frac{10}{L}\log_{10}\left(\frac{P_{out}}{P_{in}}\right) \tag{1.10}$$

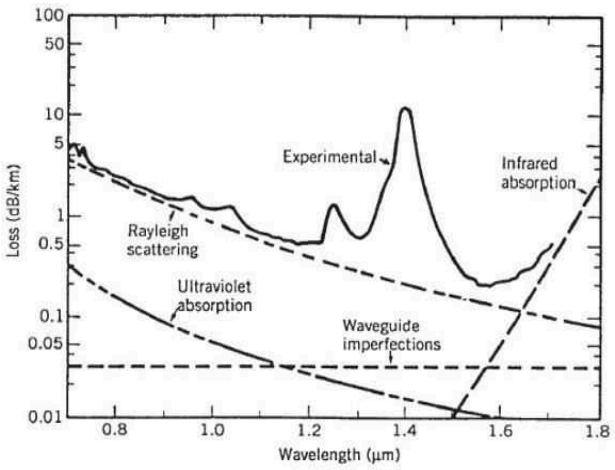

Figure 1- 18 : Loss spectrum of singlemode fiber. The wavelength dependence of several fundamental loss mechanisms is also shown [1].

Fiber losses depend on the wavelength of transmitted light. Figure 1- 18 shows the loss spectrum α(λ) of a single-mode fiber made in 1979 [1]. The fiber exhibited a loss of only about 0.2 dB/km in the wavelength region near 1.55 μm, the lowest value first realized in 1979. This value is close to the fundamental limit of about 0.16 dB/km for silica fibers [1]. The loss spectrum exhibits a strong peak near 1.39 μm and several other smaller peaks. A secondary minimum is found to occur near 1.3 μm, where the fiber loss is below 0.5 dB/km. Since fiber dispersion is also minimum near 1.3 μm, this low-loss window was used for second-generation lightwave systems. Fiber losses are considerably higher for shorter wavelengths and exceeds 5 dB/km in the visible region, making it unsuitable for long-haul transmission. Several factors contribute to overall losses; their relative contributions are also shown in Figure 1- 18. The two most important among them are material absorption and Rayleigh scattering.

1.3.2.2 Chromatic Dispersion

The main advantage of single-mode fibers is that intermodal dispersion is absent simply because the energy of the injected pulse is transported by a single mode. However, pulse broadening does not disappear altogether. The group velocity associated with the fundamental mode is frequency dependent because of chromatic dispersion. As a result, different spectral components of the pulse travel at slightly different group velocities, a phenomenon referred to as *group-velocity dispersion* (GVD), *intramodal dispersion*, or simply *fiber dispersion* [1]. Intramodal dispersion has two contributions, material dispersion and waveguide dispersion. This causes intersymbol interference which results in an increase of the bit error rate (BER) of the communication system.

D represents the chromatic dispersion parameter $ps.nm^{-1}.km^{-1}$ defined by:

$$D = -\frac{2\pi c}{\lambda^2}\frac{d^2\beta}{d\omega^2} = -\frac{2\pi}{\lambda^2}\beta_2 \tag{1.11}$$

$\beta_2 = d^2\beta/d\omega^2$ is known as the group velocity dispersion parameter (GVD). λ is the optical wavelength. The dispersion spectrum of a conventional silica single mode fiber is shown in Figure 1- 19. D is equal to about 15-18 $ps.nm^{-1}.km^{-1}$ around the wavelength 1550 nm.

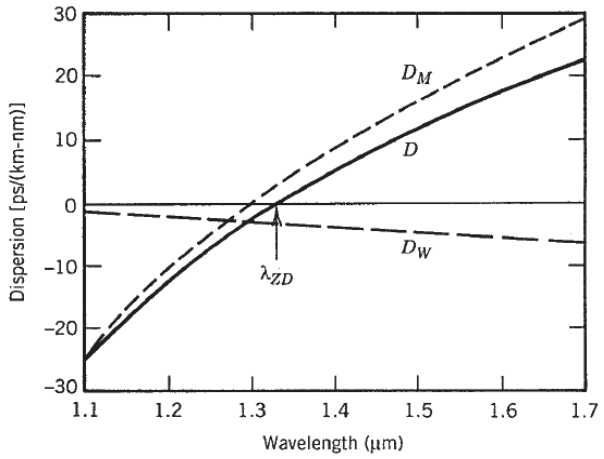

Figure 1- 19 : Dispersion spectrum of a conventional single-mode silica fiber. The total dispersion D and the relative contributions of the material dispersion D_M and of the waveguide guide dispersion D_W are also shown [1].

One way of expressing the frequency response of the chromatic dispersion of a channel is given by the Royset model [34]**.** This transfer function is given by:

$$H = \cos\left(\frac{\pi f^2 \lambda^2 DL}{c}\right) - \alpha_H \left(1 - j\frac{f_c}{f}\right) \sin\left(\frac{\pi f^2 \lambda^2 DL}{c}\right) \tag{1.12}$$

Where L is the optical distance and f is the modulation frequency. f_c is the frequency at which the transient and adiabatic chirp have the same amplitude, and c is the speed of light in vacuum.

1.3.2.3 Polarization mode dispersion

The polarization mode dispersion (PMD) is a modal dispersion in which two orthogonal polarization modes of light at the same wavelength are propagated at different speeds because of the birefringence of the fiber, causing an expansion of optical pulses. PMD is relatively small compared to the effects of GVD. However, PMD becomes a limiting factor for systems designed to operate over long distances at high rates [35]. The PMD value we have used is given in Table 3 in chapter 3.

1.3.2.4 Non- linearities of the optical fiber

The basic operational principles of optical transmission can be explained assuming that the optical fiber medium is linear. The linearity assumption is valid if the launched power does not exceed several milliwatts in a single channel system. In modern WDM technology, high-power semiconductor lasers and optical amplifiers are employed, and the influence of fiber nonlinearities becomes important. Moreover, in some special cases, the fiber nonlinearities may be used to enhance the fiber transmission capabilities (e.g., soliton transmission).

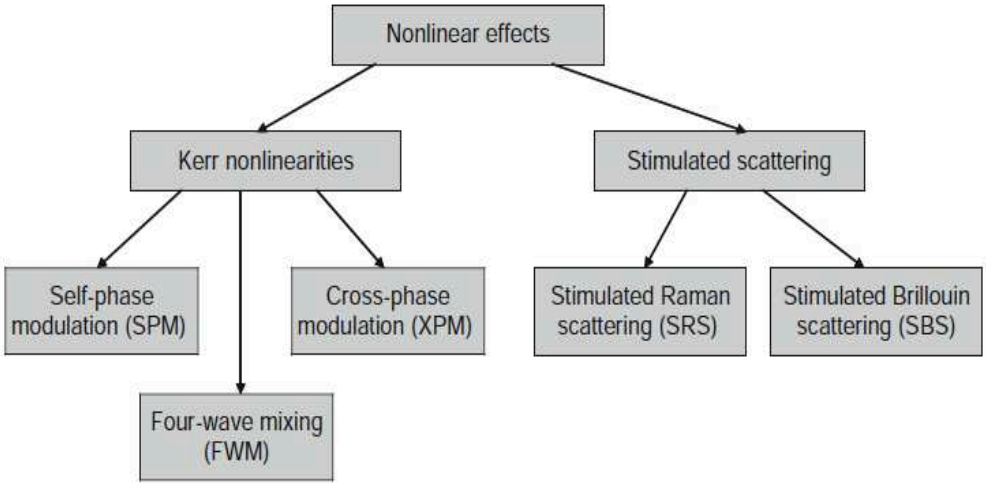

Figure 1- 20 : Classification of fiber nonlinearities [18].

There are two major groups of fiber nonlinearities related either to the nonlinear refractive index (Kerr effect) or to nonlinear optical scattering, which are illustrated in Figure 1- 20. The Kerr effect occurs due to the dependence of the index of refraction on light intensity, and fiber nonlinearities belonging to this category are (1) self-phase modulation (SPM), (2) crossphase modulation (XPM), and (3) four-wave mixing (FWM). SPM is related to the single optical channel. The variation of power within the channel causes changes in the refractive index, which leads to phase distortion. In XPM, the refractive index changes due to variations in power not only in the observed channel but also due to variation in powers of other wavelength channels leading to phase distortion. In FWM, several wavelength channels interact to create new channels. This effect is dependent on both the power of the interacting channels and on chromatic dispersion. There are two types of stimulated scattering: stimulated Raman scattering and stimulated Brillouin scattering, which can be used for amplification of the optical signal [18].

1.3.3 *PIN photodiode*

There are two types of photodetectors that are used for direct detection, the PIN photodiode, and the APD photodiode. In this section we describe the PIN photodiode which is used in our system as the direct detection component for the OOFDM signal, we also describe the noise sources in the photodiode.

1.3.3.1 Structure and principle

A PIN diode is a diode with a wide undoped intrinsic semiconductor region between a p-type semiconductor and an n-type semiconductor region.

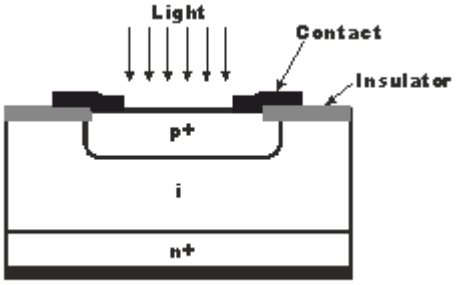

Figure 1- 21 : p-i-n photodiode structure [36]

The photocurrent I_{pin} is directly proportional to the incident optical power P_{in}:

$$I_{pin} = RP_{in} \tag{1.13}$$

Where R is the *responsivity* of the photodetector (in units of A/W). The responsivity R can be expressed in terms of a fundamental quantity μ, called the *quantum efficiency* and defined as

$$\mu = \frac{electron\ generation\ rate}{photon\ incident\ rate} = \frac{I_p/q}{P_{in}/hv} = \frac{hv}{q}R \tag{1.14}$$

Table 2 shows the characteristics of common PIN photodiodes depending on the material used.

Table 2: Characteristics of common PIN photodiodes [1]

Parameter	Symbol	Unit	Si	Ge	InGaAs
Wavelength	λ	µm	0.4-1.1	0.8-1.8	1.0-1.7
Responsivity	R	A/W	0.4-0.6	0.5-0.7	0.6-0.9
Quantum efficiency	µ	%	75-90	50-55	60-70
Dark current	I_d	nA	1-10	50-500	1-20
Rise time	T_r	ns	0.5-1	0.1-0.5	0.02-0.5
Bandwidth	Δf	GHz	0.3-0.6	0.5-3	1-10
Bias voltage	V_b	V	50-100	6-10	5-6

1.3.3.2 Noise at receiver stage

Shot noise and thermal noise are the two fundamental noise mechanisms responsible for current fluctuations in all optical receivers even when the incident optical power *Pin* is constant. Of course, additional noise is generated if *Pin* is itself fluctuating.

I. Shot noise

Shot noise is a manifestation of the fact that an electric current consists of a stream of electrons that are generated at random times. It was first studied by Schottky in 1918 and has been thoroughly investigated since then [1].

RMS shot noise is given by:

$$\sigma_{sh}^2 = \langle |i(t) - I|^2 \rangle = 2qIB_e = 2qRP_{in}B_e \quad (1.15)$$

Where B_e is the electrical bandwidth of the receiver.

II. Relative intensity noise (RIN)

RIN noise will be measured at the photodiode and will add to shot noise. The RIN noise variance is given by:

$$\sigma_{RIN}^2 = RP_{in}^2 RINB_e \quad (1.16)$$

III. Thermal Noise

At a finite temperature, electrons move randomly in any conductor. Random thermal motion of electrons in a resistor manifests as a fluctuating current even in the absence of an applied voltage. This additional noise component is referred to as thermal noise [1]. The noise variance of the thermal noise is given by:

$$\sigma_{th}^2 = \frac{4K_BT}{R_L}B_e \quad (1.17)$$

Where T is the absolute temperature, k_B is the Boltzmann constant and R_L is the load resistor.

1.3.3.3 Photodiode sensitivity

The sensivity is the minimum input power at the receiver that can permit good transmission performances. Figure 1- 22 shows the state of the art of high speed receiver sensitivity versus the transmission speed. A BER of 10^{-9} is considered valid in this work. For the PIN photodiode, it's sensivity is about -21 dBm at 10 Gb/s due to the shot noise, and it attains almost -13 dBm at 40 Gb/s. This sensivity can be enhanced by using an optical preamplification. The figure shows that the receiver sensitivity can be enhanced from -12.5 dBm up to -28 dBm for a 40 Gb/s transmission rate by using an EDFA-PIN configuration.

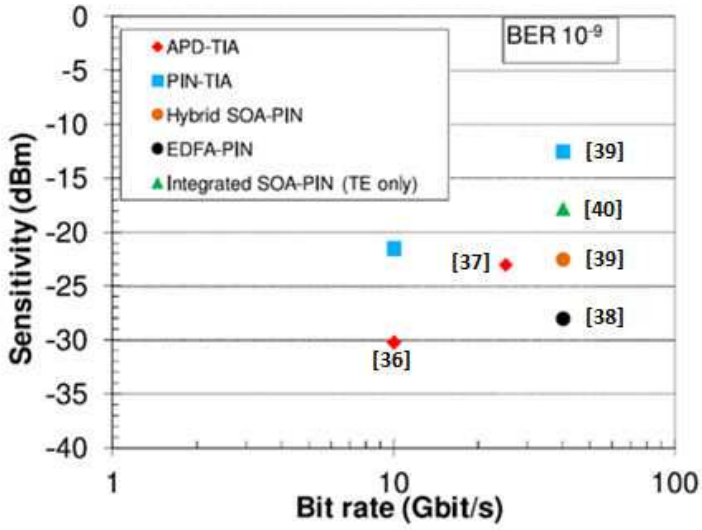

Figure 1- 22 : State of the art receiver sensitivity versus bit rate [37, 38, 39, 40, 41].

1.3.4 *Analog to Digital Converter (ADC) and Digital to Analog Converter (DAC)*

Analog to digital converter (ADC) and digital to analog converter (DAC) are key devices in system transmission of advanced modulation format. ADC presents a major limiting factor in the progress towards higher rates mainly due to aperture jitter, i.e. inability of ADCs to sample at precisely defined times. Figure 1- 23 shows the effective number of bits (ENOB) as a function of input frequency for high-performance electronic ADCs, as reviewed by Walden [42]. The improvement of ADC performances could be obtained by using optical sources, and by benefitting from the rapid progress in electronic photonic integration via the silicon photonics technology platform [43].

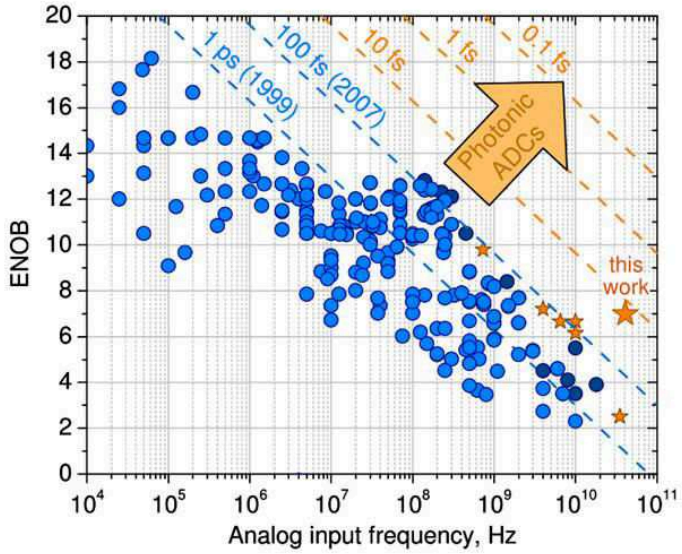

Figure 1- 23 : "Walden plot" showing ENOB of existing ADCs as a function of analog input frequency [42, 43].

In order to numerically show the influence of the ADC and DAC, we use an IMDD-OFDM-16 QAM signal comprising 32 subcarriers with a data rate of 3 Gb/s. This numerical transmission system is explained in chapter 3. Figure 1- 24 shows the simulation setup for electrical back to back transmission.

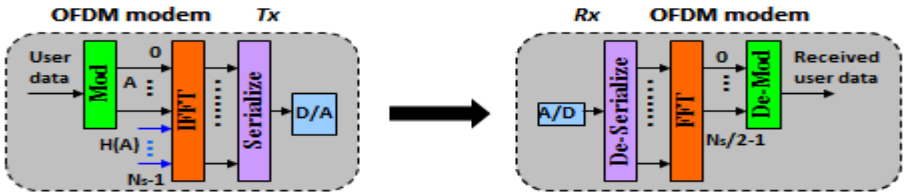

Figure 1- 24: OFDM electrical back to back simulation setup.

We modify the quantization level in the ADC/DAC to study the influence of quantization noise on OFDM transmission. Figure 1- 25 shows the variation of the EVM based on the number of quantization bits of the DAC and ADC separately and also their combined influence (maintaining equal quantization between the two).

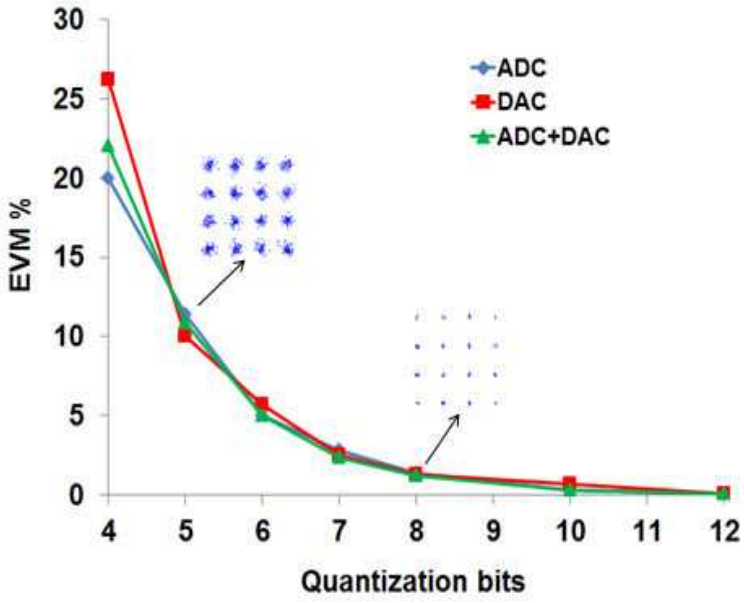

Figure 1- 25 : EVM and simulated constellations of OFDM signal at 3 Gb/s electrical back to back connection according to the number of quantization bits of the DAC and ADC for (a) blue curve: ADC varies and DAC set to 12, (b) red curve: DAC varies and ADC set to 12, (c) green curve: both ADC and DAC vary with same ENOB.

The constellations are displayed graphically to illustrate the quantization impact on the received signal quality. Datasheets of the components that we have used in the experimental setup in chapter 3 give quantization values 12 and 8 respectively to the OFDM encoder and decoder. The figure shows that for quantization values less than 8 we start to have a high degradation in EVM.

1.4 Semiconductor Optical Amplifiers (SOAs)

Several types of optical amplifiers have been developed during the 1980s, and the use of optical amplifiers for long haul transmission systems became widespread in the 1990s. There are two main types of optical amplifiers: semiconductor optical amplifier (SOA) and fiber amplifiers such as erbium doped fiber amplifiers (EDFA). The EDFA is currently the optical amplifier of choice in long haul applications at 1.55 µm. The fiber amplifiers are attractive due to their high gain, high saturation power, and low noise. On the other hand; SOAs have a number of salient advantages including small footprint, low power dissipation, full coverage of the entire fiber transmission window, large-scale monolithic integration capability and potentially low cost, the utilization of SOAs to perform both linear and nonlinear functionalities required in advanced high-speed optical communications systems has been the subject of intensive research over the recent decades [27, 44]. As nonlinear elements, SOA-based all-optical signal processing functions have been widely investigated, which include, for example, signal regeneration and switching, wavelength conversion, as well as logic gates. As linear elements, use has been made of SOAs to conduct in-line optical amplification of wavelength division multiplexed (WDM) signals for metropolitan area networks (MANs). And as mentioned in section 1.1, the employment of SOAs as intensity modulators has also attracted special research interest for cost-sensitive application scenarios such as WDM passive optical networks (WDM-PONs).

1.4.1 *Semiconductor optical amplifier structure [45]*

An SOA is an optoelectronic device that can, under appropriate operating conditions, amplify an incident light signal. A basic structure of an SOA is shown in Figure 1- 26. Its main element the active region provides optical gain when the amplifier is electrically pumped. Pumping is necessary to achieve the population inversion and therefore stimulated emission. An integrated waveguide is used to contain the wave signal in the active region.

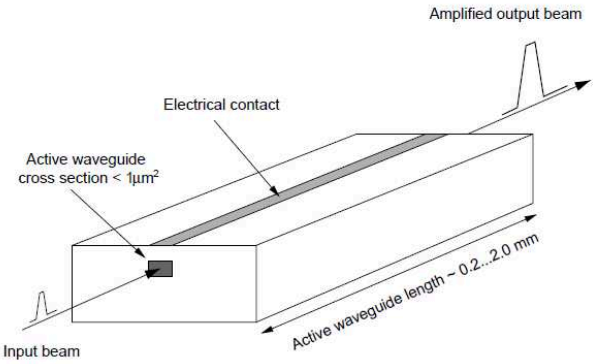

Figure 1- 26 : The basic structure of a semiconductor optical amplifier.

The type of material used in the active region of the SOA determines its gain spectrum and its operational characteristics. SOAs are used primarily in wavelength regions around 1.3 µm and 1.55 µm, and are made of the same III-V materials as those used to manufacture laser sources in these regions. These materials are III-V semiconductors, which include InP, InGaAs, InGaAsP, AlGaAs and InAlGaAs. The SOA generally has an antireflection treatment on its input and output sides in order to minimize reflectivity, but there is a reflective SOA structure (RSOA) in which one side has a high reflectivity (Figure 1- 27) in which the signal is reflected and propagates backward. The advantage of such a configuration is that for the same bias current we can double the optical gain. The active area of an SOA can be manufactured by stacking material whose dimensions along one or more axes are sufficiently small so that its energy levels are discretized, these are called quantum materials [5]. Figure 1- 28 shows the classification of these materials according to their spatial confinement. An SOA with an active region whose dimensions are significantly greater than the de Broglie wavelength, $\lambda_B = h/p$ (where p is the carrier momentum) is named a bulk device. In the case where the active region has one or more of its dimensions (usually the thickness) of the order of λ_B, the SOA is named a quantum-well (QW) device. It is also possible to have multiple quantum-well (MQW) devices consisting of a number of stacked thin active layers separated by thin barrier (non-active) layers. The SOA types with quantum material are: multi quantum well SOA (MQW-SOA), quantum dash SOA (QDash-SOA), and quantum dot SOA (QD-SOA). They have a wider bandwidth and higher saturation optical power. However, they have higher polarization sensitivity compared to the bulk SOA.

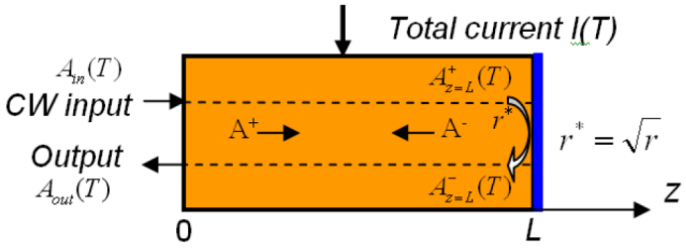

Figure 1- 27 : RSOA principle [28].

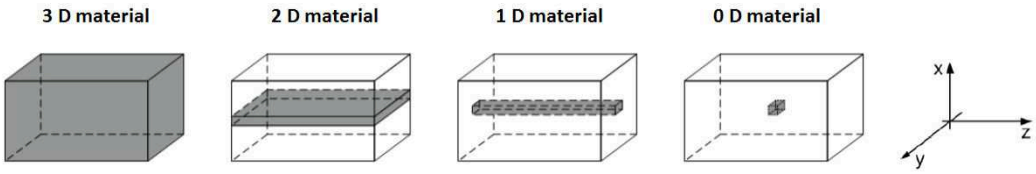

Figure 1- 28: Illustration of spatial confinement of a Bulk, a Quantum Well, a Quantum Dash, and a Quantum Dot SOA [5].

1.4.2 *SOA characteristics*

1.4.2.1 SOA gain, saturation output power, and noise factor

Probably the most important operational parameter of an optical amplifier in many applications is its gain, i.e. the ratio of the signal power at the output to the input power. The gain spectrum of a particular SOA depends on its structure, material, confinement factor, SOA length, losses, and operational parameters. The optical gain is given by:

$$G = \frac{P_{out}}{P_{in}} \tag{1.18}$$

Where Pin is the signal input injected power and, Pout is the signal output power. The SOA amplified spontaneous emission (ASE) noise influence from the system point of view is often determined by the noise factor. The noise factor F is used as a figure of merit of the optical amplifier and is defined as the ratio between the signal to noise ratio (SNR) at the input and the SNR at the output of the amplifier:

$$F = \frac{\left(\frac{S}{N}\right)_{in}}{\left(\frac{S}{N}\right)_{out}} \tag{1.19}$$

The gain of an SOA is influenced both by the input signal power and ASE induced saturation. As the signal power increases the carriers in the active region become depleted leading to a decrease in the amplifier gain. The SOA gain saturation is measured for an output optical power for which its gain decreases by 3 dB. This gain saturation can cause significant signal distortion. It can also limit the gain achievable when SOAs are used as multichannel amplifiers.

1.4.2.2 Amplified spontaneous emission

The amplified spontaneous emission is due to spontaneous recombination and inconsistently emits photons at any point in the active area of the SOA. It is a source of broadband noise that is involved in the gain saturation of the SOA and can be presented as a white noise with a flat frequency response characterized by a Gaussian distribution. The power of the ASE of the amplifier can be given as follows:

$$P_{ASE} = n_{sp} h\nu (G - 1) B_0 \tag{1.20}$$

Where G is the gain at the optical frequency ν. B_0 is the optical bandwidth of the filter used after the SOA. h is Planck's constant. n_{sp} is the population inversion

factor. The noise of an SOA may be linked to the ASE power (P_{ASE}) by the following expression [46]:

$$F = \frac{SNR_{in}}{SNR_{out}} = \frac{2P_{ASE}}{h\nu G B_0} + \frac{1}{G} \quad (1.21)$$

B_0 depends on the optical spectrum analyzer resolution $\Delta\lambda$ according to $B_0 = c(\Delta\lambda/\lambda^2)$, where c is the speed of light in vacuum. NF (Noise Figure) in dB is related to the noise factor as following: NF (dB) = 10 $\log_{10}$F. P_{ASE} is the ASE output power.

1.4.2.3 Non-linearities of the SOA

Nonlinearities in SOAs are principally caused by carrier density changes induced by the amplifier input signals. The main types of nonlinearity are: Self gain modulation (SGM), Cross gain modulation (XGM), cross phase modulation (XPM), self-phase modulation (SPM), four-wave mixing (FWM) and cross polarization modulation (XPolM).

1.4.2.4 Phase amplitude coupling factor and chirp in SOA

The phase amplitude coupling factor, (α_H) expresses the change of the refractive index with respect to carrier density caused by amplitude variation of an incident optical signal [47]. Modeling α_H is generally estimated using the equivalent refractive index n_{eq} and modal gain Γg_m and defined as follows: [47]

$$\alpha_H(N,\lambda) = -\frac{4\pi}{\lambda}\frac{\frac{\partial n_{eq}(N,\lambda)}{\partial N}}{\frac{\partial \Gamma(N,\lambda) g_m(N,\lambda)}{\partial N}} \quad (1.22)$$

Where n_{eq} is the effective active area index, N is the carrier density, Γ is the confinement factor, g_m is the material gain. $\partial\Gamma g_m/\partial N$ can be calculated by numerical differentiation of the net gain, without account for losses. $\partial n_{eq}/\partial N$ is linearized and can be written as follows [29]:

$$\frac{\partial n_{eq}}{\partial N} = \frac{\partial n_{eq}}{\partial N}\Big|_{\lambda_{ref}} + \frac{\partial^2 n_{eq}}{\partial N \partial \lambda}\Big|_{\lambda_{ref}} (\lambda - \lambda_{ref}) \quad (1.23)$$

Where λ_{ref} is a reference wavelength. The changes in refractive index and gain are opposite in sign giving a positive value of α_H. When the SOA gain changes, the phase shift also changes due to phase-amplitude coupling and thus induces frequency chirp.

If we consider the SOA as a black box, we can introduce an effective α-factor ($\alpha_{H,eff}$). $\alpha_{H,eff}$ can be linked to the SOA total phase-to-gain changes and it can be given by [48]:

$$\alpha_{H,eff} = -2\frac{\Delta\Phi}{ln\left(\frac{\Delta P_{out}}{P_{in}}\right)} \tag{1.24}$$

Where $\Delta\Phi$ is the output phase variation, ΔP_{out} is the output power variation of the input signal P_{in}. The input signal is in continuous wave mode and the gain variation is induced by a bias current modulation or by an input power variation of a pump optical signal. The chirp $\Delta\upsilon$ is the frequency deviation caused with the phase variation of the signal at the SOA output:

$$\Delta\upsilon(t) = -\frac{1}{2\pi}\frac{\partial\Phi(t)}{\partial t} = \frac{\alpha_{eff}}{4\pi P(t)}\frac{\partial P(t)}{\partial t} \tag{1.25}$$

Where P(t) is the output power signal of the input CW power P_{in}. When we use modulators, one speaks of a signal with positive or negative chirp. When a signal exhibits a positive frequency deviation during its rising edge (resp. negative during its falling edge) we say that the signal is positively chirped. Similarly a negatively chirped signal shows a negative frequency deviation during its rising edge. For the SOA, when it is used as a wavelength converter (using XGM), the output probe signal has a positive chirp [48]. In contrary, when the bias current of the SOA is modulated [27] (i.e: the SOA is used as in intensity modulator), the modulated output signal has a negative chirp.

1.4.2.5 SOAs/RSOAs as external modulators

SOAs/RSOAs can be used to intensity modulate a CW optical signal from a laser source. Intensity modulation can be achieved by simply modulating the amplifier current with a suitable data signal, as shown in Figure 1- 29. The current modulation modulates the amplifier gain and thereby the input optical signal. The modulation bandwidth is limited by the amplifier carrier lifetime [27]. In our case, the input electrical current will be modulated by our OFDM signal.

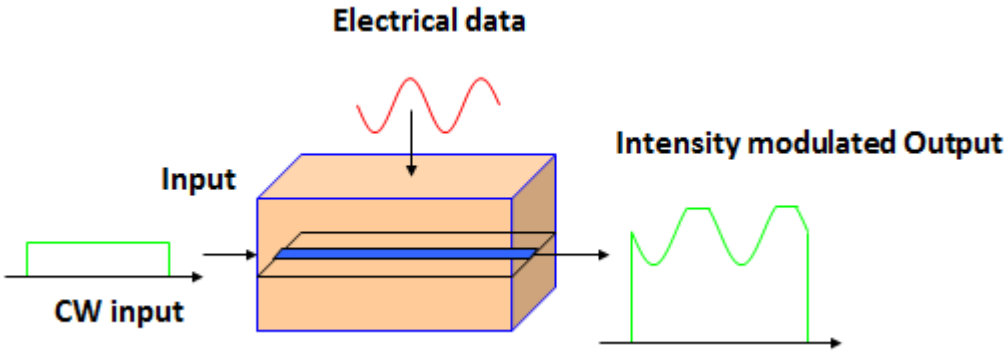

Figure 1- 29: SOA/RSOA intensity modulation principle.

The employment of SOAs and RSOAs as intensity modulators has attracted research interest for cost-sensitive application scenarios such as WDM passive optical networks. Nevertheless, direct modulation of RSOAs is bandwidth-limited (typically to around 1GHz) due to long carrier lifetime. The bandwidth could be increased to around 7.8 GHz by using a two electrode RSOA [49]. Moreover; to increase transmission capacity, several techniques were implemented in order to compensate for the R-SOA limited bandwidth by using electrical and optical equalization, and by using adaptatively modulated OFDM [50, 51, 52, 53, 54].

1.5 Conclusion

In this chapter we have shown the evolution of optical fiber networks. We focused on the need for higher transmission capacities in optical access networks and some techniques that are applied in order to achieve this higher capacity. We have then discussed the OFDM modulation technique, and its potential for enhancing the transmission capacity for future access networks. We have detailed the main components of an optical IMDD-OOFDM communication link, and have also focused on SOAs characteristics and their potential use for IMDD-OOFDM systems.

PART 1

2 WIDEBAND TIME DOMAIN RSOA MODELING AND EXPERIMENTAL VALIDATION

2.1 Introduction

We present in this chapter a comprehensive SOA model. Many studies have been conducted with the aim of accurately simulating the static and dynamic behavior of the SOA component. Different complex modeling methods of SOAs are available in the literature [55, 56, 57, 58, 59, 60]. We have used a wideband time domain field-based rate equation model developed in the Ph.D. work of P.Morel [5, 6] using ADS, and we have incorporated this model in our developed OFDM IMDD co-simulation platform. The SOA model used in this study simulates most of the effects of non-linearities of SOA as self gain modulation (SGM), cross gain modulation (XGM), self-phase modulation (SPM), cross phase modulation (XPM), phase amplitude coupling, and four wave mixing (FWM) [61]. Modeling was performed over a wide range of incident optical power, wavelength and bias current.

The chapter starts by explaining in detail the theory of the SOA model used. We then optimize the model parameters so as to fit with an RSOA component we use in an experimental IMDD-OOFDM setup as will be presented in chapter 3. Finally we compare experimental and simulated static and dynamic characterization results of the RSOA.

2.2 Wideband time domain SOA/RSOA field model

We will describe now in detail the SOA model used and implemented in ADS [5, 6]. The active area of the SOA is divided into several calculation sections; this allows having more accurate results for the propagating optical field signal since the carrier density is not constant and varies along the device length. Figure 2- 1 shows the SOA length L divided into M sections. L is the total length of the active region and L_s is the length of a single section. The + and - signs correspond to the direction of propagation along the increasing and decreasing z directions where z is the position along the device. N_k represents the carrier density in the k^{th} calculation section. The coupling losses between the optical fiber and the active area of the SOA are $CL^{\pm}_L$ left and $CL^{\pm}_R$ right. R_L and R_R represent the reflectivity on the left and right sides of the SOA, respectively. We assume that the optical signal and the ASE signal move from one calculation section to the other without any reflection. In each calculation section, the carrier density, the field of the optical signal, and the ASE intensity are calculated. The total I_{bias} is equally divided into the individual calculation sections where $I_{el,k}$ is the electrical bias current applied on the k^{th} calculation section.

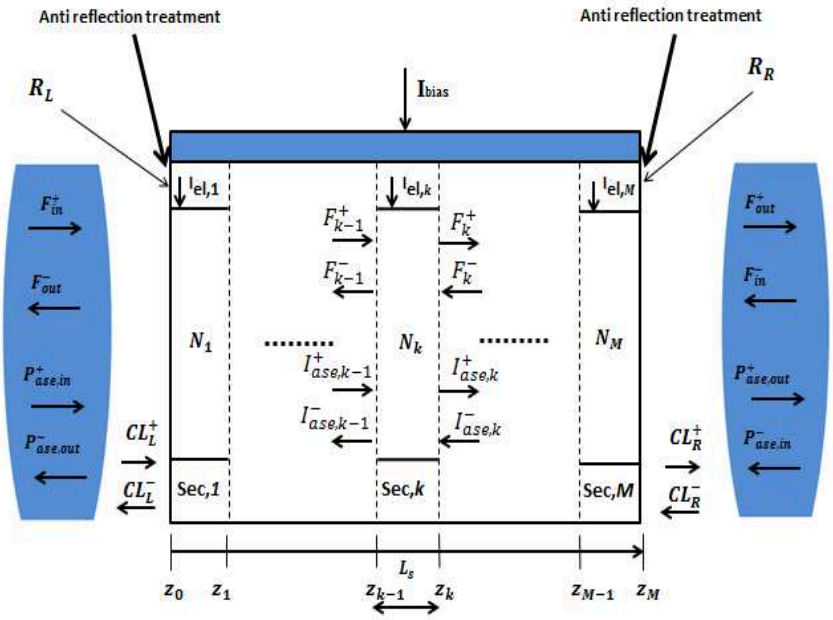

Figure 2- 1 : Principle of cutting the cavity of the SOA into M calculation sections.

For the SOA active region sides at z_0 and z_M, fieldss in the active region of SOA can be expressed as follows:

$$F_0^+(t) = \left(1 - \sqrt{R_R}\right)\sqrt{\frac{\Gamma CL_R^+}{wd}}F_{in}^+(t) + \sqrt{R_R}F_0^-(t) \tag{2.1}$$

$$F_M^-(t) = \left(1 - \sqrt{R_L}\right)\sqrt{\frac{\Gamma CL_L^-}{wd}}F_{in}^-(t) + \sqrt{R_L}F_M^+(t) \tag{2.2}$$

$$I_{ase,0}^+(t) = (1 - R_R)\frac{\Gamma CL_R^+}{wd}P_{ase,in}^+(t) + R_R I_{ase,0}^-(t) \tag{2.3}$$

$$I_{ase,M}^-(t) = (1 - R_L)\frac{\Gamma CL_L^-}{wd}P_{ase,in}^-(t) + R_L I_{ase,M}^+(t) \tag{2.4}$$

$F_{in}^{\pm}$ and $F_{out}^{\pm}$are respectively the input and output optical fields of the active region of the SOA on left and right sides. $P_{ase,in}^{\pm}$ and $P_{ase,out}^{\pm}$ are ASE power to the input and to the output of the active area. F_{k-1}^+ *and* $I_{ase,k-1}^+$ *are* respectively the optical field signal and ASE intensity to the input of the section k, propagating in the + direction. Similarly, F_k^- *and* $I_{ase,k}^-$ propagate in the inverse direction. Γ is the optical confinement factor in the active layer, w is the width and d is the thickness. Similarly, the output field signals of the two output sides and the ASE power can be written as follows:

$$F_{out}^-(t) = \left(1 + \sqrt{R_R}\right)\sqrt{\frac{wdCL_R^-}{\Gamma}}F_0^-(t) - \sqrt{R_R CL_R^+ CL_R^-}F_{in}^+(t) \tag{2.5}$$

$$F_{out}^{+}(t) = \left(1 + \sqrt{R_L}\right)\sqrt{\frac{wdCL_L^{+}}{\Gamma}}F_M^{+}(t) - \sqrt{R_L CL_L^{+} CL_L^{-}}F_{in}^{-}(t) \tag{2.6}$$

$$P_{ase,out}^{+}(t) = (1 - R_L)\frac{wdCL_L^{+}}{\Gamma}I_{ase,M}^{+}(t) - R_L CL_L^{+} CL_L^{-} P_{ase,in}^{-}(t) \tag{2.7}$$

$$P_{ase,out}^{-}(t) = (1 - R_R)\frac{wdCL_R^{-}}{\Gamma}I_{ase,0}^{-}(t) - R_R CL_R^{+} CL_R^{-} P_{ase,in}^{+}(t) \tag{2.8}$$

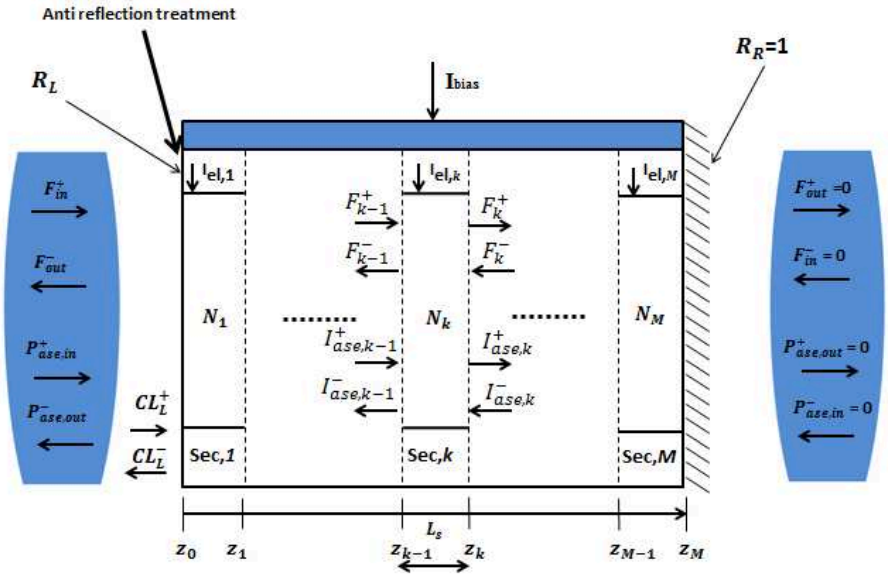

Figure 2- 2 : RSOA configuration.

To simulate an RSOA, we just put R_R = 1 and R_L = 0. Figure 2- 2 shows this modification.

2.2.1 *Propagation of signals in an optical calculation section*

The following equation describes the time domain optical field signal propagation in the SOA according to the model in [6]:

$$F_k^{\pm} = e^{ik_{N_k,\omega_i}^{(0)}L_s}\left[1 - \frac{i}{2}g_{n_{N_k,\omega_i}}^{(1)}L_s\frac{d}{dt} + \left(ik_{N_k,\omega_i}^{(2)}\frac{L_s}{2} - \frac{\left(g_{n_{N_k,\omega_i}}^{(1)}\frac{L_s}{2}\right)^2}{2}\right)\frac{d^2}{dt^2}\right]\left(F_k^{\pm}\left(t - \frac{n_g(N_k,\omega_i)}{c}L_s\right)\right) \tag{2.9}$$

Where

$$g_{n_{N_k,\omega_i}}^{(1)} = \left.\frac{\partial g_n(N_k,\omega)}{\partial\omega}\right|_{\omega_i} \tag{2.10}$$

$k(N_k, \omega_i)$ is the wavevector where N_k is the carrier density in the k-th calculation section and ω_i is the angular frequency of the optical signal i, the wavevector describes the effect of the environment on the amplitude and phase of the electromagnetic wave. It is a function of the refractive index and the net gain of the medium. the different derivatives of $k(N_k, \omega_i)$ can be given according to the following relationships:

$$k^{(0)}_{N_k\omega_i} = k(N_k, \omega_i) = \frac{\omega_i}{c} n_{eq}(N_k, \omega_i) + \frac{i}{2} g_n(N_k, \omega_i) \tag{2.11}$$

$$k^{(1)}_{N_k\omega_i} = \frac{n_g(N_k, \omega_i)}{c} + \frac{i}{2} \frac{\partial g_n(N_k, \omega_i)}{\partial \omega}\Big|_{\omega_i} \tag{2.12}$$

$$k^{(2)}_{N_k\omega_i} = \frac{1}{c} \frac{\partial n_g(N_k, \omega_i)}{\partial \omega}\Big|_{\omega_i} + \frac{i}{2} \frac{\partial^2 g_n(N_k, \omega_i)}{\partial \omega^2}\Big|_{\omega_i} \tag{2.13}$$

Where $n_{eq}(N_k, \omega_i)$, $n_q(N_k, \omega_i)$, and $g_n(N_k, \omega_i)$ are respectively the equivalent refractive index of the guided mode, the group index, and the net gain of the k^{th} section. $k^{(0)}_{N_k,\omega_i}$ describes the static phase and gain. $k^{(1)}_{N_k,\omega_i}$describes the group delay and gain spectral slope, and $k^{(2)}_{N_k,\omega_i}$ describes the spectral dispersions relative to index and gain.

In what follows, we substitute for some equations ω_i with λ ($\omega_i = (2\pi c)/\lambda$). The refractive index has a linear relationship with the carrier density and the wavelength as following:

$$n_{eq}(N_k, \lambda) = n_{eq0} + \frac{\partial n_{eq}}{\partial N_k}(N_k - N_0) + \frac{\partial n_{eq}}{\partial \lambda}(\lambda - \lambda_0) \tag{2.14}$$

The group index can be derived from the definition of the refractive index with the following relationship:

$$n_q(N_k, \omega_i) = n_{eq}(N_k, \omega_i) + \omega_i \frac{\partial n_{eq}(N_k, \omega_i)}{\partial \omega}\Big|_{\omega_i} \tag{2.15}$$

Where N_0 is the carrier density at transparency and λ_0 is the wavelength at the gain peak for $N = N_0$. The net gain, which is defined as the difference between the modal gain and guide losses α (N_k, λ) is given by the following equation:

$$g_n(N_k, \lambda) = \Gamma(N_k, \lambda) g_m(N_k, \lambda) - \alpha(N_k, \lambda) \tag{2.16}$$

Where the material gain is defined by:

$$g_m(N_k,\lambda) = \begin{cases} \dfrac{3g_p(N_k)(\lambda-\lambda_z(N_k))^2}{(\lambda_z(N_k)-\lambda_p(N_k))^2} + \dfrac{2g_p(N_k)(\lambda-\lambda_z(N_k))^3}{(\lambda_z(N_k)-\lambda_p(N_k))^3} & if \quad \lambda \le \lambda_z(N_k) \\ 0 & if \ \lambda > \lambda_z(N_k) \end{cases} \tag{2.17}$$

With

$$\begin{cases} g_p(N_k) = a_0(N_k - N_0) + a_0 a_1 N_0 e^{-\frac{N_k}{N_0}} \\ \lambda_p(N_k) = \lambda_{0+} b_0(N_k - N_0) + b_1(N_k - N_0)^2 \\ \lambda_z(N_k) = \lambda_{z0+} z_0(N_k - N_0) + z_1(N_k - N_0)^2 \end{cases} \tag{2.18}$$

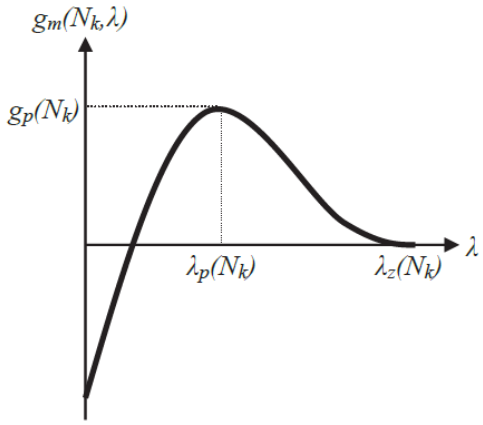

Figure 2- 3 : Plot defining the shape of the material gain $g_m(N_k,\lambda)$ [29].

λ_p (N_k) is the wavelength at the gain peak, λ_z (N_k) and g_p (N_k) are respectively the wavelength at transparency and bandgap material gain. $\Gamma(N_k, \lambda)$ is the confinement factor. It has a linear dependence on N and λ. In addition, we define the following paramets:

a_1 : Digital correction coefficient for the low carrier densities.
b_0 : Coefficient for linear variation of the gain peak with the carrier density.
b_1 : Coefficient of quadratic variation of the gain peak with the carrier density.
λ_{z0}: Wavelength at transparency for N = N_0.
z_0 : Coefficient of linear variation of the bandgap energy with the carrier density.
z_1 : Coefficient of quadratic variation of the bandgap energy with the carrier density

Equation for $\Gamma(N_k, \lambda)$ is given by the following formula:

$$\Gamma(N_k, \lambda) = \Gamma_0 + \Gamma_N(N_k - N_0) + \Gamma_\lambda(\lambda - \lambda_0) \quad (2.19)$$

Where Γ_0 is the confinement factor for $N = N_0$ and $\lambda = \lambda_0$. Γ_N and Γ_λ are constants related to the confinement factor with variation depending on the carrier density and the wavelength. The losses in the SOA are defined as following:

$$\alpha(N_k, \lambda) = \Gamma(N_k, \lambda)\alpha_a(N_k, \lambda) + \big(1 - \Gamma(N_k, \lambda)\big)\alpha_c + \alpha_s \quad (2.20)$$

Where losses in the active region α_a are linearly dependent on the carrier density and the wavelength:

$$\alpha_a(N_k, \lambda) = \alpha_0 + \alpha_N(N_k - N_0) + \alpha_\lambda(\lambda - \lambda_0) \quad (2.21)$$

With:

- α_0: losses for $N = N_0$ and $\lambda = \lambda_0$ in the active zone
- α_N: differential function of N representing losses in the active zone
- α_λ : spectral variation function representing losses in the active zone
- α_c : losses in the confinement layers
- α_s : losses of optogeometric defects

2.2.2 *Modelling of amplified spontaneous emission (ASE)*

ASE is one of the main phenomenas which degrade the performance of an SOA. When the signal strength is weak ASE degrades the signal to noise ratio (SNR). The increase in signal strength leads to a reduction in ASE power and therefore improved SNR. The equations below show the propagation of the ASE intensity in both + and -directions:

$$I^+_{ase,k} = e^{g_n(N_k, \lambda_{ase})L_s} I^+_{ase,k-1} + I_{sp}(N_k, \lambda_{ase}) \quad (2.22)$$

$$I^-_{ase,k-1} = e^{g_n(N_k, \lambda_{ase})L_s} I^-_{ase,k} + I_{sp}(N_k, \lambda_{ase}) \quad (2.23)$$

Where $I_{sp}(N_k, \lambda_{ase})$ is the spontaneous emission generated in a k^{th} calculation section:

$$I_{sp}(N_k, \lambda_{ase}) = \frac{\Gamma(N_k, \lambda_{ase})}{wd} \frac{hc}{\lambda_{ase}} r_{sp}(N_k, \lambda_{ase}) \frac{e^{g_n(N_k, \lambda_{ase})L_s} - 1}{g_n(N_k, \lambda_{ase})} \quad (2.24)$$

Where r_{sp} (N_k, λ_{ase}) is the rate of spontaneous emission of the k^{th} section, it is expressed in terms of material gain coefficient [5], h is Plank's constant and c is the speed of light in vacuum.

2.2.3 *Carrier density evolution in the SOA*

Here we give the equation for carrier density evolution which describe the dynamics of carriers N_k in the k^{th} section. The carrier density is calculated based on the electrical current injected into the k^{th} calculation section $I_{el,k}$, unstimulated recombination rate $R_{nst,k}$, stimulated recombination due to the optical injected signal $R_{sig,k}$, and the rate of recombination due to amplified spontaneous emission $R_{ase,k}$. The carrier density for section k is given by:

$$\frac{dN_k}{dt} = \frac{I_{el,k}}{q_e L_s wd} - R_{sig,k}(N_k) - R_{ase,k}(N_k) - R_{nst,k}(N_k) \tag{2.25}$$

Where q_e is the absolute value of the electron charge. $R_{sig,k}$ is the recombination rate due to M_{sig} signals propagating in the k^{th} section and is given by:

$$\begin{aligned} R_{sig,\mathrm{k}}(N_\mathrm{k}) &= \sum_{i=1}^{M_{sig}} R_{sig,\mathrm{k}}(N_\mathrm{k}, \omega_i) \\ &\approx \sum_{i=1}^{M_{sig}} \frac{g_m(N_\mathrm{k}, \omega_i)}{\hbar\omega_i} \frac{e^{g_n(N_\mathrm{k},\omega_i)L_s}}{g_n(N_\mathrm{k}, \omega_i)L_s} \left(\left|\mathrm{F}^{+}_{\mathrm{k}-1,\mathrm{i}}\right|^2 + \left|\mathrm{F}^{-}_{\mathrm{k,i}}\right|^2\right) \end{aligned} \tag{2.26}$$

Where ω_i is the angular frequency of the i^{th} signal. The recombination rate due to the amplified spontaneous emission is determined by taking into account the ASE spectral dependence. This is achieved by defining M_{ase} pseudo-modes. The pseudo-modes take into account the entire spectrum of the amplified spontaneous emission. Their number depends on the accuracy required for the numerical calculation. $R_{ase,k}$ due to pseudo-modes M_{ase} in each section is calculated as follows:

$$R_{ase,\mathrm{k}}(N_\mathrm{k}) = \sum_{j=1}^{M_{ase}} R_{ase,\mathrm{k}}(N_\mathrm{k}, \omega_j) \tag{2.27}$$

Where $R_{ase,k}(N_k,\omega_j)$ is the recombination rate due to a single pseudo-mode with ω_j angular frequency, it is given by the following equation:

$$\begin{aligned} &R_{ase,\mathrm{k}}(N_\mathrm{k}) \\ &= \frac{g_m(N_\mathrm{k}, \omega_j)}{\hbar\omega_j} \frac{e^{g_n(N_\mathrm{k},\omega_j)L_s} - 1}{g_n(N_\mathrm{k}, \omega_j)L_s} \left(I^{+}_{ase,\mathrm{k}-1} + I^{-}_{ase,\mathrm{k}}\right) \\ &+ 2g_m(N_\mathrm{k}, \omega_j) \frac{\Gamma(N_\mathrm{k}, \omega_j)}{wd} \frac{e^{g_n(N_\mathrm{k},\omega_j)L_s} - g_n(N_\mathrm{k}, \omega_j)L_s - 1}{\left(g_n(N_\mathrm{k}, \omega_j)\right)^2 L_s} r_{sp}(N_\mathrm{k}, \omega_j) \end{aligned} \tag{2.28}$$

For the unstimulated recombination rate, we use the common expression:

$$R_{nst,\mathrm{k}}(N_\mathrm{k}) = A_{nr}N_\mathrm{k} + B_{ns}N_\mathrm{k}^2 + C_{Au}N_\mathrm{k}^3 + D_{leak}N_\mathrm{k}^{5.5} \qquad (2.29)$$

Where A_{nr}, B_{ns}, C_{Au} and D_{leak} are respectively the coefficients of non-radiative recombination, spontaneous recombination, Auger effect, and recombination coefficient representing the leakage currents.

2.3 Experimental validation of the RSOA model

In order to calculate the M differential equations related to the M calculation sections, we use an electronic circuits simulator [6]. The equivalent circuit is implemented in the Agilent Technologies ADS software. It allows several kinds of simulations such as DC (direct current) simulation, AC (alternating current) simulation, temporal (transient) and HB (harmonic balance) simulations. The used model has been validated for several SOAs [5]. In this study, we use a RSOA available in the laboratory (CIP SOA-RL-OEC-1550) whose characteristics are given in Appendix-A, model parameters are given in Appendix-B. We characterized the RSOA in static regime in terms of the RSOA output power and its ASE output power over a wide range of wavelengths, input powers and bias currents in order to fit simulation results on experimental ones by adjusting the RSOA model parameters thanks to an optimization program that was developed in Lab-STICC/ ENIB.

2.3.1 Characterisation of RSOA in static regime

In static regime the characterization of the RSOA in terms of gain, NF, and power saturation over a wide range of wavelengths, input powers and bias currents is done in direct measurement and in pump probe configuration. The next figures show all results, from Figure 2- 4 to Figure 2- 11, where we have a good agreement that we obtained between measurement and simulation.

I. RSOA optical gain vs wavelength for different input power

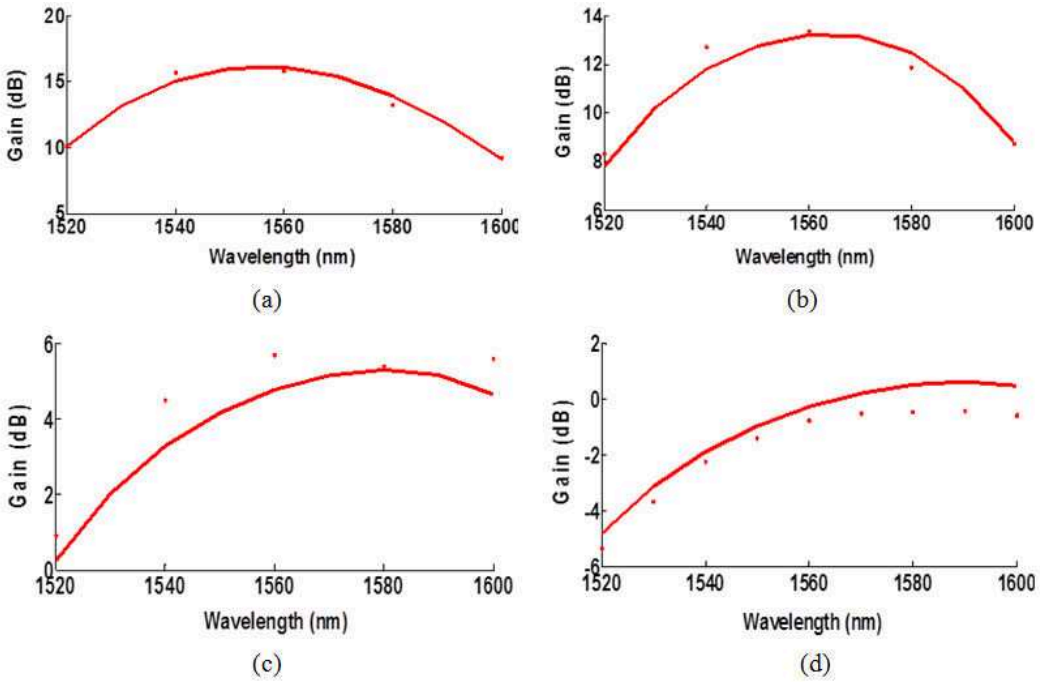

Figure 2- 4 : Measurements (points) and simulated (solid line) results of the optical gain as a function of the wavelength for a bias current of 70 mA and an input power of (a) -20 dBm, (b) -10 dBm, (c) 0 dBm, and (d) 4 dBm.

The figure above shows a particular case for the bias current of 70 mA in which we have done most of our measurements, we see that we have very good fitting for four different optical input powers ranging from 4 dBm to -20 dBm, and for an 80 nm optical bandwidth range.

II. RSOA optical gain vs bias current

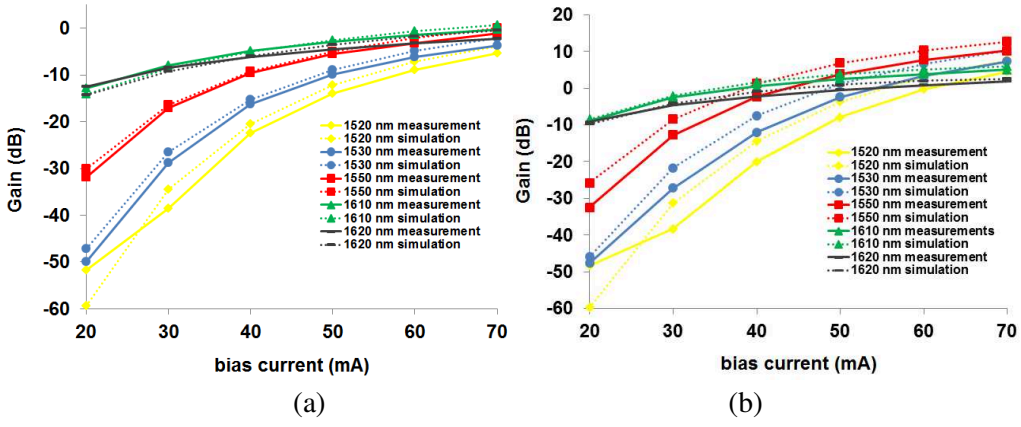

Figure 2- 5 : RSOA gain versus its bias current for different wavelength values for (a) 3.3 dBm optical input power and (b) -10 dBm optical input power.

Figure 2- 5 shows the RSOA's gain versus bias current for 3.3 dBm and

-10 dBm optical input power. This is an important information for using the RSOA as an intensity modulator. In fact these results are of great interest to choose the bias current of the RSOA to be a compromise in order to have a sufficient gain but also with keeping a sufficient gain variation so as not to clip the RF current. In addition, these plots show that for the 1610 and 1620 nm wavelengths, the obtained gain variation will be very small when compared to other wavelengths and this coud explain in the dynamic regime the weakness of the photodetected output electrical signal level (Figure 2- 13(b)).

III. RSOA noise figure

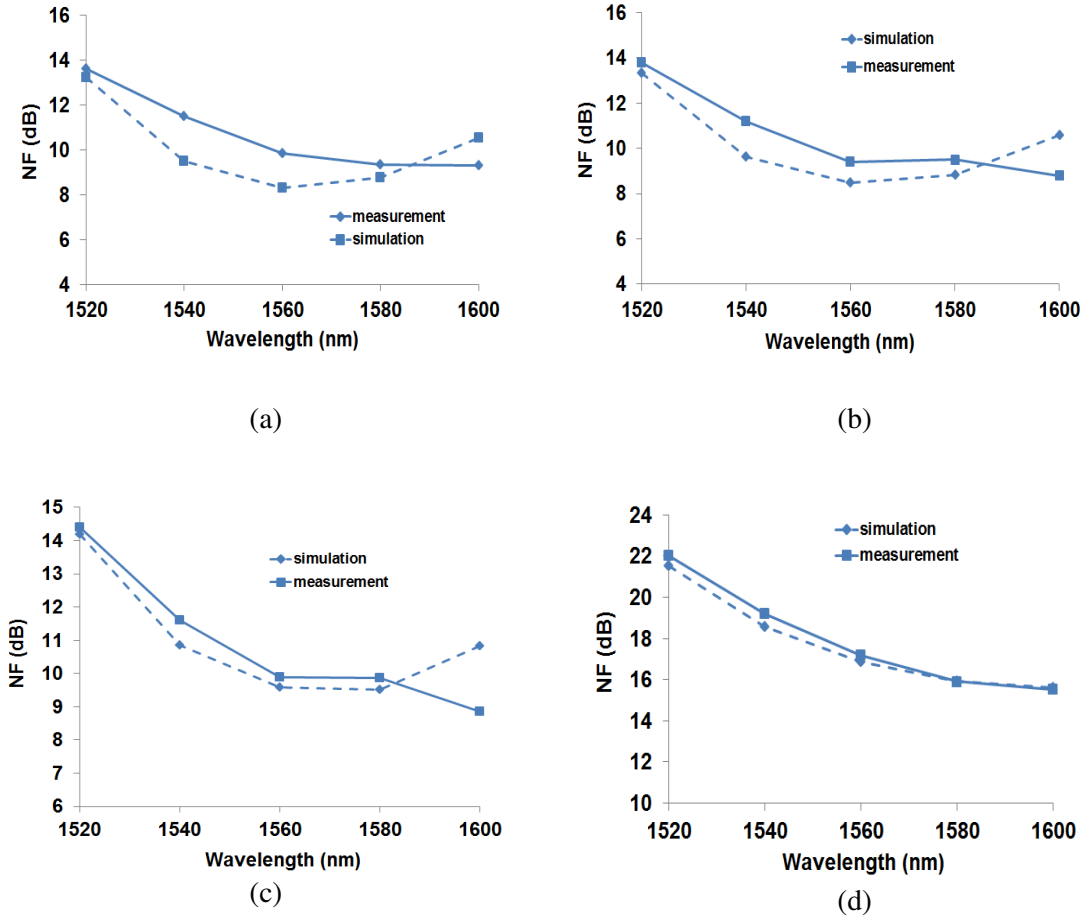

Figure 2- 6 : Measurements (dots) and simulated (solid lines) of the NF in function of the wavelength for a bias current of 60 mA and an input power of (a) -30 dBm, (b) -20 dBm (c) -10 dBm, (d) 4 dBm.

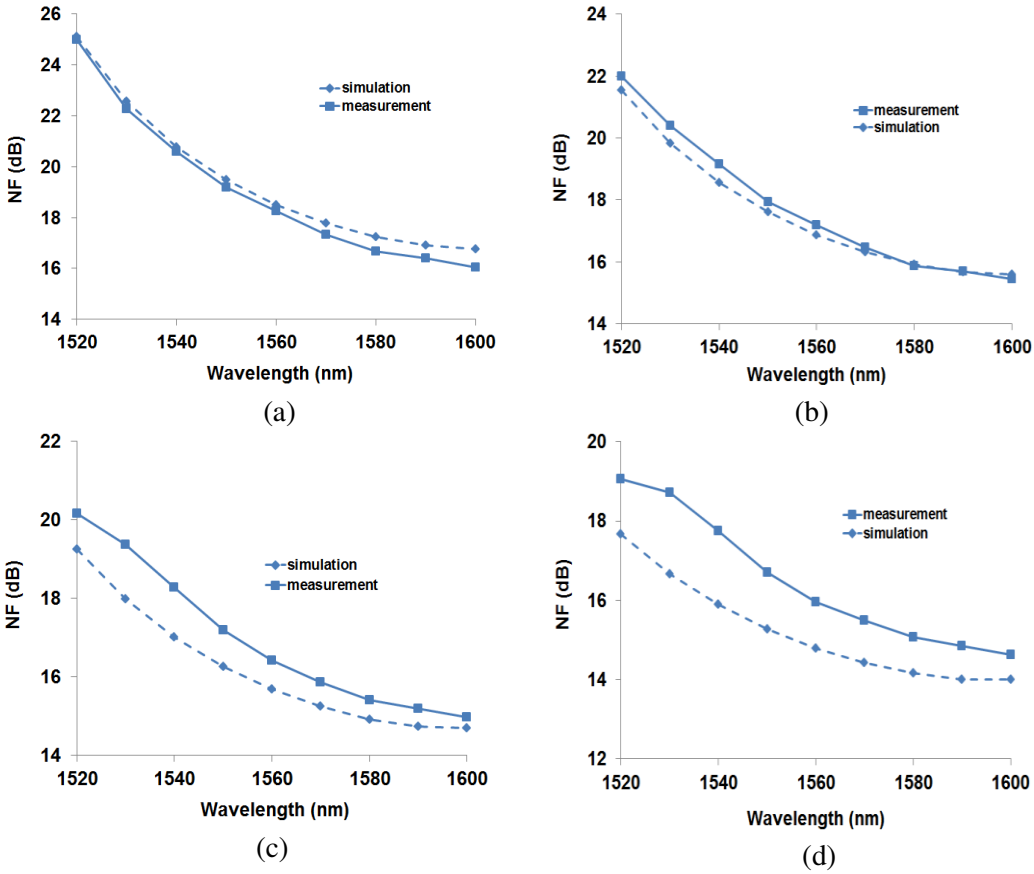

Figure 2- 7 : Measurements (dots) and simulated (solid lines) of the NF in function of the wavelength for an input power of 4dBm and a bias current of (a) 50 mA,(b) 60 mA (c) 70 mA, (d) 80 mA.

As we can see in Figure 2- 6 and Figure 2- 7, we have a good agreement between simulation and measurement for the noise figure values for four different optical input powers and for four different bias current values for a wavelength range of 80 nm. Moreover, we notice that the NF is higher for the 4 dBm input power case, we also notice that we have higher noise figure values for the low wavelength range.

IV. RSOA gain and NF in a pump probe configuration

In chapter 3 we develop a co-simulation setup that simulates an important optical networking application for future optical OFDM systems which is wavelength conversion. Wavelength conversion of an OOFDM signal is performed using the cross gain modulation effect of the RSOA.

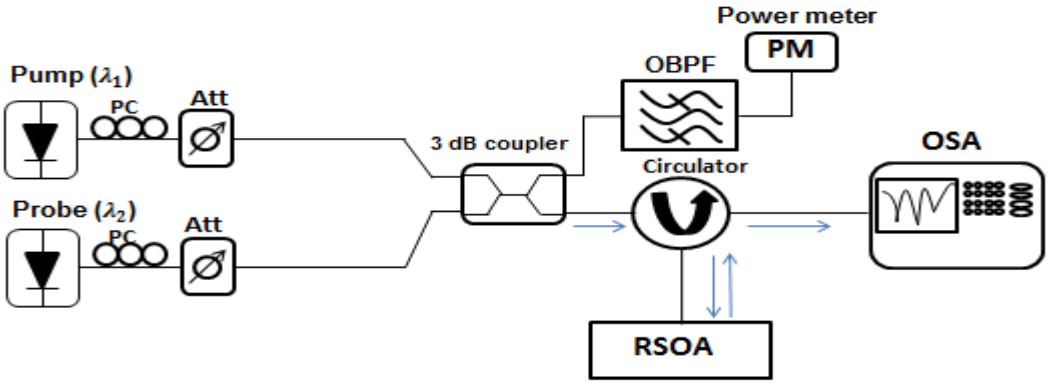

Figure 2- 8 : schematic diagram of the static setup used in characterizing the RSOA in a pump probe configuration, PC: polarization controller, Att: attenuator, OSA: optical spectrum analyzer.

Figure 2- 8 shows the schematic representation of the experimental setup used for the RSOA static characterization in a pump probe configuration. We have a fixed CW laser source at λ_1 and a tunable CW laser source at λ_2. Both signals are combined using a 3 dB coupler and are inserted into the RSOA. At the output of the RSOA is an optical spectrum analyzer (OSA). The OSA is used to detect the signal power and the ASE signal. We use these values to determine the Gain and the NF of the RSOA in a pump probe configuration.

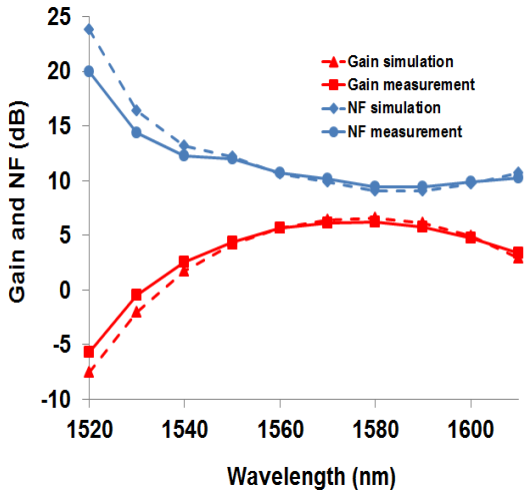

Figure 2- 9 : Gain and NF of the RSOA in a pump probe configuration, the bias current is 80 mA, and the pump and probe input powers are -2 dBm each. Pump wavelength is at 1560 nm.

As we can see in Figure 2- 9, there is a good agreement between simulation and measurement for both NF and Gain results for the RSOA.

V. Saturation power

The saturation power is one of the main parameters of the SOA that is generally used to indicate the upper limit of the linear amplification of the SOA. Ideally, it should be as high as possible. The saturation power is defined either

depending on the input or according to the output power. The saturation power at the output can be generally expressed by the following formula [62]:

$$P_{sat,out} = P_{sat}\, ln(2) = \frac{h\nu . wd}{\Gamma a_0 \tau} ln(2) \qquad (2.30)$$

Where hυ is the energy of a photon, the coefficient a_0 is the differential gain and τ is the carrier lifetime. Figure 2- 10 shows the saturation power at the entrance and exit of the RSOA obtained for a bias current of 70 mA and a wavelength of 1560 nm.

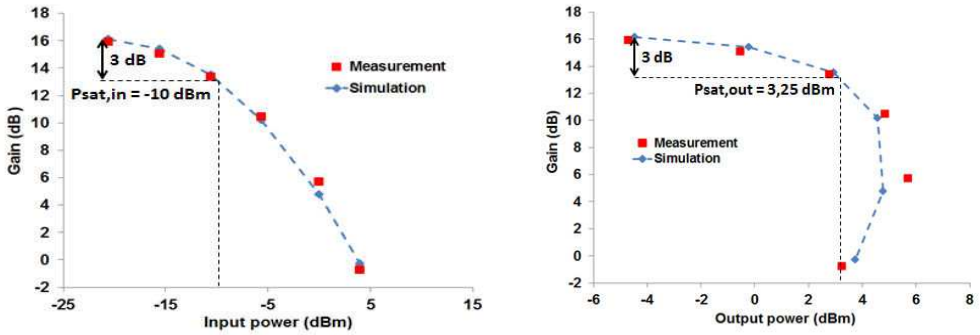

(a) (b)

Figure 2- 10 : Numerical and experimental results of the saturation power as function of (a) the input power and (b) the output power of the RSOA. The RSOA bias current is 70 mA and the input wavelength is 1560 nm.

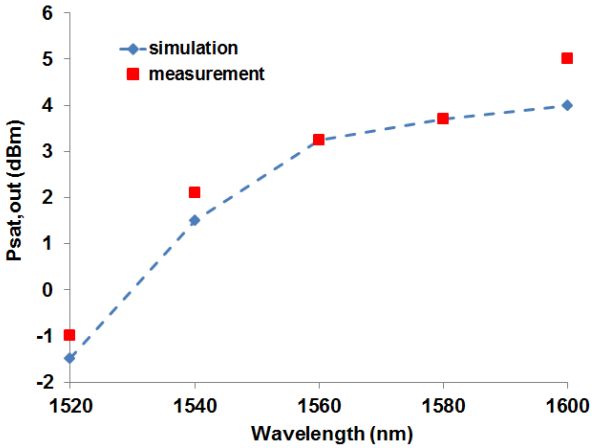

Figure 2- 11 : Numerical and experimental results of the Output saturation power of the RSOA versus wavelength for a bias current of 70 mA.

The saturation power changes with wavelength. It is very important to properly simulate its dependence on wavelength for broadband simulations. Figure 2- 11 shows the saturation power P_{sat_out} in function of the wavelength obtained experimentally and numerically for the RSOA. Figure 2- 11 shows that we have almost good agreement between simulation and measurement, we also

notice that the saturation output power becomes much higher at long wavelength values.

2.3.1 *Dynamic characterization*

2.3.1.1 Direct modulation and frequency response

In dynamic regime, we directly modulated the RSOA by a sinusoidal signal and we measure its electrical bandwidth over the 100 nm-wide optical wavelength range. Figure 2- 12 shows the experimental setup for this measurement, a signal generator sends a sinusoidal signal at a certain frequency, a DFB laser sends a CW optical power signal to the RSOA. An optical band pass filter filters the output of the RSOA at the desired wavelength, a photodetector with 8 GHz bandwidth detects the modulated optical signal at the output of the RSOA, and an electrical signal analyzer detects the power level of the received signal after the photodetector at the modulation frequency fm.

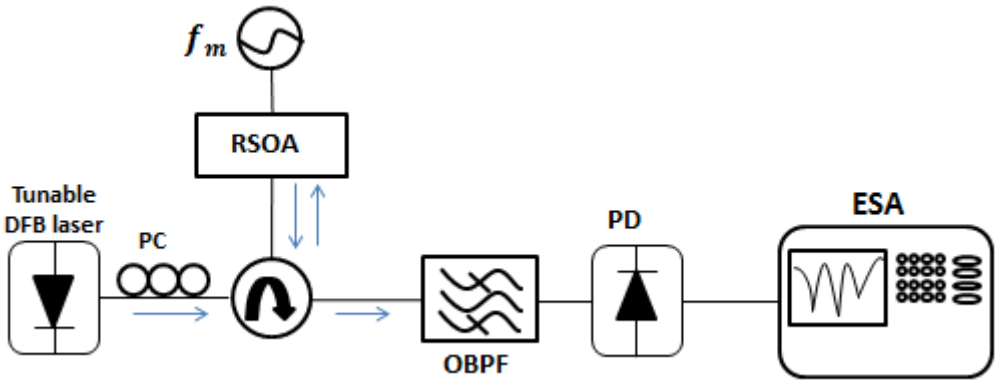

Figure 2- 12 : Setup used for the dynamic characterization of the RSOA, PC: polarization controller, OBPF: optical band pass filter, PD: photodetector, ESA: electrical signal analyzer.

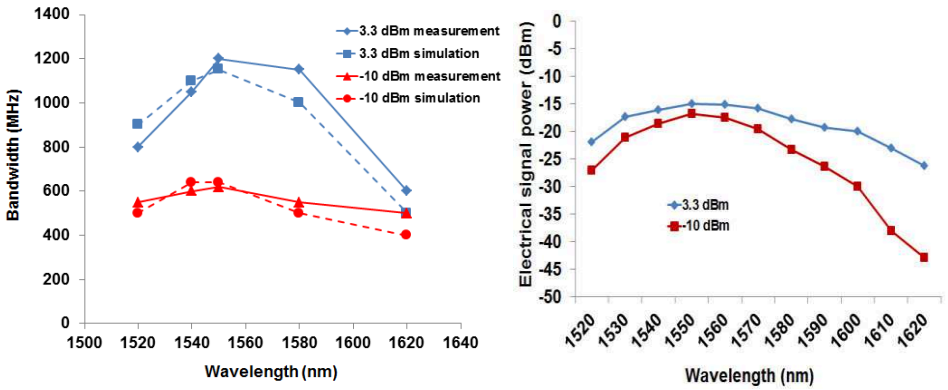

(a) (b)

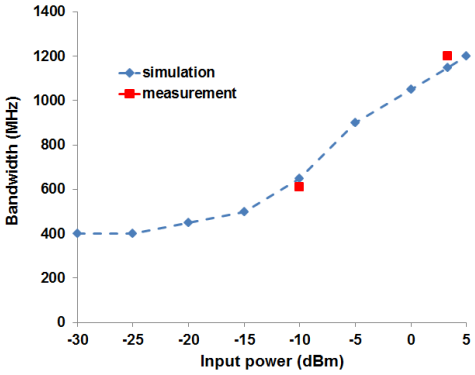

(c)

Figure 2- 13 : (a) RSOA photodetected output electrical bandwidth and (b) signal level versus wavelength for two injected optical powers of 3.3 dBm and -10 dBm for 60 mA bias current. (c) RSOA electrical bandwidth versus optical input power for 1550 nm, and 60 mA bias current.

The results in Figure 2- 13(a) show that the electrical bandwidth increases from almost 650 MHz to 1200 MHz for the 1550 nm wavelength by increasing the optical input power injected into the RSOA. This effect is well known and has been shown in previous simulations [28] as it is due to the reduced effective carrier lifetime obtained at higher optical input power. The simulation results in Figure 2- 13(c) confirm that the RSOA modulation bandwidth increases for input optical power in saturation regime. Moreover, we can see in Figure 2- 13(a) that the bandwidth is lower on each side of the wavelength spectral response due to the fact that the effective carrier lifetime increases as we go far away from the maximum gain wavelength. The measured electrical signal level versus wavelength at 100 MHz is also given in Figure 2- 13(b). The modulated signal level is also lower for low and high wavelength regions and thus leads to a reduced signal to noise ratio and reduced RSOA modulation efficiency for these wavelengths.

2.3.1.2 XGM frequency response

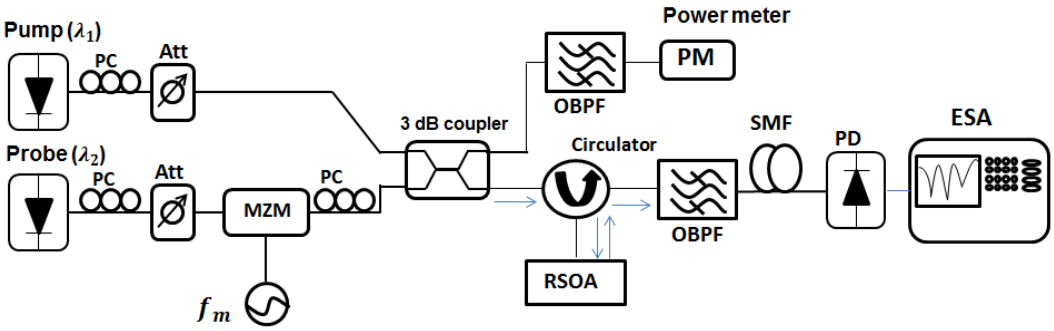

Figure 2- 14 : schematic diagram of the dynamic characterization of the RSOA in a pump probe configuration. PC: polarization controller; Att: attenuator; MZM: Mach-Zehnder modulator; PD: photodiode; PM: power meter, OBPF: optical band pass filter.

Figure 2- 14 shows the dynamic characterization setup of the RSOA in a pump probe configuration. We have a CW fixed laser source at λ_1 and a CW tunable laser source at λ_2. A sinusoidal signal at 0 dBm input electrical power is used to modulate the CW input optical signal at λ_2 by using a MZM. The output sinusoidal optical signal is combined with the CW signal at λ_1 by an optical 3 dB coupler. The output of the coupler is inserted into the RSOA. At the output of the RSOA, the probe signal at λ_2 is selected by a tunable optical filter. At the output of the filter the signal is detected by a 8 GHz photodetector and sent to an electrical signal analyzer. Figure 2- 15 shows the bandwidth for the pump and the probe signals of -2 dBm mean power at the input of the RSOA and for the RSOA bias current of 80 mA. As we can see, the RSOA bandwidth remains between 1400 MHz and 1700 MHz for the wavelength range from 1520 nm up to 1600 nm. The pump wavelength is at 1556 nm.

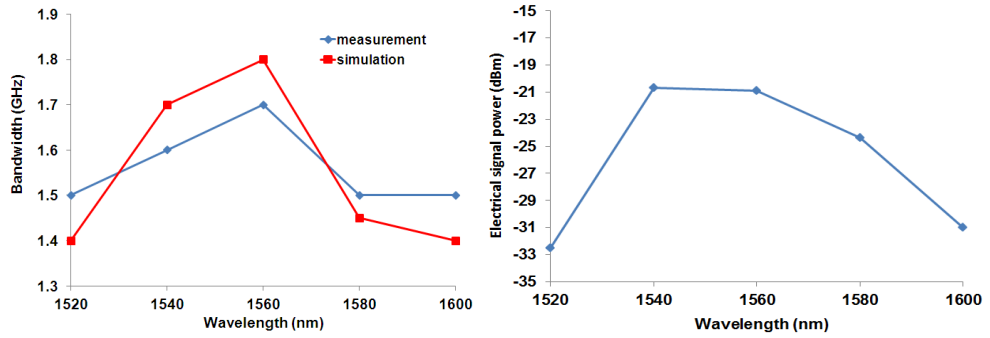

(a) (b)

Figure 2- 15 : (a) Electrical bandwidth for RSOA in a pump probe configuration.(b) Electrical magnitude power of the probe signal at 100 MHz

Figure 2- 15 (b) shows the photodetected signal power level of the probe signal at 100 MHz at the RSOA output, which depends on probe gain spectrum and its saturation power.

2.3.1.3 Phase amplitude coupling factor

$\alpha_{H,eff}$ is measured by method proposed by Devaux given in [61]. It is obtained through the small signal frequency response of an RSOA and a dispersion medium used in a pump-probe configuration, as shown in Figure 2- 14. In this technique, a pump intensity-modulated signal and a CW probe signal are injected into the RSOA. The pump signal is used to induce gain modulation in the RSOA. At the output of the RSOA, the probe modulated signal propagates in a dispersive single-mode fiber of 56 km length. By this means, the chirp induced by the phase amplitude coupling is carried by the probe and the signal $\alpha_{H,eff}$ factor can be easily calculated from the frequencies with high extinctions in the measured fiber output response [61]. In the following of the manuscript, we use α_H instead of $\alpha_{H,eff}$ to simplify the notation.

Figure 2- 16(a) shows the results of measurements and simulations of α_H within the optical gain bandwidth of the RSOA. In simulations α_H is obtained from the defenitions given in chapter 1. A good agreement is obtained between the two results for an optical bandwidth of 60 nm.

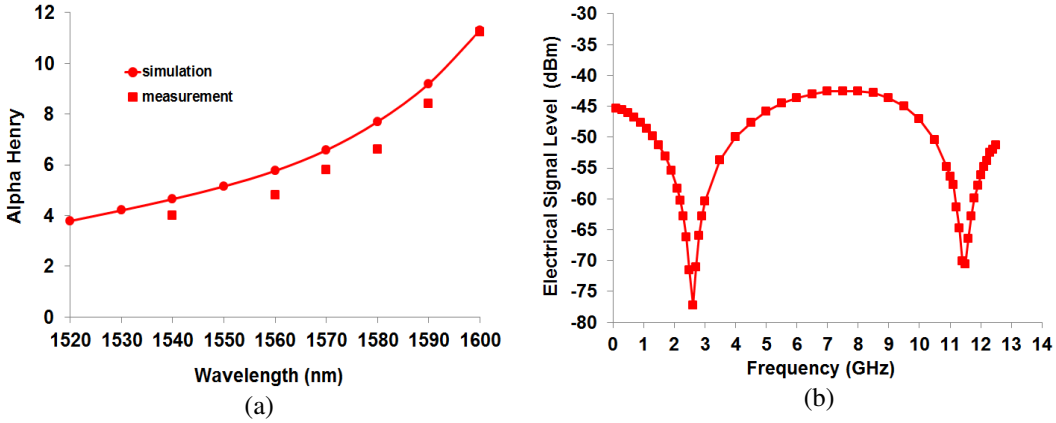

(a) (b)

Figure 2- 16 : (a) Measurements and simulations of phase amplitude coupling factor (α_H) versus wavelength for a bias current of 80 mA and a pump probe optical input power of -7 dBm, pump signal wavelength is 1550 nm (b) Measured frequency response of a 56 km SMF for the same conditions as in (a). The probe signal wavelength is 1560 nm.

In function of power, the simulation in Figure 2- 17 shows that α_H decreases in saturation regime [29].

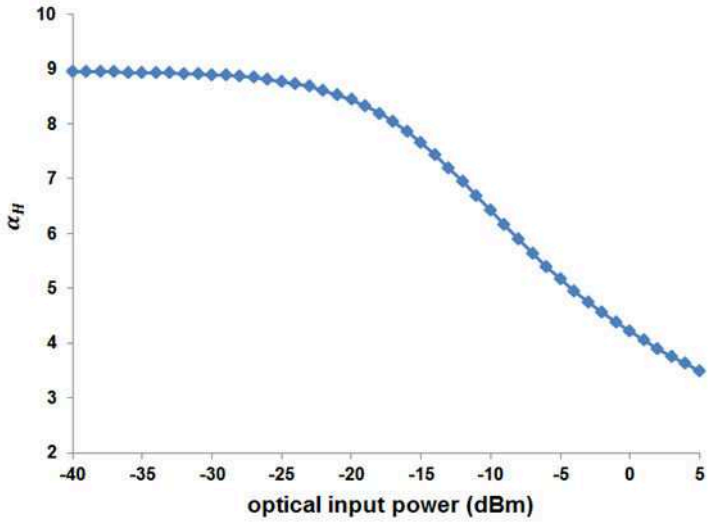

Figure 2- 17 : α_H versus Input power for an RSOA at 1560 nm, 65 mA bias current.

2.3.1.4 Direct modulation Harmonic and Intermodulation distortion product results

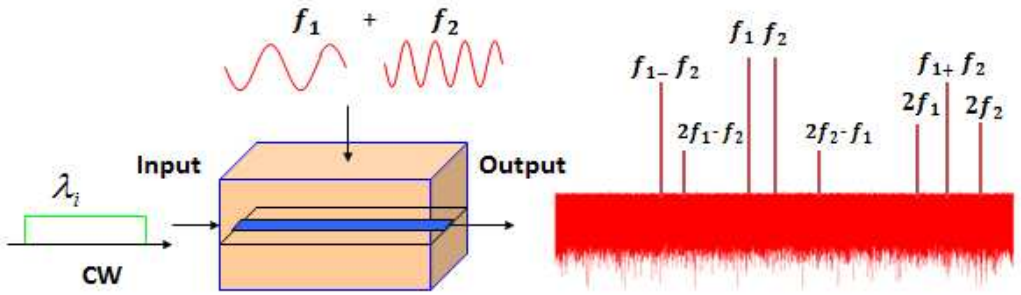

Figure 2- 18 : Principle scheme for RSOA, second order harmonics, 2nd, and 3rd order intermodulation products by two input electrical signals at frequencies f_1 and f_2.

As the RSOA is a non linear device, it will present high order harmonics and intermodulation products in presence of a two tone signal (Figure 2- 18). These products are obtained using a transient simulation in ADS. The comparison between simulation and measurement of second order harmonic distortion (HD2) and second order intermodulation distortion (IMD2) is done on one operating point to check the validity of the simulations and is represented in Figure 2- 19.

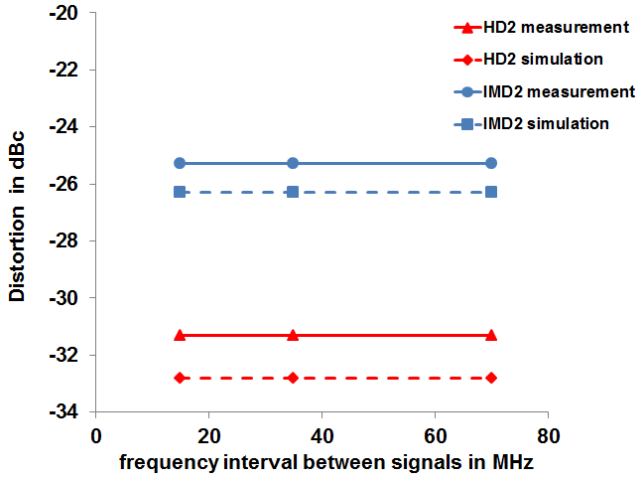

Figure 2- 19 : Simulation and measurement distortion dBc values for 2nd order harmonic and IMD2 signals as function of frequency interval between signals,(1 mA input AC current, Input power to the RSOA is 2 dBm, bias current is 60 mA)

Figure 2- 20 and Figure 2- 21 shows the simulation of HD2, IMD2 and third order intermodulation distortion (IMD3). The results show that IMD2 and HD2 are higher for short wavelength values. This shows a higher nonlinearity at short wavelength values which can lead to degradation in performance at these wavelengths.

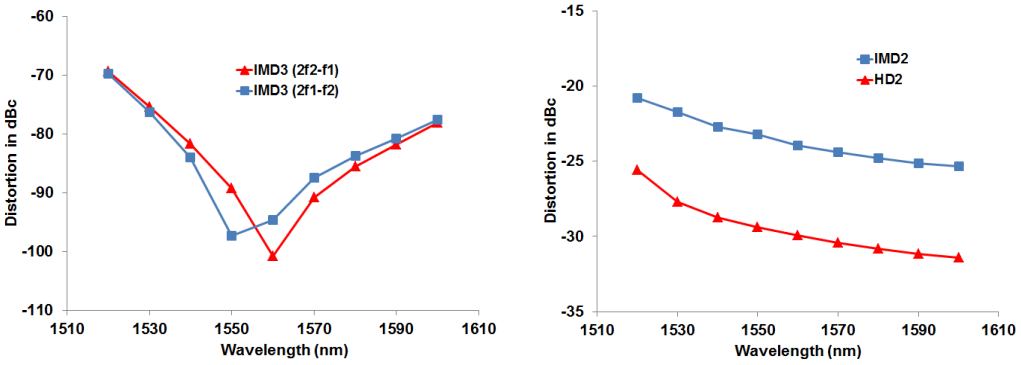

(a) (b)

Figure 2- 20: Distortion simulation dBc values for (a) IMD3 signals (b) IMD2 and HD2, as function of wavelength for a 7 mA input AC current, Input power to the RSOA is -20 dBm, bias current is 65 mA.

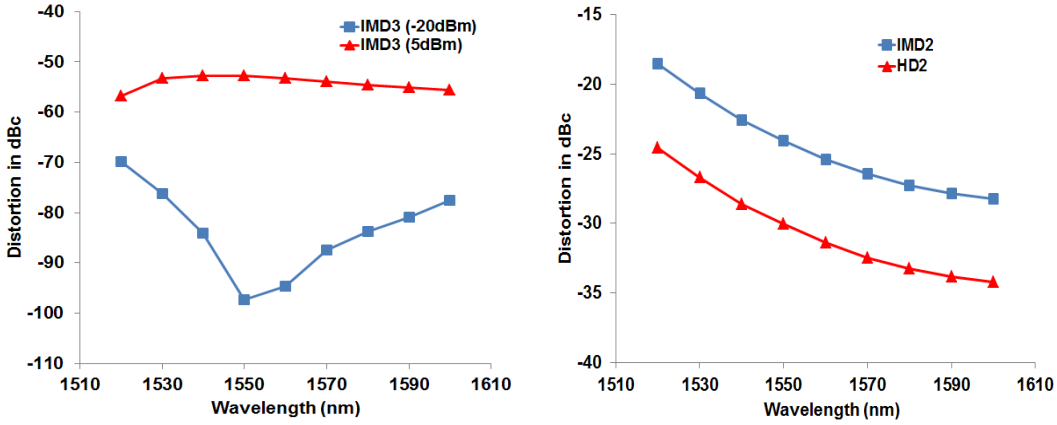

(a) (b)

Figure 2- 21: Distortion simulation dBc values for (a) IMD3 signals (b) IMD2 and HD2, as function of wavelength for a 7 mA input AC current, Input power to the RSOA is 5 dBm, bias current is 65 mA.(for case (a) we have two input powers).

2.4 Conclusion

In this chapter, we have presented a comprehensive wideband time domain RSOA field based model implemented under ADS software. We have used an optimization program developed at ENIB in order to fit the model to an RSOA component that we have used in experimental measurements. The RSOA has been characterized experimentally and by simulation with good agreement between them in terms of gain, NF, saturation power, α_H, and electrical bandwidth, over a wide range of optical input powers, bias currents and wavelengths.

3 EXPERIMENTAL AND NUMERICAL ANALYSIS OF AN RSOA AS AN INTENSITY MODULATOR AND AS WAVELENGTH CONVERTER FOR IMDD-OFDM TRANSMISSION SYSTEMS

3.1 Introduction

In this chapter we present the developed co-simulation platform for IMDD-OOFDM transmission systems. We also present the measurement setup using the RSOA as intensity modulator and wavelength converter. We perform a numerical and experimental study in which we analyze the transmission performance in terms of different parameters. We also make a numerical study in which we enhance the transmission capacity using AMOOFDM for both a mono and a two electrode RSOA configuration in presence of an ideal optical preamplification.

In a final section, we demonstrate experimentally the feasibility of OOFDM signals wavelength convertion exploiting XGM nonlinearity in the RSOA. Using the developed co-simulation platform, we study the wavelength conversion system capacity by using AMOOFDM.

3.2 TRANSMISSION LINK MODEL

In this section, we present the transmission link model of IMDD OFDM that we used in our work. This model has been developed at Bangor University [63] to simulate the generation, transmission, and detection of IMDD OFDM signals for metropolitan and access networks.

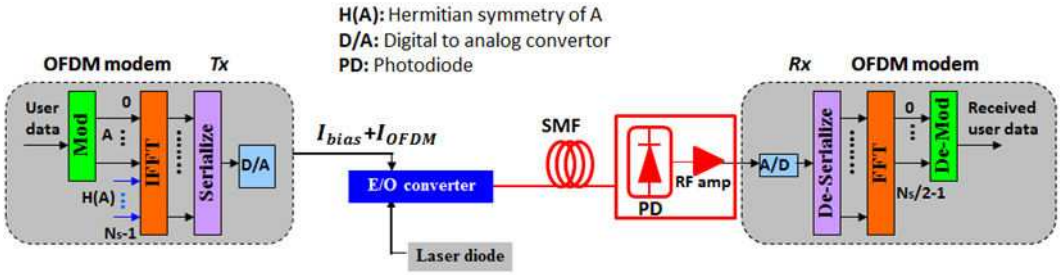

Figure 3- 1 : OFDM IMDD system.

The developed IMDD OFDM based transmission link is shown in Figure 3- 1, it includes an OFDM transmitter involving an E/O converter performing intensity modulation, a PIN photon detector and an OFDM receiver. The generation, transmission and detection of the OFDM signals are modeled following procedures similar to those reported in [63, 64]. These procedures are outlined as follows:

In the transmitter, an incoming binary data sequence is serial to parallel converted, encoded and subsequently truncated into a large number of sets of complex data, and each set contains the same number of subcarriers. Several modulation formats are implemented as DPSK, QPSK, 16 QAM, and up to 256 QAM. At the input of the inverse fast Fourier transform (IFFT), a complex conjugate of the original encoded data within each subcarrier set is introduced,

which is specially arranged to satisfy the Hermitian symmetry in respect to the original data. After applying an IFFT, a real-valued parallel symbol is generated. A cyclic prefix is then added to the front of the symbol. By utilizing a parallel-to-serial converter, these parallel symbols are serialized, forming a long digital sequence. After passing through a digital-to-analog converter (DAC), a real-valued electrical OFDM signal is produced, to which a dc bias current is also added to drive directly the E/O converter to modulate the injected CW optical wave. A cyclic prefix and a cyclic suffix that occupy 25 % of the OFDM symbol are added to guard against intersymbol interference. A clipping ratio of 13 dB is used on the OFDM signal so as to mimimize the distortion caused by high PAPR signals. The signal line rate is calculated using the expression:

$$R_{signal} = \sum_{k=1}^{M_s} S_k = \frac{\sum_{k=1}^{M_s} n_k}{T_b} = \frac{f_s \sum_{k=1}^{M_s} n_k}{2M_s(1+\eta)} \tag{3.1}$$

Where M_s is the total number of data-carrying subcarriers in the positive frequency bins, S_k is the signal bit rate corresponding to the k-th subcarrier, n_k is the total number of binary bits conveyed by the k-th subcarrier within one symbol period T_b, fs is the ADC/DAC sampling rate, and η is the cyclic prefix parameter. In the receiver, the optical signal is detected by a PIN photo detector. In the receiver we take into account the shot, the thermal, and the RIN noises. We also take into account the noise added by the electrical to optical converter (ASE noise). A preamble synchronization technique is used in which we send preamble data signals at certain time samples of the sent subcarriers (every 50 time samples), the received preamble data at the receiver is used to compensate the channel imperfections. ADC first converts the electrical signal into a digital waveform, after removing the cyclic prefix, an FFT is applied. The subcarriers in the positive frequency bin are finally serialized, from which the original data stream can be recovered using the known modulation format on each subcarrier and finally the bit error rate (BER) and EVM are calculated.

3.3 Co-simulation platform

In this section, we will present the co-simulation platform for OFDM IMDD that we developed using Matlab, VPI and ADS softwares. Figure 3- 2 shows the OFDM IMDD co-simulation platform, the transmitter and receiver are implemented in MATLAB and explained in section 3.2. The RSOA model is implemented in ADS and is decribed in chapter 2. The SMF is simulated by VPI photonics software. The main parameters that were set for this fiber are listed in Table 3.

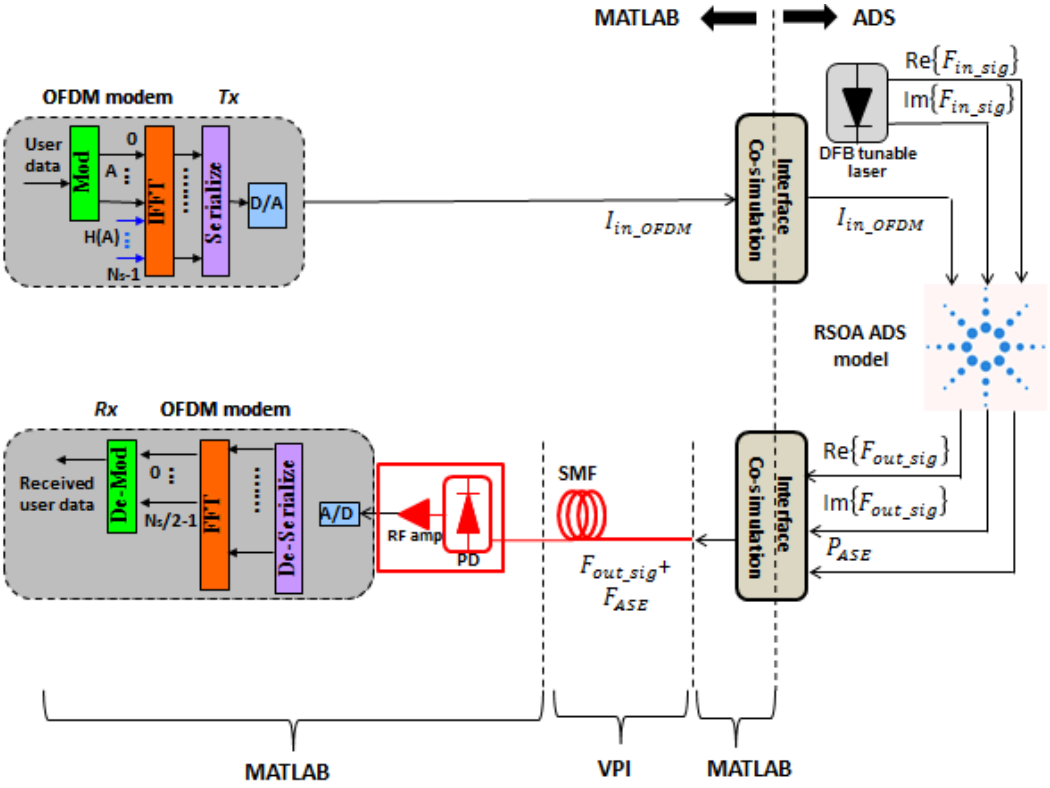

Figure 3- 2 : OFDM IMDD RSOA system co-simulation platform.

Table 3 : SMF simulation parameters

Parameters	Symbol	Value	Unit
Group refraction index	n_g	1.47	
Attenuation	A	0.2e-3	dB/m
Dispersion coefficient	D	18.5e-6	s/m^2
Polarization mode dispersion coefficient	D_p	3.16e-15	$s/\sqrt{m}$
Nonlinearity index	n_2	2.6e-20	m^2/W
Effective area	A_{eff}	80e-12	m^2

The simulation parameters of the RSOA (input time domain OFDM electrical signal, input optical power, bias current, wavelength, ext.…) are generated from MATLAB and imported into the RSOA model. I_{in_OFDM} is the OFDM generated electrical current. At the input of the RSOA, we inject a continuous wave optical field with reference phase set to zero. At the output of the RSOA we have a complex optical field and the optical power of the ASE. The

output signals are combined and inserted into the VPI SMF link. Finally, the output of the SMF link is filtered by an optical band pass filter with an optical bandwidth of $\Delta\lambda = 0.3$ nm, detected by a photodetector and demodulated by the OFDM receiver implemented in MATLAB.

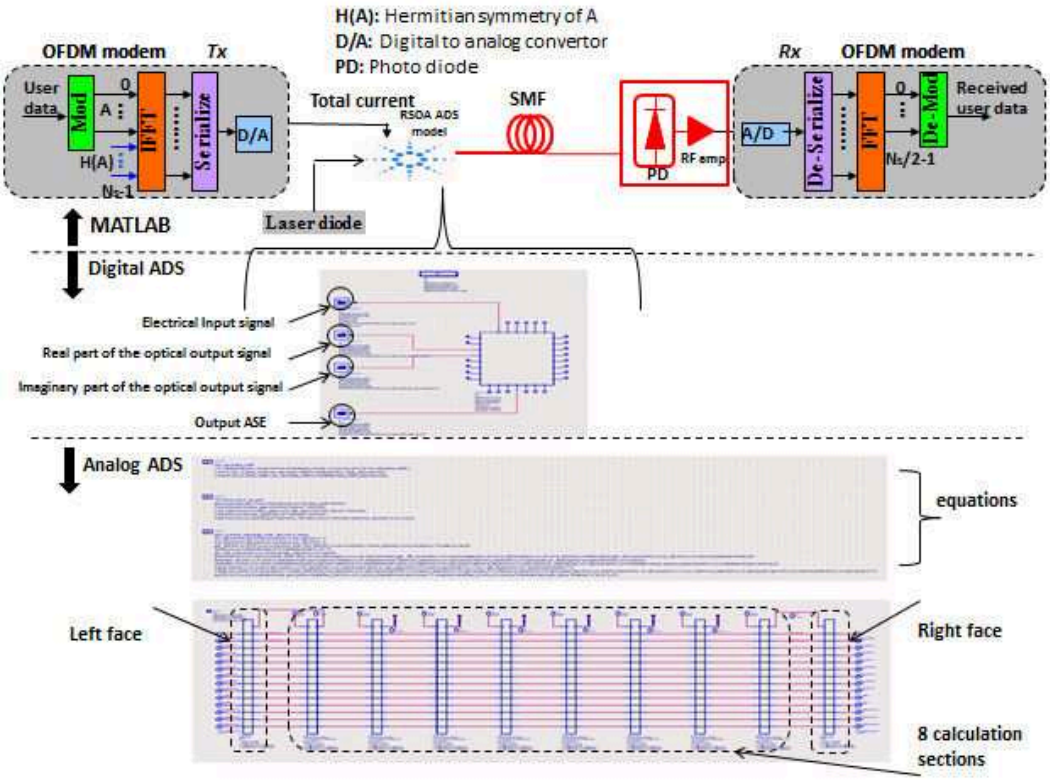

Figure 3- 3 : Parts of the RSOA ADS model used in the co-simulation platform.

Figure 3- 3 shows some details of the RSOA ADS model used in the co-simulation platform, first we have the digital interface of ADS that simulates the time domain input and output field signals, then we have the analog ADS simulation that applies the SOA model developed analytical equations. Our used SOA model is divided into 8 calculation sections to take into account the gain saturation along the RSOA length [5]. In the co-simulation platform, P_{ASE} is used to calculate the noise due to ASE by calculating the standard deviation of the ASE power at the output of the SOA [65]:

$$\sigma_{ASE}(t) = \sqrt{\frac{P_{ASE}(t)}{2}} \tag{3.2}$$

Where $P_{ASE}(t)$ is the ASE power after an optical filter with an optical bandwidth of $\Delta\lambda = 0.3$ nm which is the bandwidth of the tunable optical filter used after the RSOA. The field ASE noise ($F_{ASE}(t)$) is then given by the following relationship [65]:

$$F_{ASE}(t) = \sigma_{ASE}(t)(N_1(0,1) + jN_2(0,1)) \qquad (3.3)$$

Where $N_1(0,1)$ and $N_2(0,1)$ are two randomly generated numbers having a mean distribution of zero, a unit variance, but different initial values.

3.4 OFDM IMDD experimental setup

Figure 3- 4 shows the schematic representation of an OFDM IMDD experimental setup performed in ENIB - Lab-STICC, UMR CNRS 6285. Figure 3- 5 shows the devices used in the experimental setup.

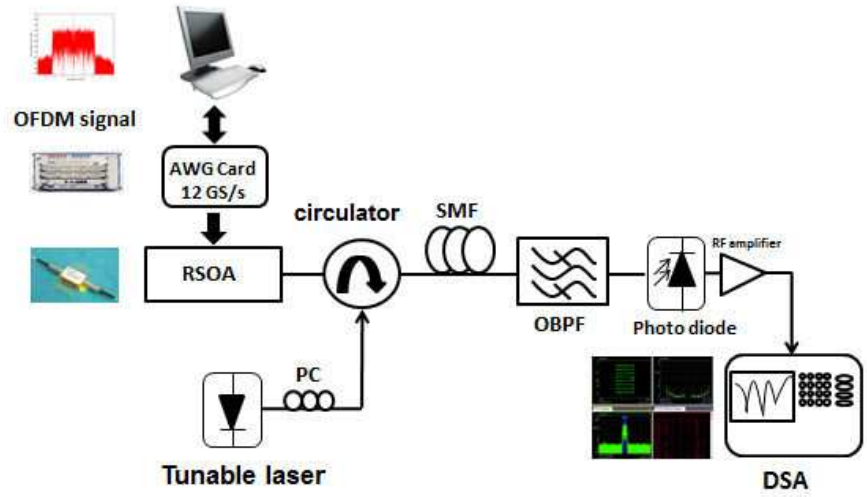

Figure 3- 4 : Schematic diagram of the used experimental setup.

Figure 3- 5 : Photo of used experimental setup.

In the developed experimental setup the time domain OFDM signal is generated using an arbitrary waveform generator (AWG) for generating analog signals. We used an Agilent M8190A AWG card at a rate of 12 GS/s and a resolution of 12 bits. The electrical-optical conversion of the OFDM signal is

performed by the RSOA (CIP SOA-RL-OEC-1550), The RSOA length is around 700 µm and it has at 1550 nm a gain of around 20 dB and a saturation output power of about 5 dBm. The output signal from the RSOA is filtered using a tunable optical filter. The filtered optical signal is transmitted into a SMF with different lengths. The output of SMF goes into direct detection with a photo detector having 8 GHz bandwidth. The obtained signal is amplified by an RF amplifier and then sampled by a 40 Gb/s oscilloscope of the Agilent DSA91304A digital signal analyzer. The demodulation is performed by the vector signal analyzer (VSA) software VSA89600 which preforms the EVM calculation as can be seen in Figure 3- 6.

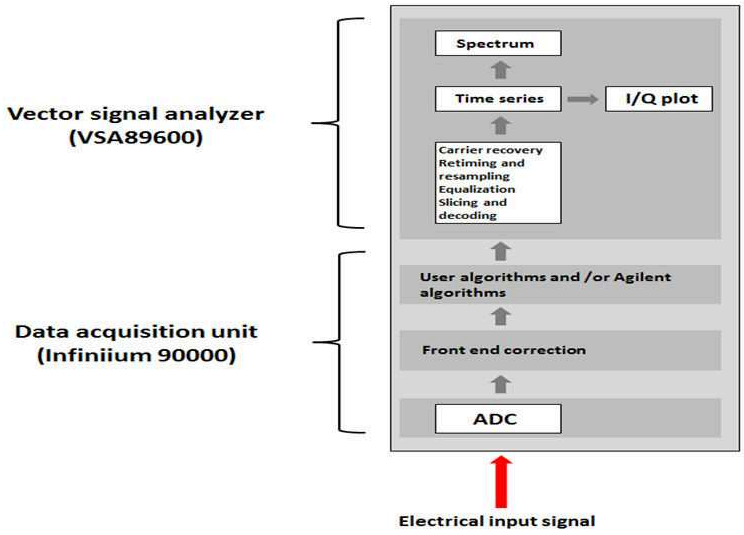

Figure 3- 6 : block diagram of the digital signal analyzer used (document from Agilent technologies)

3.5 Experimentally generated OFDM signal

The generated baseband OFDM has 1 subcarrier as DC and 31 positive frequency subcarriers, among which 5 subcarriers are used to set a guard band against the aliasing bandwidth caused by sampling since when the measurements were done, no anti-aliasing filter was available. Moreover, at least 4 subcarriers (more for high bandwidth signals) are used as pilot tone subcarriers for synchronization purposes. For most of our measurements we have used 16 QAM modulation format, 500 MHz and 2 GHz bandwidth values as channel bandwidth (over the 32 subcarriers). Figure 3- 7 shows a representation of the generated OFDM signal from the AWG card.

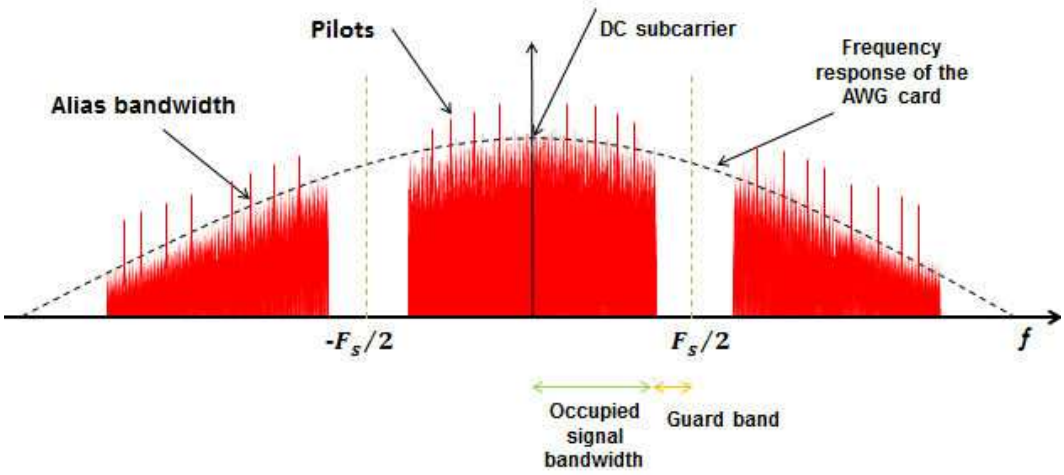

Figure 3- 7 : Shape of the OFDM signal transmitted from the AWG card.

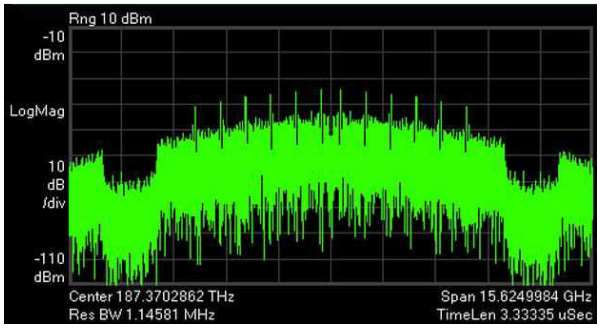

Figure 3- 8 : Spectrum of measured OFDM signal on an optical VSA.

Additionally, 25% of the symbol duration is defined as a cyclic prefix/ cyclic suffix (CP/CS) for avoiding inter-symbol interference and helping in synchronization. In our case, we chose a clipping factor of 13 dB [27]. Figure 3- 8 shows the detected OFDM signal at the DSA, since the VSA software is designed for optical signals it displays the optical frequency (in THz), but in reality we demodulate the baseband real electrical signal. For the simulation platform, A preamble synchronization technique is used in which we send preamble data signals at certain time samples of the sent subcarriers (every 50 time samples), the received preamble data at the receiver is used to compensate the channel imperfections. On the contrary, we use pilot tone synchronization in measurement. We do not use a back-to-back calibration to compensate the AWG and DSA impairements.

3.5.1 *Back to back fitting for simulation and measurement platforms*

3.5.1.1 Electrical back to back

In order to fit the simulation with measurements, we perform a back to back measurement in electrical domain for IMDD OFDM for several electrical bandwidths (Figure 3- 9) with OFDM-16 QAM format modulation. We take into

account in this setup the oscilloscope noise, and the DAC/ADC effective quantization levels. Datasheets of the DAC/ADC used in the experimental bench give quantization values of 12 and 8 respectively to the OFDM encoder and decoder (DAC and ADC). But we find, in agreement with a simulation platform for coherent OFDM [29], and from simulations that the effective number of bits (ENOB) for the DAC and ADC in order to have the same results as experimental measurements are 12 and 6.5 respectively. As it can be seen in Figure 3- 10, we have a good agreement between measurement and simulation for wide electrical bandwidth of the OFDM-16 QAM format modulation. We recall that the BER of 2*10E-3 will correspond to 12.5% for 16 QAM.

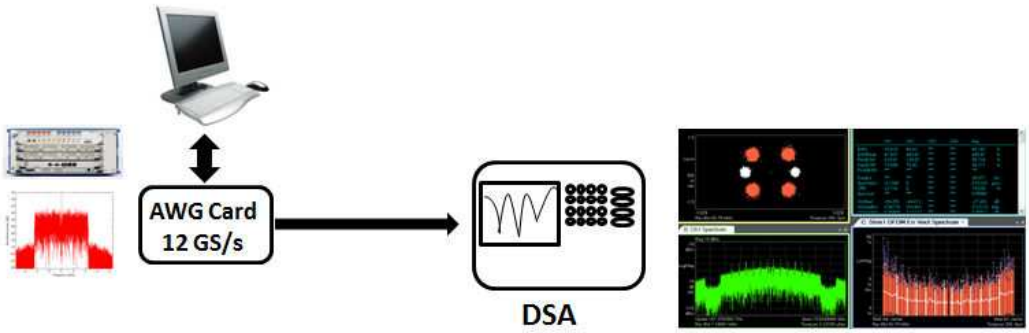

Figure 3- 9 : Experimental setup used for fiting the co-simulation platform in the electrical back to back configuration

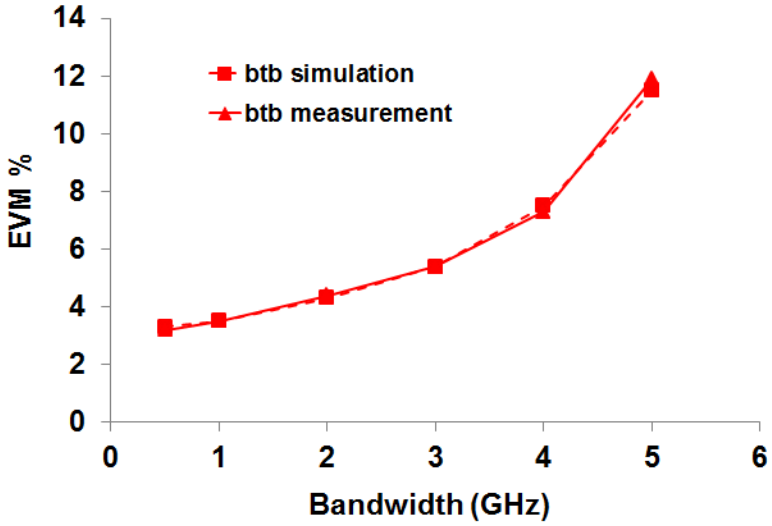

Figure 3- 10 : Electrical back to back EVM as a function of bandwidth for OFDM-16 QAM After fiting

3.5.1.2 Influence of optical receiver in direct transmission

In order to take into account in direct transmission without the RSOA, the influence of the optical setup: losses, photodiode noises at the receiver, we perform an optical simulation by modulaing a Mach Zehnder Modulator (MZM) by an OFDM signal as seen in Figure 3- 11. This setup is the back to back setup for the wavelength conversion simulation platform.

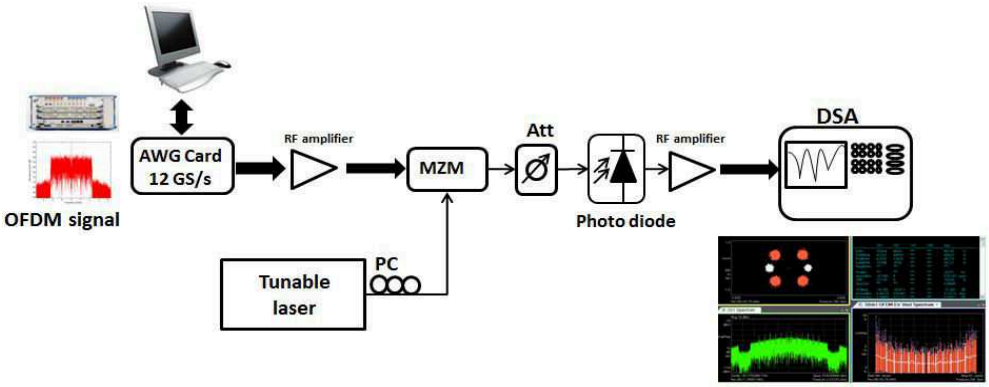

Figure 3- 11 : experimental setup used for calibrating the back to back optical system response in terms of optical OFDM signal input power to the photodiode.

The plot of both simulation and measurement with respect to the input power of the photo detector can be seen in Figure 3- 12.

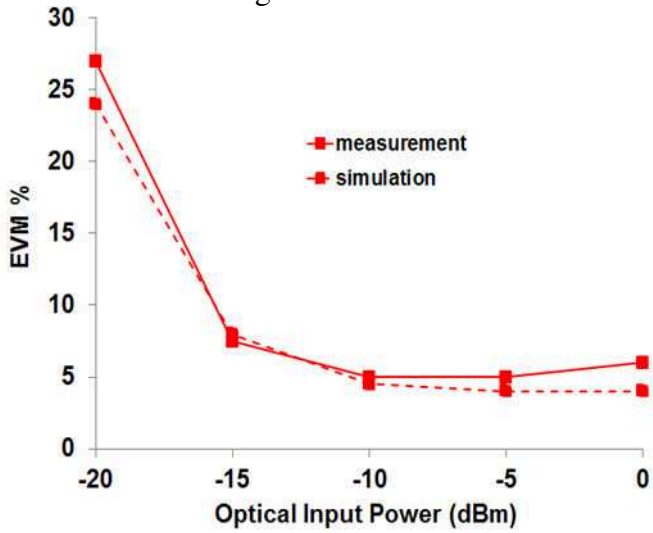

Figure 3- 12 : EVM vs optical OFDM -16 QAM 500 MHz input signal to the photodiode in an optical back to back configuration with a MZM

3.6 Experimental and numerical analysis of IMDD OFDM transmission performances using the RSOA

We study in this section, the performances of the RSOA as an intensity modulator of optical OFDM in function of its optical input power, the signal wavelength, the signal bandwidth and the transmission fiber length. In the following the signal line rate is considered to be valid when the condition of the EVM corresponding to a Bit Error Rate total (BER_T) $\leq 2\times10^{-3}$ is satisfied [27].

3.6.1 *Impact of input power and modulation bandwidth on the transmission performance*

We started our analysis by modulating the RSOA in function of optical incident power within its modulating bandwidth with an OFDM-16 QAM signal of 500 MHz bandwidth with an effective bit rate of 1.3 Gb/s. For this case, the RSOA bias current is 65 mA, the signal wavelength is 1560 nm, and the

magnitude of the OFDM current is 7 mA. Figure 3- 13(a) shows the EVM of an OFDM-16 QAM signal obtained by measurement and by simulation with good agreement. The results show that we have a high degradation of EVM when we decrease the optical input power to the RSOA. At this signal bandwith, we can realize a transmission with an EVM corresponding to a BER = $2*10^{-3}$ for powers higher than –20 dBm.

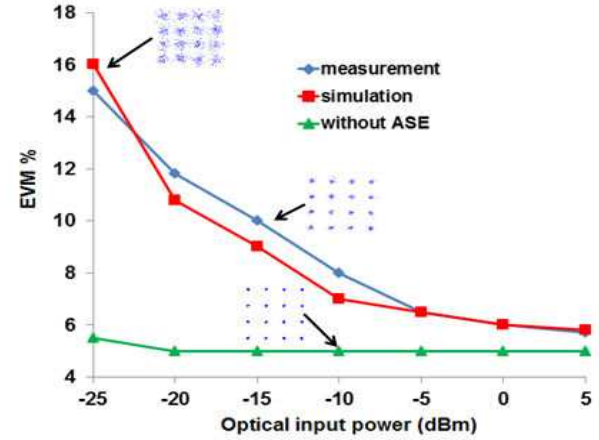

(a)

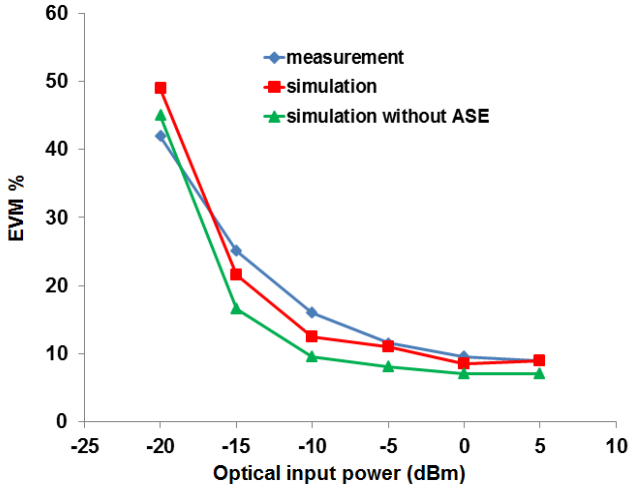

(b)

Figure 3- 13 : EVM vs RSOA Input power for (a) 500 MHz OOFDM-16 QAM signal and (b) 2 GHz OOFDM-16 QAM signal at a wavelength of 1560 nm and a bias current of 65 mA.

This can be related to the fact that when we decrease the optical input power to the RSOA we have a higher ASE noise level and a lower optical output signal level as we can see in Figure 3- 14 leading to a degradation in the output signal to noise ratio (OSNR). To evaluate the influence of the ASE, we have canceled the ASE noise at the receiver input in the numerical simulations. The obtained results show that without the ASE noise, the EVM is almost 5% for all optical input powers. This shows that the ASE is the main parameter for the EVM degradation at low optical input powers for the low bandwidth case.

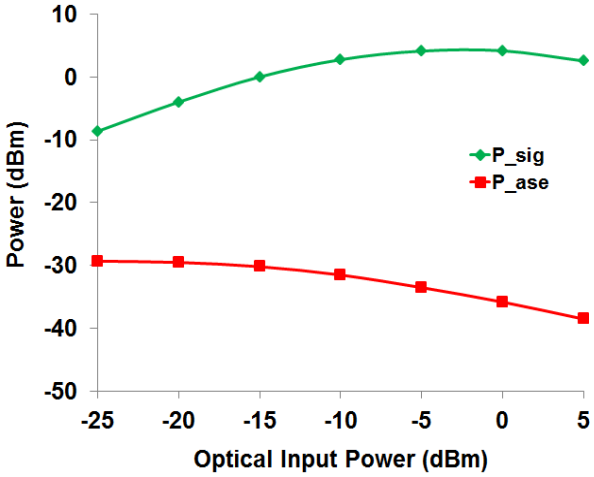

Figure 3- 14 : RSOA static charcterisation of the output signal power and ASE signal power versus the RSOA input signal power.

We then evaluate the influence of the RSOA modulation bandwidth. We first increase the signal bandwith to 2 GHz (Figure 3- 13 (b)), which is higher than the RSOA modulation bandwidth (chapter 2, Figure 2- 13). The effective bit rate in this case is 5.2 Gb/s, the RSOA bias current is 65 mA, the signal wavelength is 1560 nm, and the magnitude of the OFDM current is 7 mA. For these results, we have also a good agreement between simulation and measurement. The obtained EVM shows a much higher increase with lower optical input power when compared to the 500 MHz signal bandwidth case. At this signal bandwith, we can realize a transmission with an EVM corresponding to a BER = $2*10^{-3}$ for powers higher than –5dBm. We also do a simulation for the case of cancelling ASE noise but we find that cancelling ASE noise does not enhance a lot the transmission performance for low optical input powers as is the case for the 500 MHz signal bandwidth.

To enhance the transmission performance of the IMDD OFDM system, we performed a numerical study by enhancing the receiver sensitivity of the photodetector by using an ideal optical preamplification before the PIN photodiode [66]. It will be interesting to validate this experimentally in a future work. In fact, by numerical calculation, we amplify the 2GHz OFDM-16 QAM signal and the ASE noise at the input of the receiver to have a fixed mean power value of 0 dBm. In Figure 3- 15, the results show that we can realize a transmission with an EVM corresponding to a BER = $2*10^{-3}$ for powers higher than –15 dBm instead of -5 dBm. When we removed the ASE noise, the EVM tends to the back to back values. Figure 3- 16 (a) shows the effect on EVM of individual subcarriers by ampliying the input power to the photodetector to reach 0 dBm for the 2 GHz OFDM-16 QAM signal.

In Figure 3- 16 (b),(c), we present the simulation of EVM for each subcarrier for the 2 GHz signal case and with keeping the optical input power at the photodetector constant at 0 dBm for 5 dBm and -20 dBm injected optical power into the RSOA in presence and in absence of the ASE. In this figure, we show the influence of the RSOA bandwidth at high frequency subcarriers which is

more obvious at -20 dBm RSOA input power case compared to the 5 dBm case due to the decrease of the bandwidth at low optical input power (Figure 2- 13). If the ASE noise is removed (Figure 3- 16 (c)), the EVM is almost the same for both input powers.

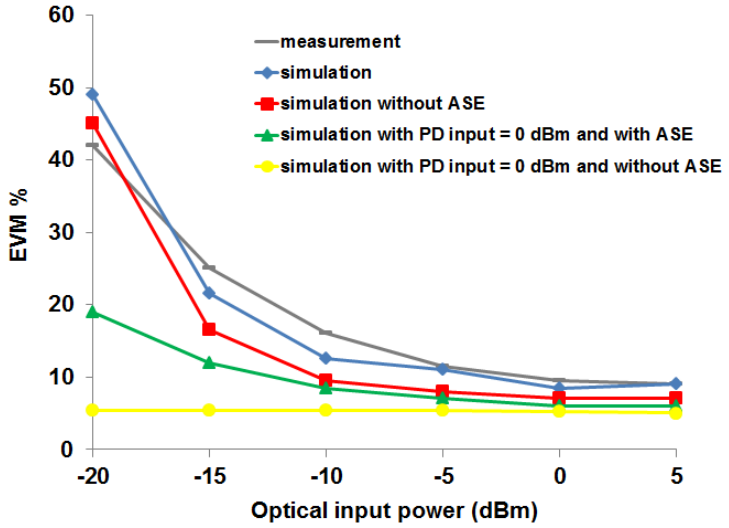

Figure 3- 15 : EVM vs Input power for 2GHz OFDM-16 QAM, the bias current is 65 mA, the wavelength is 1560 nm. (PD: photodetector).

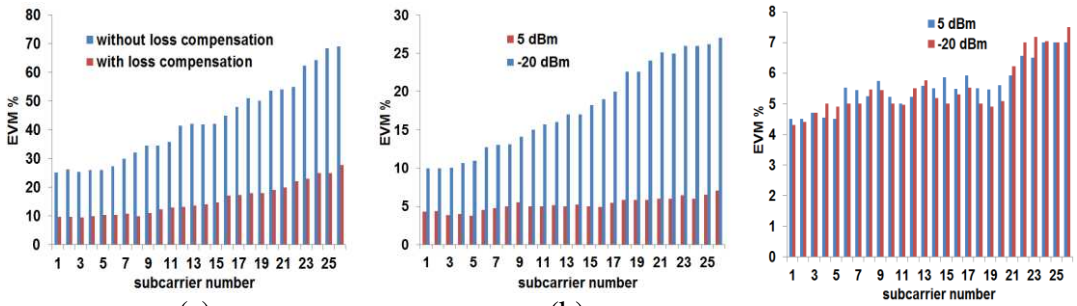

(a) (b) (c)

Figure 3- 16 : Numerical calculation of the EVM versus subcarrier number for a 2GHz OOFDM-16 QAM signal for the cases of (a) compensating the losses in which photodetector input power is 0 dBm, and without compensating the losses, input power to the RSOA is -20 dBm. (b) For two optical input powers to the RSOA, input power to the photodetector is kept at 0 dBm and with ASE noise, and (c) same as (b) but without ASE noise.

By increasing the signal bandwidth with the same operating point for the RSOA in presence of 5 dBm optical incident power at its input, Figure 3- 17 shows the EVM versus bandwidth for an OFDM-16 QAM transmission, We notice first that we have good agreement between simulation and measurement for bandwidths up to 5 GHz. We also see that we have a successful 3 GHz OFDM 16 QAM transmission that gives a system capacity of 7.8 Gb/s. We made also the same study by using the ideal optical preamplification configuration in which we have 0 dBm at the photodetector input, we then have a successful 6 GHz OFDM 16 QAM transmission at a data rate of 15.6 Gb/s.

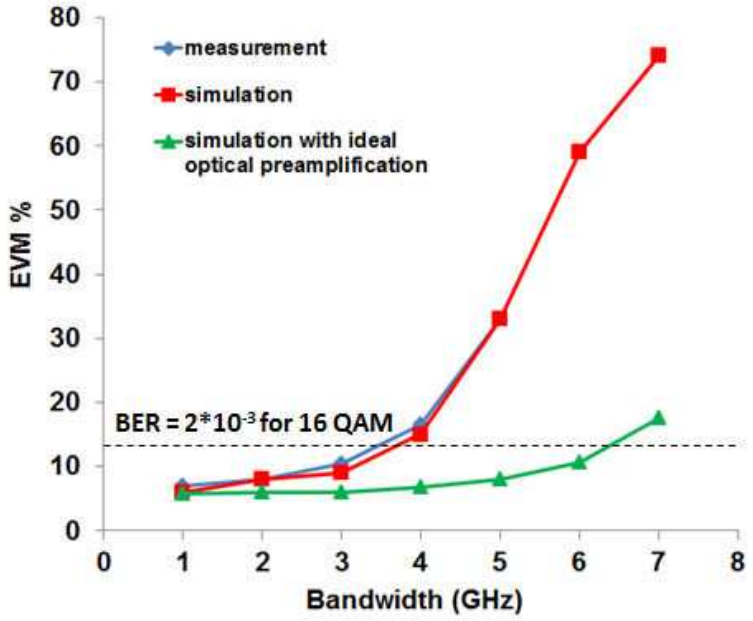

Figure 3- 17: EVM versus bandwidth for an OFDM-16 QAM transmission, RSOA input power is 5 dBm, the wavelength signal is 1560 nm, the bias current is 65 mA, the OFDM current is 7 mA.

3.6.3 Impact of fiber length on the transmission performance

We perform measurements and simulations for different transmission fiber length values between the RSOA and the photodetector. We use an EDFA before the photo detector in presence of a fiber length of 55 km and 80 km. Figure 3- 18 shows the effects of 55 km and 80 km SMF lengths for input powers to the RSOA as low as -25 dBm on a 500 MHz OFDM-16 QAM transmission. It shows also that in this configuration the simulation and the measurement results always keep good agreement.

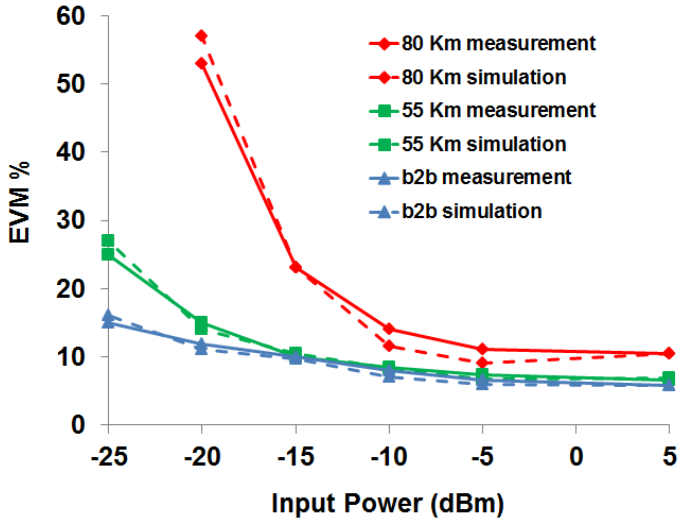

Figure 3- 18 : EVM vs RSOA input power for 16 QAM-OOFDM signal for different SMF lengths. The signal bandwidth is 500 MHz, the RSOA is biased at 65 mA bias current, The OOFDM signal is at 1570 nm, the OFDM current is 7 mA.

Nevertheless, the used signal bandwidth of 500 MHz in this transmission is not wide enough in order to study the influence of RSOA chirp due to the coupling phase amplitude factor α_H. So, by simulation, we transmit a 3 GHz OFDM-16QAM signal. We did first a simulation by imposing $\alpha_H = 0$, Figure 3-19(a) shows the simulation results with a 65 mA bias current, -15 dBm input power to the RSOA and 1560 nm wavelength. To focus only on α_H influence, we do the simulation by maintaining the optical input power at the photodetector at 0 dBm to compensate fibre attenuation and without ASE. In fact, with $\alpha_H = 0$, the EVM increased because the RSOA as an intensity modulator produces negative frequency chirp, this negative chirp compensates the dispersion induced chirp in the fiber [27]. Figure 3- 19 (b) illustrates the influence of canceling the RSOA chirp on the degradation of the EVM for every OOFDM – 16 QAM subcarrier where we can notice a fading effect that shifts to lower frequency by increasing the fibre distance [67]. Figure 3- 20 shows the EVM for each subcarrier for the cases of keeping or removing the RSOA chirp in presence of 80 km of SMF fiber. We notice that the RSOA α_H helps in reducing strongly the fading effect and consequently increase the transmission performances in function of the RSOA input optical power.

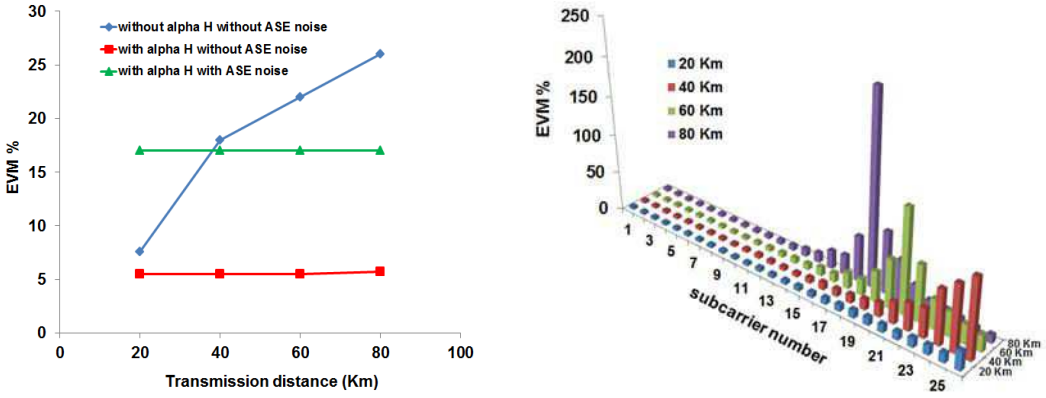

(a) (b)

Figure 3- 19 : (a) EVM versus transmission distance (b) EVM% per subcarrier for $\alpha_H = 0$ in function of transmission distance and for a 3 GHz OFDM-16 QAM signal, RSOA bias current is 65 mA, OFDM current is 7 mA, input power to RSOA is -15 dBm, wavelength is 1560 nm.(photodetector input = 0 dBm for all cases).

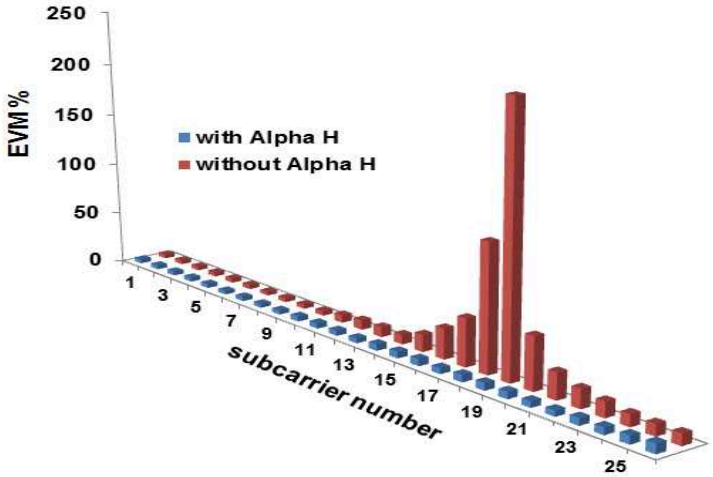

Figure 3- 20 : EVM per subcarrier in presence of 80 km fibre with $\alpha_H = 0$ and with $\alpha_H \neq 0$ for a 3 GHz OFDM-16 QAM signal, RSOA bias current is 65 mA, OFDM current is 7 mA, input power to RSOA is -15 dBm, wavelength is 1560 nm.(photodetector input = 0 dBm for all cases).

3.6.4 Influence of RSOA intermodulation distorsion in presence of multicarrier modulation format

In this part, we study the impact of RSOA non-linearities when we use an OFDM multicarrier modulation. Hence, we perform measurements and numerical simulations with the usual 26 data-carrying subcarrier OFDM-QPSK & OFDM-16 QAM signals and with only one data-carrying subcarrier OFDM-QPSK & OFDM-16 QAM signals as the last ones are not subject to intermodulation distortions. This was done for 20 km and 80 km SMF distances. The 32 subcarrier OFDM signal bandwidth is 500 MHz so as to be in the RSOA bandwidth, bias current is 65 mA, and wavelength is 1570 nm, OFDM current is 7 mA. Figure 3-21 and Figure 3- 22 show the EVM degradation for using OFDM signals compared to using single carrier signals for almost all input power values .This degradation is even stronger for low input power values. It should be noted that the results in Figure 3- 22 show good agreement between simulation and measurement for both OFDM and single carrier results and for 20 km and 80 km SMF transmission distances.

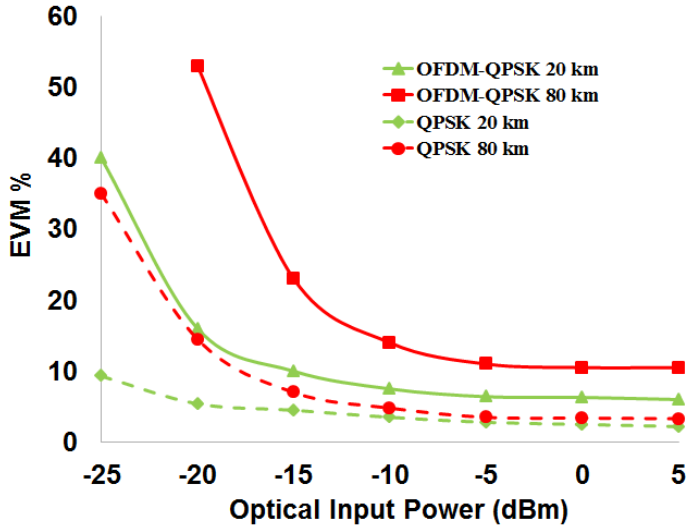

Figure 3- 21 : 26 data-carrying subcarriers OFDM-QPSK versus single subcarrier OFDM QPSK (noted QPSK) for 20 km and 80 km SMF distances and for a 500 MHz channel bandwidth.

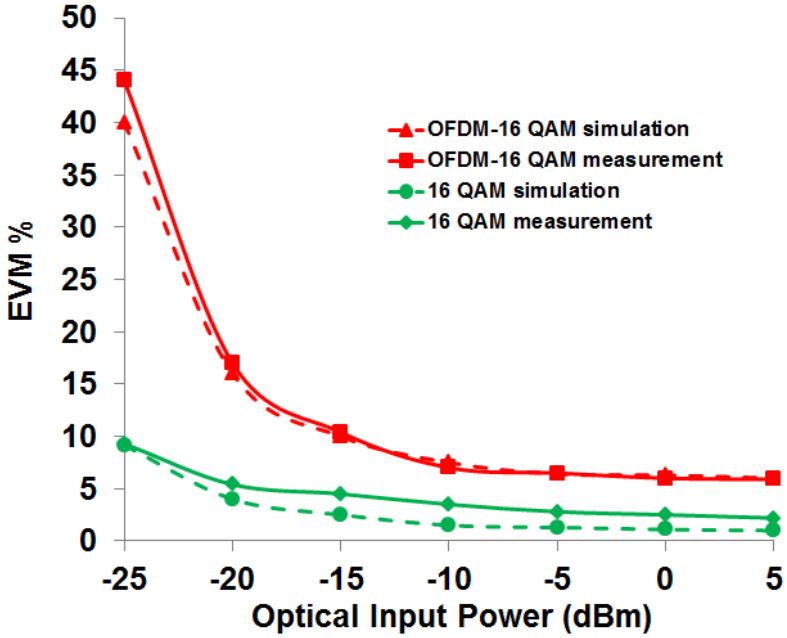

Figure 3- 22 : 26 data-carrying subcarriers OFDM-16 QAM versus single subcarrier OFDM 16 QAM (noted 16 QAM) for 20 Km SMF for a 500 MHz channel bandwidth

.

By increasing the number of subcarriers in a channel bandwidth of 1 GHz, as we can see in Figure 3- 23, there is almost no change in EVM for an OFDM-16 QAM optical measurement. The RSOA bias current is 65 mA, the input power to the RSOA is 5 dBm, and the wavelength is 1560 nm.

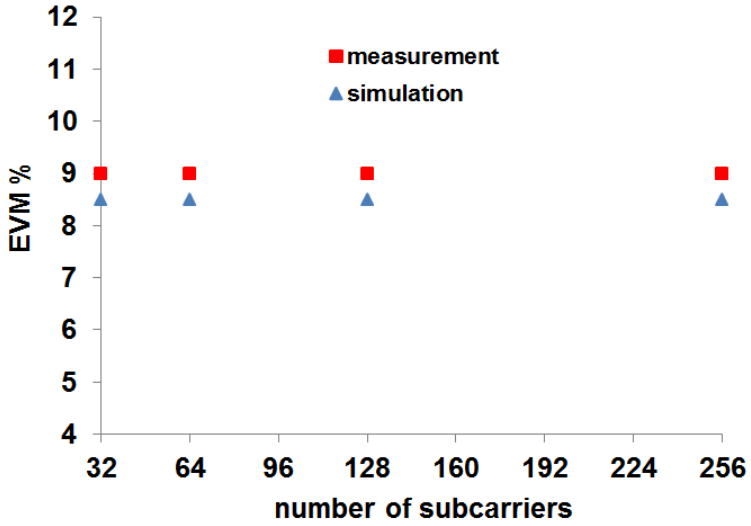

Figure 3- 23 : EVM vs number of subcarrier.

3.6.1.1 Impact of wavelength on the transmission performance

In this part we study the influence of wavelength on the OFDM transmission in function of different parameters. As we can see in Figure 3- 24, we have a 2 GHz OFDM-16 QAM signal with 45 mA and 65 mA bias current. The input power to the RSOA is 5 dBm. We have a degradation of the transmission performance with lower bias current especially at low wavelength values, this is due to the increased IMD2 (Figure 2- 21). The figure shows good qualitative agreement between simulation and measurement. These results show we can use the RSOA as intensity modulator for 16 QAM-OOFDM signal over a wavelength range of 70 nm with a system capacity of at least 5.2 Gb/s.

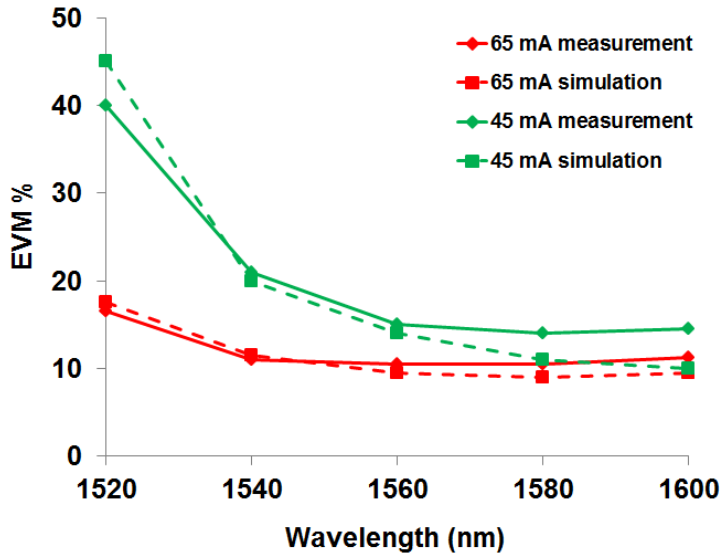

Figure 3- 24 : EVM vs wavelength for 2 GHz OOFDM signal for two bias current values.

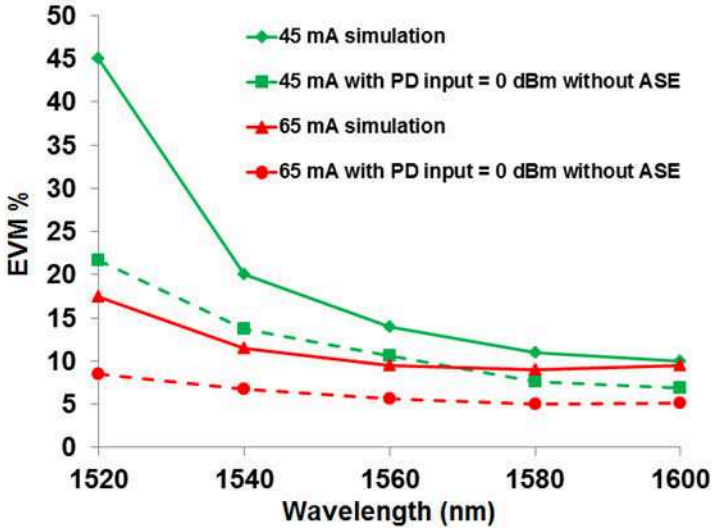

Figure 3- 25 : EVM vs wavelength for 2 GHz OOFDM signal for two bias current values and for the case of applying preamplification.(PD: photodiode).

Figure 3- 25 is the same as Figure 3- 24 but with preamplification and without ASE noise, the results show that even with preamplification and without ASE noise we have a degradation in EVM for short wavelength values.

3.7 Numerical study of enhancing the transmission performance of IM-OFDM systems using two methods (AMOOFDM and two electrode RSOA)

The concept of Adaptive Modulated Optical OFDM (AMOOFDM) is that we adjust the modulation format on each subcarrier according to its transmission response quality. The highest signal modulation format that can be used on each subcarrier is identified by negotiations between the transmitter and the receiver in the initial stage of establishing a connection over the SMF system [63, 64]. The signal modulation format can vary from differential binary phase shift keying (DBPSK), quadrature PSK (QPSK), and 8 quadrature-amplitude modulation (QAM) to 256 QAM. Generally speaking, a high (low) modulation format is used on a subcarrier suffering a low (high) transmission loss, this will cause a more efficient transmission performance without having high bit error rates for subcarriers suffering from high power loss. In our work, we verify the BER value on each individual subcarrier, if the BER $\leq 2\times10^{-3}$ we consider the transmission of the poposed format valid, and the modulation format is changed if the BER > 2×10^{-3}. For the next paragraphs, we perform a numerical study of enhancing the transmission performance of IM-OFDM systems using two methods: AMOOFDM, and two electrode RSOA.

3.7.1 *AMOOFDM transmission performances of the RSOA over 100 nm wavelength range*

In this part we make a first numerical study of the use of AMOOFDM technique with 20 km, 60 km, and 100 km fiber transmission distance, and over an optical bandwidth of 100 nm. Figure 3- 26 shows system capacity versus wavelength for an AMOOFDM signal for different fiber transmission distances. We use 6 GHz bandwidth signal. The RSOA bias current is 65 mA, the input power to the RSOA is 7 dBm, the OFDM current is 20 mA, and the input power to the photodiode is fixed at 0 dBm in all cases, we have also used an RF amplifier after the RF amplifier of the photodiode in order to further enhance the SNR at the DSA. The results show that using AMOOFDM technique we can attain at least a 8.9 Gb/s transmission capacity over a 100 nm optical bandwidth for fiber distances as long as 100 km even with a severe fading (Figure 3- 27). It is limited by low wavelength values as we explained in the precedent paragraph (3.6.1.1).

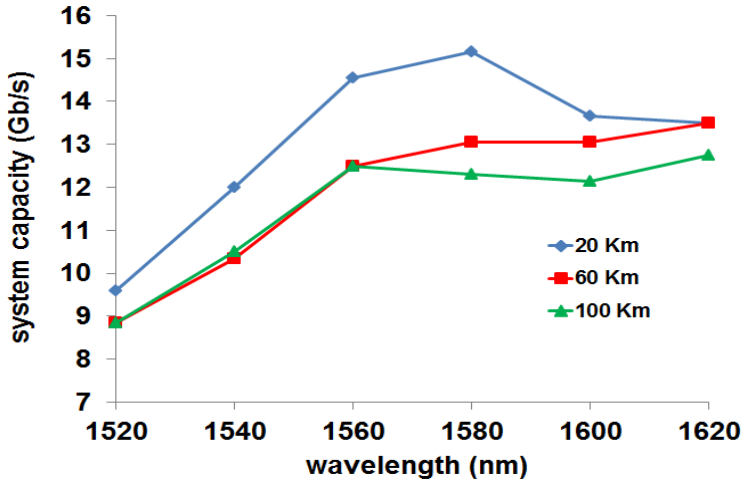

Figure 3- 26: System capacity versus wavelength for an AMOOFDM signal for different fibre transmission distances.

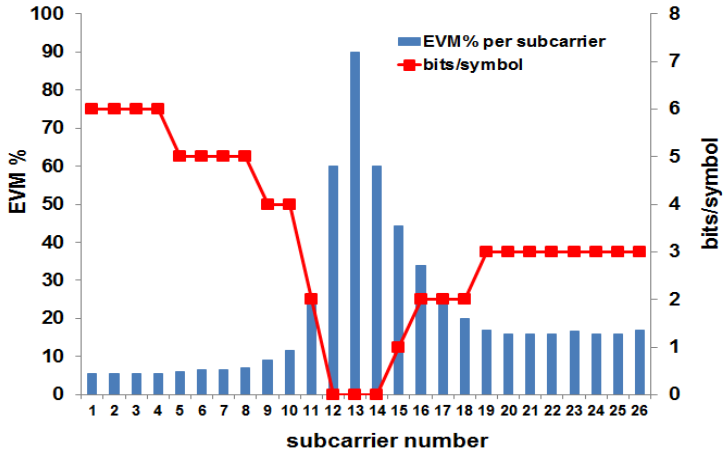

Figure 3- 27: EVM and in its corresponding bit/symbol by using AMOOFDM for each subcarrier for a transmitted signal over a 100 Km SMF.

Table 4 : Modulation format for the used bits/symbol.

Bits/symbol	Modulation format
1	DBPSK
2	QPSK
3	8 QAM
4	16 QAM
5	32 QAM
6	64 QAM
7	128 QAM
8	256 QAM

Figure 3- 27 shows the concept of AMOOFDM with fiber fading and degradation due to bandwidth, we can see that for a 6 GHz bandwidth, and for 100 km, we have fading effect even for a high input power and with $\alpha_H \neq 0$. The initial EVM values are obtained in the initial stage of making a transmission with 16 QAM modulation on all subcarriers, after that we have the new modulation formats adapted according to the measured EVM and we retransmit the signal with the modulation formats seen in the figure for example. Table 4 shows the respective modulation format for the used bits/symbol.

3.7.2 *AMOOFDM transmission performances in a two electrodes RSOA configuration*

As our RSOA model gave good results compared to measurement, we investigated the potential of using our RSOA in a two electrodes RSOA configuration on the transmission performance of an AMOOFDM signal. Figure 3- 28 shows the three used RSOA configurations: the one-electrode RSOA, the two-electrode RSOA for the case of modulating the input section (we shall call it 2-electrode-A), and the two electrode RSOA for the case of modulating the mirror section (we shall call it 2-electrode-B).

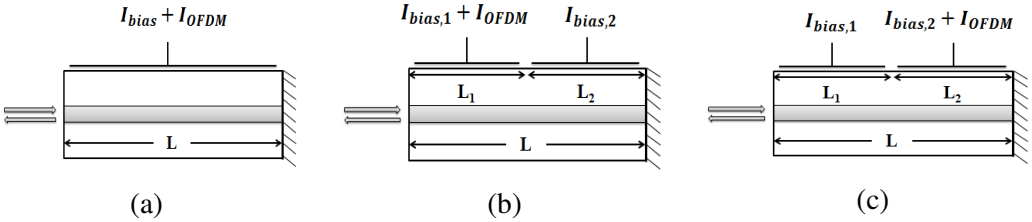

Figure 3- 28: Three studied RSOA configurations, (a) one electrode, (b) two electrodes with modulating the input section, (c) two electrodes with modulating the mirror section.

We choose the two electrode RSOA configurations with $L_1 = L_2$, with the total length corresponding to that of our 1-electrode RSOA (Appendix -B). We fixed the total bias current to 65 mA with a maximum of 45 mA per electrode. Table 5 shows the operating points for the three configurations.

Table 5: simulation parameters for the two-electrode RSOA configurations.

configuration	I_1	I_2	I_{OFDM}
2-RSOA-A	35 mA	30 mA	7 mA
2-RSOA-B	45 mA	20 mA	7 mA
1 electrode	65 mA	0	7 mA

The obtained static and dynamics caracteristics of the three configurations in presence of an optical input power to the RSOA configurations of 0 dBm at a 1560 nm wavelength are shown in Table 6. Figure 3- 29 shows the frequency response for the three configurations. The results in Table 6 show that we have very close gain with quasi identical ASE output power at 1560 nm. We find that the phase-amplitude coupling factor α_H is higher for the 2-electrode-B configuration, and we have a big enhancement for the electrical bandwidth for the 2-electrode-B case. The bandwidth was measured starting from 50 MHz.

Table 6: Some important factors for the three RSOA configurations.

factor	1-electrode	2-electrode-A	2-electrode-B
P_{out} (dBm)	3.9	4.0	3.0
P_{ase}(dBm)	-36.2	-35.9	-35.5
α_H	4.2	4.2	5.8
bandwidth	1.3 GHz	750 MHz	3.1 GHz

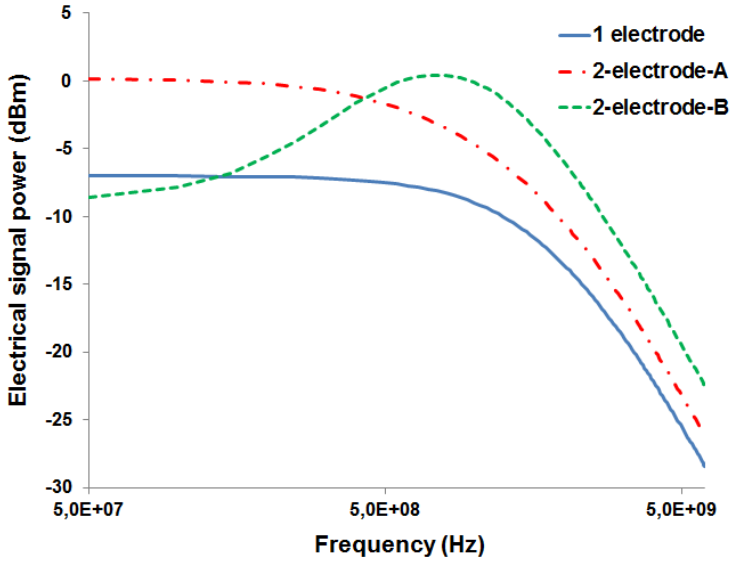

Figure 3- 29: Electrical bandwidth for the three RSOA configurations.

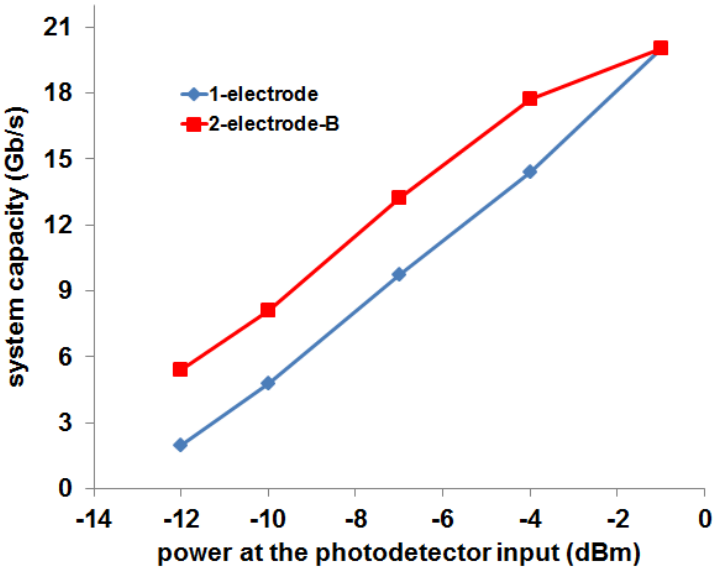

Figure 3- 30: system capacity versus photodetector input optical power for two RSOA configurations.

Figure 3- 30 shows the system capacity versus photodetector input power for 1 electrode and 2-electrode-B configurations for an AMOOFDM signal, the results show that the 2-electrode-B configuration enhances the system capacity by at least 3 Gb/s for input powers to the photodiode at -4 dBm and lower. This is important for enhancing the transmission system power budget for long transmission distances. Figure 3- 31 shows the system capacity versus transmission distance for three RSOA configurations for an AMOOFDM signal, the preamplification technique is applied in this case (the input power to the photodiode is fixed at 0 dBm in all cases), the results show in one hand that the two configurations of the two electodes RSOA present better performances than the mono electrode RSOA. On the other hand, the 2-electrode-B outperforms the two other configurations especially for 20 Km SMF case.

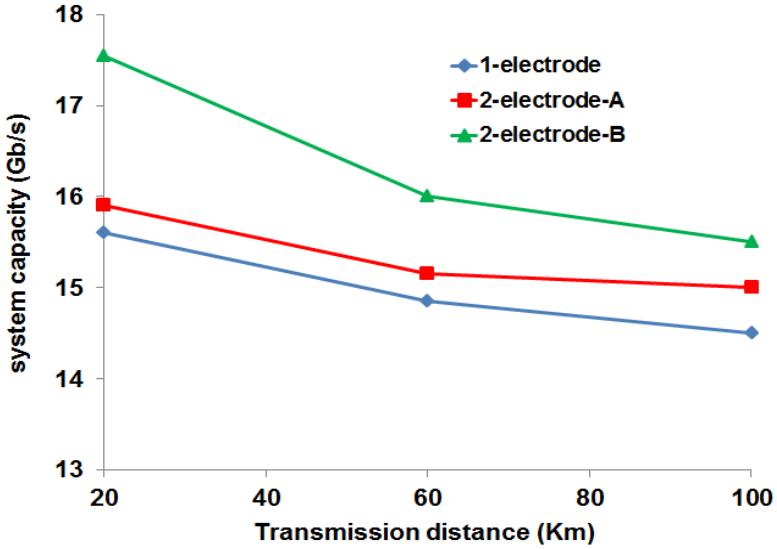

Figure 3- 31: System capacity versus transmission distance for the three RSOA configurations.

3.8 Wavelength conversion function of an IM-OFDM format

In this part, we perform the wavelength conversion of an IM-OFDM signal, using the cross gain modulation effect of the RSOA. Wavelength conversion is required in a wavelength-division multiplexing (WDM) network. Figure 3- 32 shows the principle of this wavelength conversion by XGM in an SOA for an IM-OFDM signal. We have at the input of the SOA a continuous wave (CW) probe input signal, and an intensity modulated (IM)-OFDM pump signal at another wavelength. The XGM effect in the SOA causes the gain of the pump signal to be imposed on the probe signal. Hence, at the output of the SOA we have the amplified IM-OFDM signal and the converted IM-OFDM signal.

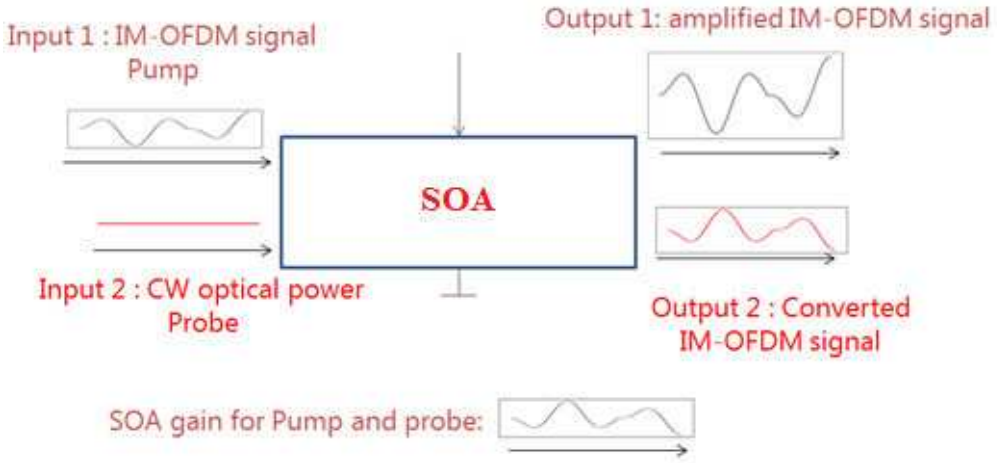

Figure 3- 32 : Principle of XGM wavelength conversion in an SOA.

3.8.1 *OOFDM wavelength conversion co-simulation platform*

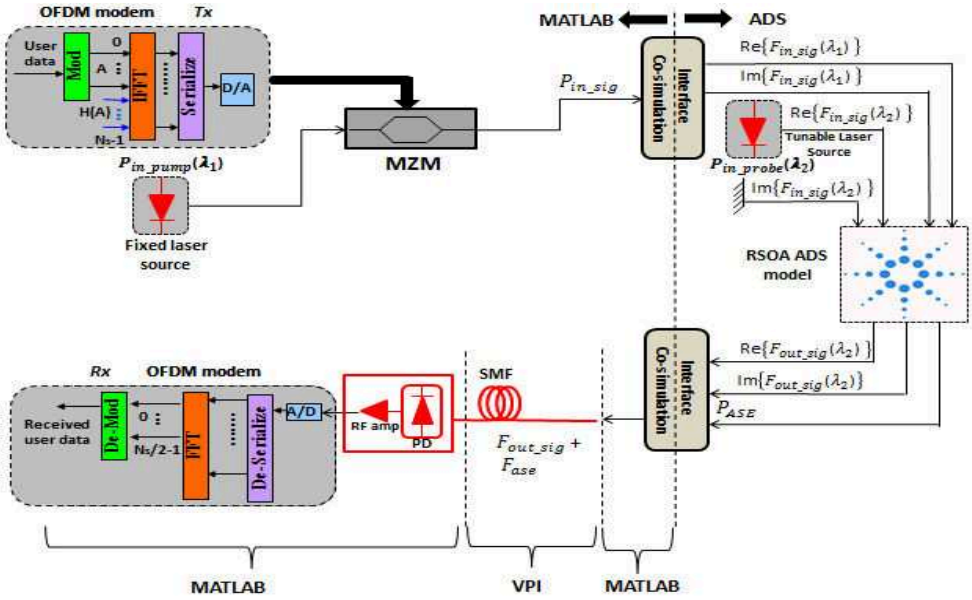

Figure 3- 33 : IM-OFDM wavelength conversion co-simulation platform using RSOA.

Figure 3- 33 shows the simulation setup for wavelength conversion of an optical IM-OFDM signal using the cross gain modulation. The IM-OFDM signal is transmitted from the OFDM modem to the Mach Zehnder Modulator (MZM) implemented in MATLAB and used as an optical intensity modulator. The output of the MZM is defined as the pump signal at wavelength λ_1. The probe CW optical signal at a tunable wavelength value λ_2 is inserted into ADS. The pump signal at the output of the MZM is injected into the RSOA ADS model through the co-simulation interface. At the output of the RSOA we detect the λ_2 signal and the ASE output power around λ_2 in 0.3 nm bandwidth which is the bandwidth of the experimentally used optical filter. The output signals are combined and inserted into the VPI SMF link. Finally, the output of the SMF link is demodulated by the OFDM receiver implemented in MATLAB.

3.8.2 *Wavelength conversion experimental system setup*

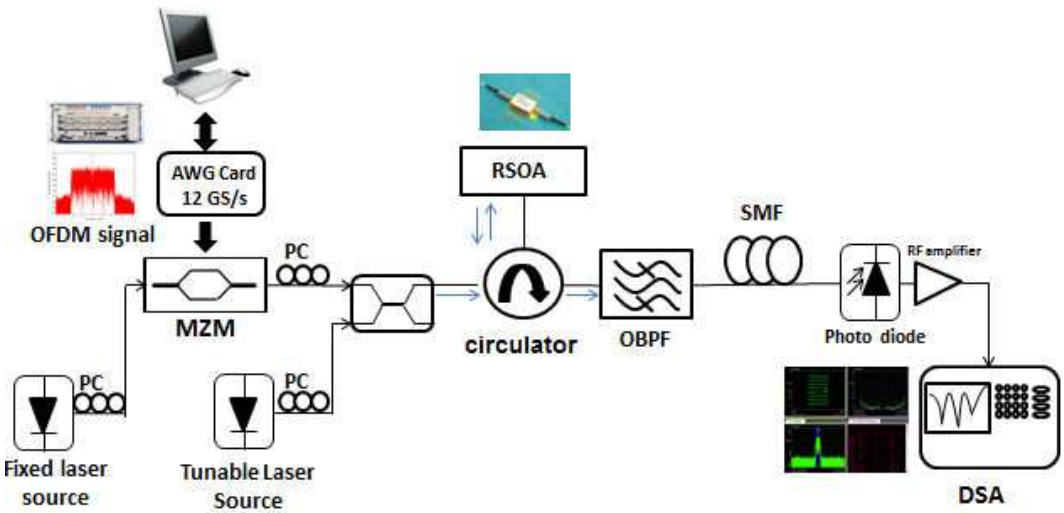

Figure 3- 34 : Experimental setup of the OFDM wavelength conversion.

The schematic representation of the experimental setup is shown in Figure 3- 34, we first generate an OFDM signal using Agilent M8190A AWG. The generated electrical signal is used to intensity modulate a continuous wave (CW) optical signal coming from a DFB laser at 1556 nm by using a Mach Zehnder Modulator (MZM). At the output of the MZM an optical IM-OFDM signal is obtained, called in the following as the pump signal. This pump signal in addition to a CW optical signal coming from a tunable laser source and named as the probe signal are injected in the RSOA via an optical circulator. At the RSOA output, an optical filter is used to get only the probe converted signal. This obtained signal is transmitted through a SMF and then directly photo-detected and sampled by the 40GS/s oscilloscope. Afterward the signal is demodulated and analyzed by the vector signal analyzer from Agilent Technologies.

3.8.3 *Experimental and Numerical results with 20 Km SMF*

The results are done for input power values of -3 dBm for pump and 4.5 dBm for probe signals. The RSOA bias current is 80 mA. The results are also done for three different electrical bandwidths of 500 MHz, 1 GHz, and 2 GHz. The back to back setup when using a MZM for wavelength conversion gives a 5 % value for the EVM.

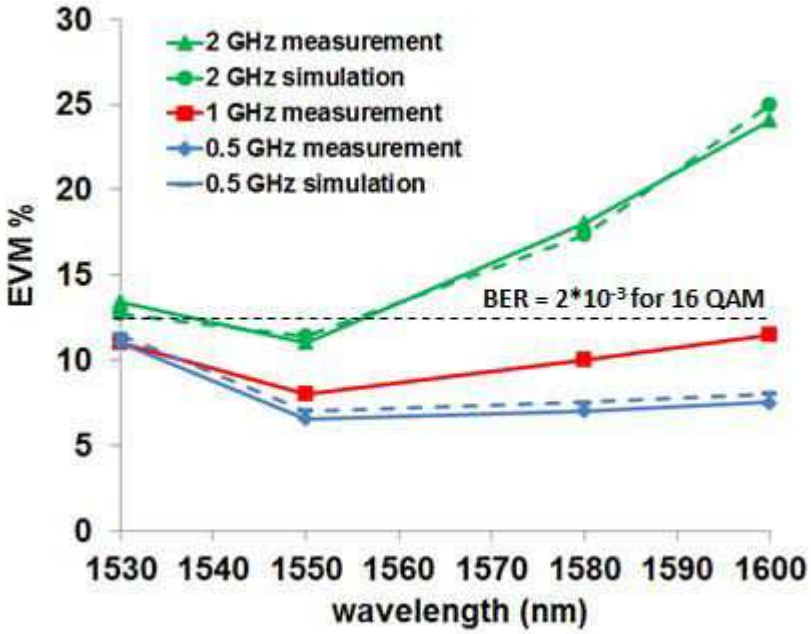

Figure 3- 35 : RSOA wavelength conversion results.

The results show first good agreement between simulation and measurement over wide range of optical wavelength. They show that the EVM for low and high wavelength is more degraded due to the wavelength dependance of the conversion efficiency as depicted in AC characterization in Figure 2- 15(b). This wavelength conversion function can be performed over 70 nm with a channel bandwidth up to 1 GHz with an effective signall bit rate of 2.6 Gb/s.

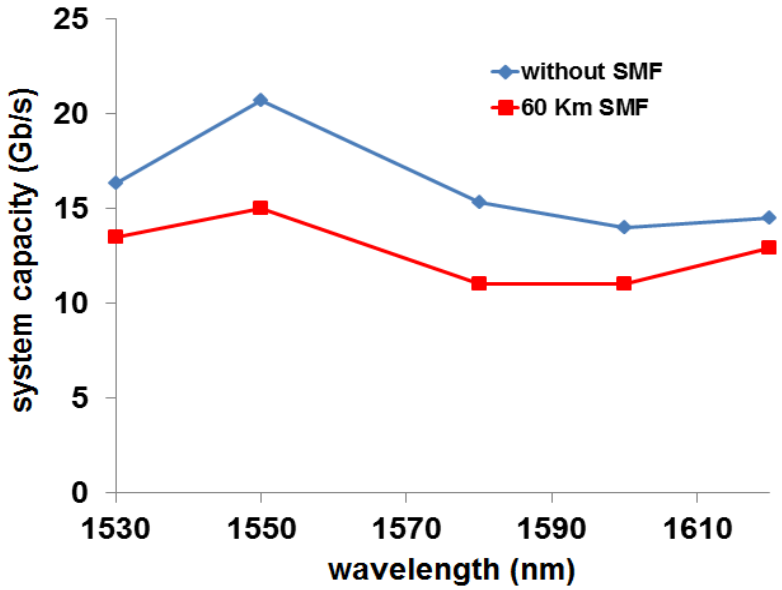

Figure 3- 36: Simulations of system capacity versus wavelength for an AMOOFDM converted signal.

By using in simulation the AMOOFDM technique, Figure 3- 36 shows that the system capacity can be enhanced over 90 nm optical wavelength range for a converted AMOOFDM signal both in back to back (without SMF) and with a 60 km SMF length by keeping the photodiode input power at 0 dBm. For this simulation, we use a pump input power of 0 dBm, a probe input power of 5 dBm. Although the RSOA used is not designed for wavelength conversion applications since it is considered as a linear RSOA, we can obtain a system capacity that is at least 14.5 Gb/s for an optical bandwidth of 90 nm in the optical back to back configuration, and a system capacity of at least 11 Gb/s for the case of having a 60 km fiber length.

3.9 Conclusion

In this chapter we have demonstrated that the developed co-simulation platform for OOFDM IMDD and OOFDM wavelength conversion transmission systems present good agreement with the measurement. Thanks to this co-simulation platform and our experimental setup, we have analyzed the RSOA-based IMDD-OOFDM transmission performances in terms of optical input power, fiber length, ASE noise, electrical bandwidth, number of subcarriers and we compared a single carrier transmission to a multicarrier one. We showed that by using an ideal optical preamplification, we could obtain a successful 6 GHz OFDM 16 QAM transmission at a data rate of 15.6 Gb/s.

Moreover, we showed by simulation that by using an AMOOFDM signal transmission over an 100 nm wavelength range, we can reach at least a 8.9 Gb/s transmission capacity for fiber lengths as long as 100 km. Moreover, we show an improvement of the transmission capacity up to 17.5Gb/s thanks to a two electrode RSOA configuration in the case of 20 km SMF length.

Finally, in this work we experimentally demonstrated for the first time to the best of our knowledge the feasibility of performing wavelength conversion over 70 nm of OOFDM-16QAM optical signals using the XGM effect in an RSOA. Moreover, using an AMOOFDM technique, we can increase the system capacity over 90 nm to at least 11 Gb/s for a 60 km SMF length.

PART 2

4 THEORETICAL AND NUMERICAL STUDY OF AN AMOOFDM IMDD TRANSMISSION SYSTEM USING DIFFERENT SOA STRUCTURES

4.1 Introduction

In this chapter we perform a theoretical and numerical study of an AMOOFDM transmission system using three different SOA configurations; we first present the results of previous work on using this system with a DFB lasers, an SOA, and an RSOA as intensity modulators.

We then present our new work of using Quantum Dot SOA (QD-SOA), two electrode SOA (2ESOA) and two cascaded SOAs in a counter-propagating configuration (TC-SOA-CC) as intensity modulators with the developed AMOOFDM IMDD system. This new work was done as collaboration between AUL University Lebanon, ENIB in France, and Bangor University in UK.

We have developed a model for each SOA type, verified the models in static domain, and performed a study of the transmission system in terms of system capacity vs reach performance, optimum operating conditions, signal clipping effect, and fiber chromatic dispersion effects.

4.2 TRANSMISSION LINK MODEL

The used AMOOFDM model is explained in chapter 3, section 3.2, It should be pointed out that the back-to-back performance of the AMOOFDM model shows excellent agreement with the analytical predictions [68] for signals using identical modulation formats across all subcarriers. More importantly, the feasibility of this model has also been verified by agreement obtained between numerical results and experimental measurements for the transmission of 10-Gb/s IMDD DQPSK optical OFDM signals in a 1000-m multimode-fiber link employing a DFB laser [69]. And by the agreement between numerical results and experimental measurements for the transmission of 6-Gb/s IMDD 16 QAM signals in a 25 Km SMF employing a RSOA [28].

4.2.1 *SMF model*

The SMF model developed and employed successfully in [28, 70] is adopted, the widely adopted split-step Fourier method is used to model the propagation of the optical signal down a SMF [70]. It is well known that for a sufficiently small fiber step length, this treatment yields an accurate approximation to the real effects. In simulations, the effects of loss, chromatic dispersion, and optical power dependence of the refractive index are included. The effect of fiber nonlinearity-induced phase noise to intensity noise conversion is also considered upon photo detection in the receiver.

4.3 AMOOFDM IMDD transmission performances of different SOAs Structures and configurations

In this section, we first explain the results of previous work using the AMOOFDM IMDD transmission model with a DFB laser, an SOA, and an RSOA [27, 28, 63]. We then present and compare our new work for the AMOOFDM IMDD transmission performance using QD-SOA, two electrode SOA (2ESOA), and two cascaded SOAs in a counter-propagating configuration (TC-SOA-CC) as intensity modulators with the developed AMOOFDM IMDD system.

4.3.1 *AMOOFDM IMDD using DFB laser as intensity modulator*

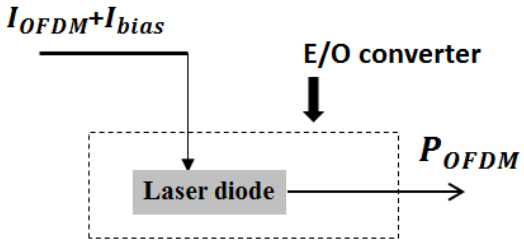

Figure 4- 1 : DFB E/O converter configuration

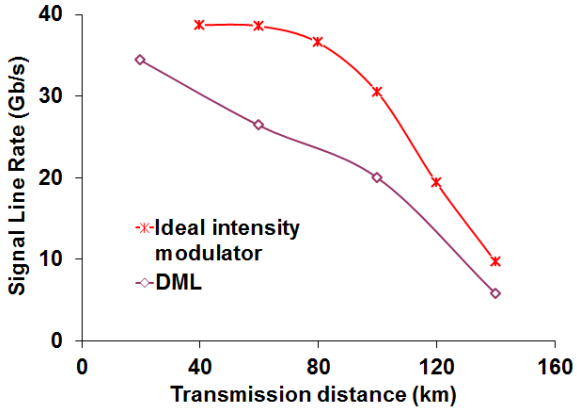

Figure 4- 2 : System capacity comparison between DFB laser and ideal IM [63].

Numerical simulations of the transmission performance of AMOOFDM IMDD signals have been undertaken in DFB-based SMF links without involving optical amplification and dispersion compensation [63]. This work has been done at Bangor University; It has been shown that a 30-Gb/s-over-a-40-km SMF transmission with a loss margin of > 4.5 dB is feasible. In addition, the laser frequency chirp and the transmission-link loss have been identified to be the key factors limiting the maximum achievable capacity-versus-reach performance of the technique. The first factor is dominant for transmission distances of < 80 km and the second one for transmission distances of > 80 km. Figure 4- 2 shows the system capacity versus reach performance for the used DFB model and that of an

ideal intensity modulator. In simulating the ideal intensity modulator, a simple square root operation is applied to the sum of the OFDM and DC currents.

4.3.2 *AMOOFDM IMDD using SOA as intensity modulators*

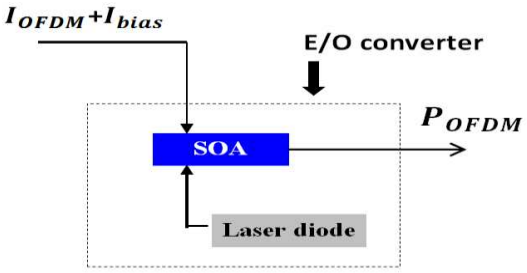

Figure 4- 3 : SOA E/O converter configuration

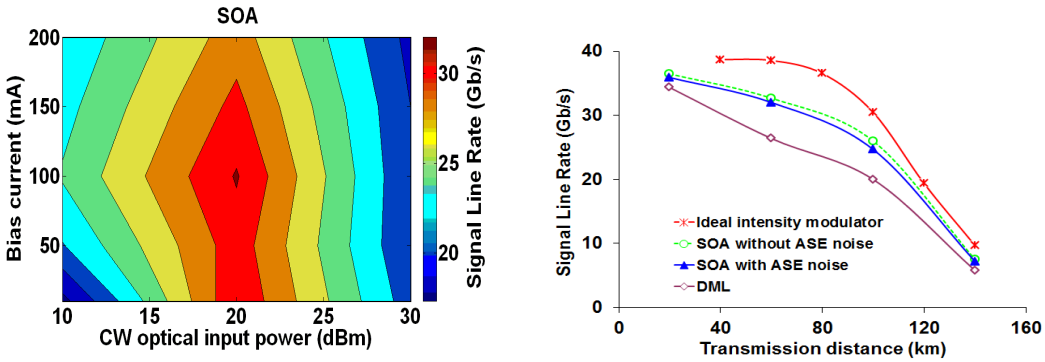

(a) (b)

Figure 4- 4 : (a) SOA performance versus bias current and optical input power (b) transmission capacity versus distance for Ideal IM, SOA, and DFB laser configurations.

Detailed investigations of the transmission performance of AMOOFDM signals using SOA-based intensity modulators have been undertaken in SMF IMDD systems without optical amplification and chromatic dispersion compensation [27]. This work was done through collaboration between Bangor University at UK and AUL University in Lebanon.

A comprehensive SOA theoretical model has been developed in [71], which has been successfully employed in describing the propagation of strong picosecond optical pulses in SOAs, Figure 4- 4 (a) shows a contour plot of the SOA as an intensity modulator in which the bias current and optical input power are optimized for maximum transmission capacity. Figure 4- 4 (b) shows that the optimized SOA-based intensity modulators support a 30 Gb/s signal transmission over a 80 km SMF, which doubles the transmission performance offered by DFBs in the transmission systems of similar configuration. The above-mentioned performance enhancement is mainly due to the considerably reduced frequency chirp effect resulting from the strong SOA gain saturation-induced decrease in SOA effective carrier lifetime [27]. Relatively low extinction ratio and clipping of the SOA modulated AMOOFDM signals have been identified to be the key

factors limiting the maximum achievable transmission performance. In addition, results have also indicated that both the optimum SOA operating conditions and the maximum achievable AMOOFDM transmission performance are insusceptible to variations in SOA parameters [27]. Such a unique feature may offer great opportunities for: a) easing practical system designs, b) enhancing flexibility and robustness of transmission systems to component perturbation and extreme environmental conditions, and finally c) further reducing cost in system installation and maintenance.

4.3.3 *AMOOFDM IMDD using RSOA*

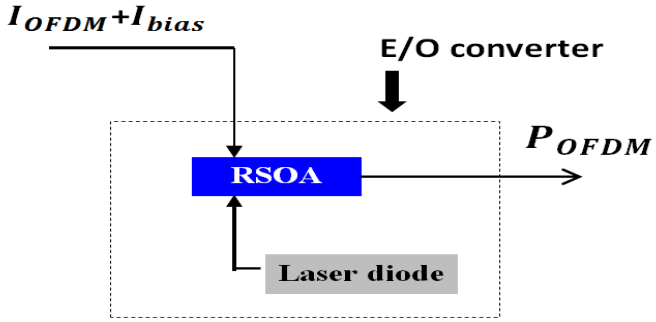

Figure 4- 5 : RSOA E/O converter configuration

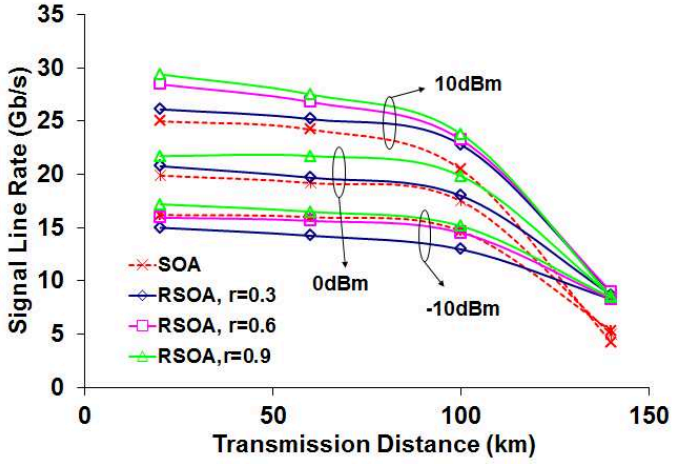

Figure 4- 6 : System capacity versus Transmission distance for SOA and RSOA

The use of an RSOA was investigated [28] and compared to semiconductor optical amplifiers (SOAs) [72, 73]. SOAs exhibit better optical linearity as they have relatively higher input saturation powers. It is very interesting to note in Figure 4- 6 that, in comparison with the SOA intensity modulators, the RSOA intensity modulators subject to injected optical powers of >-10dBm are capable of improving the signal line rate over the entire transmission distance range including both the chromatic dispersion-dominant performance region (<100km) and the loss-dominant performance region (>100km). In addition, it can also be seen in Figure 4- 6 that, the use of RSOA intensity modulators is more effective in the loss-dominant performance region, as

the RSOA enhanced signal extinction ratio can offset, to some extent, the transmission link loss.

4.4 Quantum-dot semiconductor optical amplifier as Intensity modulator for OFDM signal

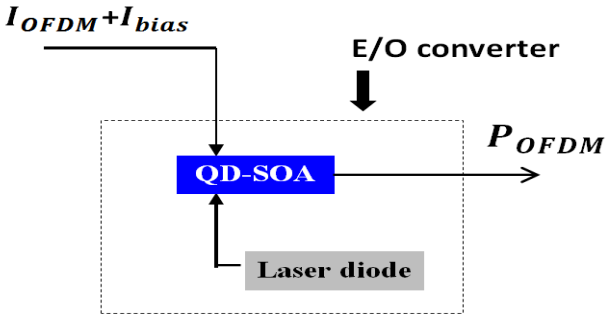

Figure 4- 7 : QD-SOA E/O converter configuration

Numerical simulations are undertaken for the first time, to extensively explore the feasibility of utilizing QD-SOA-IMs in IMDD AMOOFDM. Here special effort is given to addressing the following technical challenges:

- Development of a comprehensive theoretical QD-SOA-IM model by taking into account the effects of both quantum dots and wetting layer (WL).

- Identification of key QD-SOA-IMs-associated physical mechanisms considerably affecting the AMOOFDM transmission performance.

- Performance comparisons between QD-SOA-IMs and SOA-IMs to highlight the advantages of QD-SOA-IMs for use in IMDD AMOOFDM PON systems.

- Exploration of the feasibility of effectively utilizing the QD-SOA-IMs-induced frequency chirp to improve the transmission performance of IMDD AMOOFDM PON systems.

Quantum-dot semiconductor optical amplifiers (QD-SOAs) have demonstrated a large number of salient features for use in various application scenarios from all-optical signal processing to optical communications. Some of these features are: ultrafast gain recovery [74], large saturation power [75], patterning-free optical amplification [76], and high operation speed [77, 78, 79]. QD-SOAs have picosecond dynamic gain recovery speeds, implying that they can offer much higher modulation bandwidths. In addition, experimental demonstrations of record high penalty free QD-SOA output powers of 23dBm [76] suggest that desired linear intensity modulation operation is also feasible.

Therefore, it is greatly advantageous if use can be made of QD-SOA intensity modulators (QD-SOA-IMs) in AMOOFDM transmitters.

4.4.1 *QD-SOA-IM model*

Based on rate equations, a number of theoretical QD-SOA models governing the interactions between the carrier density and optical signal have been published to describe the input-output optical characteristics of QD-SOAs [78, 80, 81, 82, 83, 84]. In QD-SOAs, the wetting layer (WL) is a thin material layer, where QDs are grown. The WL layer acts as a free carrier reservoir, from which the carriers quickly transfer to the QDs where they will be available for stimulated recombination. The bias current is assumed to be directly injected into the WL. Strictly speaking, a typical energy band of a QD-SOA active layer consists of multiple energy states in the conduction and valence bands. Within a QD two energy states, i.e., the excited state (ES) and the ground state (GS), can be considered, this theoretical treatment is known as the 3-level rate equation model (3LREM) [80, 81, 82]. A 4LREM QD-SOA model [78] has also been developed, in which an additional energy level is introduced between the QDs and the WL.

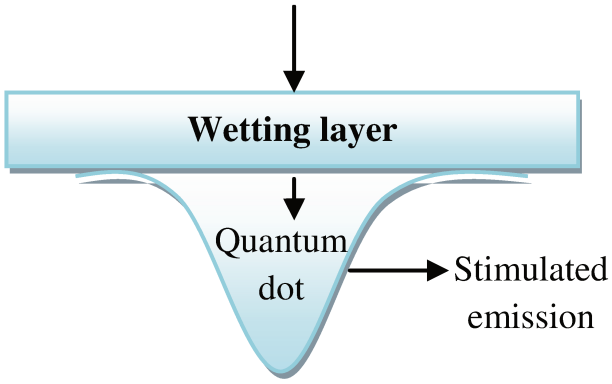

Figure 4- 8 : Carrier injection model in the conduction band of a QD. We take into account only the ground state in each QD.

In this work, making use of a significantly simplified but effective 2LREM QD-SOA model [83, 84, 85], we developed a theoretical QD-SOA-IM model in which all the QDs in the SOA are assumed to be identical and uniform, and there exists only one confined energy level in the conduction and valence band of each QD. The intermediate (excited) state is replaced by calculating the carrier occupation probability near the band edge of the WL. The WL is populated by the injected current and serves as a reservoir of carriers, as illustrated in Figure 4- 8. The 2LREM model is valid for cases where there exists a large population of carriers in the WL, which couples to discrete QDs on a picoseconds time scale, whilst at the same time the two carrier population levels undergo recombination processes, stimulated emission and pumping [83, 84, 85]. Similar to the treatments presented in [27, 86, 28], in developing the QD-SOA-IM model, various ultrafast intraband dynamic processes are ignored, which include carrier

heating, spectral hole-burning, two-photon absorption and ultrafast nonlinear refraction. Such an assumption is justified because of the following two reasons:

1) The DACs/ADCs involved in the AMOOFDM transceivers have sampling rates of typically <20GS/s, which correspond to sampling time durations of >50ps. Such time durations are much longer than the intraband dynamic process response times of typically ~1ps. For a QD-SOA-IM subject to an optimum optical input power, the corresponding effective intraband carrier lifetime is approximately 30ps, which is even larger for practical optical input power conditions of <10dBm for QD-SOA-IMs. Therefore, the effective intraband carrier lifetime is far beyond the intraband dynamic process response times.

2) The optical gain saturation properties of the QD-SOA-IMs are mainly determined by the strong DC component of an optical signal propagating in the QD-SOA-IMs. For example, at the front facet of the QD-SOA-IMs, the modulated optical signals with noise-like waveforms have relatively small signal extinction ratios of approximately 1dB [27, 86, 28].

The above-mentioned two points indicate that it is sufficiently accurate to neglect the influence of the intraband dynamic process on the optical gain saturation characteristics of the QD-SOA-IMs for the transmission systems of interest in present work.

Following the procedure in [27, 86, 87, 88, 28] making the transformation $T = t - z/v_g$ with v_g and T being the group velocity and the reduced time measured in a reference frame moving with the optical signal, respectively. z is the distance in longitudinal direction, i.e. z=0 and L stands for the input and output facets of the QD-SOA-IM, and L is the length of the QD-SOA-IM active region. The optical field, A(z,T), can be written as

$$A(z,T) = \sqrt{P(z,T)}exp[j\Phi(z,T)] \tag{4.1}$$

Where P(z,T) and Φ(z,T) are the optical power and phase, respectively. The propagation of the optical signal along the QD-SOA-IM is governed by:

$$\frac{\partial P(z,T)}{\partial z} = g(z,T)P(z,T) \tag{4.2}$$

$$\frac{\partial \Phi(z,T)}{\partial z} = -\frac{1}{2}\alpha g(z,T) \tag{4.3}$$

Where α is the linewidth enhancement factor (LEF) associated with the interband transitions. g(z,T) is the optical gain and can be linearly related to the carrier density in the active region via $g(z,T) = \Gamma a(N_d - N_0)$ with a being the differential

gain, Γ being the optical confinement factor, N_d being the total carrier density of all QDs, and N_0 being the transparency carrier density. If we define

$$h_d(T) = \int_0^L g(z', T)\, dz' \tag{4.4}$$

And taking into account the 2LREM model presented in [84, 85] and the above-mentioned assumptions, the temporal gain governing the dynamic characteristics of the QD-SOA-IM can be obtained:

$$\frac{dh_d(T)}{dT} = \frac{h_w(T)}{\tau_{w\to d}}\left[1 - \frac{h_d(T)}{h_{max}}\right] - \frac{h_d(T)}{\tau_{dr}} - \left[exp(h_d(T) - 1)\frac{P_{in}(T)}{\hbar\omega_0 \frac{wd}{\Gamma a}}\right] \tag{4.5}$$

$$\frac{dh_w(T)}{dT} = \frac{[h_{in}(T) - h_w(T)]}{\tau_{wr}} - \frac{h_w(T)}{\tau_{w\to d}}\left(1 - \frac{h_d(T)}{h_{max}}\right) \tag{4.6}$$

With

$$h_{max} = \int_0^L G_{max} dz = \int_0^L \Gamma a(N_{max} - N_0)\, dz \tag{4.7}$$

$$h_{in} = \int_0^L \frac{\Gamma a J(T)\tau_{wr}}{ed} dz \tag{4.8}$$

Where $h_w(T)$ is the total integrated gain factor corresponding to the WL. $\tau_{w\to d}$ is the electron relaxation time from the WL to the ground state in the QDs, τ_{wr} is the spontaneous radiative lifetime in the WL and τ_{dr} is the spontaneous radiative lifetime in the QDs. h_{max} is the maximum value of the integrated gain and G_{max} is the unsaturated gain. $P_{in}(T)$ is the power of the optical input wave. e is the electron charge, J(T) is the injection current density, d is the WL thickness, ω_0 is the frequency of the optical signal and w is the width of the WL region. The power and phase of the modulated optical signal at the output of the QD-SOA-IM are, therefore, given by:

$$P_{out}(T) = P_{in}(T)exp[h_d(T)] \tag{4.9}$$

$$\Phi_{out}(T) = \Phi_{in}(T) - \frac{1}{2}\alpha h_d(T) \tag{4.10}$$

Here $\Phi_{in}(T)$ is the phase of the optical input wave. Apart from intensity modulation, the QD-SOA-IM also imposes amplified spontaneous emission (ASE) noise onto the modulated optical signal. The total ASE power, P_{ASE}, can be calculated by [89]

$$P_{ASE} = \left[N_f exp\left(h_d(T)\right) - 1\right] B_0 \hbar\omega_0 \tag{4.11}$$

$P_{ASE} = \left(N_f G - 1\right) B_0 \hbar\omega_0$ Where N_f is the QD-SOA noise figure, B_0 is the optical bandwidth and $\hbar\omega_0$ is the photon energy. In the model, the impact of amplified spontaneous emission on gain saturation is ignored for simplicity. Eqs.(4.6)-(4.11) are the final set of equations, which can be easily solved numerically when G_{max}, $P_{in}(T)$ and $\Phi_{in}(T)$ are known. After adding the ASE noises into $P_{out}(T)$ and $\Phi_{out}(T)$, the final intensity modulated optical signal can be obtained.

4.4.2 *OOFDM system Simulation parameters*

In this section, we present simulation parameters that will be adopted in the numerical simulations throw-out this chapter. It is noted that all parameters are based on commercially available components. In simulating AMOOFDM modems, 64 subcarriers are used, in which 31 carry real data; one contains no power and the remaining 32 are the complex conjugate of the aforementioned subcarriers. The modulation formats used on these subcarriers vary from DBPSK, DQPSK, and 8 QAM to 256 QAM depending upon the frequency response of a given transmission link. For simplicity, the powers of all subcarriers are assumed to be identical regardless of their modulation formats. To overcome link dispersion, the cyclic-prefix parameter η is taken to be 25%. The ADCs are adopted with a 7-bit resolution at a sampling rate of r_s = 12.5 GS/s. The parameters mentioned above give a signal bandwidth in the positive frequency bins of 12.5/2 = 6.25 GHz, a subcarrier bandwidth of 6.25/32 ≈ 195 MHz, and a total symbol length of 6.4 ns, of which 1.6 ns is occupied by the cyclic prefix. The clipping level in the modem is fixed at 13 dB. A p-i-n photodetector is used, in which a quantum efficiency of 0.8 is assumed. The receiver sensitivity of the p-i-n photo detector is −19dBm corresponding to a 10-Gb/s NRZ with a BER of 1.0×10^{-9}. Based on the aforementioned parameters and received optical powers, both shot and thermal noise associated with the detection process can be computed. A single optical signal channel operating at 1550 nm is considered here.

4.4.3 *QD-SOA simulation parameters*

Table 7 shows the parameters used in simulating the SOA-IM/QD-SOA-IM, SMF, and the photo-detector. It should be noted that, for practical QD-SOAs, their α values may vary significantly from a value as low as α=0.1 in InAs QD lasers near the gain saturation regime [90] to a huge value as large as α=60 recently measured in InAs/InGaAs QD laser [91]. Specific band structures also

play a significant role in determining the α value [90, 91, 92]. In addition, α parameter is dependent upon injection current, photon energy and temperature [93]. Considering the fact that a typical value of α ≈ (2-7) can be considered [84], in this work, α is set at 5 for both the SOA-IM and QD-SOA-IM.

Table 7 : QD-SOA-IM, SOA-IM, SMF, and PIN simulation parameters [27, 78, 86, 83, 84, 28]

QD-SOA-IM	
Parameter	**Value**
$\tau_{w\rightarrow d}$	6ps
τ_{wr}	0.2ns
τ_{dr}	0.4ns
SOA-IM/QD-SOA-IM	
Parameter	**Value**
Cavity Length	300 μm
Width of active region	1.5 μm
Depth of active region	0.27 μm
Carrier lifetime SOA	0.3ns
Confinement factor (SOA)	0.35
Confinement factor (QD-SOA)	0.1
Differential gain	$3\times10^{-20}m^2$
Linewidth enhancement factor	5
Group velocity	$8.43\times10^{7}m/s$
Optical frequency	1550nm
Carrier density at transparency	$1.05\times10^{24}m^{-3}$
Noise figure	8dB
Unsaturated gain	20dB
SMF	
Parameter	**Value**
Effective area	$80\ \mu m^2$
Dispersion	17.0ps/nm/km
Dispersion slope	0.07ps/nm/nm/km
Dispersion wavelength	1550nm
Loss	0.2dB/km
Kerr coefficient	$2.35\times10^{-20}m^2/W$
PIN	
Parameter	**Value**
Quantum efficiency	0.8
Noise current density	8pA/√Hz

4.4.4 *Static and dynamic QD-SOA performances*

4.4.4.1 Optical gain saturation characteristics

In order to gain an in-depth understanding of the effect of the QD-SOA-IM gain saturation on the AMOOFDM transmission performance, Figure 4- 9(a) is plotted to show the QD-SOA gain versus CW optical input power for different bias currents. It can be seen in Figure 4- 9(a) that the QD-SOA optical input

saturation power increases significantly with increasing bias current. It can also be observed in Figure 4- 9(a) that, for optical input powers of < 0dBm, the gain variation for bias current varying from 100mA to 200mA is almost independent of bias current. The physical mechanism behind such behavior is that the QD-SOA charge neutrality defined in [94] is assumed in the ground state only. In Figure 4-9(b), comparisons of the gain versus bias current between the SOA and QD-SOA are presented for three optical input powers of 0dBm, 10dBm and 20dBm. As seen in Figure 4- 9(b), the QD-SOA reaches saturation much faster than the conventional SOA when an identical bias current is applied. This is due to the fact that the effective carrier lifetime of the QD-SOA is much smaller than that of the SOA. Generally speaking the QD-SOA modulation bandwidth is proportional to the inverse of the effective carrier lifetime. All the results shown in Figure 4- 9 agree well with those obtained in [80, 83, 85], indicating the validity of the developed QD-SOA-IM model in this work.

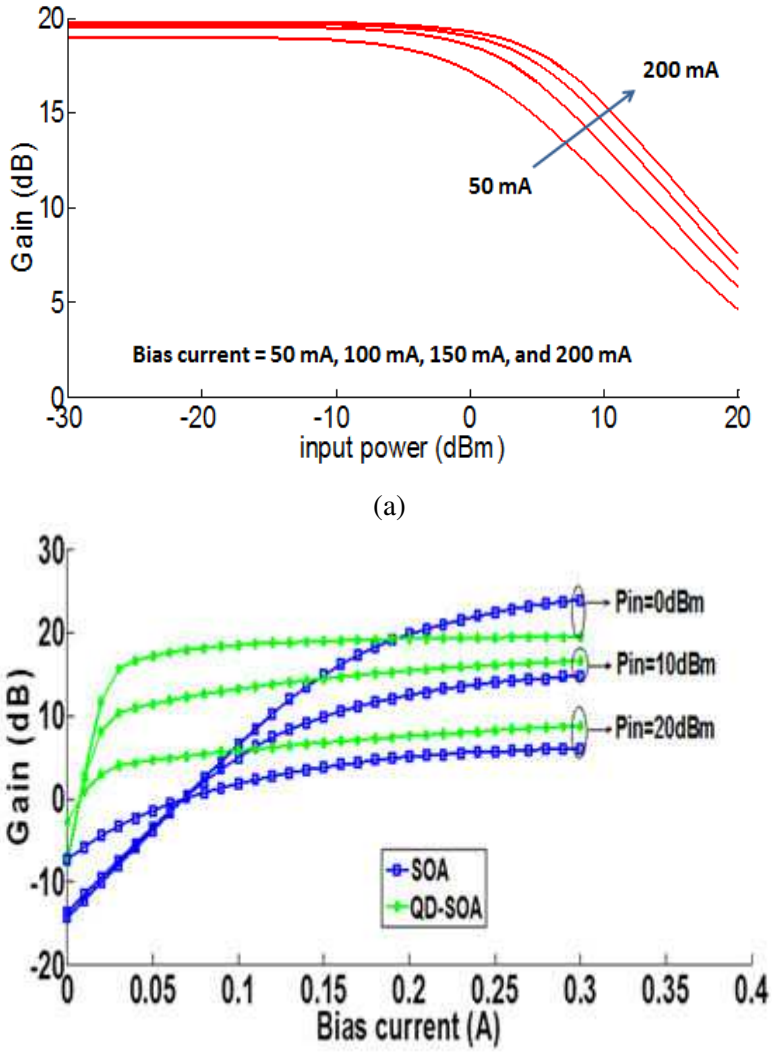

Figure 4- 9 : QD-SOA-IM gain saturation characteristics for different operating conditions. (a) gain versus optical input power. (b) gain versus bias current

Figure 4- 10 (a) shows the normalized frequency response of the QD-SOA-IM for 0 dBm optical input power. Figure 4- 10 (b), (c) and (d) present the spectra of the modulated AMOOFDM signals at the output facet of the QD-SOA-IM subject to different CW optical input powers. It can be seen in Figure 4- 10 that the larger the CW optical input power to the QD-SOA-IM is, the wider the signal bandwidth obtained due to reductions in both effective carrier lifetime and signal spectral distortion. Clearly, this leads to the improved transmission performance. At the same time, however, a large CW optical input power also brings about serious signal clipping due to the reduced slope of the gain – current curve, which can be seen in Figure 4- 9 (b).

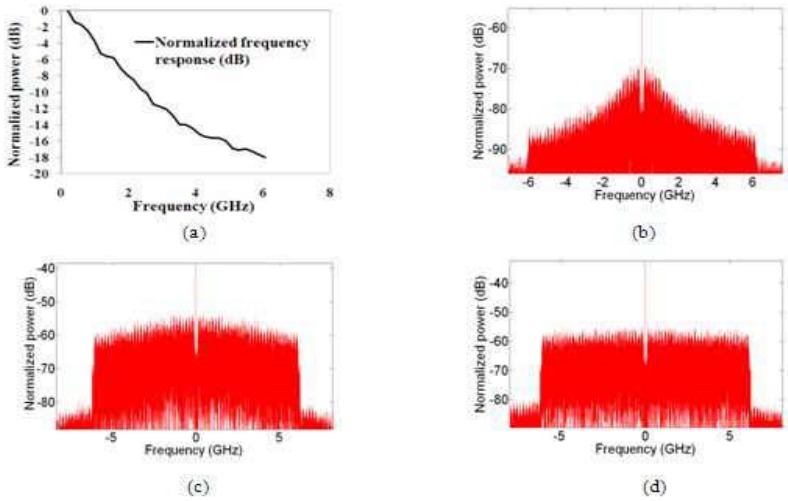

Figure 4- 10 : (a) Normalized frequency response of QD-SOA for 0 dBm optical input power. Spectrum of a modulated AMOOFDM signal at the output facet of the QD-SOA-IM subject to different CW optical input powers: (b) 0dBm, (c) 10dBm, and (d) 20dBm.

4.4.5 *Simulated system transmission performance using QD-SOA*

In numerical simulations, throughout this chapter, the signal line rate is calculated using the same expression as mentioned in [27, 95, 96, 44, 28].

4.4.5.1 Impact of bias current and optical input power

Figure 4- 11 shows contour plots to demonstrate the achievable AMOOFDM transmission capacity of a 60km IMDD SMF transmission system for both the SOA-IM and the QD-SOA-IM as function of bias current and CW optical input power, in most of the coming results we will compare the new results of the new SOA configurations to those of the previous work using an SOA [27] in order to better explain the results. The peak-to-peak (PTP) driving current is set to 80mA. As seen from the contour plots in Figure 4- 11, in comparison with the SOA-IM, for both bias current and CW optical input power, the QD-SOA-IM has much broader variation ranges of optical input power and input bias current, over which higher signal bit rates are achievable. For example, to achieve signal bit rates of >30Gb/s, the SOA-IM requires a CW optical input

power to vary in a 3dB range between 19dBm to 21dBm; whilst the QD-SOA-IM allows a CW optical input power to vary in a 20dB range between 10dBm and 30dBm. More importantly, to achieve achieve signal bit rates of >30Gb/s, the QD-SOA-IM allows the injection of CW input powers as low as 10dBm which is more practical than 20 dBm. Clearly, the QD-SOA-IM considerably extends the optical input power range, and subsequently improves the performance robustness of the PON systems.

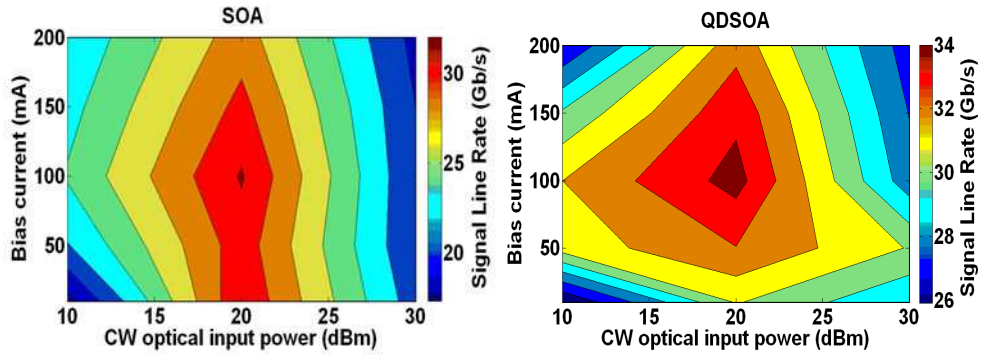

(a) **(b)**

Figure 4- 11 : Contour plot of signal line rate as a function of CW optical input power and bias current after transmitting through a 60km SMF IMDD transmission system. (a) SOA-IM, (b) QD-SOA-IM.

Figure 4- 11 also shows that the optimum CW optical input powers are 20dBm for both the QD-SOA-IM and SOA-IM. For optical input powers less than the optimum CW optical power value, the degradation of the signal transmission capacity is due to the long effective carrier lifetime. This is seen clearly in Figure 4- 11, as a relatively small optical input power gives rise to a long effective carrier lifetime and thus a narrower modulation bandwidth. While for CW optical powers higher than the optimum value, the degradation is due to a decrease in signal extinction ratio. Figure 4- 12 shows the signal extinction ratio as a function of CW optical input power for the SOA-IM and QD-SOA-IM. In obtaining Figure 4- 12, a bias current of 100mA and a driving current PTP value of 80mA are adopted. It can be seen in the figure that the SOA-IM outperforms the QD-SOA-IM in signal extinction ratio for CW optical input powers less than 20dBm. This effect is examined once again in discussing results for long transmission distances (>100 km).

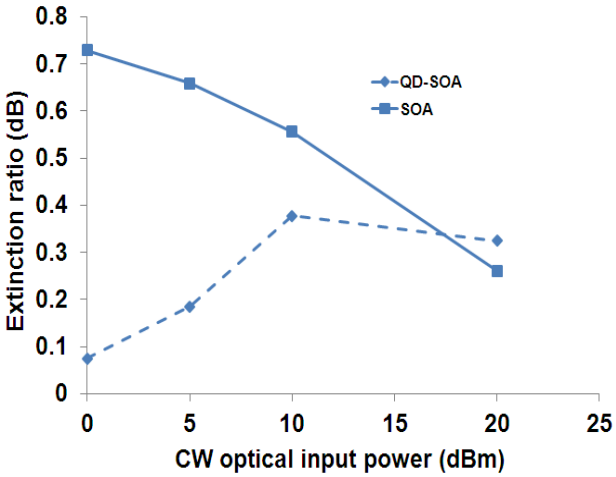

Figure 4- 12 : Comparison of signal extinction ratios for SOA-IMs and QD-SOA-IMs as a function of CW optical input power.

Now we discuss the bias current range. As shown in Figure 4- 11, the QD-SOA-IM also considerably broadens the bias current variation range to achieve signal bit rates of >30Gb/s, and both the SOA-IM and the QD-SOA-IM have similar optimum bias current values of 100mA. For bias currents larger than this optimum value, the reduction in signal line rate is due to the reduction in signal extinction ratio of the modulated signal and the increase in signal clipping effect; while for bias currents smaller than the optimum bias current range, the increase in effective carrier lifetime plays a dominant role in reducing the signal line rate [27].

4.4.5.2 Impact of driving current PTP

In addition to the CW optical input power and bias current, it is also important to study the influence of the OFDM driving current PTP on the AMOOFDM transmission performance. For QD-SOA-IMs and SOA-IMs, Figure 4- 13 and Figure 4- 14 show driving current PTP-dependent transmission performance for 10dBm and 20dBm optical input powers at various transmission distances. In obtaining Figure 4- 13 and Figure 4- 14, the bias current is set to be 100mA. It can be seen that, compared to the SOA-IM, the QD-SOA-IM always improves the AMOOFDM transmission performance over transmission distances of less than 120km. The optimum PTP value of the driving current is transmission-distance dependent: for transmission distances of <60km, the optimum PTP value is found to be 80mA.

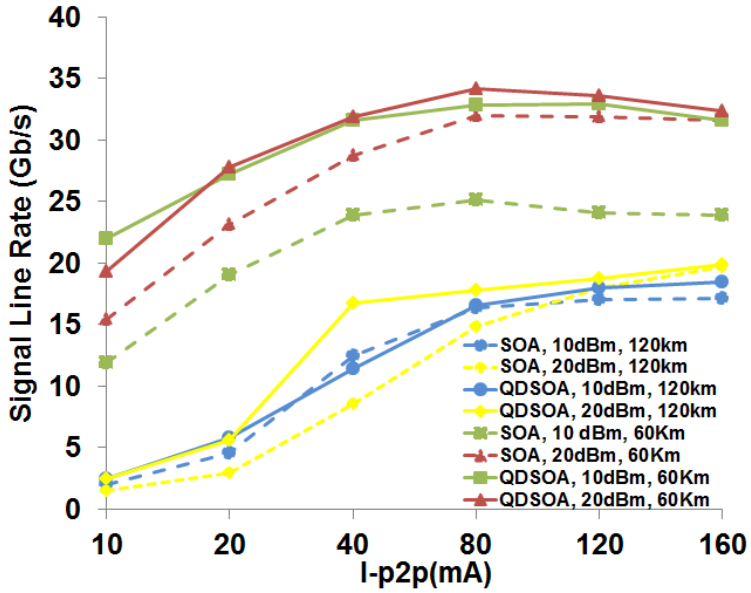

Figure 4- 13 : Signal line rate of QD-SOA-IMs and SOA-IMs as a function of driving current PTP for different optical input powers and transmission distances.

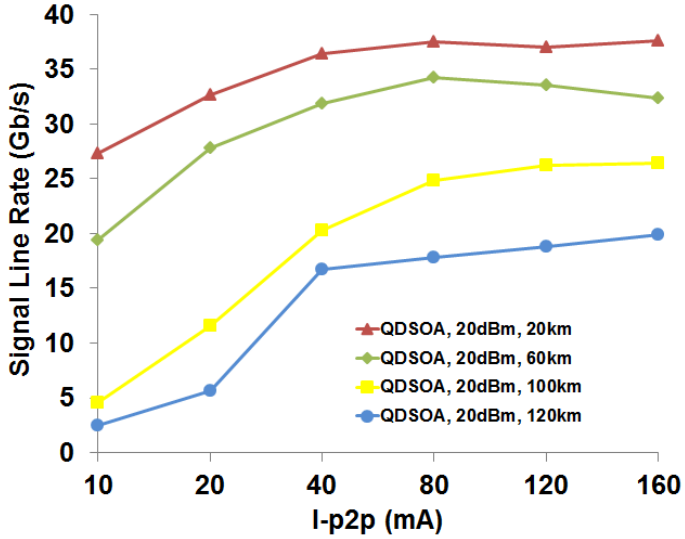

Figure 4- 14 : Signal line rate as a function of driving current PTP for different transmission distances.

For transmission distances longer than 100km, the optimum PTP value is found to be 160mA. This can be explained by considering the fact that, after transmitting long distances (>100km), the significantly attenuated optical signal requires a high driving current PTP to achieve an acceptable BER. For PTPs larger than this optimum value, the reduction in signal line rate is due to the increased signal clipping effect due to the nonlinear gain current curve of the QD-SOA-IM, while for PTPs smaller than the optimum value, the reduction in signal capacity is due to the decrease in signal extinction ratio.

4.4.5.3 Optimized AMOOFDM transmission performance and physical limitations

Having identified the optimum QD-SOA-IM operating conditions including bias current, driving current PTP and CW optical input power, the maximum achievable signal bit rate of the AMOOFDM transmission system incorporating the QD-SOA-IMs is investigated in this section.

The numerical results are plotted in Figure 4- 15 and Figure 4- 16, where the identified optimum QD-SOA-IM operating conditions are adopted, i.e., a bias current of 100mA, a driving current PTP of 80mA. Signal bit rate comparisons are also made in Figure 4- 15 between the QD-SOA-IM, the SOA-IM and an ideal intensity modulator (IM). In simulating the ideal IM, a simple square root operation is applied to the sum of the electrical OFDM driving current and dc bias current. It can be seen in Figure 4- 15 that, the QD-SOA-IM outperforms the SOA-IM in signal bit rate for all transmission distances of up to 140km. For transmission distances of 20km, the QD-SOA-IM offers signal bit rates almost identical to the ideal IM.

Figure 4- 16 shows that, up to 120km, the performances supported by the QD-SOA-IMs are much better than those supported by the SOA-IMs for CW optical input powers of 10dBm and 20dBm. This indicates that the QD-SOA-IMs are capable of supporting signal line rates higher than those corresponding to the SOA-IMs by using 10dB lower optical input powers. In addition, Figure 4- 16 also shows that the QD-SOA-IMs subject to 5dBm optical input powers can achieve better transmission performance than the SOA-IMs subject to 10dBm input optical powers for transmission distances of <60km. For optical input powers of <5dBm, the superiority of the SOA-IMs over the QD-SOA-IMs for longer transmission distances is due to the fact that the QD-SOA-IMs have gain-current curves with flat slopes (Figure 4- 9(b)), leading to severe signal clippings and lower signal extinction ratio as seen in Figure 4- 12.

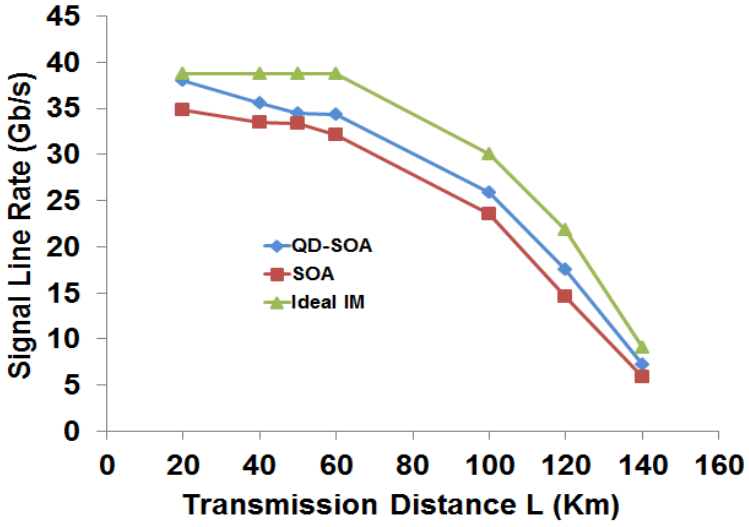

Figure 4- 15 : Maximum achievable signal transmission capacity versus reach performance of AMOOFDM signals for various intensity modulators. The optical input power is fixed at 20dBm.

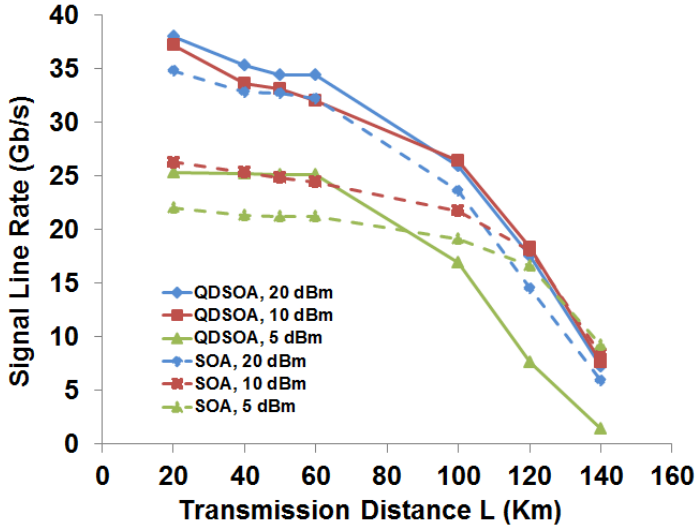

Figure 4- 16 : Signal line rate versus reach performance for various input optical powers.

To demonstrate the QD-SOA-IM-induced strong signal clipping effect, as stated above, Figure 4- 17 is plotted to compare the waveforms of the QD-SOA-IM- and ideal IM- modulated AMOOFDM signals for input optical power of 10dBm. Figure 4- 17 shows that the QD-SOA-IM modulated waveform is clipped compared to that corresponding to an SOA (the peak to peak level is smaller). The strong clipping effect associated with the QD-SOA-IM leads to degradation in the signal quality. In particular, the signal clipping effect is more important for long transmission distances.

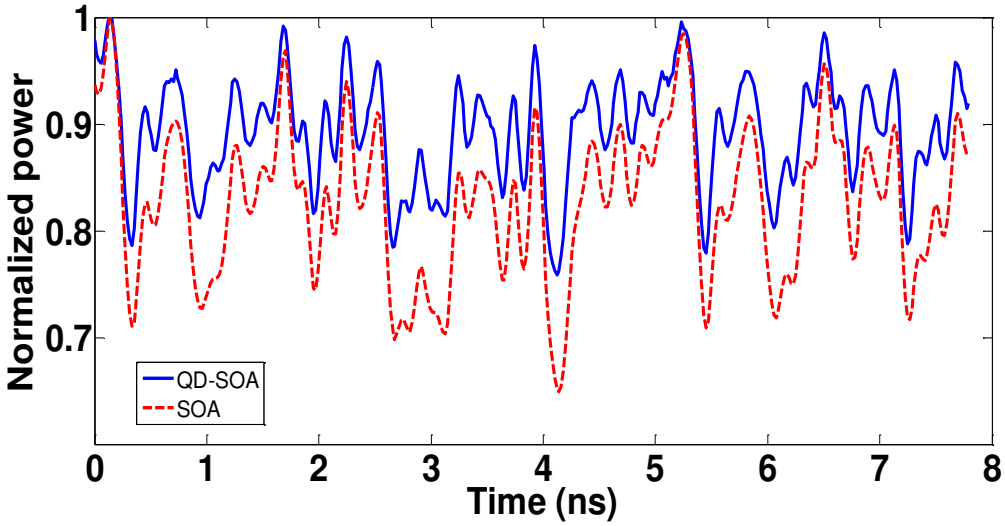

Figure 4- 17 : Comparison of normalized AMOOFDM signal waveforms generated by a QD-SOA-IM, and an ideal IM for 10 dBm optical input power.

4.4.5.4 Impact of negative frequency chirp

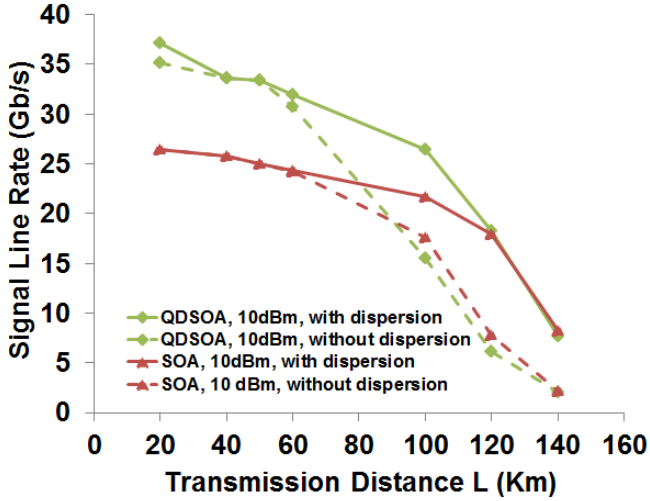

Figure 4- 18 : Signal line rate versus reach performance for cases of including and excluding chromatic dispersion. The optical input power is fixed at 10dBm.

OOFDM has strong resilience to CD in both coherent and IMDD transmission systems. In addition to that, the CD compensation approach can further improve the AMOOFDM transmission performance in IMDD transmission systems as explained in [28] regarding the impact of the presence of the square law-photon detector. It is well known that an SOA-IM imposes negative frequency chirps on the modulated optical signals [27, 44], the negative frequency chirp effect can be used to mitigate the positive fibre chromatic dispersion effect [27], as shown in Figure 4- 18. As expected, the fiber dispersion compensation effect is more pronounced for long transmission distances, and the QD-SOA-IMs have much stronger dispersion compensation capability compared to SOA-IMs. As square-law photon detection cannot preserve perfectly the chromatic dispersion-induced optical phase shift in the electrical domain, better dispersion compensation from the QD-SOA induced negative chirp can reduce the phase variation, thus leading to the improved AMOOFDM transmission performance.

4.5 Two electrode-based SOA intensity modulators

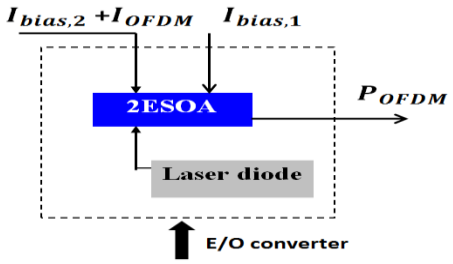

Figure 4- 19 : 2E-SOA E/O converter configuration

The SOA approach suffers from the limited electrical modulation bandwidths. The modulation bandwidth of standard SOAs reaches 1GHz and

using high optical confinements we can reach 2GHz. Previously published results show that the use of a two electrode-based SOA (2E-SOA) drastically improves the modulation bandwidth of an SOA from 2GHz up to 6 GHz [97], and even to above 7.8 GHz as a colourless source for WDM-PONs [49]. In this work, we demonstrate, for the first time in our knowledge, that the use of a 2E-SOA as an intensity modulator (2E-SOA-IM) by using adaptively modulated OOFDM (AMOOFDM) signals in intensity-modulation and direct-detection (IMDD) system can significantly improve the signal line rate compared to those supported by a single electrode (SOA-IM).

4.5.1 *SOA-Based Intensity Modulator Model [27]*

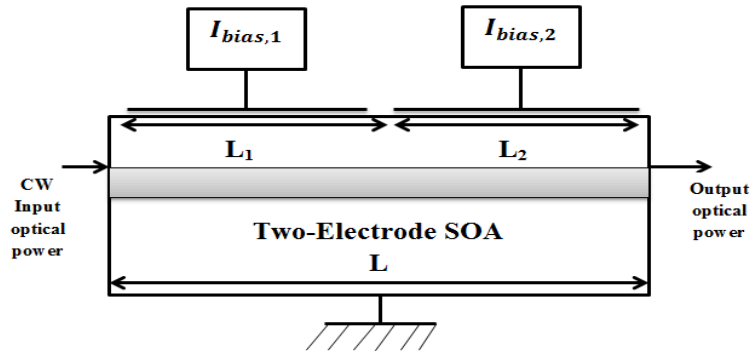

Figure 4- 20 : Schematic of the proposed two electrode SOA (2E-SOA).

The 2E-SOA used in this new proposed configuration is composed of two sections of lengths L_1 and L_2, respectively, where the first section acts as a preamplifier and the second one operates as an intensity modulator (Figure 4- 20). The total length of the single SOA is L with L=L1+L2. The first section of the 2E-SOA is biased with only DC bias current $I_{bias,1}$ and the second section is driven simultaneously with DC bias current $I_{bias,2}$ and the OFDM electrical driving current. The total current I_{bias} is equal to the sum of $I_{bias,1}$ and $I_{bias,2}$. The theoretical 2E-SOA model adopted here is similar to that presented in [27]. The parameters used in simulating the 2E-SOA-IM/ SOA-IM, SMF, and the photon detector are shown in [27]. For fair performance comparisons in simulating the transmission performance, the 2E-SOA-IM and SOA-IM have the same parameters.

4.5.1.1 SOA model

We will briefly explain the SOA-IM model used in [27] , by taking into account carrier depletion owing to stimulated emission as well as major intraband dynamic processes such as carrier heating, spectral hole-burning, two-photon absorption and ultrafast nonlinear refraction, a comprehensive SOA theoretical model has been developed [71], which has been successfully employed in describing the propagation of strong picosecond optical pulses in SOAs, ultrafast

switching characteristics of terahertz optical asymmetric demultiplexers, phase conjugation of picosecond optical pulses, and active picosecond optical pulse reshaping in SOAs. In developing the SOA-IM model, various ultrafast intraband dynamic processes are ignored, which include carrier heating, spectral hole-burning, two-photon absorption and ultrafast nonlinear refraction. Such an assumption is justified for the same reasons mentioned for the QD-SOA model in section 4.4.1.

The exclusion of the intraband carrier processes simplifies significantly the SOA theoretical model. In the 2E-SOA-IM model, we consider the two electrode SOA as two cascaded SOAs of length L1 and L2 and biased by $I_{bias,1}$ and $I_{bias,2}$. As explained for the QD-SOA model in section 4.4.1, when a transformation of the wave propagation equation is made to the retarded reference frame, $T = t - z / v_g$ with t, z, and v_g being the time, the transmission distance and the group velocity, respectively. The optical field in each SOA is defined as:

$$A(z,T) = \sqrt{P(z,T)}\exp[j\,\phi(z,T)] \tag{4.12}$$

With $P(z,T)$ and $\Phi(z,T)$ being the optical power and phase, respectively. The set of equations which govern the propagation of the optical signal traveling through the SOAs are obtained as follows:

$$\frac{\partial g(z,T)}{\partial T} = \frac{g_0(T) - g(z,T)}{\tau_c} - \frac{g(z,T)}{E_{sat}}P(z,T) \tag{4.13}$$

$$\frac{\partial P(z,T)}{\partial z} = g(z,T)P(z,T) \tag{4.14}$$

$$\frac{\partial \phi(z,T)}{z} = -\frac{1}{2}\alpha g(z,T) \tag{4.15}$$

Where g(z,T) is the optical gain defined as $g(z,T) = \Gamma a[N(T) - N_0]$ with N[T] and N_0 being the carrier density and the carrier density at transparency, Γ is the confinement factor and a is the differential gain. $g_0(T)$ is the small signal gain of the SOA, which can be expressed as $g_0(T) = \Gamma a N_0[I(T) / I_0 - 1]$, here I(T) is the total injected current including the dc bias current and the driving current, and I_0 is the current required at transparency. $\boldsymbol{\tau_c}$ is the carrier lifetime. $\boldsymbol{E_{sat} = \hbar\omega_0 wd/\Gamma a}$ is the SOA saturation energy with $\boldsymbol{\omega_0}$, w and d being the frequency of the optical signal, the width, and the depth of the SOA active region, respectively. α is the linewidth enhancement factor. In deriving (4.14), the SOA linear internal loss effect is incorporated into a slight increase in carrier density required at transparency. By integrating (4.13)–(4.15) over the entire SOA cavity length L, a set of equations can be obtained as follows:

$$\frac{\partial h(T)}{\partial T} = \frac{g_0(T)L - h(T)}{\tau_c} - \frac{P_{in}(T)}{E_{sat}}\{\exp[h(T)] - 1\} \tag{4.16}$$

$$P_{out}(T) = P_{in}(T)\exp[h(T)] \tag{4.17}$$

$$\phi_{out}(T) = \phi_{in}(T) - \frac{1}{2}\alpha h(T) \tag{4.18}$$

With

$$h(T) = \int_0^L g(z,T)dz \tag{4.19}$$

Where $P_{out}(T)$ and $\Phi_{out}(T)$ are the power and phase of the modulated optical signal, $P_{in}(T)$ and $\Phi_{in}(T)$ are the power and phase of the optical input wave. Equations (4.16)–(4.18) can be easily solved numerically when I(T), $P_{in}(T)$ and $\Phi_{in}(T)$ are made known.

Apart from intensity modulation, the SOA also imposes amplified spontaneous emission (ASE) noise onto the modulated optical signal. The total ASE power can be calculated as done for the QD-SOA model in section 4.4.1.

$$P_{ASE} = (N_f G - 1)B_0 \hbar w_0 \tag{4.20}$$

Equations (4.16)–(4.18) and (4.20) are the final set of equations, which are used in numerical simulations.

After adding the ASE noises into $P_{out}(T)$ and $\Phi_{out}(T)$, and subsequently introducing them into (4.12), the intensity modulated optical signal can be obtained. In the receiver, the transmitted optical signal can be detected using a square-law photon detector. It should be pointed out, in particular, that the validity of the SOA intensity modulator model developed here is confirmed by the excellent agreement between the theoretical results and experimental measurements as mentioned in ***[27]***.

4.5.2 *Simulated transmission performance*

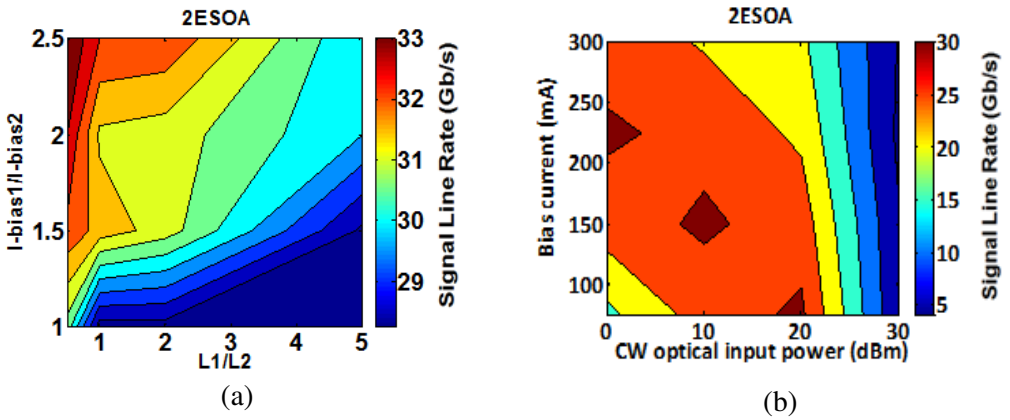

Figure 4- 21 : Contour plot of signal line rate for 2E-SOA-IM of a 60km SMF IMDD transmission system.

(a) As function of L_1/L_2 and $I_{bias,1}/I_{bias,2}$ for CW input optical power 10dBm, L=300µm, and I_{bias} = 150 mA.
(b) As function of CW input optical power and the bias current, where $L_1=L_2=150$ µm and $I_{bias,1}=2I_{bias,2}$.

In order to identify the optimum operating conditions of the 2E-SOA-IM that corresponds to the maximum AMOOFDM transmission performance and to compare such performance with the SOA-IM, Figure 4- 21 shows the contour plots demonstrating the achievable AMOOFDM transmission capacity of a 60km IMDD SMF transmission system. The peak-to-peak (PTP) driving current is set to be 80mA. CW input optical power 10dBm, L=300µm, and I_{bias} = 150 mA.
It can be seen that a signal bit rate higher than 30Gb/s is achievable at $L_1/L_2=1$ and $I_{bias,1}/I_{bias,2}=2$, (Figure 4- 21a), which indicates that the DC current density in the pre-amplification 2E-SOA section should be higher than the DC current density of the electrode that is used as an intensity modulator. It was noticed that we can increase the signal bit rate higher by increasing the $I_{bias,1}/I_{bias,2}$ ratio to 2.5 and by choosing L_1/L_2 = 0.5 but this will put a lot of bias current on a small section making it physically not practical. Figure 4- 21b shows the contour plot for the 2E-SOA-IM as a function of CW input optical power and the total bias current I_{bias} where $L_1=L_2=150$µm and $I_{bias,1}=2I_{bias,2}$. There exists three optimum operating condition regions for the 2E-SOA-IM, corresponding to which maximum signal line rates are observed as following: the CW input optical power is 20dBm and I_{bias}=75mA, 10dBm and 150mA, 0dBm and 225mA respectively. While it has been shown [27] that the optimum single SOA operating condition region is at 20dBm and 100mA, which implies that using the 2E-SOA-IM reduces the input optical power consumption. Having identified the optimum 2E-SOA-IM operating conditions including the bias current and length of each section, as well as CW input optical powers, the maximum achievable signal line rate of the AMOOFDM transmission system incorporating the 2E-SOA-IM is investigated

below. The numerical results are plotted in Figure 4- 22 where $I_{bias,1}=2I_{bias,2}=100mA$, $I_{bias}=100mA$ for the single SOA and a driving current PTP of 80mA is used for both configurations. The length of the two sections is given as $L_1=L_2=150\mu m$. The length of the single SOA is 300µm. For different input optical powers, 0 and 10dBm, we have made comparisons between the performances of the 2E-SOA-IM with that of the single SOA-IM.

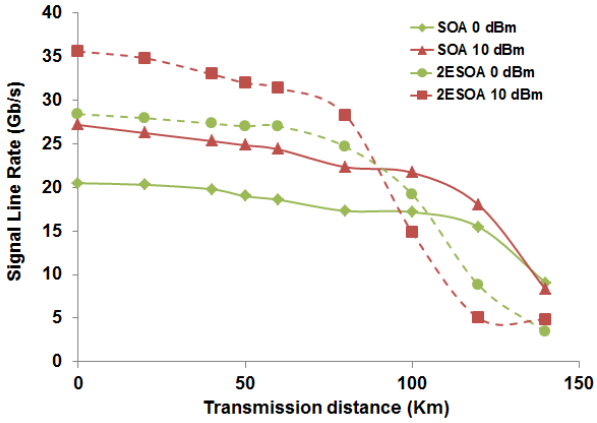

Figure 4- 22 : Signal transmission capacity versus reach performance of AMOOFDM signal for SOA-IM and 2E-SOA-IM.

As shown in Figure 4- 22, the 2ESOA for 0 dBm and 10 dBm optical input powers outperform the SOA for the same input powers for transmission distances up to 90 Km; Moreover, the 2ESOA with 0 dBm input power outperforms the SOA with a 10 dBm input power, the enhancement in system capacity is due to the fact that the 2E-SOA has a higher modulation bandwidth as compared with the single SOA as shown and explained in [97, 49]. On the other hand, for long transmission distances, the SOA outperforms the 2E-SOA, this is due to the fact that the second section of the 2E-SOA has a higher input power in comparison with the SOA, in [27] we have seen that the extinction ratio reduces with increasing input power due to a decline in the slope of the linear current-gain curve, and this effect is dominant on the transmission performance for long transmission distances. The bandwidth of the 2ESOA in Figure 4- 22 for 10 dBm input power is around 2 GHz, while it is 1.3 GHz for the SOA for 10 dBm input power, while the ER is 0.53316 dB and 0.42693 dB for the SOA and the 2E-SOA respectively.

4.6 Two cascaded SOAs in a counter propagating configuration

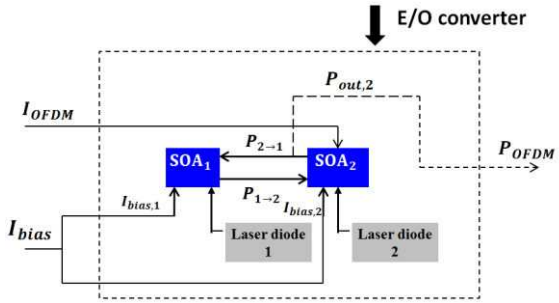

Figure 4- 23 : TC-SOA-CC E/O converter configuration

The two cascaded semiconductor optical amplifiers in a counter-propagating configuration (TC-SOA-CC) has been proposed for all optical signal processing [98]. It was shown in [98] that the two cascaded SOAs have improved performance over the single SOA configuration. In particular, a measured extinction ratio (ER) up to 20dB was obtained for close contra-directional signal wavelengths and for a wide range of optical input powers. Based on this configuration, a number of various functions have been also proposed. For example, all optical switching [98] and logic NOR function [99] have been realized with a high extinction ratio (ER) ≥12dB over a wide range of wavelengths. The all-optical inverted and non-inverted wavelength conversions feasibility has also been demonstrated to deliver an ER≥7dB over a wide range of wavelengths [100]. All optical logic OR gate can be easily achieved with an ER≥7dB [101]. In addition, the theoretical and experimental static characterizations of the TC-SOA-CC were studied [98]. A deeper understanding of this configuration in the dynamic regime is provided in [102], where the frequency responses obtained at the TC-SOA-CC optical outputs and the evolution of the effective carrier lifetimes and the gains for each signal in each SOA are shown. In this work, we will show the performance results of this configuration as an E/O converter (Figure 4- 23) by using AMOOFDM signals in the intensity-modulation and direct-detection (IMDD) system explained in chapter 3 section 3.2. In fact, in this configuration a feedback controls the evolution of the two SOA's gain.

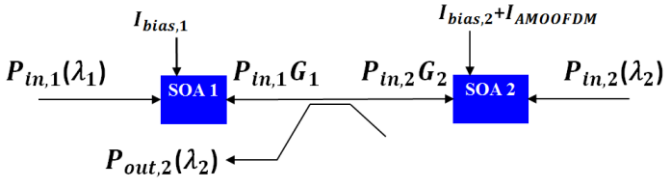

Figure 4- 24 : Schematic view of a TC-SOA-CC with contra propagating signals

Special effort is given to addressing the following technical challenges:

- Development of a comprehensive theoretical TC-SOA-CC-IMs model where the SOA_1 acts as an amplifier and the SOA_2 behaves as an intensity modulator.

- Identification of key TC-SOA-CC-IMs associated physical mechanisms considerably affecting the AMOOFDM transmission performance.

- Identification of optimum TC-SOA-CC-IMs operating conditions that correspond to the maximum AMOOFDM transmission performance.

- Performance comparisons between TC-SOA-CC-IMs and SOA-IMs to highlight the advantages of TC-SOA-CC-IMs for use in IMDD AMOOFDM PON systems.

- Exploration of the feasibility of effectively utilizing the TC-SOA-CC-IMs -induced frequency chirp to improve the transmission performance of IMDD AMOOFDM PON systems.

4.6.1 *TC-SOA-CC-based intensity modulator models*

The schematic diagram of the TC-SOA-CC-IMs where the SOA_1 acts as an amplifier and the SOA_2 works as an intensity modulator is shown in Figure 4-24. As explained before, each SOA receives two optical powers from its front facet and rear facet. The theoretical TC-SOA-CC model adopted here is an extension of the theoretical SOA intensity modulator models presented in [27] knowing that each SOA is subject to receive forward A^+ and backward A^- propagating optical signals. Similar to the treatments presented in [98, 96, 44], in developing the TC-SOA-CC model, various ultrafast intraband dynamic processes are ignored, which include carrier heating, spectral hole-burning, two photon absorption and ultrafast nonlinear refraction [88]. Following the procedure in [98, 96, 44, 89, 103], the optical field is defined as

$$A_i^{\pm}(z,T) = \sqrt{P_i^{\pm}(z,T)}exp\left[j\varphi_i^{\pm}(z,T)\right] \quad (4.21)$$
$$(if\ i = 1, SOA_1; if\ i = 2, SOA_2).$$

With $P_i^+(z,T)$and $\varphi_i^+(z,T)$ being the optical power and phase, respectively, at the forward direction of the input signal along SOA_i and $P_i^-(z,T)$ and $\varphi_i^-(z,T)$ being the optical power and phase, respectively, at the backward direction of the input signal along SOA_i. A set of equations which govern the propagation of the optical signal travelling through each SOA are obtained as follows:

$$\frac{\partial g_i(z,T)}{\partial T} = \frac{g_{0,i} - g_i(z,T)}{\tau_{c,i}} - \frac{g_i(z,T)}{E_{sat,i}}(|A_i^+(z,T)|^2 + |A_i^-(z,T)|^2) \quad (4.22)$$

$$\frac{\partial P_i^{\pm}(z,T)}{\partial z} = \pm g_i(z,T) P_i^{\pm}(z,T) \quad (4.23)$$

$$\frac{\partial \varphi_i^{\pm}(z,T)}{\partial z} = \pm \frac{1}{2} \alpha g_i(z,T) \quad (4.24)$$

These parameters in the equations are defined in section 4.5.1.1.

By integrating (4.22)–(4.24) over the entire SOA_i cavity length L_i and simplifying the calculations by considering $\lambda_1 = \lambda_2$, the temporal gain governing the dynamic characteristics of the TC-SOA-CC-IM can be obtained:

$$\frac{\partial h_1(T)}{\partial T} = \frac{g_{0,1}L_1 - h_1(T)}{\tau_{c,1}} - \frac{P_{in1}(T) + P_{out2}(T)}{E_{sat,1}}(exp[h_1(T)] - 1) \quad (4.25)$$

$$\frac{\partial h_2(T)}{\partial T} = \frac{g_{0,2}L_2 - h_2(T)}{\tau_{c,2}} - \frac{P_{in2}(T) + P_{out1}(T)}{E_{sat,2}}(exp[h_2(T)] - 1) \quad (4.26)$$

Where

$$h_i(T) = \int_0^{L_i} g_i(z,T)dz \quad (4.27)$$

The power and phase of the modulated optical signals at the output of each SOA are, therefore, given by:

$$P_{out,i}(T) = P_{in,i}(T)exp[h_i(T)] \quad (4.28)$$

$$\varphi_{out,i}(T) = \varphi_{in,i}(T) - \frac{1}{2}\alpha h_i(T) \quad (4.29)$$

The total ASE power, $P_{ASE,i}$, can be calculated by [89] :

$$P_{ASE,i} = \left[N_{f,i} exp\left(h_i(T)\right) - 1\right] B_{0,i} \hbar \omega_{0,i} \quad (4.30)$$

Under the optimum operating conditions identified in this work, within the adopted 6.25GHz signal bandwidth region, the total ASE power for each SOA is approximately >30dB lower than the optical powers of both the injected CW beams and the modulated AMOOFDM signals. The exclusion of the effect of ASE noises on SOA gain saturation does not affect the accuracy of the results presented. For simplicity, such an effect is not considered in the theoretical model. Equations (4.25)-(4.30) are the final set of equations, which are used in numerical simulations. After adding the ASE noises into $P_{out,i}(T)$ and $\varphi_{out,i}(T)$, the intensity modulated optical signal $P_{out,2}$ can be obtained. For the transmission system considered here, the validity of the TC-SOA-CC-IM model is verified by qualitative static results agreement between theoretical results obtained here and various experimental measurements at device level [98, 99, 100].

4.6.2 *TC-SOA-CC Simulation parameters*

We use the same simulation parameters identified in section 4.4.3 in Table 7 for the TC-SOA-CC-IM/ SOA-IM, SMF, and the photon detector, which are the optimum values identified in [104]. For fair performance comparisons in simulating the performance of the TC-SOA-CC-IM/SOA-IMs, each SOA in the proposed configuration, and the single SOA-IM in [27], have the same set of parameters.

4.6.3 *Static characteristics of TC-SOA-CC*

To understand and analyze all results that will be obtained later in dynamic simulations, it is important to study the optical gain characteristic effects of the TC-SOA-CC. Based on previous results [102], we have noticed that the evolutions of the effective carrier lifetimes $\tau_{1,2}$ follow those of the gains $G_{1,2}$ of the $SOA_{1,2}$ respectively. Indeed, the carrier lifetime τ_i is inversely proportional to the total injected optical power $P_{tot,i}$ in the SOA_i [27]. Figure 4- 25(a) shows the evolution of gains G_1 of the SOA_1 and G_2 of the SOA_2 versus the input optical power $P_{in,1}$ at $\lambda_1=\lambda_2=1550$nm and for two different values of $P_{in,2}$ of -15dBm and 10dBm.

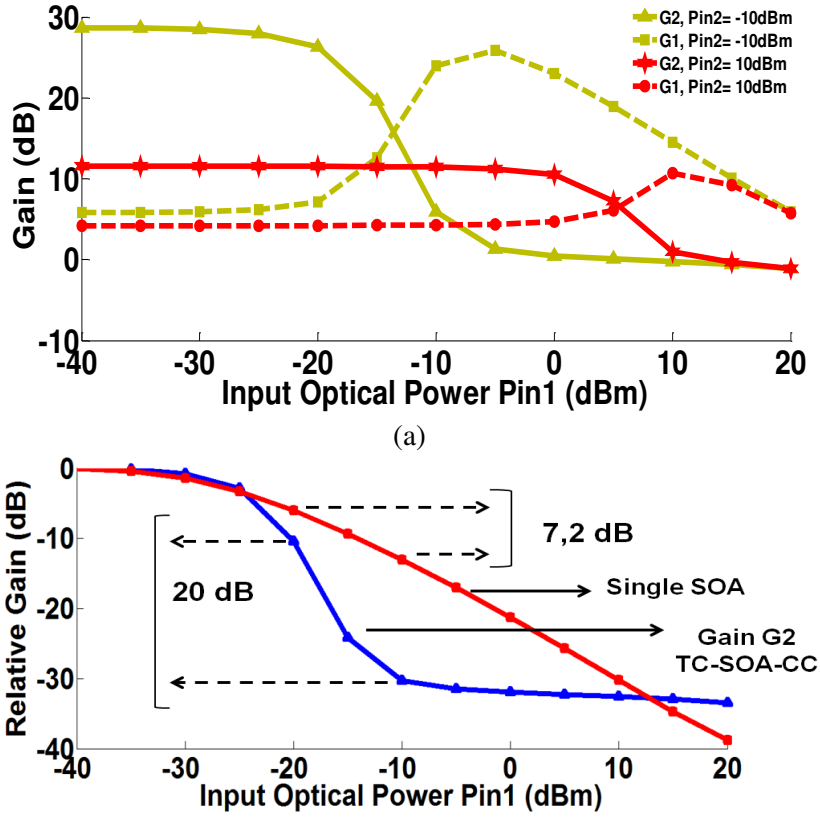

Figure 4- 25 : (a) Gains G_1 and G_2 versus the input optical power $P_{in,1}$ with $I_{bias,1}$= $I_{bias,2}$= 280mA, (b) Relative gain G_2 versus the input optical power $P_{in,1}$ for TC-SOA-CC and for a single SOA with $I_{bias,1}$= $I_{bias,2}$= 280mA

We observe that in presence of a low power $P_{in,1}$, the signal $P_{in,2}$ profits from the high gain G_2 (unsaturated) allowing it to saturate the gain G_1 of the SOA_1. In this case, the power $P_{tot,1}$ is strong and therefore τ_1 is short. On the other hand the power $P_{tot,2}$ is weak and therefore τ_2 is long. By increasing $P_{in,1}$, the SOA_1 output optical power injected in the SOA_2 becomes important and saturates the gain G_2. This reduction in G_2 can induce an increase in G_1 by the counter-reaction process. In this situation, the power $P_{tot,1}$ is weak and therefore τ_1 is long. On the other hand, the power $P_{tot,2}$ is strong and therefore τ_2 is short. It is well known that the SOA_2 modulation bandwidth and its effective carrier lifetime τ_2 have an inverse relationship. Moreover, this behavior explains the positive gain variations of SOA_1 and the negative gain variation of SOA_1 obtained for a certain power range. This range shifts to high powers if $P_{in,2}$ increases. In the TC-SOA-CC-IM model, the SOA_2 works as an intensity modulator, Figure 4- 25(b) shows the evolution of the relative gain of SOA_2 G_2 versus the input optical power $P_{in,1}$ at $\lambda_1=\lambda_2$=1550nm and for $P_{in,2}$=-15dBm for two configurations. The first one is done using the TC-SOA-CC configuration and the second is realized by using one of the two SOAs. The obtained results show that the SOA_2 gain nonlinearity is strongly accentuated in comparison with the transfer function using only one SOA. By varying $P_{in,1}$, the Gain G_2 steep slope is 20dB per 10dB (input range) for the TC-SOA-CC instead of 7.2dB for one SOA (Figure 4- 25(b)). These results in

Figure 4- 25(a) and Figure 4- 25(b) are confirmed by qualitative agreement with the experimental measurements as presented in [98, 99, 100, 102]. In addition, it can be easily found from Figure 4- 25(b) and the above explanations that, the TC-SOA-CC reaches its strongly saturated region using a lower input optical power much faster than the single SOA resulting in significantly reduced effective carrier lifetime τ_2 of SOA_2 and thus wide TC-SOA-CC bandwidths. Moreover, this leads to the improved transmission performance in comparison with single SOA at these lower optical input powers.

Given the central role of the electrical current-induced SOA_2 optical gain variation in determining the quality of the modulated AMOOFDM signals, Figure 4- 26 is plotted to show the gain G_2 as a function of bias current $I_{bias,2}$ for different values of $P_{in,1}$ and $P_{in,2}$ using TC-SOA-CC. It can be seen from Figure 4- 26 that, to obtain a desired linear current-gain slope, the bias current $I_{bias,2}$ must be set at 50mA for a wide range of $P_{in,1}$ and $P_{in,2}$. A sharp gain-current slope gives a high extinction ratio of the modulated AMOOFDM signal. On the other hand, and in order to make a comparison between both configurations, Figure 4- 26(d) shows the gain G_2 versus the bias current $I_{bias,2}$ for TC-SOA-CC and gain G versus I_{bias} for the single SOA. It can be seen from this figure that compared with the SOA, the TC-SOA-CC has a lower gain-current slope which decreases the extinction ratio of the AMOOFDM signals.

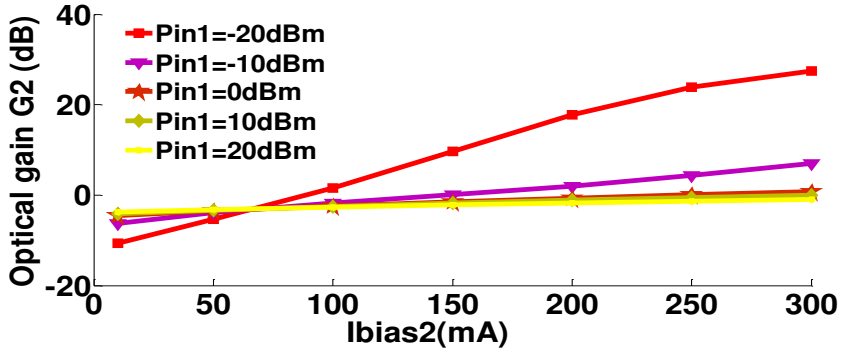

(a)

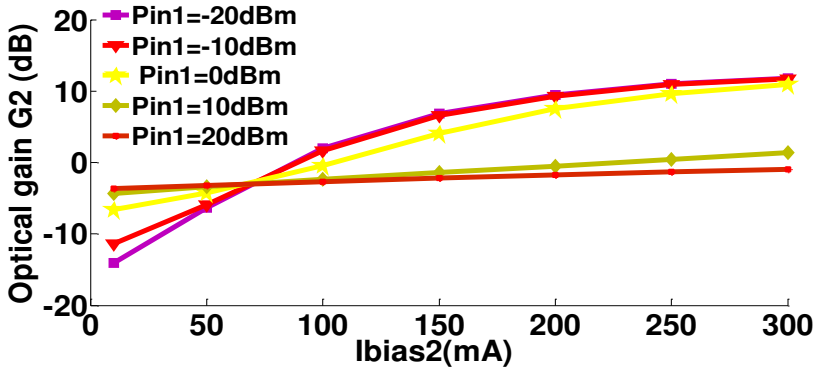

(b)

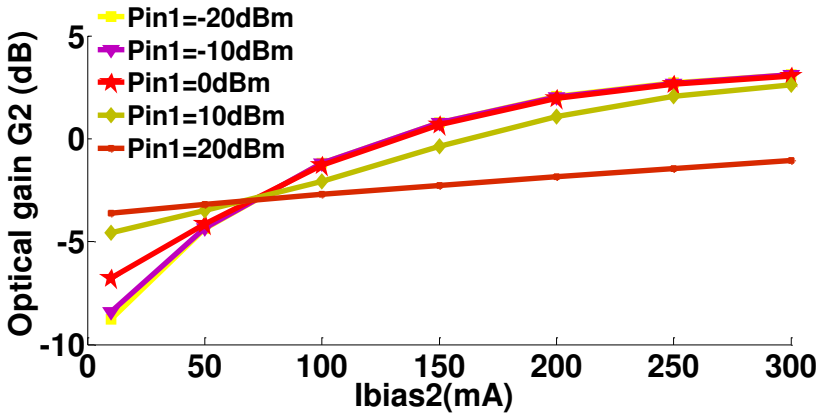

(c)

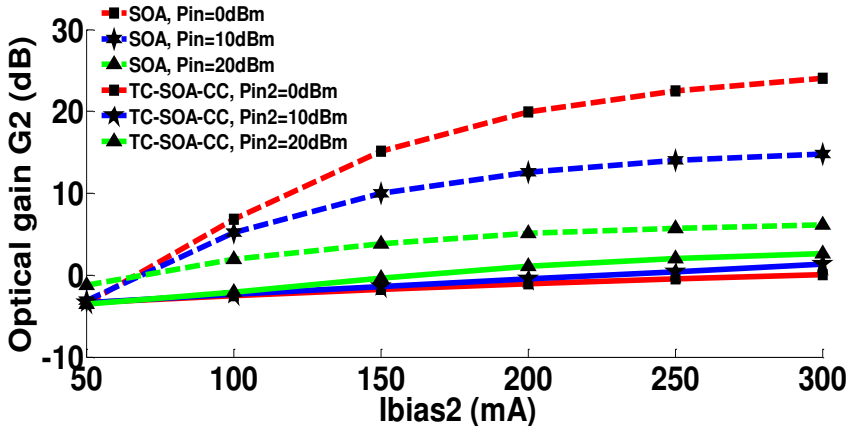

(d)

Figure 4- 26 : Optical gain G_2 of SOA_2 versus $I_{bias,2}$ with $I_{bias,1}$=280mA. (a) $P_{in,2}$ =-10dBm, (b) $P_{in,2}$ =10dBm, (c) $P_{in,2}$ = 20dBm, (d) $P_{in,1}$=10dBm

4.6.4 *Effect of carrier lifetime*

Figure 4- 27(a) shows $P_{tot,2}$ for the TC-SOA-CC and $P_{out,SOA}$ for the single SOA as function of input optical power $P_{in,1}$ for several values of $P_{in,2}$ using the same bias current I_{bias}=$I_{bias,2}$=50mA, and $I_{bias,1}$=280mA, the figure shows that we have an almost high input power to SOA_2 regardless of the input powers used for SOA_1 or SOA_2. Moreover, $P_{tot,2}$ is always higher than P_{out} using single SOA for all values of input optical power, this high power will cause the effective carrier lifetime of SOA_2 $\tau_{2(TC\text{-}SOA\text{-}CC\text{-}IM)}$ to be always smaller than the effective carrier lifetime of the single SOA $\tau_{(SOA\text{-}IM)}$ for all values of $P_{in,1}$ and $P_{in,2}$. Figure 4- 27(b) shows the ratio of the effective carrier lifetime of SOA_2 using TC-SOA-CC-IM over the effective carrier lifetime of the SOA-IM with $I_{bias,1}$=280mA and I_{bias}=$I_{bias,2}$=50mA. Here, the effective carrier lifetime for the single SOA can be calculated as given in [27], for SOA_2 of the TC-SOA-CC-IM, it can be derived from equation (4.26)

$$\frac{1}{\tau_2} = \frac{1}{\tau_c}\left(1 + \frac{G_2\left(P_{in,2} + P_{out,1}\right)}{P_{sat,2}}\right) \tag{4.31}$$

For the SOA-IM

$$\frac{1}{\tau} = \frac{1}{\tau_c}\left(1 + \frac{G \times P_{in}}{P_{sat}}\right) \tag{4.32}$$

As can be seen from Figure 4- 27(b), the ratio of τ_2/τ is shown for a wide range of input optical powers, we have a smaller effective carrier lifetime for the TC-SOA-CC in comparison with the single SOA, and this difference will help to explain the higher signal capacities that we will see using the TC-SOA-CC-IM.

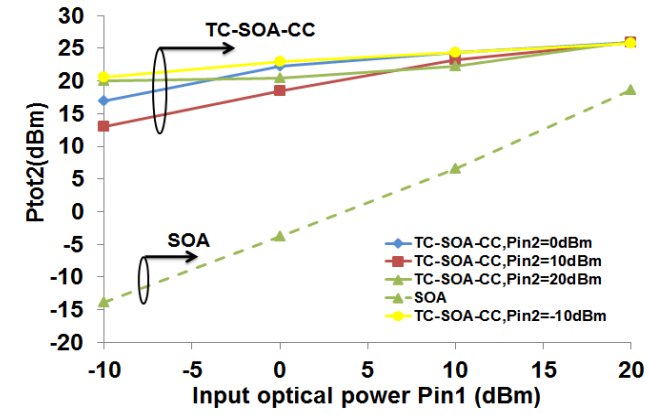

(a)

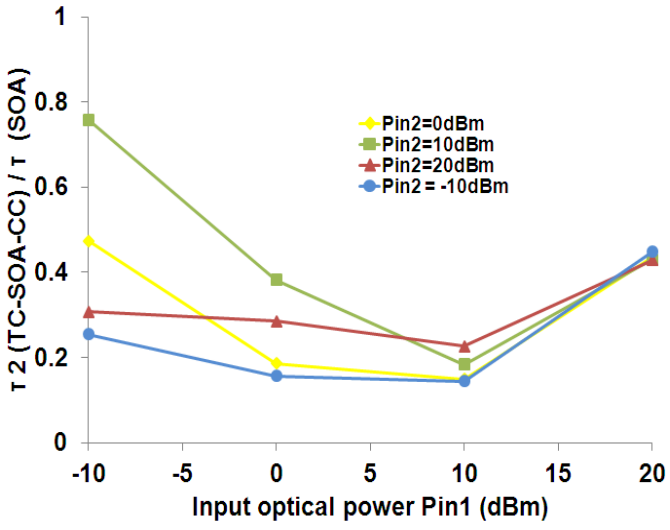

(b)

Figure 4- 27 : (a) $P_{tot,2}$ and $P_{out,SOA}$ as function of input optical power $P_{in,1}$ for several values of and $P_{in,2}$, (b) the ratio of $\tau_{e2(TC\text{-}SOA\text{-}CC\text{-}IM)}/\tau_{e(SOA\text{-}IM)}$ as function of $P_{in,1}$ for several values of $P_{in,2}$.

4.6.5 *Impact of bias current and optical input power on the Transmission performances*

The previously discussed results in the static study suggest that the improved transmission performance is possible using the TC-SOA-CC-IM in comparison with the single SOA for the IMDD-SMF system based on AMOOFDM. Therefore, the OFDM electrical driving current is injected in the SOA_2 in addition to the bias current $I_{bias,2}$, and the output optical signal $P_{out,2}$ produced from SOA_2 is considered to be the output modulated AMOOFDM signal that enters the optical fiber.

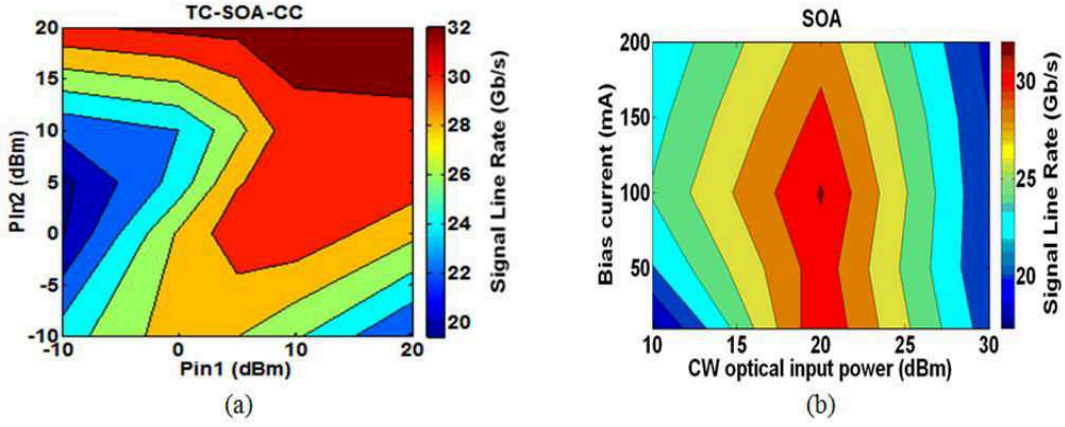

Figure 4- 28 : Contour plot of signal line rate. (a) TC-SOA-CC-IM with Ibias,1=280mA and Ibias,2=50mA. (c) Single SOA-IM.

Figure 4- 28 shows contour plots to demonstrate the achievable AMOOFDM transmission capacity of a 60km IMDD SMF transmission system for both the TC-SOA-CC-IM and the single SOA-IM. The peak-to-peak (PTP) driving current is set to 80mA and $\lambda_1=\lambda_2=1550$nm. Figure 4- 28(a) shows the contour plot as function of $P_{in,1}$ and $P_{in,2}$ and Figure 4- 28(b) shows the contour plot as function of optical input power and bias current for the single SOA. As seen from the contour plots in Figure 4- 28, the TC-SOA-CC-IM in comparison with the SOA-IM has much broader variation ranges of optical input power, over which higher signal line rates are achievable. It can be seen, to achieve signal bit rates of almost 30Gb/s, the SOA-IM requires a CW optical input power to vary in a 3 dB range between 19dBm to 21dBm, whilst the TC-SOA-CC-IM allows $P_{in,2}$ to vary in a 20dB range between 0dBm and 20dBm with $P_{in,1}$ having a value between 5dBm and 20dBm.

4.6.5.1 Signal line rate versus the input optical power Pin,1 and bias current Ibias,1

In addition to the impact of the bias current $I_{bias,2}$ of the SOA_2, it is also important to study the influence of the input optical power and bias current of the amplifier SOA_1 on the AMOOFDM transmission performance of a 60km IMDD

SMF transmission system for both the TC-SOA-CC-IM and the single SOA-IM. Figure 4- 29 shows the signal line rate versus the input optical power $P_{in,1}$ for several values of the bias current $I_{bias,1}$ (50, 150, 200 and 280mA) and for $P_{in,2}$=0dBm (Figure 4- 29(a)), $P_{in,2}$=10dBm (Figure 4- 29(b)) and 20dBm (Figure 4- 29(c)). The driving current peak-to-peak (PTP) is set to be 80mA and $\lambda_1=\lambda_2$=1550nm. In all what follows, the bias current $I_{bias,2}$=50mA for the TC-SOA-CC and I_{bias}=50mA for the single SOA. Based on previous results [27], the maximum signal rate using single SOA is achieved at I_{bias}=100mA, so it will always be shown to make a reasonable comparison. From Figure 4- 29(a)-(b), it can be seen that increasing $I_{bias,1}$ from 50mA till 280mA and $P_{in,1}$ from -10dBm till 20dBm improves the AMOOFDM transmission performance for both configurations. And we can also notice that for this wide range of $I_{bias,1}$, and $P_{in,1}$, the TC-SOA-CC-IM compared with the SOA-IM will end up producing a considerable improvement of the transmission performance. For instance, at low input optical power $P_{in,1}=P_{in,2}$=0dBm, using the TC-SOA-CC-IM, we can benefit of almost 70% increase in signal line rate. Under the strongly saturated optical gain region, $P_{in,1}$=20dBm, the quality of the modulated AMOOFDM are similar.

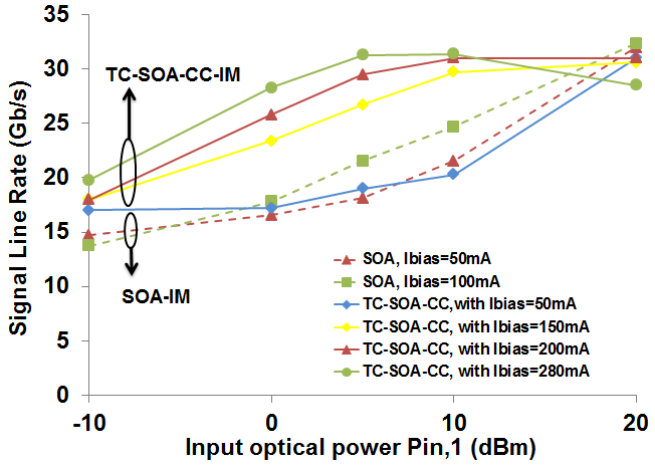

(a)

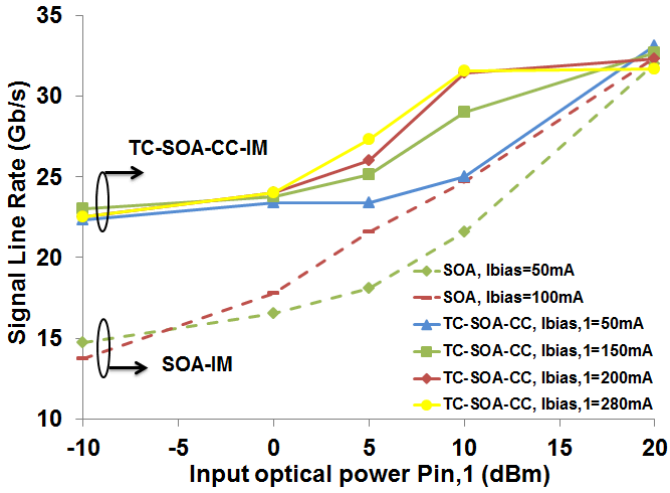

(b)

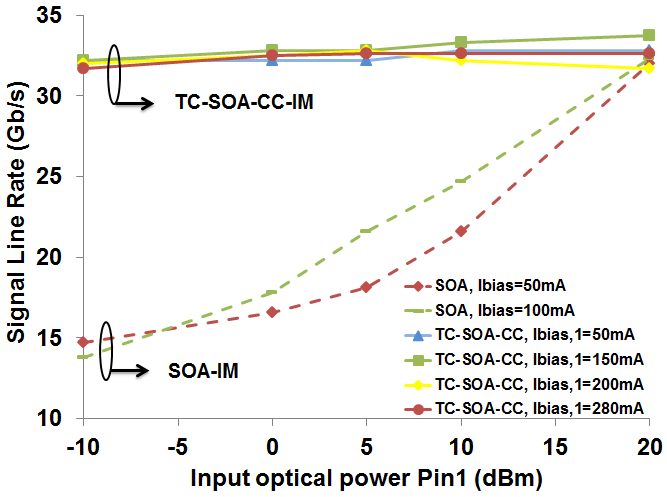

(c)

Figure 4- 29 : Signal line rate of TC-SOA-CC-IM and SOA-IM as a function of the input optical power $P_{in,1}$. (a) $P_{in,2}$=0dBm, (b) $P_{in,2}$=10dBm, (c) $P_{in,2}$=20dBm.

In Figure 4- 29(c), and for a wide range of $P_{in,1}$ varying between -10dBm and 20dBm, increasing $I_{bias,1}$ will result with a flat AMOOFDM transmission performance for the TC-SOA-CC-IM which is always greater than what's reached with a single SOA. This is because the superiority of the signal line rate for the TC-SOA-CC-IM at $P_{in,2}$=20dBm (Figure 4- 29(c)) compared with that obtained at $P_{in,2}$=10dBm (Figure 4- 29(b)) is due to the decrease of the effective carrier lifetime when you increase the power $P_{in,2}$ and to the increase of the linear gain-current curve as shown in Figure 4- 29(d). For instance, at $P_{in,1}$= -10dBm and $P_{in,2}$=20dBm , we can boost the signal line rate with almost 115% which will be more than twice the transmission performance offered by single SOA. This enhancement in system capacity is due to the lower effective carrier lifetime of SOA_2 in comparison with the one SOA configuration for a big range of $P_{in,1}$ as we have seen in Figure 4- 27.

4.6.6 *Signal line rate versus transmission distance*

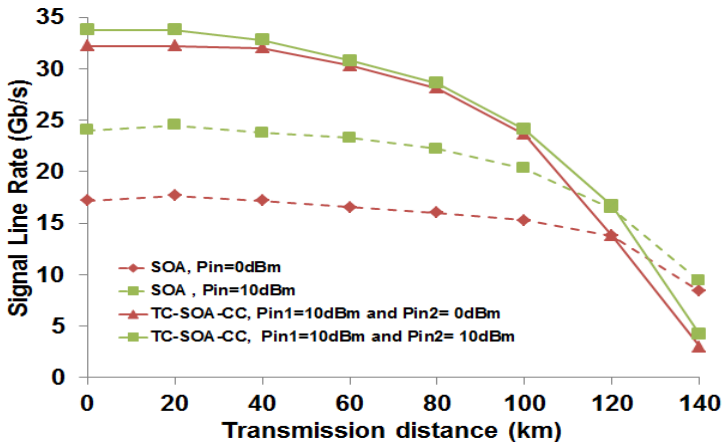

Figure 4- 30 : Signal transmission capacity versus reach performance of AMOOFDM signal for various transmission systems.

Having identified the optimum TC-SOA-CC-IM operating conditions including bias current, driving current PTP and CW input optical powers, the maximum achievable signal line rate of the AMOOFDM transmission system incorporating TC-SOA-CC-IM is investigated in this section. The numerical results are plotted in Figure 4- 30 where $I_{bias,2}$ = 50 mA, $I_{bias,1}$ = 280 mA, I_{bias}=50mA for the single SOA, the input optical power of the SOA_1 amplifier is $P_{in,1}$ = 10dBm and a driving current PTP of 80mA is used. For different input optical powers 0 and 10dBm (i.e $P_{in,2}$ for TC-SOA-CC), we have made a comparison between the performances of the TC-SOA-CC-IM with that of the single SOA-IM.

As shown in Figure 4- 30, the TC-SOA-CC-IM outperforms the SOA-IM in signal line rate for distances less than 120km. Very similar to those observed in the directly modulated lasers (DML)/SOA/RSOA/QDSOA-based SMF IMDD transmission system [63, 27, 44, 28], for the TC-SOA-CC-IM, Figure 4- 30 shows a CD-dominant performance region and a link loss-dominant performance region for transmission distances of less than 100km and greater than 100km, respectively. Over the first performance region, as expected from discussions in [63], significant performance differences are revealed among the intensity modulators, whilst their performance differences are abated considerably over the second performance region. In particular such an enhancement is more pronounced over the CD dominant performance region. For instance, at $P_{in,2}$=0dBm and 60km SMF, the TC-SOA-CC-IM supports approximately the double of the transmission performance corresponding to the SOA-IM. Figure 4-30 shows that, up to 120km, the performances supported by the TC-SOA-CC-IM for CW input optical power 0dBm are much better than those supported by the SOA-IM for 10dBm. This indicates that the TC-SOA-CC-IM is capable of supporting signal line rates higher than those corresponding to the SOA-IM by using 10dB lower input optical powers. Figure 4- 30 also shows that the TC-SOA-IM offers signal line rate almost identical for the two injected optical input powers $P_{in,2}$=0 and 10dBm. For longer transmission distances higher than 120km, the superiority of the SOA-IM over the TC-SOA-CC-IM is due to the fact that the TC-SOA-CC has gain-current curves with lower slopes (Figure 4- 26(d)) compared to single SOA, leading to lower signal ER, and thus higher signal degradation for the link loss dominant performance region.

To demonstrate the TC-SOA-CC-IM induced low ER for long transmission distance, Figure 4- 31 is plotted to compare the waveforms of the TC-SOA-CC-IM, SOA-IM and ideal-IM modulated AMOOFDM signals. The numerical results are plotted with $I_{bias,2}$=50mA, $I_{bias,1}$=280mA, $P_{in,1}$=$P_{in,2}$=10dBm, a driving current PTP of 80mA and for the SOA-IM the bias current and the input optical power are to be set to I_{bias}=50mA and P_{in}=10dBm, respectively. Figure 4-31 shows that the TC-SOA-CC-IM modulated waveform is attenuated compared to those corresponding to SOA and ideal intensity modulators. The ER associated with the TC-SOA-CC-IM leads to severe degradation in the signal quality and in particular for long transmission distance.

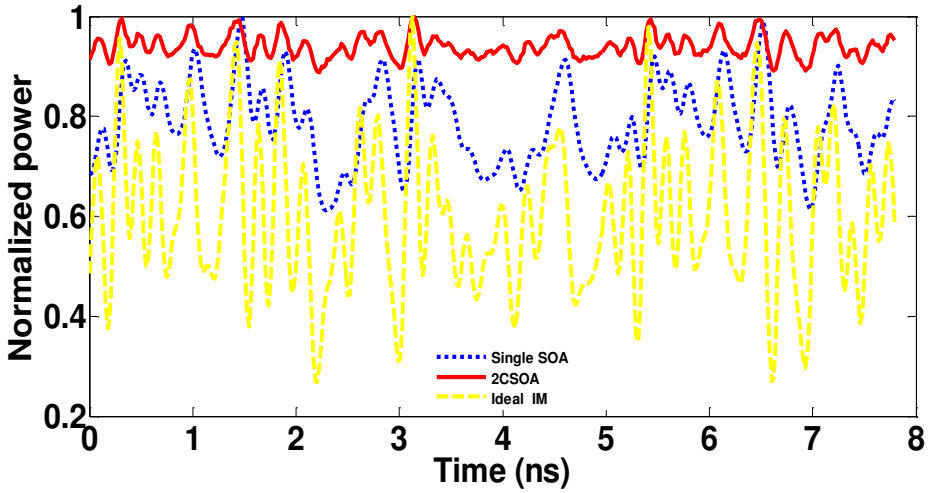

Figure 4- 31 : Normalized AMOOFDM signal waveforms generated by a TC-SOA-CC-IM, single SOA-IM and ideal-IM

4.6.7 *Impact of negative frequency chirp*

As mentioned for the QD-SOA in section 4.4.5.4, the SOA as an intensity modulator produces negative frequency chirp, and as in our configuration the SOA_2 plays the role of intensity modulator then this still holds well for the TC-SOA-CC-IM. To demonstrate the effectiveness of the aforementioned CD compensation approach for the SOA/TC-SOA-CC intensity modulated AMOOFDM signals in IMDD standard SMF transmission systems, in Figure 4-32 performance comparisons are made for the cases of including and excluding fiber CD. The numerical results are plotted in Figure 4- 32 where $I_{bias,2}$=50mA, $I_{bias,1}$=280mA, $P_{in,1}$=$P_{in,2}$=10dBm and a driving current PTP of 80mA is used. For the single SOA-IM the bias current and the input optical power are to be set to I_{bias}=50mA and P_{in}=10dBm, respectively. As it can be seen from Figure 4- 32, for long transmission distances, an improved transmission performance for the case of including fiber chromatic dispersion for the two intensity modulators is seen, and the TC-SOA-CC-IM have much stronger dispersion compensation capability compared to SOA-IM.

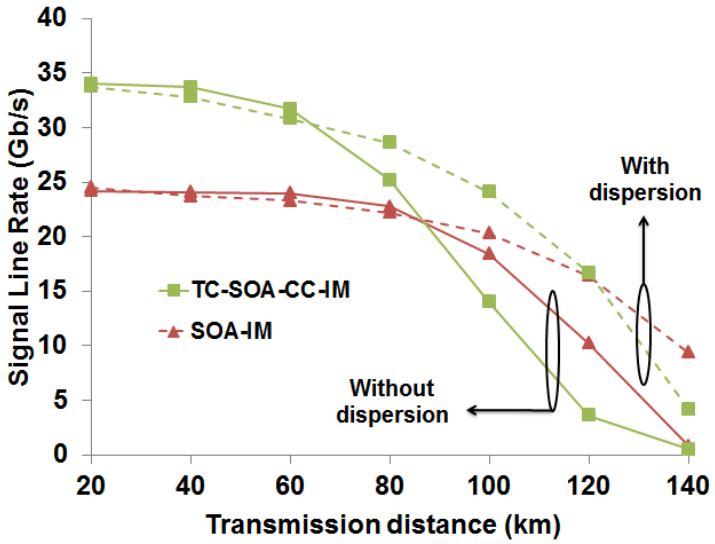

Figure 4- 32 : Signal line rate versus reach performance for the cases of including and excluding the CD.

In addition the use of TC-SOA-CC-IM is more effective regarding the capability to benefit from dispersion compensation for shorter distances starting at 60km SMF, whilst for the SOA-IM starting at 90km. It should be pointed out that, the SOA/TC-SOA-CC negative frequency chirp is a function of operating conditions, suggesting that such dispersion compensation technique is dynamically controllable.

4.7 Comparison between the three SOA structures

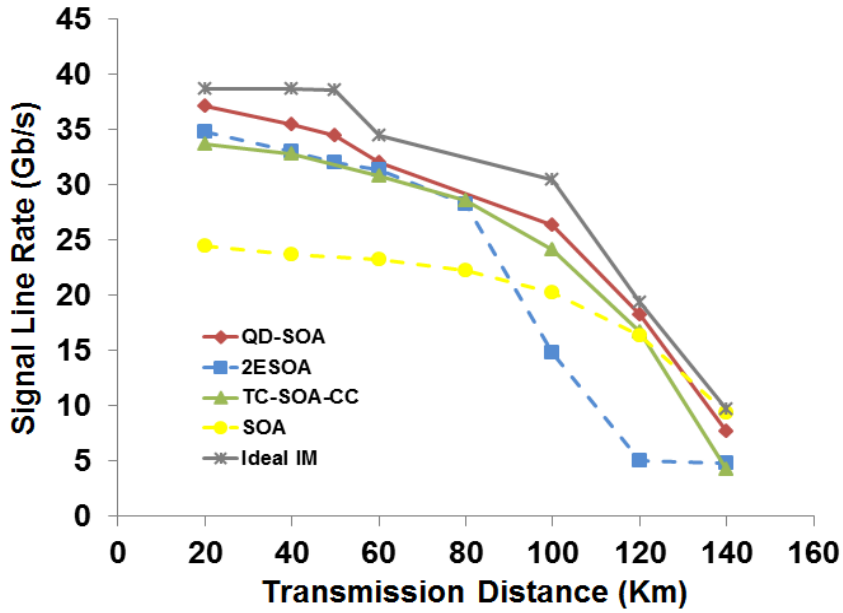

Figure 4- 33 : Signal line rate versus reach performance for five different IM configurations.

The figure above shows a comparison between the 3 different SOA configurations used in this chapter plus an SOA and an Ideal intensity modulator for an optical input power of 10 dBm. The results show that the best performance in terms of capacity is for that of the QD-SOA, the QD-SOA performance reached that of an ideal intensity modulator for 20 km transmission distance and for the transmission distances between 120 km and 140 km. The TC-SOA-CC modulator comes after the QD-SOA in performance, but the SOA will outperform it for distances beyond 120 km. The two electrode SOA performs as the TC-SOA-CC up to 80 km, after that we see a very sharp degradation due to the low signal extinction ratio of the 2E-SOA which generally degrades the performance for transmission distances beyond 100 km. The SOA performance is much less than the other configurations, but is better than the 2E-SOA for distances beyond 90 km and is better than the TC-SOA-CC for distances beyond 120 km.

4.8 Conclusion

Extensive explorations have been undertaken, for the first time, of the feasibility of utilizing QD-SOAs, two cascaded SOAs, and two electrode SOAs as intensity modulators for AMOOFDM IMDD systems for applications in next generation PONs. For the QD-SOA, taking into account the QD and WL effects, a theoretical QD-SOA-IM model has been developed, based on which optimum QD-SOA-IM operating conditions have been identified together with major physical factors considerably affecting the system performance. It has been shown that, in comparison with previously reported SOA-IMs, QD-SOA-IMs can not only considerably improve the AMOOFDM transmission performance but also broaden the optimum operating condition ranges. In particular, for achieving signal bit rates of >30Gb/s over >60km SMFs, QD-SOA-IMs allows a 10dB reduction in CW optical input powers injected into the modulator. In addition, QD-SOA-IMs can also be used to compensate the chromatic dispersion effect. Results have also shown that signal clipping and small signal extinction ratio play dominant roles in determining the maximum achievable AMOOFDM transmission performance.

As for the two cascaded SOAs, It has been shown that the TC-SOA-CC-IM in comparison with the SOA-IM has much broader variation range of optical input power, over which higher signal line rates are achievable. In addition, the TC-SOA-CC-IM is capable of supporting signal line rates higher than corresponding to the SOA-IM by using lower input optical powers, and it is also shown that at low input optical power, we can increase the signal line rate up to 115% which will be more than twice the transmission performance offered by single SOA. For transmission distances up to 120km, the performance supported by the TC-SOA-CC-IM for CW input optical power 0dBm is higher than that supported by the SOA-IM for 10dBm optical input power. For long transmission distances, the TC-SOA-CC-IM has much stronger CD compensation capability compared to the SOA-IM. In addition the TC-SOA-CC-IM is more robust to CD

compensation for shorter distances starting at 60km SMF, whilst for the SOA-IM starting at 90km. For future work, it is interesting to study the potential of the TC-SOA-CC to achieve non inverted wavelength conversion of an AMOOFDM signal with high efficiency since the all-optical inverted and non-inverted wavelength conversions feasibility has been demonstrated using TC-SOA-CC delivering an ER≥7dB over a wide range of wavelengths [100].

As for the two electrode SOAs, we have seen that using the 2E-SOA-IM we can have more than 30 Gb/s system capacity using 10 dB less optical input power which is more practical for optical transmission systems and less power consuming, we have also shown that using a 2E-SOA-IM we can use a 0 dBm optical input power and have a higher transmission performance in comparison with the SOA-IM with 10 dBm optical input power for transmission distances up to 90 Km.

These results demonstrate the potential of using the QD-SOA, TC-SOA-CC-IM, or 2E-SOA in future optical access networks utilizing AMOOFDM for high signal capacities and long transmission distances.

5 CONCLUSION AND PERSPECTIVE

5.1 Conclusion

The work presented in this manuscript, done in collaboration between ENIB - France and AUL - Lebanon, deals with the study of different SOA structures impact on the transmission of IMDD-OOFDM signals in the context of the access network. It was divided into two main parts. It started by an overview on IMDD-OOFDM transmission systems where, after a short presentation of the optical fiber networks evolution and some techniques applied to increase the capacity of optical access networks, we have discussed about the OFDM and IMDD-OOFDM modulation potentiality to improve the transmission capacity of such networks. We have also focused on the SOA characteristics and its interest for IMDD-OOFDM systems.

In the first part, in chapter 2, we have presented a comprehensive wideband time domain RSOA field based model implemented under ADS software. The model is fitted by optimization software to a commercial RSOA component of 750 µm length for a wide range of input powers and bias currents. We showed that we have a very good agreement between the model and the RSOA component in different static and dynamic configurations. In static regime, it was experimentally validated in terms of gain, NF, and output saturation power for a wide range of optical wavelengths, RSOA input powers, and bias currents. In dynamic regime, the RSOA model was validated in terms of electrical bandwidth, phase-amplitude coupling factor, harmonic and intermodulation distortions and XGM.

The RSOA model was then used in chapter 3 as part of a co-simulation platform for IMDD-OOFDM and OOFDM wavelength conversion transmission systems using MATLAB-ADS-VPIphotonics in which the platform is experimentally validated by measuring the EVM for a wide range of input powers, wavelengths, electrical signal bandwidths, and fiber transmission distances. Thanks to this co-simulation platform and our experimental setup, we analyzed the transmission performance in terms of optical input power, fiber length, ASE noise, electrical bandwidth, number of subcarriers, and single carrier or multicarrier transmission. We showed that by using an ideal optical preamplification, we could obtain a successful 6 GHz OFDM 16 QAM transmission at a data rate of 15.6 Gb/s. Moreover, we performed by simulation an AMOOFDM signal transmission over a 100 nm wavelength range. Results showed that a minimum transmission capacity of 8.9 Gb/s for fiber lengths up to 100 km can be reached. Furthermore, we showed an improvement up to 17.5 Gb/s thanks to a two electrode RSOA configuration in the case of 20 km SMF length. Finally, we experimentally demonstrated for the first time to the best of our knowledge the feasibility of performing wavelength conversion over 70 nm of OOFDM-16QAM optical signals using the XGM effect in an RSOA. AMOOFDM technique and preamplification permitted to increase the system capacity over 90 nm to at least 11 Gb/s for a 60 km SMF length.

In the second part of our work, in chapter 4, we investigated the feasibility of utilizing QD-SOAs, two cascaded SOAs, and two electrode SOAs as intensity modulators for AMOOFDM IMDD systems for applications in next generation PONs. For each configuration, a simplified model was derived. For the QD-SOA, optimum operating conditions were found in terms of optical input power and bias current, and the transmission capacity versus transmission distance up to 140 km was investigated. For the two-electrode SOA, optimum operating conditions were found in terms of electrode length and bias current distribution which were used to perform a high transmission capacity in function of the optical input power. The two cascaded SOA in a counter propagating configuration with AMOOFDM signals was explored in terms of optical input power. For these configurations, we have shown that, in comparison with previously reported SOA-IMs, QD-SOA-IMs can not only considerably improve the AMOOFDM transmission performance but also broaden the optimum operating condition ranges. In particular, for achieving signal bit rates of >30Gb/s over >60km SMFs, QD-SOA-IMs allows a 10dB reduction in CW optical input powers injected into the modulator. As for the two cascaded SOAs, It has been shown that the TC-SOA-CC-IM in comparison with the SOA-IM has much broader variation range of optical input power, over which higher signal line rates are achievable. As for the two electrode SOAs, we have shown that there are three optimum operating condition regions in which more than 30 Gb/s transmission capacity can be achieved. Finally, we have shown that the transmission capacity in function the transmission length of the TC-SOA-CC-IM comes after the QD-SOA-IM and the 2ESOA-IM performs as the TC-SOA-CC-IM up to 80 km.

5.2 Perspective and future work

This PHD work permitted us to develop experimental and simulation platforms for intensity modulation / direct detection transmission systems that will be very useful for further investigations. Actually, as we have seen that the SOA/RSOA electrical bandwidth is a major limiting factor of the OFDM signal transmission, using optical equalization associated with numerical techniques in order to better shape the filter response could be very interesting for future work since optical equalization has been reported to help in achieving up to 40 Gb/s transmission capacity with the RSOA [105]. Additionally, using the developed co-simulation platform will be helpful to optimize the SOA/RSOA structures for OFDM transmission for the cases of multi-electrode configuration and bias current distribution to further enhancement of the transmission capacity. Moreover, a study could be conducted to analyze the influence of the length or other SOA/RSOA parameters in order to increase the transmission performance in direct modulation and for wavelength conversion functionality. Finally, we would also like to study the SOA/RSOA configurations for different architectures of PON systems in which we evaluate the advantages or drawbacks of these

configurations in terms of optical power budget, complexity, cost efficiency, transmission capacity and distance reach.

GLOSSARY

AMOOFDM: Adaptively Modulated Optical Orthogonal Frequency Division Multiplexing
APD: Avalanche Photodiode
ASE: Amplified Spontaneous Emission
AWG: Arbitrary Waveform Generator
ADC: Analog to Digital Converter
AWGN: Additive white Gaussian noise
BL: Bit rate distance product
BER: Bit Error Rate
BPSK: Binary Phase Shift Keying
CD: Chromatic Dispersion
CP: Cyclic Prefix
CW: Continuous Wave
DFB: Distributed-Feedback
DPSK: Differential PSK
DQPSK: Differential Quadrature PSK
DSP: Digital Signal Processing
DBA: Dynamic Bandwidth Allocation
DAC: Digital to Analog Converter
EDFA: Erbium doped fiber amplifier
EVM: Error Vector Magnitude
EAM: Electro absorption modulator
ENOB: Effective number of bits
E/O: Electrical to optical converter
ES: Excited state
ER: Extinction ratio
FFT: Fast Fourier Transform
FP: Fabry-Perot
FWM: Four-wave mixing
FDM: Frequency Division Multiplexing.
GVD: Group-Velocity Dispersion
GS: Ground State
HD2: Second order harmonic distortion
HB: Harmonic Balance
QD: Qunatum Dot
QDash: Quantum Dash
QW: Quantum Well
QPSK: Quadrature Phase Shift Keying
QAM: Quadrature Amplitude Modulation
ICI: Intercarrier Interference
IFFT: Inverse Fast Fourier Transform

ISI: Inter-Symbol Interference
IMD: Intermodulation Distortion
IMDD: Intensity Modulation and Direct Detection
LAN: Local Area Network
LH: Long-Haul
LEF: Linewidth Enhancement Factor
LR-PON: Long Reach Passive Optical Network
MAN: Metropolitan Area Network
MZM: Mach-Zehnder Modulator
MMF: Multimode Fiber
MQW: Multiquantum Well
NF: Noise Figure
NG-PON: Next Generation Passive Optical Network
OFDM: Orthogonal Frequency Division Multiplexing
OSNR: Optical Signal to Noise Ratio
OOK: On Off Keying.
ONU: Optical Network Unit.
OSA: Optical Spectrum Analyzer.
OOFDM: Optical OFDM.
PAPR: Peak-to-Average Power Ratio
PMD: Polarization Mode Dispersion
PON: Passive Optical Network
RIN: Relative Intensity Noise
RMS: Root Mean Square
RSOA: Reflective SOA
SGM: Self-Gain Modulation
SNR: Signal to Noise Ratio
SOA: Semiconductor Optical Amplifier
SPM: Self-Phase Modulation
SPR: Self-Polarization Rotation
SMF: Standard Single Mode Fiber
TDM: Time Division Multiplexing
TE: Transverse Electric
TM: Transverse Magnetic
TWDM: Time and Wavelength Division Multiplexing.
TC-SOA-CC: Two Cascaded SOA in a Counter propagating configuration.
ULH: Ultra Long Haul
VSA: Vector Signal Analyzer
WAN: Wide Area Network
WDM: Wavelength Division Multiplexing
WL: Wetting Layer
XGM: Cross-Gain Modulation
XPM: Cross-Phase Modulation
XPolM: Cross-Polarization Modulation

2LREM: Second Level Rate Equation Model
3LREM: Third Level Rate Equation Model

REFERENCES

[1] G. P. Agrawal, Fiber-Optic Communication Systems, John Wiley & Sons, 1991.

[2] R. P. Giddings, E. Hugues-Salas and J. M. Tang, "30Gb/s Real-Time Triple Sub-band OFDM Transceivers for future PONs beyond 10Gb/s/λ," *Optical communication (ECOC2013),* 2013.

[3] T. Anfray, M.-E. Chaibi, D. Erasme, G. Aubin, P. Chanclou and C. Aupetit-Berthelemot, "Modulation OSSB-OFDM avec un D-EML pour l'extension de portée du réseau d'accès optique passif jusqu'à 31,7Gb/s," *Journées Nationales d'Optique Guidées JNOG2013, Volume: P168,* 2013.

[4] M. Deng, Y. Ling, X. Chen, R. Giddings, Y. Hong, X. Yi, K. Qiu and J. Tang, "Self-seeding-based 10Gb/s over 25km optical OFDM transmissions utilizing face-to-face dual-RSOAs at gain saturation," *Opt. Express,* vol. 22, no. 10, pp. 11954-11965, May 2014.

[5] P. Morel, "Modélisation des amplificateurs optiques à sémi-conducteurs : du composant au système," Mémoire de thèse, Laboratoire RESO ENIB/Brest,ED-SICMA, 2006.

[6] P. Morel and A. Sharaiha, "Wideband Time-Domain Transfer Matrix Model Equivalent Circuit for Short Pulse Propagation in Semiconductor Optical Amplifiers," *Quantum Electronics, IEEE Journal of,* vol. 45, no. 2, pp. 103-116, Feb 2009.

[7] M. Chen, J. He and L. Chen, "Real-Time Optical OFDM Long-Reach PON System Over 100 km SSMF Using a Directly Modulated DFB Laser," *J. Opt. Commun. Netw.,* vol. 6, no. 1, pp. 18-25, Jan 2014.

[8] *ICT-ALPHA project,* http://www.ict-alpha.eu/.

[9] T. Morioka, M. Jinno and H. Takara, "Innovative Future Optical Transport Network Technologies," NTT Technical Review, Vol. 9 No. 8 Aug. 2011.

[10] R. Rodes et al, "100 Gb/s Single VCSEL Data Transmission Link," *OFC, 2012, Paper PDP5D.*.

[11] [Online]. Available: IEEE 802.3, http://www.ieee802.org/3..

[12] J. Lee et al, "Serial 103.125 Gb/s Transmission over 1 km SSMF for Low-Cost, Short-Reach Optical Interconnects," *OFC, 2014, Paper PDP Th5A.5.*.

[13] T. Zuo et al, "O-band 400 Gbit/s Client Side Optical Transmission Link," *OFC, 2014, Paper M2E.4.*.

[14] J. C. Cartledge et al, "100 Gbit/s Using Intensity Modulation and Direct Detection," *ECOC, 2013, Paper We. 4. C. 3.*.

[15] T. Tanaka et al, "Experimental Demonstration of 448-Gbps+ DMT Transmission over 30-km SMF," *OFC,2014, Paper M2I.5.*.

[16] G. Raybon, "1-Tb/s dual-carrier 80-GBaud PDM-16QAM WDM transmission at 5.2 b/s/Hz over 3200 km," *Photonics Conference (IPC), IEEE, 23-27 Sept. 2012.*

[17] I. Darwazeh, T. Xu, T. Gui, Y. Bao and Z. Li, "Optical SEFDM System; Bandwidth Saving Using Non-Orthogonal Sub-Carriers," *Photonics Technology Letters, IEEE,* vol. 26, no. 4, pp. 352-355, Feb 2014.

[18] W. Shieh and I. Djordjevic, OFDM for optical communication, Academic Press, 2009.

[19] F. Saliou, P. Chanclou, B. Charbonnier, T. Duong, N. Genay, A. Gharba, J. Le Masson, C. Milion and M. Ouzzif, "SOA or EDFA amplifying 10Gbit/s OFDM signals for access networks," in *Optical Communication, 2009. ECOC '09. 35th*

European Conference on, 2009.

[20] O. O. Omomukuyo, "Orthogonal Frequency Division Multiplexing for Optical Access Networks," Ph.D. thesis, University College London, April 2013.

[21] N. A. Hussain, "A survey/ Development of Passive Optical Access Networks Technologies," *INTERNATIONAL JOURNAL OF ADVANCED RESEARCH,* 2014.

[22] J. Armstrong, "OFDM for Optical Communications," *Journal of Lightwave Technology,* vol. 27, no. 3, pp. 189-204, Feb 2009.

[23] K. Iwatsuki, "Convergence of Wireless and Wired Technologies towards Next Generation Access Networks," November 2010 - October 2013.

[24] L. A. Neto, M. Gay, L. Bramerie, C. Peucheret, Y. Frignac, J.-C. Simon, M. Thual, M. Joindot, C. Levallois, C. Paranthoen, S. Joshi, N. Chimot, F. Lelarge and P. Chanclou, "Beyond 25 Gbit/s Directly Modulated, Directly Detected OFDM Using Channel Flattening by a Fabry-Perot Filter," in *Optical Fiber Communication Conference*, 2015.

[25] R. P. Giddings, X. Q. Jin, E. Hugues-Salas, E. Giacoumidis, J. L. Wei and J. M. Tang, "Experimental demonstration of a record high 11.25Gb/s real-time optical OFDM transceiver supporting 25km SMF end-to-end transmission in simple IMDD systems," *Opt. Express,* vol. 18, no. 6, pp. 5541-5555, Mar 2010.

[26] T. Dong, Y. Bao, Y. Ji, A. Lau, Z. Li and C. Lu, "Bidirectional Hybrid OFDM-WDM-PON System for 40-Gb/s Downlink and 10-Gb/s Uplink Transmission Using RSOA Remodulation," *Photonics Technology Letters, IEEE,* vol. 24, no. 22, pp. 2024-2026, Nov 2012.

[27] J. L. Wei, A. Hamie, R. P. Giddings and J. M. Tang, "Semiconductor Optical Amplifier-Enabled Intensity Modulation of Adaptively Modulated Optical OFDM Signals in SMF-Based IMDD Systems," *Lightwave Technology, Journal of,* vol. 27, no. 16, pp. 3678-3688, Aug 2009.

[28] J. L. Wei, A. Hamie, R. P. Gidding, E. Hugues-Salas, X. Zheng, S. Mansoor and J. M. Tang, "Adaptively modulated optical OFDM modems utilizing RSOAs as intensity modulators in IMDD SMF transmission systems," *Opt. Express,* vol. 18, no. 8, pp. 8556-8573, Apr 2010.

[29] H. Khaleghi, "Influence des amplificateurs optiques à semi-conducteurs (SOA) sur la transmission cohérente de signaux optiques à format de modulation multi-porteuses (CO-OFDM)," 2013.

[30] B. Goebel, S. Hellerbrand, N. Haufe and N. Hanik, "PAPR reduction techniques for coherent optical OFDM transmission," in *Transparent Optical Networks, 2009. ICTON '09. 11th International Conference on*, 2009.

[31] C.-H. Lu and K.-M. Feng, "Reduction of high PAPR effect with FEC enhanced deep data clipping ratio in an optical OFDM system," in *Lasers and Electro-Optics Society, 2007. LEOS 2007. The 20th Annual Meeting of the IEEE*, 2007.

[32] R. Schmogrow, B. Nebendahl, M. Winter, A. Josten, D. Hillerkuss, S. Koenig, J. Meyer, M. Dreschmann, M. Huebner, C. Koos, J. Becker, W. Freude and J. Leuthold, "Error Vector Magnitude as a Performance Measure for Advanced Modulation Formats," *Photonics Technology Letters, IEEE,* vol. 24, no. 1, pp. 61-63, Jan 2012.

[33] Wiley, Wiley Encyclopedia of Electrical and Electronics Engineering, John Wiley & Sons, Inc., 1999.

[34] A. Royset, L. Bjerkan, D. Myhre and L. Hafskjaer, "Use of dispersive optical fibre for characterisation of chirp in semiconductor lasers," *Electronics Letters,* vol. 30, pp. 710-712(2), April 1994.

[35] L. Nelson, H. Kogelnik and P. Winzer, "Polarization mode dispersion and its impact on high bit-rate, fiber-optic communication systems," in *Lasers and*

Electro-Optics, 2004. (CLEO). Conference on, 2004.

[36] "http://www.radio-electronics.com/info/data/semicond/photo_diode/structures-materials.php," [Online].

[37] K. Shiba, T. Nakata, T. Takeuchi, T. Sasaki and K. Makita, "10 Gbit/s asymmetric waveguide APD with high sensitivity of -30dBm," *Electronics Letters,* vol. 42, no. 20, pp. 1177-1178, September 2006.

[38] M. Nada, Y. Muramoto, H. Yokoyama, T. Ishibashi and S. Kodama, "High-sensitivity 25 Gbit/s avalanche photodiode receiver optical sub-assembly for 40 km transmission," *Electronics Letters,* vol. 48, no. 13, pp. 777-778, June 2012.

[39] M. Achouche, A. Konczykowska, P. Brindel, F. George, L. Pierre, F. Blache, S. Vuye, H. Gariah and D. Carpentier, "–28 dBm receiver sensitivity using uni-travelling-carrier photodiode and decision flip-flop," *Eur. Conf. Exhib. Opt. Commun.,* Stockholm, Sweden, 2014.

[40] S. Takashima, H. Nakagawa, S. Kim, F. Goto, M. Okayasu and H. Inoue, "40-Gbit/s receiver with -21 dBm sensitivity employing filterless semiconductor optical amplifier," in *Optical Fiber Communications Conference, 2003. OFC 2003*, 2003.

[41] B. Mason, S. Chandrasekhar, A. Ougazzaden, C. Lentz, J. Geary, L. Buhl, L. Peticolas, K. Glogovsky, J. Freund, L. Reynolds, G. Przybylek, F. Walters, A. Sirenko, J. Boardman, T. Kercher, M. Rader, J. Grenko, D. Monroe and L. Ketelsen, "Photonic integrated receiver for 40â€…Gbit/s transmission," *Electronics Letters,* vol. 38, pp. 1196-1197(1), September 2002.

[42] R. H. Walden, "Analog-to-Digital Conversion in the Early Twenty-First Century," in *Wiley Encyclopedia of Computer Science and Engineering*, John Wiley & Sons, Inc., 2007.

[43] A. Khilo, S. J. Spector, M. E. Grein, A. H. Nejadmalayeri, C. W. Holzwarth, M. Y. Sander, M. S. Dahlem, M. Y. Peng, M. W. Geis, N. A. DiLello, J. U. Yoon, A. Motamedi, J. S. Orcutt, J. P. Wang, C. M. Sorace-Agaskar, M. A. Popovic, J. Sun, G.-R. Zhou, H. Byun, J. Chen, J. L. Hoyt, H. I. Smith, R. J. Ram, M. Perrott, T. M. Lyszczarz, E. P. Ippen and F. X. Kartner, "Photonic ADC: overcoming the bottleneck of electronic jitter," *Opt. Express,* vol. 20, no. 4, pp. 4454-4469, Feb 2012.

[44] A. Hamie, M. Hamze, J. L. Wei, A. Sharaiha and J. M. Tang, "Theoretical investigations of quantum-dot semiconductor optical amplifier enabled intensity modulation of adaptively modulated optical OFDM signals in IMDD PON systems," *Opt. Express,* vol. 19, no. 25, pp. 25696-25711, Dec 2011.

[45] M. J. Connelly, Semiconductor optical amplifiers, Kluwer Academic Publishers, 2009.

[46] D. M. Baney, P. Gallion and R. S. Tucker, "Theory and Measurement Techniques for the Noise Figure of Optical Amplifiers," *Optical Fiber Technology ,* vol. 6, no. 2, pp. 122-154, 2000.

[47] L. Occhi, L. Schares and G. Guekos, "Phase modeling based on the alpha-factor in bulk semiconductor optical amplifiers," *Selected Topics in Quantum Electronics, IEEE Journal of,* vol. 9, no. 3, pp. 788-797, May 2003.

[48] L. Occhi, "Semiconductor Optical Amplifiers made of Ridge Waveguide Bulk InGaAsP/InP: Experimental Characterisation and Numerical Modelling of Gain, Phase, and Noise," Zurich 2002.

[49] H.-S. Kim, B.-S. Choi, K.-S. Kim, D. C. Kim, O.-K. Kwon and D.-K. Oh, "Improvement of modulation bandwidth in multisection RSOA for colorless WDM-PON," *Opt. Express,* vol. 17, no. 19, pp. 16372-16378, Sep 2009.

[50] B. Schrenk, G. De Valicourt, M. Omella, J. Lazaro, R. Brenot and J. Prat, "Direct 10-Gb/s Modulation of a Single-Section RSOA in PONs With High Optical

Budget," *Photonics Technology Letters, IEEE,* vol. 22, no. 6, pp. 392-394, March 2010.

[51] A. Agata and Y. Horiuchi, "RSOA-Based 10Gb/s WDM PON using FEC and MLSE equalizers," *in Optical Fiber Communication Conference .,* Optical Society of America, 2010..

[52] G. Cossu, F. Bottoni, R. Corsini, M. Presi and E. Ciaramella, "40 Gb/s Single R-SOA Transmission by Optical Equalization and Adaptive OFDM," *Photonics Technology Letters, IEEE,* vol. 25, no. 21, pp. 2119-2122, Nov 2013.

[53] H. K. Shim, K. Y. Cho, U. H. Hong and Y. C. Chung, "Transmission of 40-Gb/s QPSK upstream signal in RSOA-based coherent WDM PON using offset PDM technique," *Opt. Express,* vol. 21, no. 3, pp. 3721-3725, Feb 2013.

[54] T. Duong, N. Genay, P. Chanclou, B. Charbonnier, A. Pizzinat and R. Brenot, "Experimental demonstration of 10 Gbit/s upstream transmission by remote modulation of 1 GHz RSOA using adaptively modulated optical OFDM for WDM-PON single fiber architecture," *Eur. Conf. Opt. Commun.,* Brussels, Belgium, Sep. 2008, Paper Th. 3.F. 1..

[55] A. Bogoni, L. Poti, C. Porzi, M. Scaffardi, P. Ghelfi and F. Ponzini, "Modeling and measurement of noisy SOA dynamics for ultrafast applications," *Selected Topics in Quantum Electronics, IEEE Journal of,* vol. 10, no. 1, pp. 197-205, Jan 2004.

[56] W. Li, G. Chen, W.-P. Huang and X. Li, "An advanced quasi-3D model for semiconductor optical amplifiers," in *Electrical and Computer Engineering, 2004. Canadian Conference on*, 2004.

[57] W. Mathlouthi, P. Lemieux, M. Salsi, A. Vannucci, A. Bononi and L. Rusch, "Fast and Efficient Dynamic WDM Semiconductor Optical Amplifier Model," *Lightwave Technology, Journal of,* vol. 24, no. 11, pp. 4353-4365, Nov 2006.

[58] J. Chi, L. Chao and M. K. Rao, "Time-domain large-signal investigation on nonlinear interactions between an optical pulse and semiconductor waveguides," *Quantum Electronics, IEEE Journal of,* vol. 37, no. 10, pp. 1329-1336, Oct 2001.

[59] M. Connelly, "Wideband dynamic numerical model of a tapered buried ridge stripe semiconductor optical amplifier gate," *Circuits, Devices and Systems, IEE Proceedings -,* vol. 149, no. 3, pp. 173-178, 2002.

[60] R. Gutierrez-Castrejon and M. Duelk, "Uni-directional time-domain bulk SOA Simulator considering carrier depletion by amplified spontaneous emission," *Quantum Electronics, IEEE Journal of,* vol. 42, no. 6, pp. 581-588, Jun 2006.

[61] F. Devaux, Y. Sorel and J.-F. Kerdiles, "Simple measurement of fiber dispersion and of chirp parameter of intensity modulated light emitter," *Lightwave Technology, Journal of,* vol. 11, no. 12, pp. 1937-1940, Dec 1993.

[62] A. Sharaiha, "Amplificateurs optiques à sémi-conducteurs," Cours Master PHOT-IN, ENIB, 2009-2010.

[63] J. Tang and K. Shore, "30-gb/s signal transmission over 40-km directly modulated DFB-laser-based single-mode-fiber links without optical amplification and dispersion compensation," *Lightwave Technology, Journal of,* vol. 24, no. 6, pp. 2318-2327, June 2006.

[64] J. Tang, P. Lane and K. Shore, "High-speed transmission of adaptively modulated optical OFDM signals over multimode fibers using directly Modulated DFBs," *Lightwave Technology, Journal of,* vol. 24, no. 1, pp. 429-441, Jan 2006.

[65] F. Ohman, S. Bischoff, B. Tromborg and J. Mork, "Noise and regeneration in semiconductor waveguides with saturable gain and absorption," *Quantum Electronics, IEEE Journal of,* vol. 40, no. 3, pp. 245-255, March 2004.

[66] C. Caillaud, P. Chanclou, F. Blache, P. Angelini, B. Duval, P. Charbonnier, D. Lanteri, G. Glastre and M. Achouche, "Integrated SOA-PIN Detector for High-

Speed Short Reach Applications," *Lightwave Technology, Journal of,* vol. 33, no. 8, pp. 1596-1601, April 2015.

[67] A. Gharba, "OFDM et allocation des ressources dans les nouvelles générations des reseaux d'acces optiques pour des systèmes mono et multi-utilisateurs," 2012.

[68] A. B. Carlson, Communication Systems: An Introduction to Signals and noise in electrical communication, New York: McGraw-Hill, 1986.

[69] N. Jolley, H. Kee, P. Pickard, J. Tang and K. Cordina, "Generation and propagation of a 1550 nm 10 Gbit/s optical orthogonal frequency division multiplexed signal over 1000m of multimode fibre using a directly modulated DFB," in *Optical Fiber Communication Conference, 2005. Technical Digest. OFC/NFOEC*, 2005.

[70] J. Wei, X. Jin and J. Tang, "The Influence of Directly Modulated DFB Lasers on the Transmission Performance of Carrier-Suppressed Single-Sideband Optical OFDM Signals Over IMDD SMF Systems," *Lightwave Technology, Journal of,* vol. 27, no. 13, pp. 2412-2419, July 2009.

[71] J. Tang and K. Shore, "Strong picosecond optical pulse propagation in semiconductor optical amplifiers at transparency," *Quantum Electronics, IEEE Journal of,* vol. 34, no. 7, pp. 1263-1269, Jul 1998.

[72] L. Guo and M. Connelly, "A novel approach to all-optical wavelength conversion by utilizing a reflective semiconductor optical amplifier in a co-propagation scheme," *Optics Communications ,* vol. 281, no. 17, pp. 4470-4473, 2008.

[73] C. Arellano and J. Prat, "Semiconductor optical amplifiers in access networks," in *Transparent Optical Networks, 2005, Proceedings of 2005 7th International Conference*, 2005.

[74] J. Kim, C. Meuer, D. Bimberg and G. Eisenstein, "Numerical Simulation of Temporal and Spectral Variation of Gain and Phase Recovery in Quantum-Dot Semiconductor Optical Amplifiers," *Quantum Electronics, IEEE Journal of,* vol. 46, no. 3, pp. 405-413, March 2010.

[75] T. Berg, S. Bischoff, I. Magnusdottir and J. Mork, "Ultrafast gain recovery and modulation limitations in self-assembled quantum-dot devices," *Photonics Technology Letters, IEEE,* vol. 13, no. 6, pp. 541-543, June 2001.

[76] T. Akiyama, M. Ekawa, M. Sugawara, K. Kawaguchi, H. Sudo, A. Kuramata, H. Ebe and Y. Arakawa, "An ultrawide-band semiconductor optical amplifier having an extremely high penalty-free output power of 23 dBm achieved with quantum dots," *Photonics Technology Letters, IEEE,* vol. 17, no. 8, pp. 1614-1616, Aug 2005.

[77] A. Rostami, H. Nejad, R. Qartavol and H. Saghai, "Tb/s Optical Logic Gates Based on Quantum-Dot Semiconductor Optical Amplifiers," *Quantum Electronics, IEEE Journal of,* vol. 46, no. 3, pp. 354-360, March 2010.

[78] M. Sugawara, T. Akiyama, N. Hatori, Y. Nakata, H. Ebe and H. Ishikawa, "Quantum-dot semiconductor optical amplifiers for high-bit-rate signal processing up to 160 Gb s -1 and a new scheme of 3R regenerators," *Measurement Science and Technology,* vol. 13, no. 11, p. 1683, 2002.

[79] O. Qasaimeh, "Effect of inhomogeneous line broadening on gain and differential gain of quantum dot lasers," *Electron Devices, IEEE Transactions on,* vol. 50, no. 7, pp. 1575-1581, July 2003.

[80] M. Sugawara, H. Ebe, N. Hatori, M. Ishida, Y. Arakawa, T. Akiyama, K. Otsubo and Y. Nakata, "Theory of optical signal amplification and processing by quantum-dot semiconductor optical amplifiers," *Phys. Rev. B,* vol. 69, p. 235332, Jun 2004.

[81] O. Qasaimeh, "Novel Closed-Form Model for Multiple-State Quantum-Dot Semiconductor Optical Amplifiers," *Quantum Electronics, IEEE Journal of,* vol. 44, no. 7, pp. 652-657, July 2008.

[82] O. Qasaimeh, "Optical gain and saturation characteristics of quantum-dot semiconductor optical amplifiers," *Quantum Electronics, IEEE Journal of,* vol. 39, no. 6, pp. 793-798, June 2003.

[83] H. Sun, Q. Wang, H. Dong and N. Dutta, "XOR performance of a quantum dot semiconductor optical amplifier based Mach-Zehnder interferometer," *Opt. Express,* vol. 13, no. 6, pp. 1892-1899, Mar 2005.

[84] H. Sun, Q. Wang, H. Dong and N. K. Dutta, "All-optical logic performance of quantum-dot semiconductor amplifier-based devices," *Microwave and Optical Technology Letters,* vol. 48, no. 1, pp. 29-35, 2006.

[85] T. W. Berg, J. Mork and J. M. Hvam, "Gain dynamics and saturation in semiconductor quantum dot amplifiers," *New Journal of Physics,* vol. 6, no. 1, p. 178, 2004.

[86] J. L. Wei, X. L. Yang, R. P. Giddings and J. M. Tang, "Colourless adaptively modulated optical OFDM transmitters using SOAs as intensity modulators," *Opt. Express,* vol. 17, no. 11, pp. 9012-9027, May 2009.

[87] G. Agrawal and N. Olsson, "Self-phase modulation and spectral broadening of optical pulses in semiconductor laser amplifiers," *Quantum Electronics, IEEE Journal of,* vol. 25, no. 11, pp. 2297-2306, Nov 1989.

[88] A. Mecozzi and J. Mork, "Saturation effects in nondegenerate four-wave mixing between short optical pulses in semiconductor laser amplifiers," *Selected Topics in Quantum Electronics, IEEE Journal of,* vol. 3, no. 5, pp. 1190-1207, Oct 1997.

[89] N. Olsson, "Lightwave systems with optical amplifiers," *Lightwave Technology, Journal of,* vol. 7, no. 7, pp. 1071-1082, Jul 1989.

[90] T. Newell, D. Bossert, A. Stintz, B. Fuchs, K. Malloy and L. Lester, "Gain and linewidth enhancement factor in InAs quantum-dot laser diodes," *Photonics Technology Letters, IEEE,* vol. 11, no. 12, pp. 1527-1529, Dec 1999.

[91] B. Dagens, A. Markus, J. Chen, J. G. Provost, D. Make, O. Le Gouezigou, J. Landreau, A. Fiore and B. Thedrez, "Giant linewidth enhancement factor and purely frequency modulated emission from quantum dot laser," *Electronics Letters,* vol. 41, no. 6, pp. 323-324, March 2005.

[92] G. Sun, J. Khurgin and R. A. Soref, "Design of quantum-dot lasers with an indirect bandgap short-period Superlattice for reducing the linewidth enhancement factor," *Photonics Technology Letters, IEEE,* vol. 16, no. 10, pp. 2203-2205, Oct 2004.

[93] S. Schneider, P. Borri, W. Langbein, U. Woggon, R. Sellin, D. Ouyang and D. Bimberg, "Linewidth enhancement factor in InGaAs quantum-dot amplifiers," *Quantum Electronics, IEEE Journal of,* vol. 40, no. 10, pp. 1423-1429, Oct 2004.

[94] X. Li and G. Li, "Static Gain, Optical Modulation Response, and Nonlinear Phase Noise in Saturated Quantum-Dot Semiconductor Optical Amplifiers," *Quantum Electronics, IEEE Journal of,* vol. 45, no. 5, pp. 499-505, May 2009.

[95] J. L. Wei, A. Hamie and J. M. Tang, "Optimization and comparison of the transmission performance of RSOA/SOA intensity-modulated optical OFDM signals for WDM-PONs," in *Optical Fiber Communication (OFC), collocated National Fiber Optic Engineers Conference, 2010 Conference on (OFC/NFOEC)*, 2010.

[96] R. P. Giddings, E. Hugues-Salas, X. Q. Jin, J. L. Wei and J. M. Tang, "Experimental Demonstration of Real-Time Optical OFDM Transmission at 7.5 Gb/s Over 25-km SSMF Using a 1-GHz RSOA," *Photonics Technology Letters, IEEE,* vol. 22, no. 11, pp. 745-747, June 2010.

[97] R. Brenot, J.-G. Provost, O. Legouezigou, J. Landreau, F. Pommereau, F. Poingt, L. Legouezigou, E. Derouin, O. Drisse, B. Rousseau, F. Martin, F. Lelarge and G. H. Duan, "High modulation bandwidth reflective SOA for optical access

networks," in *Optical Communication (ECOC), 2007 33rd European Conference and Ehxibition of*, 2007.

[98] A. Sharaiha and A. Hamie, "Comprehensive analysis of two cascaded semiconductor optical amplifiers for all-optical switching operation," *Lightwave Technology, Journal of,* vol. 22, no. 3, pp. 850-858, March 2004.

[99] A. Hamie, A. Sharaiha, M. Guegan and B. Pucel, "All-optical logic NOR gate using two-cascaded semiconductor optical amplifiers," *Photonics Technology Letters, IEEE,* vol. 14, no. 10, pp. 1439-1441, Oct 2002.

[100] A. Hamie, A. Sharaiha, M. Guegan and J. Le Bihan, "All-optical inverted and noninverted wavelength conversion using two-cascaded semiconductor optical amplifiers," *Photonics Technology Letters, IEEE,* vol. 17, no. 6, pp. 1229-1231, June 2005.

[101] A. Hamie, A. Sharaiha, M. Guegan, J. Le Bihan and A. Hamze, "All-optical logic or gate using two cascaded semiconductor optical amplifiers," *Microwave and Optical Technology Letters,* vol. 49, no. 7, pp. 1568-1570, 2007.

[102] A. Hamie, A. Sharaiha, M. Guegan, J. L. Bihan and A. Hamze, "Small-signal analysis of two cascaded semiconductor optical amplifiers in a counterpropagating configuration," *Optics Communications ,* vol. 281, no. 20, pp. 5183-5188, 2008.

[103] X. Zheng, J. L. Wei and J. M. TANG, "Transmission performance of adaptivelymodulated optical OFDM modems using subcarrier modulation over SMF IMDD links foraccess and metropolitan area networks," *Opt. Express,* vol. 16, no. 25, pp. 20427-20440, Dec 2008.

[104] J. M. Tang and K. Shore, "Maximizing the Transmission Performance of Adaptively Modulated Optical OFDM Signals in Multimode-Fiber Links by Optimizing Analog-to-Digital Converters," *Lightwave Technology, Journal of,* vol. 25, no. 3, pp. 787-798, March 2007.

[105] G. Cossu, F. Bottoni, R. Corsini, M. Presi and E. Ciaramella, "40 Gb/s Single R-SOA Transmission by Optical Equalization and Adaptive OFDM," vol. 25, no. 21, Nov,2013.

[106] G. de VALICOURT, "Conception, fabrication et évaluation de modulateurs déportés pour les réseaux d'accès et radio sur fibre," 2011.

[107] T. Muciaccia, F. Gargano and V. M. N. Passaro, "Passive Optical Access Networks: State of the Art and Future Evolution," *Photonics,* 2014.

[108] G. Cossu, F. Bottoni, R. Corsini, M. Presi and E. Ciaramella, "40 Gb/s Single R-SOA Transmission by Optical Equalization and Adaptive OFDM," vol. 25, no. 21, Nov,2013.

PUBLICATIONS

International Journals

[1] A. Hamié, **M. Hamze**, J. L. Wei, A. Sharaiha, and J. M. Tang, " Theoretical investigations of quantum-dot semiconductor optical amplifier enabled intensity modulation of adaptively modulated optical OFDM signals in IMDD PON systems", Optics Express, Vol. 19, Issue 25, pp. 25696-25711 (2011).

[2] Ali Hamié, **Mohamad Hamze**, Haidar Taki, Layaly Makouk, Ammar Sharaiha, Ali Alaeddine, Ali Al Housseini, Elias Giacoumidis and Jianming Tang, "Two cascaded SOAs used as intensity modulators for adaptively modulated optical OFDM signals in optical access networks", Opt Express. 2014 Jun 30; 22(13):15763-77.

International Conferences

[1] Ali Hamie, **M. Hamzé**, Jinlong Wei, Jianming Tang, A. Sharaiha," Improved Transmission Performance of Adaptively Modulated OFDM Signals Using Quantum Dot Semiconductor Optical Amplifier Intensity Modulators ", Proceedings of PIERS 2011 in Suzhou, September 12-16, 2011.

[2]Ali Hamie, **M. Hamzé**, Jinlong Wei, Jianming Tang, Pascal Morel, Mikael Guegan and Ammar Sharaiha, "Intensity Modulation of Optical OFDM Signals Using Low-Cost Semiconductor Laser Devices", Green Radio-over-Fibre and All Optical Technologies for Wireless Access Networks (GROWAN) 2011, Brest, France

[3] **M. Hamzé**, A. Hamié, J. L. Wei, J. M. Tang, A. Sharaiha, M. Guégan and A. Alaeddine, " Significantly Improved Optical OFDM Transmission Performances with 10dB Reduced Optical Input Powers by Quantum Dot SOA Intensity Modulators", Broadband Networks and Fast Internet (RELABIRA), 2012, Baabda, Lebanon.

[4] **M. Hamze** , Ammar, Sharaiha , Ali Hamie ,Mikael Guegan, "XGM Wavelength Conversion of an Optical OFDM Signal in a RSOA over a 90 nm Range", PIERS 2013, 112-15 August in Stockholm, SWEDEN.

[5] H. Taki, **M. Hamzé**, A. Hamié, A. Sharaiha, A. Alaeddine, P. Morel, M. Guégan “Adaptively Modulated Optical OFDM Transmission using two cascaded SOAs for optical access networks” for IEEE ICM2013 - Special Session - Optical Communications, 15-18 December, Beyrouth – Lebanon.

[6] **Mohamad Hamze**; Ali Hamie; Ammar Sharaiha; Jianming Tang , “Theoretical and numerical study of an AMOOFDM IMDD transmission system using different SOA structures”, 21st LAAS International Science Conference, Saint Joseph University (USJ), Beirut, Lebanon, April 15-17, 2015

National Conferences

[1] **M. Hamzé**, Ammar Sharaiha, Mikael Guégan et Ali Hamié, " Conversion en longueur d’onde large bande de signaux optiques DMT-OOFDM utilisatnt la modulation croisée du gain d’un SOA", Journées Nationales d'Optique Guidée (JNOG) 2012 Lyon, France.

[2] **Mohamad Hamzé**, Ammar Sharaiha, Pascal Morel, Mikael Guégan, Ali Hamié " Validation expérimentale d’une chaine de co-simulation d’émission et de réception de formats IM-OFDM à base de RSOA ", submitted to JNOG 2015.

LIST OF FIGURES

LIST OF TABLES

APPENDIX-A

RSOA Data sheet

Device #03047

CIP
Centre for Integrated Photonics

RL SOA

Measured device results on fully packaged device. CW and small signal data provided

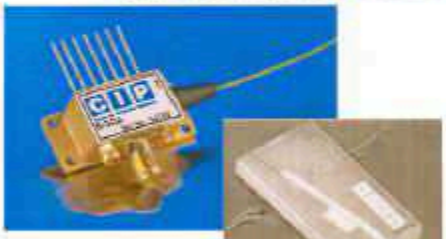

Linear Results Summary

Device tested at 80mA and 20°C at 1550nm and optical input power of -30dBm. Tabulated results and sample ASE curve shown below.

Parameter	1550nm
Integrated ASE	0.7mW
Gain	20.4dB
PDG	1.6dB
NF	6.2dB
Gain Ripple	0.2dB
Psat	3.6dBm

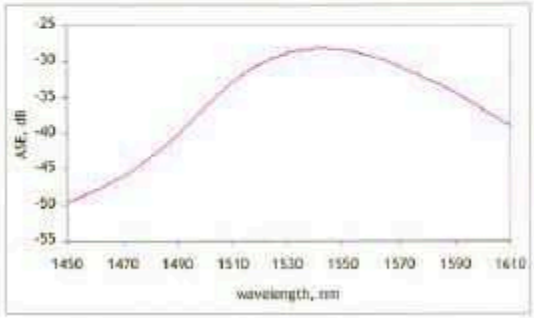

CIP Device Results Sheet

Device #03047

Centre for Integrated Photonics

Electrical bandwidth at 20°C

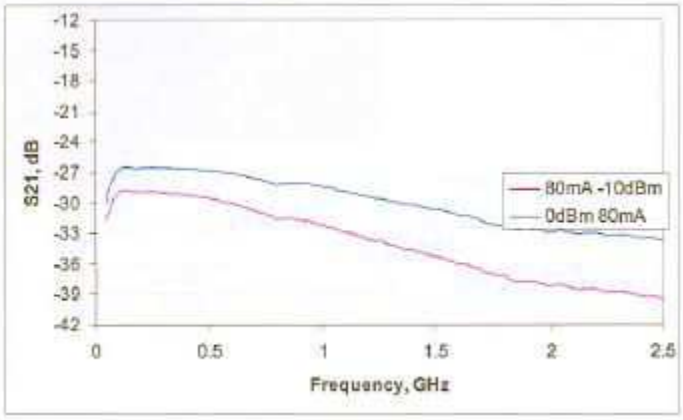

PRELIMINARY DATASHEET | SOA-RL-OEC-1550

Centre for Integrated Photonics

SOA-RL-OEC-1550 - 1.55µm Reflective Semiconductor Optical Amplifier (SOA)

Features

- 1.55µm operation
- Low polarisation dependent gain (<1.5dB)
- High small signal gain (>20dB)
- Low front facet reflectivity (<10^{-4})
- Low gain ripple (<1.5dB)
- 1.5GHz electrical bandwidth
- InP Buried Heterostructure design
- TEC cooled
- SMA style or 14 pin package available
- Available as packaged or chip-on-carrier
- APC connector provided

Application Examples

- WDM-PON colourless reflective amplifying modulator
- External cavity laser gain block
- ASE Source

Description

The SOA-RL-OEC-1550 is a low polarisation dependent gain device. It has ultra-low front facet reflectivity (<10^{-4}) and is ideal as a reflective colourless amplifying modulator in WDM-PON schemes and as a gain block for external cavity lasers. A high polarisation dependent gain device is also available (SOA-R-OEC-1550).

The SOA-RL-OEC-1550 utilises CIPs proprietary InP buried heterostructure design and is available in either a 2-pin butterfly/SMA package with a thermistor, thermo-electric cooler and single mode fibre pigtails or as a custom chip-on-carrier product. It is generally intended for use with the Angled Polished Connectors (APC) provided. The device is supplied with a 50Ω input impedance to the SMA port and has a direct modulation bandwidth of ~1.5GHz.

Optical and electrical specification

All measurements are at 20° C and 1550nm unless stated otherwise.
I = bias current, P_{in} = input optical power

Item	Test condition	Min.	Typ.	Max.	Units
Integrated ASE Power	I = 80mA		1		mW
Small Signal Gain	I = 80mA		20		dB
Gain Peak Wavelength	I = 80mA	1530		1570	nm
Polarisation Dependent Gain (PDG)	I = 80mA		1.5		dB
Noise Figure (NF)	I = 80mA		8	11	dB
Gain Ripple (R_{pl})	I = 80mA		0.5	1.5	dB
Saturated Output Power (P_{sat})	I = 80mA		3		dBm
Electrical Bandwidth (B_w)	I = 80mA P_{in} = 0dBm		1.5		GHz
Electrical Input Impedance			50		Ω

www.ciphotonics.com ....researching solutions

CIP, Adastral Park, Martlesham Heath, Ipswich, IP5 3RE, UK Tel: +44 (0) 1473 663210 info@ciphotonics.com rev E

CIP
Centre for Integrated Photonics

Absolute maximum ratings

Item	Symbol	Rating	Unit
Maximum DC current forward bias	I_{max}	85	mA
Maximum DC voltage forward bias	V_{max}	5.0	V
Maximum DC voltage reverse bias	V_{max}	2.0	V
Maximum optical input power	P_{max}	+13	dBm
RF Voltage (peak to peak)	V_{pp}	4	V
Maximum TEC current	TEC_{max}	2.0	A
Maximum TEC voltage	TEC_{max}	3.6	V
Operating temperature	T	15-40	°C
Storage temperature	T_S	10-70	°C
Fibre type	SMF-28 900um tight buffer, >1m		

Ordering Information– Part Number SOA-RL-OEC-1550

For Chip on carrier, or custom products please contact CIP Sales on +44 1473 663210 or e-mail sales@ciphotonics.com. For details of your local agent, visit www.ciphotonics.com

Wiring Diagram and Dimensions

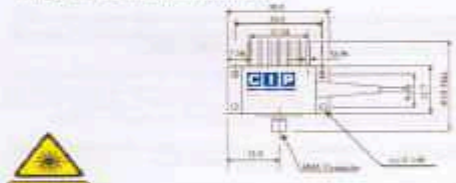

Pin Number	Connection
1	Cooler (+)
2	Cooler (-)
3	NC
4	NC
5	Case Ground
6	Thermistor (10kΩ)
7	Thermistor (10kΩ)
Dbl	Centre pin =ve (anode) Package case =ve (cathode)

Device also available in a 14 pin butterfly package

APPENDIX-B

RSOA model parameters

Parameter	Unit	Value
L	m	0.000713
w	m	2.40×10^{-6}
d	m	9.40×10^{-8}
α_0	m^{-1}	2238.801
α_N	m^2	2.39×10^{-21}
α_λ	m^{-2}	7.56×10^{10}
α_c	m^{-1}	7948.658
α_s	m^{-1}	718.8078
Γ_0		0.21301
Γ_N	m^3	-9.06×10^{-26}
Γ_λ	m^{-1}	-252327
K_g		3.0525
$\Delta\lambda_{SE}$	m	-8.09×10^{-9}
A_{st}	s^{-1}	6.01×10^{8}
B_{ns}	m^3s^{-1}	7.35×10^{-18}
C_{Au}	m^6s^{-1}	4.50×10^{-40}
N_0	m^{-3}	6.50×10^{23}
a_0	m^2	8.20×10^{-20}
a_1	m	1.2
b_0	m^4	-5.76×10^{-32}
b_1	m^7	3.53×10^{-57}
λ_{z0}	m	1.74×10^{-6}
z_0	m^4	5.44×10^{-32}
z_1	m^7	9.21×10^{-57}

APPENDIX-C

OOFDM system mathematical description

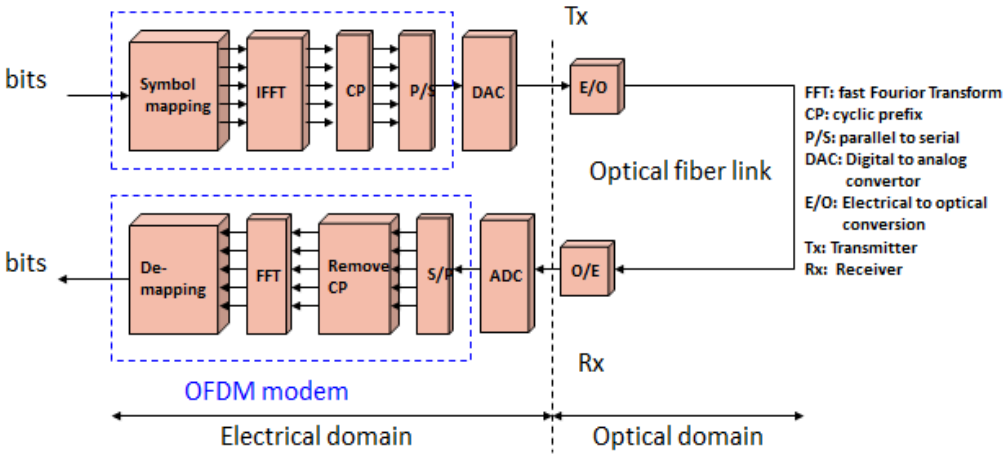

Figure a: Optical OFDM IM-DD transmission system.

A serial-to-parallel converter truncates an encoded complex data sequence into a number of sets of subcarriers. The kth subcarrier in the nth OOFDM symbol $d_{k,n}$ is given by

$$d_{k,n} = \left[R_{k,n} e^{j\theta_{k,n}} K_k\right] h(t) \qquad \text{(a.1)}$$

where the terms in the brackets in the right-hand side of (a.1) represent the k^{th} encoded data in the n^{th} symbol with the time period of T_b, $R_{k,n}$ and $\theta_{k,n}$ are defined as $R_{k,n} = \left(x_{k,n}^2 + y_{k,n}^2\right)^{1/2}$ and $\theta_{k,n} = \tan^{-1}\left(y_{k,n}/x_{k,n}\right)$ with $x_{k,n}$ and $y_{k,n}$ being the coordinates of signal constellation points, K_k is the parameter for adjusting the power of each subcarrier, and $h(t)$ is the modulation pulse shaping waveform, which is used to make different subcarriers orthogonal to each other. It is widely adopted that $h(t)$ has a rectangular pulse shape of unity magnitude over the period of T_b. Apart from real transmitted data, $d_{k,n}$ also represents pilots and training signals. The OOFDM symbol is constructed as the IFFT of the set of subcarriers. The n^{th} OOFDM symbol $\hat{S}_n(t)$can be described as

$$\hat{S}_n(t) = \sum_{k=0}^{N_S-1} d_{k,n} e^{j2\pi k\Delta f t} \tag{a.2}$$

where *Ns* is the total number of subcarriers within the OOFDM symbol, and Δf is the subcarrier frequency spacing. The symbol is a periodic function with a time period of $T_b = 1/\Delta f$. Note that in this case, each subcarrier has exactly an integer number of oscillating cycles in the time interval T_b, and the number of oscillating cycles between adjacent subcarriers differs exactly by one. This property accounts for the orthogonality between different subcarriers. The OOFDM symbol traveling in a transmission link suffers from intersymbol interference (ISI). The ISI effect can be overcome by adding a cyclic prefix to the front of each OOFDM symbol. The cyclic prefix is essentially a copy of the last fraction of each OOFDM symbol and does not carry any useful information. After inserting the cyclic prefix into the OOFDM symbol, the resulting OOFDM symbol can be expressed as

$$\bar{S}_n(t) = e^{-j2\pi\Delta f T_b} \sum_{k=0}^{N_S-1} d_{k,n} e^{j2\pi k\Delta f t} \tag{a.3}$$

where T_P is the time duration of the cyclic prefix, and the time period during which real information is carried is now reduced to $T_b - T_P$. If the cyclic prefix is larger than the expected largest delay spread to be encountered on the channel of interest, the channel dispersive effect is, therefore, localized within the prefix region only. After removing the prefix in the receiver, the fast Fourier transform (FFT) can proceed on the useful OOFDM symbols without interference between different symbols. Therefore, the cyclic prefix improves the ISI tolerance. However, the insertion of the cyclic prefix also increases the bandwidth associated with the encoded signal by a factor of $(1 + \eta)$; here, the cyclic prefix parameter η is defined as $\eta = T_P /(T_b - T_P)$. It should be pointed out that the introduction of the cyclic prefix destroys the perfect orthogonality between subcarriers, because the subcarriers may not have exactly an integer number of cycles within the symbol period. To generate the OOFDM signal sequence for signal transmission, all the OOFDM symbols obtained using (a.3) should be serialized. The concatenation of these OOFDM symbols can now be written as

$$\begin{aligned} \tilde{A}(t) &= \sum_{n=-\infty}^{\infty} \tilde{S}_n\,(t - nT_b) \\ &= \sum_{n=-\infty}^{\infty} e^{-j2\pi\Delta f T_b} \sum_{k=0}^{N_S-1} d_{k,n} e^{j2\pi k\Delta f (t-nT_b)} \end{aligned} \tag{a.4}$$

It can be seen from (a.4) that $A(t)$ is a complex function, which cannot be used to directly drive the E/O converter. To obtain a real valued OOFDM signal, the general approach for generating OOFDM symbols as described in (a.4) should be modified. Based on the folding property of discrete Fourier transform for discrete time systems, (a.4) should be written as

$$\bar{S}_n(t) = e^{-j2\pi\Delta f T_b} \sum_{k=0}^{2N_s-1} d_{ck,n}\, e^{j2\pi k\Delta f t} \tag{a.5}$$

here, for subcarriers at 0, 1, . . . , $Ns - 2$, $Ns - 1$, Ns, $Ns + 1$, . . . , $2Ns - 2$, $2Ns - 1$, $d_{ck,n}$ takes the sequence of $\{d_{0,n}, d_{1,n}, \ldots, d_{(Ns-2),n}, d_{(Ns-1),n}, d^*_{0,n}, d^*_{1,n}, \ldots, d^*_{(Ns-2),n}, d^*_{(Ns-1),n}\}$. $d_{k,n}$ ($k = 0, 1, \ldots, Ns - 2,1$) is given in (1) and $d^*_{k,n}$ is the complex conjugate of $d_{k,n}$. In addition, to achieve $Im\left(\bar{S}_n(t)\right) = 0$, $Im\left(d_{0,n}\right) = Im\left(d^*_{0,n}\right) = 0$should be satisfied. Considering the complex nature of the encoded data, the only way for satisfying this requirement is to set the powers on these two subcarriers to zero. This means that these two subcarriers are simply dropped off and not utilized for transmitting information. In (a.5), both the total number of subcarriers and the signal bandwidth are doubled when compared with (a.3). Subcarriers in both the negative and positive frequency bins carry information. However, only information contained in the positive frequency bin is recovered in the receiver after transmission. Introducing (a.5) into (a.4), the real valued OOFDM signal is given by

$$\begin{aligned} \bar{A}(t) &= \sum_{n=-\infty}^{\infty} \bar{S}_n(t - nT_b) \\ &= \sum_{n=-\infty}^{\infty} e^{-j2\pi\Delta f T_b} \sum_{k=0}^{N_s-1} d_{k,n} e^{j2\pi k\Delta f (t-nT_b)} \end{aligned} \tag{a.6}$$

To limit the OOFDM signal power given in (a.6) within a predetermined range, signal clipping is used.

OOFDM Receivers

The continuous real-valued signal waveform $A_{\mathrm{DAC}}(t)$ is able to directly drive an E/O converter to produce an optical waveform $A_{\mathrm{OPTICAL}}(t)$. The optical signal is then coupled into an SMF/MMF link under a specific launching condition. The transmitted optical signal is detected by a square-law photo detector. The detected signal is given by

$$A_{ELECTRICAL}(t) = |A_{OPTICAL}|^2 \otimes R(t) + v(t) \tag{a.6}$$

Where $R(t)$ is the impulse response of the transmission link in the electrical domain and $v(t)$ represents noise associated with the receiver. $\otimes$ is a symbol for convolution. In the work in chapter 3, both shot and thermal noises are considered, while signal–spontaneous and spontaneous–spontaneous beat noises are excluded due to the absence of optical amplifiers in the transmission link. The OOFDM receiver processes the electrical signal $A_{\mathrm{ELECTRICAL}}(t)$ using the inverse of the procedure used at the transmitter.

Mohamad HAMZE

« Etudes de différentes structures SOA pour la transmission de l'IMDD OFDM »

Résumé:

Mots-clés: Amplificateur optique à semi-conducteurs (SOA), SOA réflectif (RSOA), Modulation de type OOFDM, Modulation d'intensité et détection directe (IMDD), Modulation adaptative AMOOFDM.

Le travail de thèse porte sur une étude d'impact de différentes structures SOA sur la transmission optique de signaux OFDM modulés en intensité et reçus en détection directe (IMDD-OOFDM), dans le cadre des réseaux d'accès de nouvelle génération (NGPON). Dans la première partie du travail, nous avons d'abord validé expérimentalement la modélisation d'un RSOA sur une large plage d'utilisation. Ce modèle a ensuite été implémenté dans le cadre d'une plate-forme de co-simulation pour les systèmes de transmission IMDD-OOFDM et pour la conversion en longueur d'onde de signaux OOFDM avec une validation expérimentale. Une analyse approfondie des performances de transmission a été ensuite mené en termes de puissance optique et de longueur d'onde injectées, de longueur de fibre, de l'émission spontanée amplifiée (ASE), de la bande passante électrique et des non-linéarités du RSOA. Nous avons notamment montré théoriquement qu'une capacité minimale de transmission de 8,9 Gb/s sur 100 km pouvait être atteinte sur une plage de 100 nm avec le RSOA utilisé et avec l'aide d'une modulation adaptative (AMOOFDM). Nous avons également démontré expérimentalement, pour la première fois à notre connaissance, la conversion de longueur d'onde de signaux optiques OOFDM-16QAM sur une plage de 70 nm en utilisant l'effet XGM du RSOA.

Dans la seconde partie, nous avons développé la modélisation de plusieurs structures de SOA : un SOA à îlots quantiques (QD SOA), un SOA bi-électrodes et deux SOA cascadés en configuration contra-propagative. Nous avons étudiés leurs performances en transmission à l'aide de la modulation AMOOFDM. Nous avons montré que ces structures présentent une capacité de transmission allant jusqu'à 30 Gb/s avec des distances de transmission jusqu'à 60 km. Nous avons montré également que le QD-SOA présente de meilleures performances en termes de capacité de transmission pour des distances allant jusqu'à 140 km en comparaison avec les deux autres configurations.

Abstract:

Keywords: Semiconductor optical amplifier (SOA), RSOA, QD-SOA, orthogonal frequency division multiplexing (OFDM), Intensity modulation and direct detection (IMDD), AMOOFDM.

The thesis work deals with study of different SOA structures impact on the transmission of intensity modulation and direct detection OFDM signals in the context of the next generation access networks. In the first part of the work, we have experimentally validated a comprehensive wideband RSOA field model. It was then used as part of a co-simulation platform for IMDD-OOFDM and OOFDM wavelength conversion transmission systems. Thanks to this co-simulation platform that presents good agreement with the measurement, and our experimental setup, we analyze the transmission performance in terms of optical input power, fiber length, ASE noise, electrical bandwidth and RSOA nonlinearities. We showed by simulation that an AMOOFDM signal transmission over a 100 nm wavelength range with a minimum transmission capacity of 8.9 Gb/s for fiber lengths up to 100 km can be reached. Finally, we experimentally demonstrated, for the first time to the best of our knowledge, the feasibility of performing wavelength conversion over 70 nm of OOFDM-16QAM optical signals using the XGM effect in an RSOA.

In the second part of this work we develop a simplified quantum dot –SOA and two electrode SOA intensity modulator models and study their effect on a numerical OFDM IMDD transmission system, we also study a two cascaded SOA in a counter propagating configuration as an intensity modulator. We find that for the three configurations we can achieve a high transmission capacity of around 30 Gb/s for transmission distances up to 60 Km, we also find that the QD-SOA will have the best performance in terms of transmission capacity for distances up to 140 Km in comparison with the two other SOA configurations.